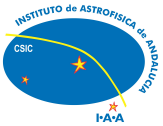

Universidad de Sevilla

Tesis doctoral
Febrero 2011

Extragalactic background light and its implications for galaxy evolution and γ-ray astronomy

[Ph. D. THESIS]

Alberto Domínguez Díaz
Universidad de Sevilla
Instituto de Astrofísica de Andalucía (CSIC)

Memoria de Tesis
presentada en la Universidad de Sevilla
para optar al grado de Doctor

Directores de tesis:
Dr. Francisco Prada Martínez
Prof. Manuel Lozano Leyva

A mis padres.

Science can teach us,
and I think our own hearts can teach us,
no longer to look round for imaginary supports,
no longer to invent allies in the sky,
but rather to look to our own efforts here below
to make this world a fit place to live in.

- Bertrand Russell -

Nothing in life is to be feared,
it is only to be understood.
Now is the time to understand more,
so that we may fear less.

- Marie Curie -

Y guiñando a la Luna, le digo amor mío,
ay que ver el Sol lo necio que ha sido
porque jamás comprenderá lo que se ha perdido.

- Jesús Bienvenido y Andrés Ramírez - Los transnochadores
(Carnaval de Cádiz)

Agradecimientos

Afortunadamente son muchas las personas a las que tengo que agradecer su apoyo, ayuda, amistad o cariño en el camino, muchas veces difícil, hasta haber llegado a completar esta tesis doctoral.

Quisiera agradecer a mi co-director de tesis Manuel Lozano por ofrecerme la oportunidad y permitirme disfrutar del lujo personal que supone, el dedicarme profesionalmente a lo que siempre he querido ser: astrofísico. También debo agradecer el apoyo de Pepe Arias. Esta tesis no hubiera sido posible sin la existencia de las becas/contratos que he disfrutado de la fundación Cámara y FPI del Ministerio de Ciencia e Innovación. Tengo que agradecer a Mariano Moles por introducirme en el tema en particular, en el que he trabajado y dedicado la mayor parte de mi tiempo durante estos últimos cinco años: la luz de fondo extragaláctica.

Esta tesis difícilmente hubiera visto la luz si no hubiera sido por el apoyo continuo tanto personal como profesional que mi co-director de tesis Paco Prada me ha dado estos últimos dos años y medio. Le estoy extraordinariamente agradecido por confiar en mi, y por todos sus consejos y enseñanzas sobre la profesión que finalmente han llevado a que esta tesis se haga realidad. Sin duda, quisiera también agradecer profundamente a Joel Primack por darme la oportunidad única de trabajar en uno de los principales centros de investigación de astronomía del mundo, la Universidad de California en Santa Cruz (UCSC). Con él, he trabajado codo con codo durante algo más de un año dandole forma a la parte principal de esta Tesis. Me ha ayudado con infinita paciencia siempre que lo he necesitado, y he tenido el inmenso placer de aprender a hacer ciencia con él.

Mi estancia en Santa Cruz ha sido, sin duda alguna, una de las experiencias más satisfactorias de mi vida, tanto a nivel personal como profesional. Allí he tenido la suerte de poder colaborar con excelentes investigadores y personas, y aprender cómo funciona un centro de investigación de primer nivel. Fundamentalmente, debo agradecer a Sandy Faber por todo el tiempo que pacientemente me ha dedicado, y su inestimable ayuda en hacerme comprender conceptos de lo que para mi era un campo de conocimiento totalmente nuevo. Igualmente agradecer a David Koo por compartir discusiones conmigo.

Muchos compañeros me han ayudado en estos años, y han sufrido montones de

preguntas por mi parte. Muy especialmente tengo que agradecer el apoyo en todo momento de Migue, también conocido como *masc*, amigo y colaborador. Una parte muy importante de la tesis se la debo a él. Además, quiero agradecer la confianza y apoyo que Miguel Ángel Pérez-Torres depositó en mi. He de agradecer a mis compañeros de la Universidad de Sevilla: Juan (quién me ha apoyado en todo momento), Miguel Antonio, Pedro y Mouloud. También, del Instituto de Astrofísica de Granada a Fabio (a quién debo una gran ayuda en las tareas de análisis de datos y comentarios a esta Tesis) y a Toño. De la colaboración MAGIC debo agradecer su ayuda, fundamentalmente en tareas de análisis, a Karsten Berger, Elisa Prandini, y Antonio Stamerra. Por suerte, también he tenido estupendos compañeros y colaboradores a los que agradecer en la UCSC: Valentino, Clementito, Feña, Javiera, Rudy, Serena, Gabor, David Rosario y Mark Mozena. Mi estancia en Santa Cruz no hubiera sido la misma sin Carlos, Giovana, Ulyses, y el tío Osvaldo, les estaré por siempre agradecidos por su cariño.

El camino hasta aqui no hubiera sido el mismo sin mis amigos y amigas: Marinero, Negri, Quino, Moncho, Dani, Jose Alonso, Momia, Neri, Juanfran, Arsenio, Perico, Caver, Javi Salas, Taki, Riki, Curro, Pelo, Boli, Rafa, Nono, Javi Alanís, Nuria, Lola, Rocío, Alba, Lucre y Cristi. Agradezco especialmente a Nuria el estar a mi lado en cualquier parte del mundo, y su cariño todos estos años.

Finalmente, debo mencionar a toda mi familia en el sentido amplio de la palabra, incluyendo tíos, primos, abuelos, y su memoria. Muy especialmente he de mencionar a mis hermanos, Ale y Patricia, y el mayor abrazo de todos es para quienes dedico esta Tesis, mis padres (má y pá): Pepy y Antonio. Ellos son de donde vengo, y quienes me han señalado el camino a seguir.

Resumen

Durante mi doctorado me he dedicado a estudiar la luz de fondo extragaláctica (EBL de sus siglas en inglés), tanto desde el punto de visto de la evolución de galaxias como sus consecuencias para la propagación de fotones γ. He adquirido experiencia observacional y en análisis de datos con el telescopio Čerenkov MAGIC, y he participado activamente en los grupos de trabajos de AGNs y GRBs de la colaboración. También he investigado la detectabilidad de alguna de las características espectrales esperadas en los espectros γ de AGNs como consecuencia de la existencia de las particulas denominadas *axion-like*.

La EBL es de importancia fundamental tanto para entender completamente el proceso de evolución de galaxias como para la astronomía γ. Sin embargo, el espectro completo de la EBL no ha sido determinado todavía ni a partir de funciones de luminosidad de galaxias (LFs de sus siglas en inglés) observadas sobre un rango amplio de corrimientos al rojo, z, ni a partir de observaciones multifrecuencia de distribuciones espectrales de energia (SEDs de sus siglas en inglés) de galaxias.

La detección directa de la EBL es una tarea muy difícil debido a la enorme contaminación de la luz zodiacal. Otras técnicas establecen límites al fondo tales como el recuento de galaxias usando sondeos profundos (los cuales proporcionan límites inferiores) ó la observación de rayos γ provenientes de AGNs ó GRBs (los cuales proporcionan límites superiores). Existen aproximaciones fenomenológicas centradas en derivar el espectro completo de la EBL local a la vez que su evolución en el tiempo. Estas aproximaciones pueden dividirse en cuatro grupos:

(i) Evolución hacia delante. Esto es una aproximación teórica que sigue la evolución de galaxias usando modelos semi-analíticos.

(ii) Evolución hacia detrás, la cual comienza con observaciones de funciones de luminosidad de galaxias locales (o de bajo corrimiento al rojo) y las extrapola hasta corrimientos al rojo más altos.

(iii) Evolución de la población de galaxias inferida sobre corrimiento al rojo. La evolución de galaxias es inferida aqui usando alguna cantidad derivada de observaciones tales como la tasa de formación estelar (SFR de sus siglas en inglés) del universo.

(iv) Evolución de la población de galaxias directamente observada sobre el rango de corrimientos al rojo que contribuye significativamente a la EBL.

En esta tesis construyo por primera vez un modelo empírico tipo (iv) diréctamente a partir de la observación en el infrarojo cercano de la evolución de la LF hasta corrimiento al rojo 4 dada en otro trabajo. Esta LF es la mejor medida hasta la fecha de la evolución cosmológica de galaxias en la banda K, donde la absorción de polvo es menos severa que en las bandas ópticas. Esto se combina con una estimación de fracciones de galaxias según su SED en el rango de corrimiento al rojo 0.2-1 a partir de un catálogo multifrecuencia de $\sim$6000 galaxias del sondeo All-wavelength Extended Groth Strip International Survey (AEGIS). La caracterización de las SEDs de galaxias se basa en ajustar la fotometría en nuestro catálogo, desde el ultravioleta (UV de sus siglas en inglés) hasta el infrarojo (IR de sus siglas en inglés), a la librería SWIRE, la cual contiene 25 SEDs diferentes y completas (incluyendo galaxias con AGNs).

Nuestra metodología consiste en contar galaxias para normalizar el modelo usando la función de luminosidad (a partir de otro trabajo, tal cómo se ha mencionado anteriormente) y asociar estadísticamente a cada galaxia en la LF un tipo de SED de SWIRE en tres rangos diferentes de magnitud. A partir de aquí, se calculan densidades de luminosidad desde el UV hasta el IR lejano hasta corrimiento al rojo 4. Integrando estas densidades de luminosidad en el tiempo se estima directamente la evolución de la EBL y su formación. Se calculan además otros observables tales como la densidad de SFR del universo ó la contribución a la EBL bolométrica a partir de las diferentes poblaciones de galaxias. Estos son discutidos y comparados con datos y otros modelos. También se calculan directamente las incertidumbres en la EBL.

La EBL tiene importantes consecuencias para la astronomía de rayos γ porque fotones de muy alta energía (VHE de sus siglas en inglés, 30 GeV-30 TeV) provenientes de fuentes extragalácticas son atenuados por producción de pares con fotones de la EBL. Conocer la EBL es esencial para corregir los espectros observados a VHE y recuperar los espectros que observariamos si no hubiera efecto de la EBL (el conocido como espectro *intrínseco*). Todas las fuentes cosmológicas observadas en el régimen de VHE debe ser corregido por este efecto para estudiar las propiedades intrínsecas de las fuentes. Se deriva la atenuación de rayos γ a partir de nuestro modelo y se aplica a algunos blazars extremos observados con telescopios Čerenkov: Mrk 501 ($z = 0.034$) observado usando los telescopios HEGRA hasta más de 20 TeV, 3C 279 ($z = 0.536$) observado por la colaboración MAGIC, y 3C 66A ($z = 0.444$) observado con los telescopios VERITAS.

Como miembro de la colaboración MAGIC he participado activamente en los grupos de trabajo de AGNs y GRBs, realizando algunas campañas observacionales. He tenido la oportunidad de reducir datos y analizar algunos GRBs y AGNs como los presentados en esta tesis: GRB 100316A y PKS 1222+216. Discuto los límites que observaciones de rayos γ establecen en la intensidad de EBL (en consecuencia, a la

evolución de galaxias) a partir de suposiciones en los espectros intrínsecos de VHE, y los límites que los espectros intrínsecos de VHE establecen en el conocimiento actual en los mecanismos de emisión a VHE. A partir de la precisión en los espectros recuperado, se concluye que la EBL es bien conocida desde el UV hasta el IR medio, pero que se necesitan esfuerzos independientes de astronomía IR y de rayos γ para reducir las incertidumbres en el IR lejano.

La emisión a VHE en blazars está en general bien descrita por el modelo sincrotrón auto-Compton (SSC de sus siglas en inglés). Sin embargo, observaciones recientes a VHE parecen llevar a espectros tan pronunciandos y variables que difícilmente son descritos por el modelo SSC estándar. Hay algunas soluciones a estas observaciones tales como altas incertidumbres sistemáticas y estadísticas en las observaciones de rayos γ, o alguna extensión al SSC estándar, pero incluso así estos son resultados muy desafiantes. Otra interesante posibilidad viene de física no estándar. Se postula la existencia de axiones o partículas como axiones (ALPs de sus siglas en inglés) que en la presencia de campos magnéticos (dentro de los blazars o a través del medio intergaláctico, (IGM de sus siglas en inglés) pueden oscilar a fotones y vice-versa permitiendo atravesar la EBL sin interacciones, y así reduciendo la atenuación esperada. Esta posibilidad fue explorada teóricamente en un trabajo anterior, en el cúal participé, poniendo en el mismo marco el efecto esperado en la fuente y a través del IGM, y es aplicada y discutida en esta tesis a observaciones reales de blazars.

La Tesis esta organizada de la siguiente forma: el Capítulo 1 da una breve introducción al presente conocimiento sobre evolución de galaxias y su relación con los diferentes campos de radiación que llenan el universo. El Capítulo 2 describe la construcción de un modelo empírico para la EBL a partir de LF, un catálogo multifrecuencia de galaxias, y de plantillas de galaxias. El Capítulo 3 revisa la técnica Čherenkov para la observación de rayos-γ de fuentes astronómicas, y se centra en una descripción del experimento MAGIC, y su cadena de análisis con dos ejemplos de análisis dados en el Capítulo 4. El Capítulo 5 muestra la atenuación computada para nuestro modelo de EBL para fuentes de VHE tomadas de la literatura. Se da una descripción del efecto que ALPs podría tener sobre observaciones reales de espectros de VHE en el Capítulo 6. Finalmente, en el Capítulo 7 se destacan algunas conclusiones, y se presentan planes de futuras investigaciones en el Capítulo 8.

Summary

During my Ph. D. I have been focused on understanding the extragalactic background light (EBL) from the galaxy evolution point of view as well as its consequences for the propagation of extragalactic γ-ray photons. I have acquired observational and data-analysis experience with the MAGIC Čerenkov telescopes, and been actively involved in the AGN and GRB MAGIC working group. I have also investigated the detectability of some signature in the AGN γ-ray spectra derived from the postulated existence of axion-like particles.

The EBL is of fundamental importance both for understanding the entire process of galaxy evolution and for γ-ray astronomy. But the overall spectrum of the EBL has never been determined directly from galaxy luminosity functions (LFs) over a wide redshift, z, range and from multiwavelength observations of galaxy spectral energy distributions (SEDs).

The direct observation of the EBL is a difficult task due to the huge contamination from zodiacal light. Other techniques set limits on the background such as measuring galaxy counts using deep surveys (which provides lower limits) or the γ-ray observation of AGNs or GRBs (which provides upper limits). There are phenomenological approaches focused on deriving an overall spectrum of the local EBL as well as its evolution over redshift. These approaches may be divided in four different groups:

(i) Forward evolution. This is a theoretical approach that follows galaxy evolution using semi-analytical models.

(ii) Backward evolution, which begins with local or low-redshift observation of galaxy LFs and extrapolates them to higher redshifts.

(iii) Evolution of the galaxy population inferred over redshift. The galaxy evolution is inferred here using some quantity derived from observations such as the star formation rate (SFR) density of the universe.

(iv) Evolution of the galaxy population directly observed over the range of redshifts that contributes significantly to the EBL.

In this dissertation I build for the first time an empirical model type (iv) directly from the observation in the near-IR of the evolving galaxy LF up to redshift 4 given by other work. This LF is the best measurement to date of the cosmological galaxy evolution in the K-band, where dust absorption is less severe than in optical bands. This is combined with an estimation of galaxy SED-type fractions in the redshift range 0.2-1 from a multiwavelength catalog of $\sim$6000 galaxies from the All-wavelength Extended Groth Strip International Survey (AEGIS). The characterization of the galaxy SEDs relies on fitting the photometry in our catalog, from the ultraviolet (UV) to the infrared (IR), to the SWIRE template library, which contains 25 different overall galaxy SEDs (including AGN-galaxies).

Our methodology consists on counting galaxies for normalizing the model using the LF by the other work mentioned above, and attaching statistically a SWIRE SED-type to every galaxy in the LF in three different magnitude ranges. From here, luminosity densities from the UV up to the far-IR are calculated up to redshift 4. Integrating these luminosity densities over redshift the evolving EBL and its build up is directly estimated. Other observables such as the SFR density of the universe or the contribution to the bolometric EBL from the different galaxy populations are calculated, discussed, and compared with data and other models. The EBL uncertainties directly from the data are calculated as well.

The EBL has important consequences for γ-ray astronomy because very high energy (VHE, 30 GeV-30 TeV) photons coming from extragalactic sources are attenuated by pair-production with EBL photons. It is essential to know the EBL to correct the observed VHE spectra and to recover the spectra that would be observed if there were no effect from the EBL (the so-called *intrinsic* spectra). All the cosmological sources observed in the VHE regime must be corrected by this effect in order to study intrinsic properties of the sources. The γ-ray attenuation from our EBL model is derived and applied to some extreme blazars observed with Čerenkov telescopes: Mrk 501 ($z = 0.034$) observed using the HEGRA telescopes up to more than 20 TeV, 3C 279 ($z = 0.536$) observed by the MAGIC collaboration, and 3C 66A ($z = 0.444$) observed with the VERITAS telescopes.

I am a full member of the MAGIC collaboration, which is an array of the two largest Čerenkov telescopes with the lowest energy threshold, interested on measuring γ-ray photons in the VHE range. As an active member of the AGN and GRB working group I describe in my dissertation the MAGIC experiment, the analysis chain, and several observational tasks done through my Ph. D. such as observational campaigns, daily technical checks, and the analysis of GRBs and AGNs: GRB 100316A and PKS 1222+216. I discuss the constraints that γ-ray observations set on the EBL intensity (therefore to galaxy evolution) from assumptions on the intrinsic VHE spectra, and the constraints that intrinsic VHE spectra calculated using our model set to the current knowledge on the VHE emission mechanisms. From the precision in the recovered spectra, it is concluded that the EBL is well constrained from the UV to the mid-IR, but independent efforts from IR and γ-ray astronomy are needed

in order to reduce the uncertainties in the far-IR.

The VHE emission in blazars is in general well described by the synchrotron self-Compton (SSC) model. But recent VHE observations seem to lead to so steep and variable spectra that are hardly described by the standard SSC model. There are some solutions to these observations such as very high systematic and statistical uncertainties in the γ-ray observations, or some extension to the standard SSC, but still these are very challenging results. Another exciting possibility comes from non-standard physics. It is postulated the existence of axions and axion-like particles (ALPs) that in the presence of magnetic fields (within the blazars or through the intergalactic medium, IGM) may oscillate into photons and vice-versa allowing to come through the EBL with no interaction, thus reducing the expected attenuation. This last possibility was theoretically explored putting together in the same framework the expected effect within the source and through the IGM in a previous work, which I participated in, and is applied and discussed in this dissertation to real observations of blazars.

This Thesis is organized as follows: Chapter 1 gives a brief introduction to the current understanding on galaxy evolution and its relation with the different background radiation fields filling the universe. Chapter 2 describes the building of an empirical model for the EBL from LF, a multiwavelength galaxy catalogue, and galaxy templates. Chapter 3 reviews the Čerenkov technique for astronomical γ-ray observations, and focuses on a description of the MAGIC experiment, and its analysis chain with two analysis examples given in Chapter 4. Chapter 5 shows the attenuation computed from our EBL model for some VHE sources taken from the literature. A description of the effect that ALPs might have on real VHE γ-ray spectra is given in Chapter 6. Finally, in Chapter 7 some conclusions are highlighted, and future research plans are presented in Chapter 8.

Index

List of Tables

List of Figures

1

Introduction

In the last years a huge progress in the knowledge about how galaxies form and evolve has been made thanks to the enormous galaxy data sets that are now available from multiwavelength studies and to the establishment of a standard framework for describing the properties of our universe.

1.1 The Λ cold dark matter cosmological framework

At the beginning of the twentieth century there were still intense debates between astronomers because of the nature of *spiral nebulae* observed in the sky. It was not clear at that time whether those nebulae were either in our galaxy (which was suppose to be all the universe) or *island universes* outside our galaxy (being the universe much larger than previously thought). Vesto Slipher observed back in 1912 the first Doppler shifts in some of these *spiral nebulae* discovering that almost all such nebulae were going away from us but he did not grasp the cosmological implications of this fact. Albert Einstein published his general relativity theory in 1915, which describes the fundamental interaction of gravitation as a result of space-time being curved by matter and energy. In 1922 Alexander Friedmann derived some equations from the Albert Einstein equations of general relativity making some simply assumptions about the universe such as isotropy and homogeneity at large scales, also known as the cosmological principle. The Friedmann equations led necessarily to a dynamic universe. Alternatively, Hubble started to develop in 1924 a series of distance indicators using the 2.5 m (100 inch) Hooker telescope at Mount Wilson Observatory. This allowed him to estimate distances to spiral nebulae whose redshifts had already been measured mainly by Slipher. In 1929, Hubble discovered a correlation between distance and recession velocity (if the redshift is interpreted as a measure of recession speed), which is now known as Hubble's law and the confirmation that those spiral nebulae were indeed outside our own galaxy. An essential result from the Hubble research was that galaxies where moving away from each other in such a way that

the greater the distance between any two galaxies, the greater their relative speed of separation. This observational fact discovered by Hubble was supported by the solutions to the Friedmann equations found by Georges Lemaître in 1927 of an expanding universe. In 1931 Lemaître went further and suggested that the evident expansion in forward time required that the Universe contracted backwards in time, and would continue to do so until it could contract no further, bringing all the mass of the universe into a single point where and when the fabric of time and space came into existence. Later, this hypothesis was called the Big Bang model. The Big Bang was the event which led to the formation of the universe. According to this model, the universe was originally in an extremely hot and dense state that expanded rapidly. It has since then cooled by expanding to the present diluted state, and continues to expand today.

During the 1930s other cosmologies were proposed to explain Hubble's observations: the Milne model, the oscillatory universe (originally suggested by Friedmann, but advocated by Albert Einstein and Richard Tolman), and Fritz Zwicky's tired light hypothesis. In 1948, independently, Fred Hoyle and Hermann Bondi & Thomas Gold proposed the Steady State model, whereby new matter is created as the universe seemed to expand, nevertheless it does not change its appearance over time, and it does not have neither a beginning nor an end. The universe in this model was flat, infinitely large, infinitely old (homogeneity and isotropy were extended in time as well as space) and was continuously creating matter to stabilize the mass energy density of the expanding space. In this model, the universe is roughly the same at any point in time.

The following years, the Steady State and the Big Bang models were the dominant cosmological pictures. Alternatively, other researchers advocated of the Big Bang model such as George Gamow introduced the big bang nucleosynthesis (whose predictions on element abundance in the universe would be confirmed by observations) and whose associates, Ralph Alpher & Robert Herman, predicted the cosmic microwave background (CMB) radiation (see Sec. 1.4.3). Eventually, the observational evidence, most notably from radio source counts, began to favor Big Bang over Steady State. Other problems with the Steady State model began to emerge in the late 1960s, when observations apparently supported the idea that the universe was in fact changing: quasars and radio galaxies were found only at large distances (therefore existing only in the distant past), not in closer galaxies. Whereas the Big Bang model predicted as much, Steady State predicted that such objects would be found everywhere, including close to our own galaxy. The discovery and confirmation of the CMB radiation in 1964 (already predicted by Gamow and some properties by Alpher & Herman) by Arno Penzias & Robert Willson secured the Big Bang as the most suitable model of the origin and evolution of the cosmos. Within the Steady State theory this background radiation is the result of light from ancient stars which has been scattered by galactic dust. However, this explanation has been unconvincing to most cosmologists as the CMB is very smooth, making it difficult to explain

how it arose from point sources, and the microwave background shows no evidence of features such as strong polarization which are normally associated with scattering. Furthermore, its spectrum is so close to that of an ideal black body that it could hardly be formed by the superposition of contributions from dust clumps at different temperatures as well as at different redshifts.

In parallel to these facts, in the 1930s Fritz Zwicky tried to explain some observations of velocity dispersion in galaxy clusters introducing a non-visible type of matter called *dark matter*. (This is that it does not emit any electromagnetic radiation.) More and more data came in the following years at galactic (see review from Bertone, Hooper & Silk 2005), galaxy cluster, and cosmological scales (Spergel et al. 2007) supporting the existence of large amounts of this elusive kind of matter in order to explain observations. Many observational evidences of the existence of dark matter came later: rotational speeds of galaxies, orbital velocities of galaxies within clusters, gravitational lensing, morphology of the CMB, the light element abundances and large scale structure. Since then, there have been proposed a very large number of candidates to dark matter, ranging from already known objects such as brown dwarfs to exotic particles such as neutralinos, or axions (see Chap. 6).

Since the late 1990s huge strides in Big Bang cosmology have been made as a result of major advances in telescope technology as well as the analysis of copious data from satellites such as the Cosmic Background Explorer (COBE) and the Hubble Space Telescope (HST). Thanks to the study of the CMB by the COBE satellite the prediction about the nature of dark matter being *cold* (Blumenthal et al. 1985, in opposition to *hot* and *warm* describing dark matter properties such as mass) was confirmed. Later discoveries by Colless et al. (2001) (see Fig. 1.1) on the observed large scale structure of the universe confirmed these results. Even more precise and accurate measurements of many of the parameters of the Big Bang model are now available thanks to the Wilkinson Microwave Anisotropy Probe (WMAP) (Komatsu et al. 2011) and better will be with data by the Planck satellite already launched in 2009.

Another unexpected discovery came in 1998 from observations of type Ia supernovae (Riess et al. 1998). The expansion of the universe appears to be accelerating. This is modeled in the Einstein general relativity equations as the cosmological constant Λ that represents a *vacuum energy* associated with space-time itself, rather than its matter content, and is a source of gravitational field even in the absence of matter. The contribution of such vacuum energy to the total energy of the universe seems to be crucial, attending to the analysis of type Ia supernovae (Perlmutter et al. 1999) and the estimations of the cosmological parameters from the CMB (Komatsu et al. 2011; Larson et al. 2011).

The joint model that put together the Big Bang with a universe dominated by dark energy and dark matter is the current standard model in cosmology called Λ cold dark matter (ΛCDM). Table 1.1 shows the best fit parameters of the ΛCDM framework using the latest data from the CMB measured by WMAP shown in Fig. 1.2. The flat

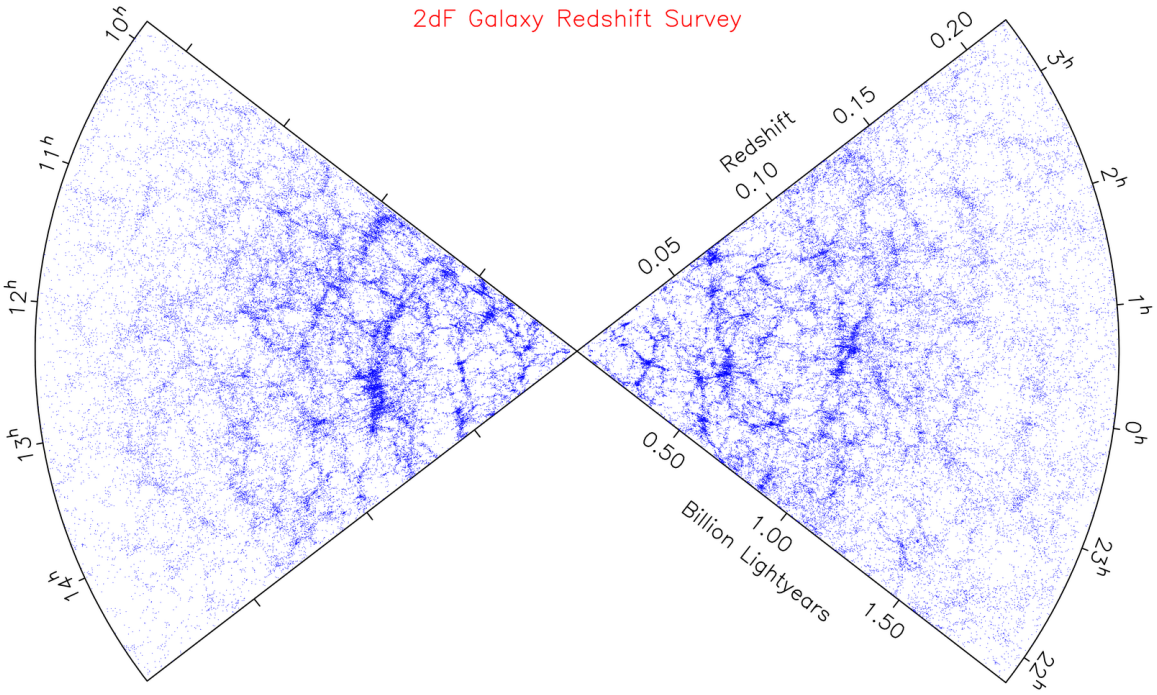

Figure 1.1 The portion of the universe surveyed by the 2dF Galaxy Survey (Colless et al. 2001). Every blue point is a galaxy and the Earth is at the center of the plot. It is noticeable how galaxies are distributed in filaments between voids. A universe dominated by hot dark matter would have a different structure than this.

universe described by the ΛCDM cosmology has three main components: baryonic matter (protons, neutrons, and electrons[1]), cold dark matter, and dark energy. The relative quantities are given by $\sim 4\%$, $\sim 21\%$, and $\sim 75\%$, respectively.

The result of intense researches over a century both from the theoretical as well as the observational side led to the ΛCDM paradigm, or standard model, that describes an accelerated expanding universe dominated by an unknown type of energy and matter, but with a behaviour well determined as a whole. The ΛCDM model is remarkable in that it describes a dynamic, evolving universe, from the initial singularity, inflation, spatial expansion and the creation of all matter through the formation of more than 100 billion visible galaxies from a fixed quantity of matter. It foretells a future in which the metric expansion of space will carry all galaxies away from each other at speeds greater than light, and observers in each galaxy will see only their own galaxy in an otherwise empty universe.

There is currently active research into many aspects of the ΛCDM model, which is likely to slightly (or strongly) change as new information becomes available due to some known problems, both from the theoretical as well as observational point of

[1]In cosmology, it is standard practice to include electrons in the same group that baryons, though are actually leptons.

WMAP Cosmological Parameters Model: lcdm+sz+lens Data: wmap7			
$10^2\Omega_b h^2$	$2.258^{+0.057}_{-0.056}$	$1-n_s$	0.037 ± 0.014
$1-n_s$	$0.0079 < 1-n_s < 0.0642$ (95% CL)	$A_{\rm BAO}(z=0.35)$	$0.463^{+0.021}_{-0.020}$
C_{220}	5763^{+38}_{-40}	$d_A(z_{\rm eq})$	14281^{+158}_{-161} Mpc
$d_A(z_*)$	14116^{+160}_{-163} Mpc	$\Delta^2_{\mathcal{R}}$	$(2.43 \pm 0.11) \times 10^{-9}$
h	0.710 ± 0.025	H_0	71.0 ± 2.5 km/s/Mpc
$k_{\rm eq}$	$0.00974^{+0.00041}_{-0.00040}$	$\ell_{\rm eq}$	137.5 ± 4.3
ℓ_*	302.44 ± 0.80	n_s	0.963 ± 0.014
Ω_b	0.0449 ± 0.0028	$\Omega_b h^2$	$0.02258^{+0.00057}_{-0.00056}$
Ω_c	0.222 ± 0.026	$\Omega_c h^2$	0.1109 ± 0.0056
Ω_Λ	0.734 ± 0.029	Ω_m	0.266 ± 0.029
$\Omega_m h^2$	$0.1334^{+0.0056}_{-0.0055}$	$r_{\rm hor}(z_{\rm dec})$	285.5 ± 3.0 Mpc
$r_s(z_d)$	153.2 ± 1.7 Mpc	$r_s(z_d)/D_v(z=0.2)$	$0.1922^{+0.0072}_{-0.0073}$
$r_s(z_d)/D_v(z=0.35)$	$0.1153^{+0.0038}_{-0.0039}$	$r_s(z_*)$	$146.6^{+1.5}_{-1.6}$ Mpc
R	1.719 ± 0.019	σ_8	0.801 ± 0.030
$A_{\rm SZ}$	$0.97^{+0.68}_{-0.97}$	t_0	13.75 ± 0.13 Gyr
τ	0.088 ± 0.015	θ_*	0.010388 ± 0.000027
θ_*	0.5952 ± 0.0016 °	t_*	379164^{+5187}_{-5243} yr
$z_{\rm dec}$	1088.2 ± 1.2	z_d	1020.3 ± 1.4
$z_{\rm eq}$	3196^{+134}_{-133}	$z_{\rm reion}$	10.5 ± 1.2
z_*	$1090.79^{+0.94}_{-0.92}$		

Table 1.1 Best fit parameters to the CMB from seven years of WMAP data for a ΛCDM cosmology. See Komatsu et al. (2011) for details and a description of every parameter.

view. From the theoretical side, the main problems might be briefly summarized in two points (e.g., Copeland, Sami & Tsujikawa 2006):

(i) The fine tuning problem: What is the physical mechanism that sets the value of Λ to its observed value which is 120 orders of magnitude smaller than the physically anticipated value, i.e., the natural energy scale of quantum gravity?

(ii) The coincidence problem: Why is the energy density corresponding to the cosmological constant just starting to dominate the Universe at the present cosmological time?

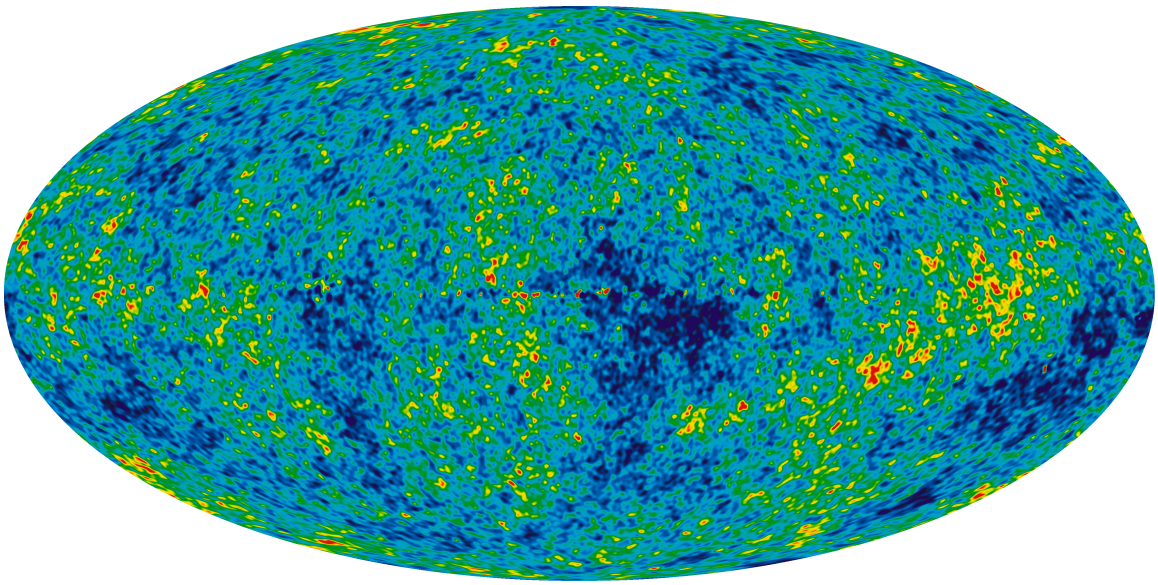

Figure 1.2 The detailed, all-sky picture of the infant universe created from seven years of WMAP data. The image reveals 13.7 billion year old temperature fluctuations (shown as color differences) that correspond to the seeds that grew to become the galaxies. The signal from our Galaxy was subtracted using the multi-frequency data. This image shows a temperature range of ± 200 μK. Image from http://map.gsfc.nasa.gov/media/101080/index.html

In addition, ΛCDM has no explicit physical theory for the origin or physical nature of dark matter or dark energy.

Observationally and generally speaking, the strongest problem focuses on the description of small scale structures (see Sánchez-Conde 2009):

(i) Large scale velocity flows: ΛCDM predicts significantly smaller amplitude and scale of flows than what observations indicate (e.g., Kashlinsky et al. 2008; Watkins, Feldman & Hudson 2009).

(ii) Brightness of type Ia supernovae at high redshift: ΛCDM predicts fainter type Ia supernovae at high z (Perivolaropoulos & Shafieloo 2009).

(iii) Emptiness of voids: ΛCDM predicts more dwarf or irregular galaxies in voids than observed (e.g., Tikhonov & Klypin 2009).

(iv) Profiles of cluster haloes: ΛCDM predicts shallow low concentration and density profiles in contrast to observations which indicate denser high concentration cluster haloes (Broadhurst et al. 2008).

(v) Profiles of galaxy haloes: ΛCDM predicts halo mass profiles with cuspy cores and low outer density while lensing and dynamical observations indicate a cen-

tral core of constant density and a flattish high dark mass density outer profile (de Blok 2005; Gentile, Tonini & Salucci 2007).

(vi) Missing satellites problem: N-body ΛCDM cosmological simulations seem to give much more substructure of dark matter within clusters and galactic haloes than what is observed (e.g., Klypin et al. 1999). It is not clear, however, how serious these problems are in view of the large uncertainties and different results obtained by different groups working in the field. Moreover, the recent discoveries of ultra-faint dwarfs in the Milky Way halo may alleviate this problem considerably (see Kravtsov 2010 for a recent review on this issue).

(vii) Sizable population of disk galaxies: ΛCDM predicts a smaller fraction of disk galaxies due to recent mergers expected to disrupt cold rotationally supported disks (Bullock, Stewart & Purcell 2009).

1.2 Structure formation in a ΛCDM universe

Galaxies are the building blocks of the universe. We aim in this section to briefly describe the current paradigm about how galaxies form and evolve in a ΛCDM universe. The key ingredients in modern theories of galaxy formation within a hierarchical clustering framework (described in Sec. 1.2.3) include radiative cooling of gas, star formation, evolution of stellar populations, metal enrichment of the interstellar medium (ISM) and intergalactic medium (IGM), galaxy merging within dark matter haloes, dynamical evolution, and supernova and active galactic nucleus (AGN) feedback. Details may be found elsewhere (e.g., Mo, van den Bosch & White 2010).

1.2.1 Initial conditions, gravitational instability, and gas cooling

The first structures in the universe formed from deviations from perfect uniformity at very early times of the universe. At this time, the universe was so dense that quantum effects are expected to be dominant, therefore a classical, general relativistic description is not valid any more. These early perturbations are thought to be consequences of quantum fluctuations in the density of the universe.

From these perturbations, a region with an overdensity will grow further in time by gravitational effects. This amplification of density perturbations are known as gravitational instability and are the seeds of larger structures. Gravitational instabilities are dependent of the cosmological model, and therefore the structures that will form later on. This is one reason why the universe that we observe today constrains cosmology, favoring a cold rather than a hot dark matter dominated universe. Non-linear, quasi-equilibrium dark matter objects as consequences of gravitational collapses (dependent on the matter content of the perturbation) play an essential role in modern theories of galaxy formation.

In a ΛCDM universe, the initial perturbations contain baryonic gas and collisionless dark matter in roughly their universal proportions. When the larger perturbation collapses, the dark matter relaxes violently to form a dark matter halo, while the gas shocks to the virial temperature, and may settle into hydrostatic equilibrium in the potential well of the dark matter halo if cooling is slow.

Gas cooling may be produced by several mechanisms depending on the temperature and density of the gas (this is generally more effective in higher density regions). If cooling time is short, the gas never comes to hydrostatic equilibrium, but rather accretes directly onto the central protogalaxy. The last consequence of cooling is that the baryonic material decouples from the dark matter halo, and accumulates as dense, cold gas in a protogalaxy at the center of the halo. In this cooling process the small angular momentum of the halo, as well as of the gas, may be conserved leading to a cold disk (a disk galaxy) in centrifugal equilibrium at the center of the halo.

1.2.2 Star formation, ISM, and IGM

Eventually, in the presence of effective cooling, all the gas flowing inwards will collapse when its self gravity dominates over the gravity of the dark matter. The gas will fragment into small pieces that will form stars. There are two star formation modes supported by observations. A *quiescent* mode in isolated disks, which usually is modelled using the empirical Schmidt-Kennicut relation (Kennicutt 1998), assuming that only gas above a fixed critical surface density forms stars. Another mode to form stars is merger-driven (see Sec. 1.2.3) known as *starburst* mode. The efficiency and timescale of the merger-driven burst mode is a function of merger ratio and the gas fraction of the progenitors (see e.g., Somerville et al. 2008). It is not clear the relative importance between the both methods, and whether this evolves with redshift. One essential quantity (still poorly known) to understand star formation is the initial mass function (IMF). It describes how mass is distributed to form stars. It is not clear whether this quantity evolves with redshift, or whether both star formation modes produce stellar populations with the same IMF.

Stars are mainly described by non-independent parameters such as masses, temperatures, luminosities, colors, ages and metallicities. Out of all these quantities colors and metallicities might need further clarification. It is known as color between the photometric bands A and B (c_{AB}) the ratio of fluxes near the effective wavelength of the two different photometric bands. Analytically, this is shown in Eq. 1.1.

$$c_{AB} = m_A - m_B = \text{const} - 2.5 \log \frac{\int_0^\infty d\lambda S_\lambda(A) f_\lambda}{\int_0^\infty d\lambda S_\lambda(B) f_\lambda} \tag{1.1}$$

where m_A and m_B are called magnitudes in the photometric band A and B, respectively. S_λ and S_λ are the telescope-receiver-filter sensitivity and f_λ the flux per unit wavelength interval. When fluxes are assumed as measured at 10 pc[2], magnitudes

[2]Distance from Earth at which stellar parallax is 1 second of arc. It is equivalent to 3.26 light

are known as absolutes.

In astronomy, it is known as metal any chemical element heavier than helium. The mass fraction of a baryonic component (e.g., hot gas, cold gas, stars) in metals is then referred to as its metallicity.

The theory of stellar evolution (unlike galaxy formation) is reasonably well understood. (Even though the understanding is not as good in the near-infrared (IR), where there are still significant uncertainties regarding the importance of contributions from thermally pulsating asymptotic giant branch stars, Maraston 2005.) It is a well known fact that stars plotted in a luminosity-temperature (or luminosity-color) diagram groups in different regions (see Fig. 1.3 and its caption for details). From a given set of initial conditions such as mass and metallicity, it is possible to compute the stellar emission and its evolution. Furthermore, if the star-formation history of the galaxy is known and we assume an IMF we can calculate the stellar emission from the galaxy (adding all the spectra from all the stars) and its evolution over time. This is done with some simple stellar population (SSP) synthesis code such as Bruzual & Charlot (2003) or Maraston (2005). In addition, these codes also give us the rates at which mass, energy, and metals are ejected into the ISM. It is important to stress that nuclear reactions during the first three minutes of the universe (also known as epoch of primordial nucleosynthesis) produced primarily hydrogen ($\sim 75\%$) and helium ($\sim 25\%$), with a very small admixture of metals dominated by lithium. Before confirmed by observations, this result was predicted by the Big Bang model. All other metals in the universe were formed at later times as a consequence of nuclear reactions in stars. When stars expel mass in stellar winds, or in supernova explosions, they enrich the ISM with newly synthesized metals. The evolution of the ISM is important because of several reasons: the luminosity and color of a stellar population depend not only on its age and IMF, but also on the metallicity of the stars. Cooling efficiency of gas depends strongly on its metallicity. Small particles of heavy elements known as dust grains play a fundamental role in absorption and re-emission of stellar light, therefore on the emitted galaxy spectral energy distribution (SED).

The most difficult part of calculating a full SED of a galaxy is the absorption and re-emission by dust. This is because the amount of radiation absorbed is strongly dependent of dust properties such as its chemical composition, geometry, and its distribution of sizes. A possible AGN should be considered as well for calculating a full galaxy SED, task that is still far from being completely understood.

The IGM is the baryonic material lying between galaxies, which galaxies form from. This is the dominant baryonic component of the universe. Its understanding is essential to understand how galaxies form and evolves, given the fact that galaxies are not isolated system but are continuously exchanging matter and energy with the IGM. The study of quasar spectra going through all the intergalactic material has become a very important tool to the study of the IGM.

---

years or 3.1×10^{13} km.

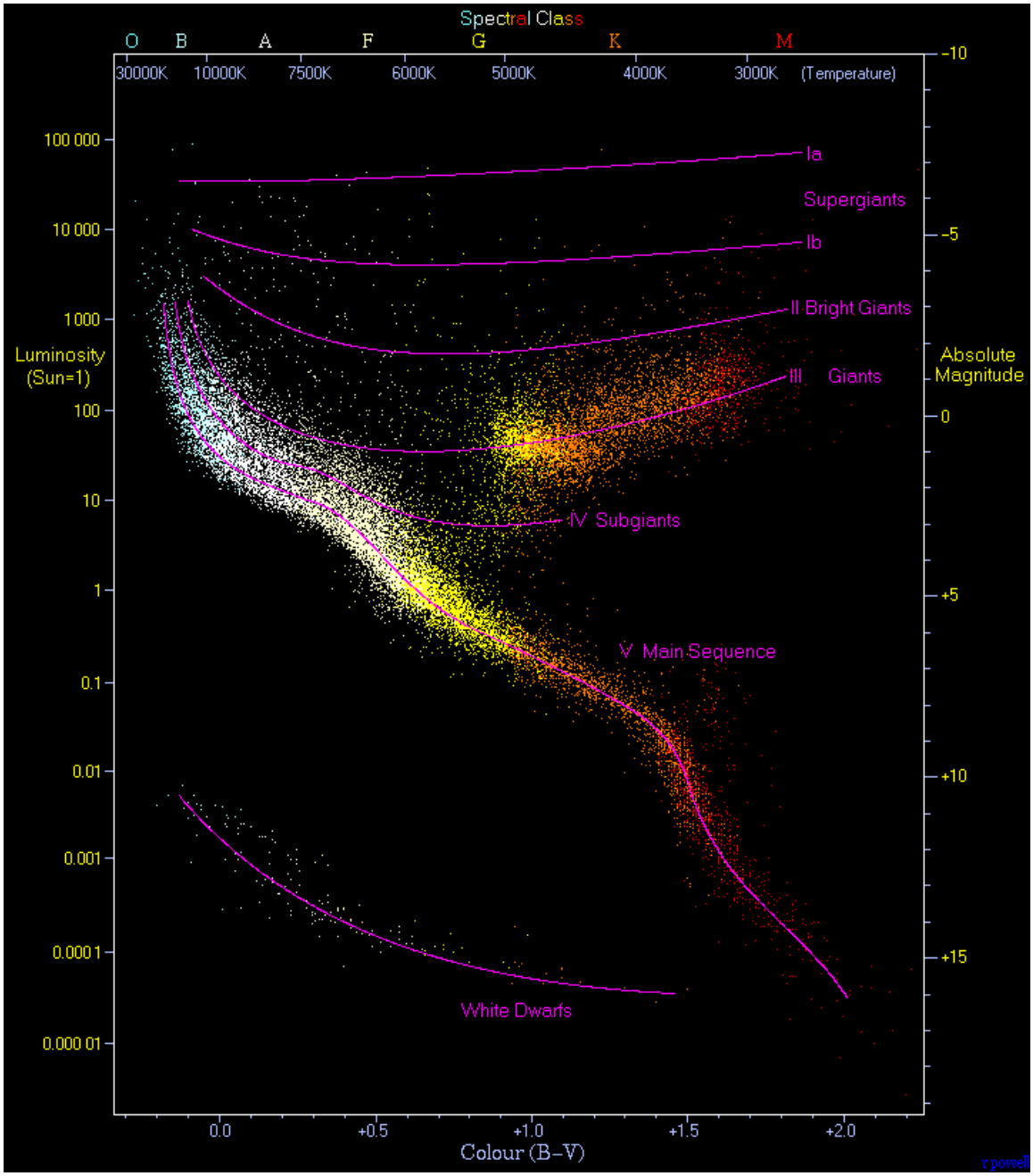

Figure 1.3 Hertzsprung-Russell diagram showing 22000 stars are plotted from the Hipparcos catalog and 1000 from the Gliese catalog of nearby stars. An examination of the diagram shows that stars tend to fall only into certain regions on the diagram. The most predominant is the diagonal, going from the upper-left (hot and bright) to the lower-right (cooler and less bright), called the main sequence. In the lower-left is where white dwarfs are found, and above the main sequence are the subgiants, giants and supergiants. The Sun is found on the main sequence at luminosity 1 (absolute magnitude 4.8) and $B - V$ color index 0.66 (temperature 5780 K and spectral type G2). Image by Richard Powell taken from http://www.wikipedia.com.

1.2.3 Hierarchichal galaxy formation

The understanding of mergers is fundamental in our current paradigm of galaxy formation where dark matter haloes interact between them in a hierarchichal *bottom-up* scenario. This means that larger dark matter haloes are formed by the merging of smaller progenitors formed from previous mergers or at the very early times from the initial density perturbations on small scales. The properties of the new systems may be very different form the original haloes. These interactions are described by the so-called *merger tree* shown in Fig. 1.4. A large number of small haloes merge forming larger haloes in what may be considered a smooth accretion.

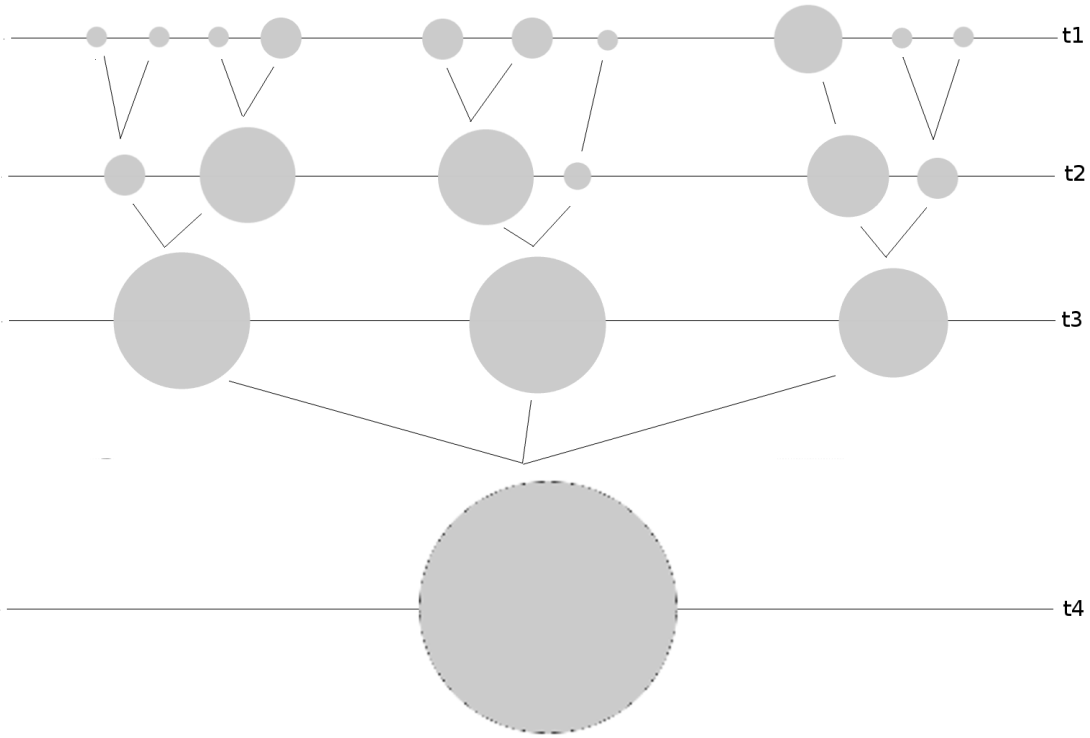

Figure 1.4 A schematic merger tree describing the hierarchichal scenario of galaxy formation. Every circle represent a dark matter halo with mass proportional to the size of the circle. It is shown how dark matter haloes merge to form larger haloes over time ($t_1 < t_2 < t_3 < t_4$) ending up in a single large mass halo at time t_4.

When two merging haloes have very different masses the smaller system orbits within the main halo for an extended period of time. Two different processes are competing to determine the eventual fate of the haloes. Dynamical friction transfers

energy from its orbit to the main halo, causing it to spiral inwards, while tidal effects remove mass from its outer regions and may eventually dissolve it completely. Dynamical friction is more effective for more massive satellites, but if the mass ratio of the initial haloes is large enough, the smaller object (and any galaxy associated with it) can maintain its identity for a long time. This is the mechanisms for the build-up of clusters of galaxies: a cluster may be considered as a massive dark matter halo hosting a relatively massive galaxy near its center and many satellites that have not yet dissolved or merged with the central galaxy. On the other hand, when two similar mass dark matter haloes merge, violent relaxation rapidly transforms the orbital energy of the progenitors into the internal binding energy of the quasi-equilibrium remnant. Any hot gas associated with the progenitors is shock-heated during the merger and settles back into hydrostatic equilibrium in the new halo. If these progenitors contain central galaxies, the galaxies also merge as part of the violent relaxation process, producing a new central galaxy in the final system that numerical simulations show that resembles a local elliptical galaxy, independently of the morphology of the progenitors. During the merger there is a strong star formation or AGN activity if the merger galaxies contained significant amount of cold gas (also known as *wet merger* in opposition to *dry mergers* when the interacting galaxies do not have enough cold gas to trigger further star formation).

1.3 Semi-analytical models of galaxy formation

In previous sections, it has been described galaxy properties such as stellar mass, star-formation rate, morphology, luminosity, color, metallicity, as well as the standard paradigm dominated by dark energy and matter where these galaxies form and evolve *bottom-up* in a hierarchichal framework. As we saw many details of galaxy formation are still uncertain. Therefore, the study of galaxies from first principles is still beyond our capabilities. Furthermore, to solve numerically many of the related problems is computationally quite expensive. There are cosmological hydrodynamical simulations where the initial density fields in both dark matter and baryonic gas are followed in time by solving the gravitational and hydrodynamical equations numerically. In principle, these simulations can follow the evolution of both the gas and dark matter without relying on simplified approximations of all the important processes. However, in practice, simulations are limited by numerical resolution and computational power. Consequently some of the physical processes still have to be modeled using analytical equations to produce observational predictions for statistical samples of galaxies in a cosmological context.

A different approach to theoretically study galaxy formation is to use semi-analytical models (SAMs), which apply simple but physically motivated recipes for the physical processes that shape galaxy formation, within the framework of structure formation predicted by ΛCDM. They trace the merger histories for a series of dark matter haloes of different (present-day) masses using N-body simulations, or

the extended Press-Schechter formalism (Press & Schechter 1974). Then, the three different baryonic components, hot gas, cold gas (presumably in a disk), and stars, are followed using analytic prescriptions.

SAMs provide predictions of bulk galaxy properties (such as star formation and chemical enrichment history, radial size, total stellar mass or luminosity, ratio of spheroid to disk, ...) for very large numbers of galaxies. SAMs have been shown to reproduce many observed properties of galaxies (e.g., Kauffmann, White & Guiderdoni 1993; Cole et al. 1994; Somerville & Primack 1999; Kauffmann et al. 1999; Cole et al. 2000; Somerville, Primack & Faber 2001), and to agree reasonably well with the results of numerical hydrodynamic simulations in their predictions for basic quantities such as the rate of accretion of cold gas and galaxy mergers (Yoshida et al. 2002; Cattaneo et al. 2007). In particular, recent models that include *radio mode* feedback from AGN reproduce quite well the global properties of massive galaxies over a broad range of cosmic history (e.g., Croton et al. 2006; Bower et al. 2006; Menci et al. 2006; Kang, Jing & Silk 2006; Monaco, Fontanot & Taffoni 2007; Somerville et al. 2008), although reproducing the properties of low-mass galaxies remains something of a challenge (Fontanot et al. 2009b; Guo et al. 2010). Radio mode feedback are associated with powerful jets observed at radio frequencies, in contrast to the *merger-triggered* mode of black hole growth.

Using a set of recipes for gas accretion and cooling, merging, star formation, stellar feedback, chemical enrichment, and optionally black hole growth and AGN feedback, a SAM outputs a distribution of ages and metallicities for all the stars within the spheroid and disk components of a galaxy. This information is convolved with SSP models (e.g., Bruzual & Charlot 2003; Maraston 2005), which specify (as discussed in Sec. 1.2.2), for a given stellar IMF, the luminosity as a function of wavelength for a stellar population of a given age and metallicity, in order to predict the unattenuated SED of starlight in the galaxy. The predictions of SSP models from different groups have largely converged in their predictions, particularly in the UV and optical, making this component of the modelling relatively robust.

For the more difficult step of predicting how this starlight is absorbed and reradiated by dust, one possible approach is to couple the predictions of a SAM directly with a radiative transfer code (e.g., Granato et al. 2000; Baugh et al. 2005; Fontanot et al. 2007) that numerically solves the physics behind. Because SAMs are not able to track the detailed internal structure or morphology of galaxies, this requires the assumption of an idealized geometry such as a spheroid plus disk (where the sizes and masses of the components are specified by the SAM). However, even this is prohibitively expensive for large numbers of galaxies, and also has the disadvantage that the simplified geometries may not be representative of the diversity of galaxy types, particularly for luminous IR galaxy or ultra-luminous infrared galaxies (ULIRG)-like objects, many of which are known to be merging systems. Moreover, the dust models contain a large number of free parameters, which must be tuned by fitting a chosen set of observations, and may or may not be constant from galaxy to galaxy or over

cosmic time.

An alternative approach is to develop an analytic or semi-analytic model to estimate the fraction of starlight that is absorbed by dust in a given galaxy, based on its geometry, metal content, and stellar populations. Early SAMs (Guiderdoni & Rocca-Volmerange 1987; Lacey et al. 1993; Guiderdoni et al. 1998; Kauffmann et al. 1999; Somerville & Primack 1999; Devriendt & Guiderdoni 2000) approached this by assuming that the face-on B or V-band optical depth of the dust in the disk is proportional to the column density of metals in the gas phase, that the inclination dependence is that predicted by a simple *slab* model in which the dust and stars are uniformly mixed, and that the wavelength dependence is given by a fixed attenuation law, such as a extinction law from our galaxy or the starburst attenuation law of Calzetti et al. (2000). Charlot & Fall (2000) proposed a two-component model that separately accounts for the extinction due to diffuse cirrus in the disk and that due to the dense birth clouds surrounding newly born stars. De Lucia & Blaizot (2007) combined the two approaches, using a *slab* model to treat the cirrus component and adopting the Charlot & Fall (2000) model to treat the young stars ($\sim 10^7$ yr). Fontanot et al. (2009a) tested a wide range of such simple analytic approaches from the literature against full radiative transfer, applied within the `MORGANA` (Monaco, Fontanot & Taffoni 2007) SAM. They concluded that bulk properties, such as luminosity functions (LFs)[3] (see Chap. 2), predicted by the SAMs using analytic dust recipes agreed quite well with the results of the full radiative transfer, at a fraction of the computational cost.

With an estimate for the total energy absorbed by dust in hand, and assuming that all of this energy is re-radiated in the IR, one can use observationally derived or observationally calibrated template SEDs describing the wavelength dependence of the dust emission (Devriendt, Guiderdoni & Sadat 1999; Chary & Elbaz 2001; Dale & Helou 2002; Lagache et al. 2004; Rieke et al. 2009), or modified Planck functions (Kaviani, Haehnelt & Kauffmann 2003) to compute IR luminosities (Guiderdoni et al. 1998; Devriendt & Guiderdoni 2000; Hatton et al. 2003; Blaizot et al. 2004). Observationally, it is known that the mid to far-IR colors (i.e., the ratio of warm to cool dust) are correlated with the total IR luminosity of the galaxy (Sanders & Mirabel 1996). Accordingly, models based on this approach use an SED library indexed by the total IR luminosity; i.e., the total IR luminosity of the model galaxy is used to select the appropriate far-IR template. Fontanot & Somerville (2010) compared this kind of approach, again applied to the `MORGANA` SAM, with the results of coupling the same SAM with the full radiative transfer code `GRASIL` (Silva et al. 1998). Again, the agreement for statistical quantities such as LFs was quite good.

[3]This is a fundamental quantity in galaxy evolution that gives the number of galaxies per volume per magnitude bin in a given band and redshift.

1.4 Diffuse extragalactic background radiation fields

Diffuse radiation from extragalactic origin filled all around our universe. This is called diffuse extragalactic background radiation (DEBRA) and contains photons over ~ 20 decades of energy, from the smallest radio waves (10^{-7} eV) to the largest γ-ray (~ 100 GeV) wavelengths. The origin and the physical processes involved are different within every wavelength range. There are plenty of observational evidences that support the existence of the DEBRA. Fig. 1.5 shows a schematic picture, based on many different data sets, of the spectral intensity (also called spectral radiance) multiplied by wavelength of the DEBRA over all the electromagnetic spectrum. This representation is convenient because the area inside the curve is the energy.

The nature and history of the universe is coded in this radiation field and any realistic cosmological model must be able to describe it. Understanding the DEBRA is a major challenge of modern cosmology with huge consequences in other fields of astrophysics, therefore extraordinary efforts are being put by theoreticians, observers, and instrumentalists to do so.

In this chapter the overall diffuse extragalactic radiation field will be divided in different regions according to their origin and physical processes involved. All of them will be briefly described in this chapter for completeness, but all our efforts in this Thesis will be focused on studying a range of the DEBRA known as the extragalactic background light (EBL) (briefly introduced in Sec. 1.4.5) and its implications for galaxy evolution and γ-ray astronomy.

1.4.1 Diffuse extragalactic γ-ray background

This is the region of the DEBRA coming from non-thermal processes, where the highest energy photons are. Therefore it is the region that challengues cosmological and particle physic models. The observed diffuse high-energy component is dominated by γ-rays produced by the interaction of cosmic rays (protons, α particles, other atomic nuclei and electrons) with the ISM known as the diffuse galactic emission. After the subtraction of this component still remains a much fainter diffuse and isotropic component of assumed extragalactic origin that is known as the diffuse extragalactic γ-ray background (EGB). The first indication that the diffuse radiation extended at higher energies than the X-ray component came from instruments in the Ranger 3 and Moon 5 satellites. In the higher energy γ-ray region the first observations were available thanks to the Explorer 11, though these measurements only gave an upper limit, it provided a refutation of the Steady State cosmological model (see Sec. 1.1). The intensity of the EGB is rather weak, a factor ~ 10 lower than it would be expected from the continuously creation of matter and antimatter in an expanding universe as described by the Steady State model. The first suggestion of an even higher energy and weaker component came from OSO-3, followed by SAS-2 (Kniffen et al. 1973) and later COS-B (Mayer-Hasselwander et al. 1982), which was

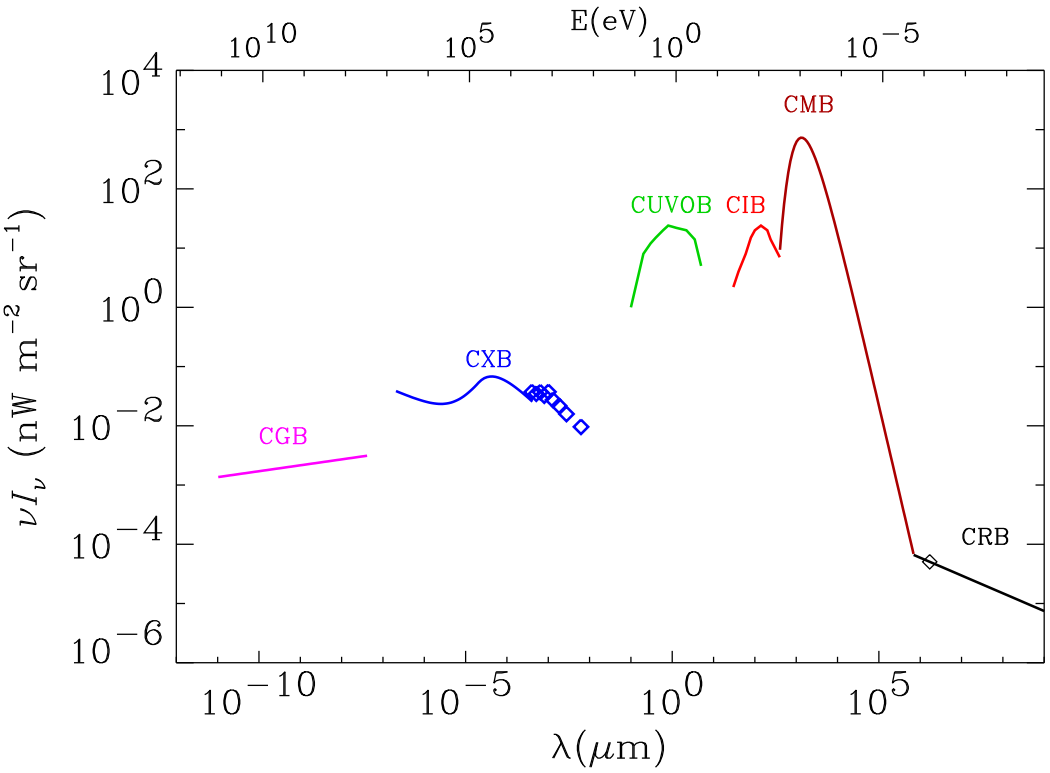

Figure 1.5 Schematic representation of the overall diffuse extragalactic or cosmic background radiation based on plenty of observational data. The cosmic radio background (CRB) is represented by a $\nu I_\nu \sim \nu^{0.3}$ spectrum, normalized to the Bridle 1967 value at 170 cm. The cosmic microwave background (CMB) is represented by a blackbody spectrum at 2.725 K. The cosmic UV-optical (CUVOB) and infrared (CIB) backgrounds are schematic representations of the work summarized in Hauser & Dwek 2001. The data for the cosmic X-ray background (CXB) are taken from Wu et al. (1991), and the curves are analytical representations summarized by Fabian & Barcons (1992). The γ-ray background (CGB) is represented by the power law given by Sreekumar et al. (1998). Figure from Hauser & Dwek (2001).

confirmed by Energetic Gamma Ray Experiment Telescope (EGRET) (Sreekumar et al. 1998). Fig. 1.6 shows the latest EGB measurements from the Large Area Telescope (LAT) instrument on board the Fermi satellite (Abdo et al. 2010c). It is noticeable that the measurements are well fitted to a simple power law up to $\sim$ 100 GeV with no spectral features that would allow to disentangle between different contributions.

The relative contribution from astrophysical processes that contribute to the EGB are still a strong source of debate, but some of them are clear. The main contribution

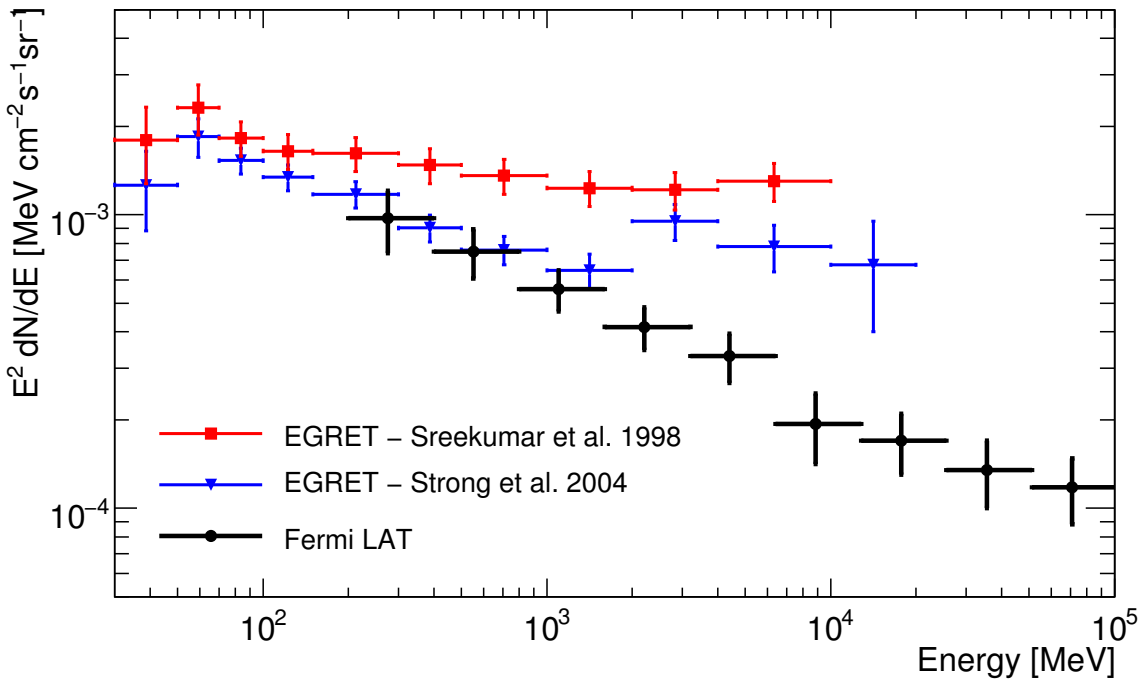

Figure 1.6 EGB intensity derived by Fermi compared with EGRET-derived intensities. The derived spectrum is compatible with a simple power-law with index $\gamma = 2.41 \pm 0.05$ and intensity $I(> 100\ \mathrm{MeV}) = (1.03 \pm 0.17) \times 10^{-5}\ \mathrm{cm^{-2}s^{-1}sr^{-1}}$ where the uncertainties are systematics dominated. Figure taken from Abdo et al. (2010c).

seems to come from unresolved AGNs (Abdo et al. 2010d), star-forming galaxies (Fields, Pavlidou & Prodanović 2010), gamma-ray bursts (GRBs), a small component from millisecond pulsars (Siegal-Gaskins et al. 2010) and from truly-diffuse emission processes. These last processes include possible signatures of large-scale structure formation, emission from interaction of ultra high energy cosmic rays with other extragalactic background radiation fields described in this sections, the postulated annihilation or decay of dark matter (Pieri, Bertone & Branchini 2008) and many other different processes (see Dermer 2007). Fig. 1.7 shows the relative contribution from sources and from a truly-diffuse component to the total EGB in red with their statistical and systematic uncertainties as measured by Fermi.

1.4.2 Cosmic X-ray background

This radiation field, also known as cosmic X-ray background (CXB), contains photons from 0.1 keV up to 100 MeV. It is usual in the literature to distinguish between soft and hard X-ray background, the former at lower and the latter to higher energies.

The first measurement of X-rays from sources outside the Solar System was pub-

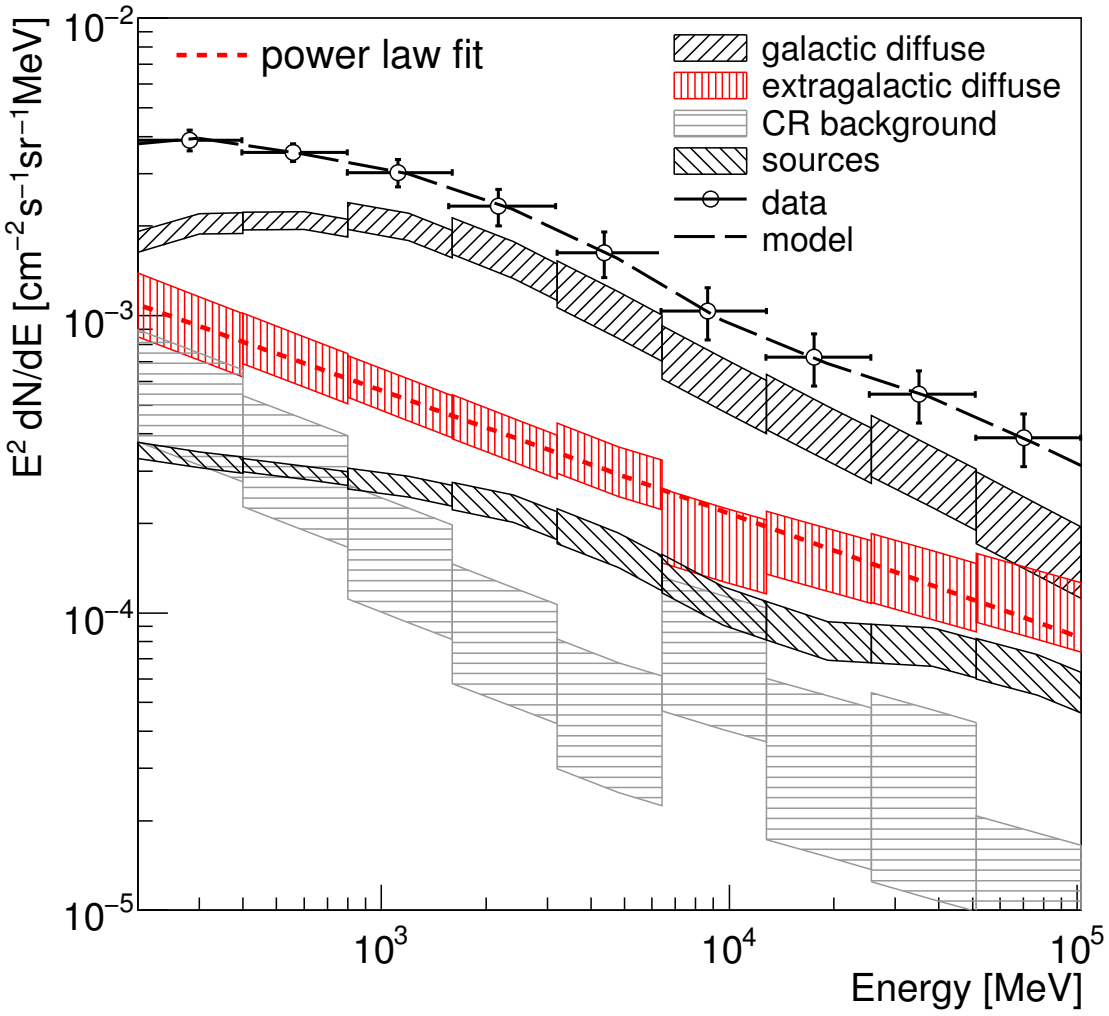

Figure 1.7 LAT measured γ-ray intensity with fit results for a galactic latitude $|b| \geq 10^\circ$ including statistical and systematic uncertainties. Note LAT data are dominated by systematic uncertainties for the energy range shown in the figure. Figure taken from Abdo et al. (2010c).

lished by Giacconi et al. (1962). There is general agreement about that this background is produced by integrated emission of point sources (Ajello et al. 2008). Deep surveys from the most recent X-ray observatories such as XMM-Newton and Chandra (Giacconi et al. 2002; Alexander et al. 2003; Hasinger 2004) have shown that basically all the CXB at energies lower than $\sim$ 2 keV has been resolved by AGNs hosting super-massive black holes. However, at energies larger than $\sim$ 6 keV, there is still an unresolved component as large as 50% of the CXB (Worsley et al. 2005). This unresolved component may be attributed to the emission of a yet undetected population of highly absorbed AGNs. Other contributions to the CXB might be from

massive X-ray binary system, supernova remnants, and hot gas in galaxy clusters.

The latest CXB measurement by the BAT instrument on board the Swift satellite are shown in Fig. 1.8 with a compilation of observations from other telescopes.

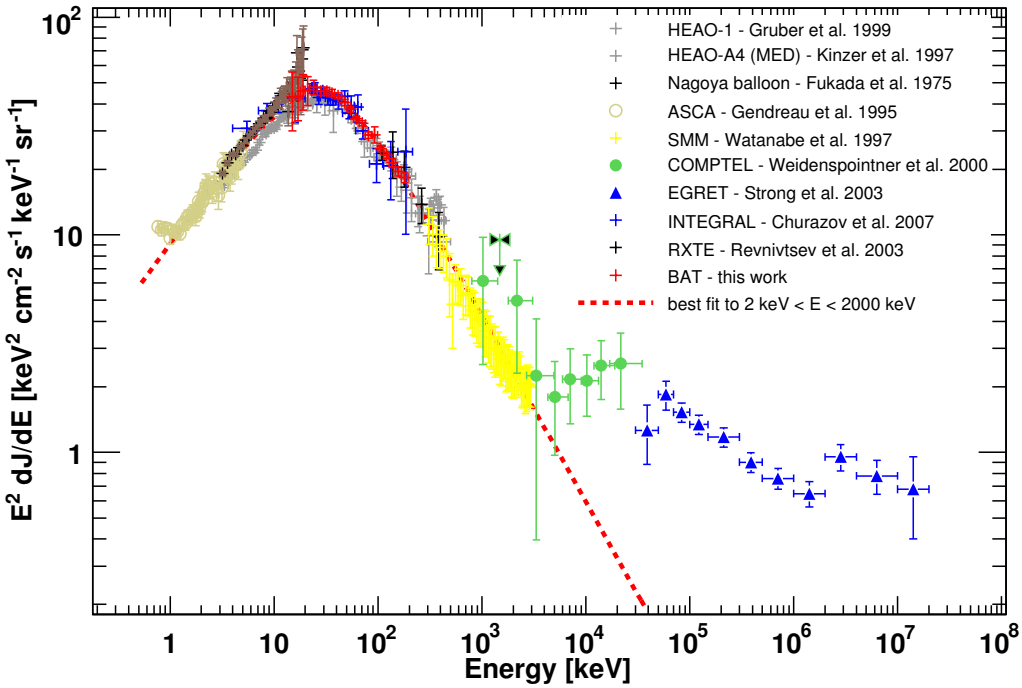

Figure 1.8 The BAT CXB measurements compared with previous results. The dashed line is the best fit to the spectrum between 2 keV $< E <$ 2000 keV. EGRET observations of the EGB at higher energies are shown as well. Figure taken from Ajello et al. (2008).

1.4.3 Cosmic microwave background

As shown in Fig. 1.5, energetically the CMB is the dominant background. As discussed in Sec. 1.1, its discovery was a great success of the Big Bang model over other competing cosmologies. It contains thermal radiation that match exactly (roughly one part in 10^5) the emission of a black body at 2.725 ± 0.001 K (and it will continue to drop as the universe expands), thus the spectrum peaks in the microwave range frequency of 160.2 GHz, corresponding to a 1.9 mm wavelength. The CMB spectrum is the most precisely measured black body spectrum in nature. The CMB is highly uniform in all directions, but shows a very specific pattern equal to that expected if a fairly uniformly distributed hot gas is expanded to the current size of the universe. In particular, the spatial power spectrum shown in Fig. 1.9 (how much difference is

observed versus how far apart the regions are on the sky) contains small anisotropies, or irregularities, which vary with the size of the region examined. They have been measured in detail by WMAP (see Fig. 1.2), and match what would be expected if small thermal variations, generated by quantum fluctuations of matter in a very tiny space, had expanded to the size of the observable universe we see today. This is still a very active field of study, with scientists seeking both better data (that will be achieved by the Planck satellite launched in 2009) and better interpretations of the initial conditions of expansion. Although many different processes might produce the general form of a black body spectrum, no model other than the Big Bang has yet explained the fluctuations. As a result, most cosmologists consider the Big Bang model of the universe to be the best explanation for the CMB.

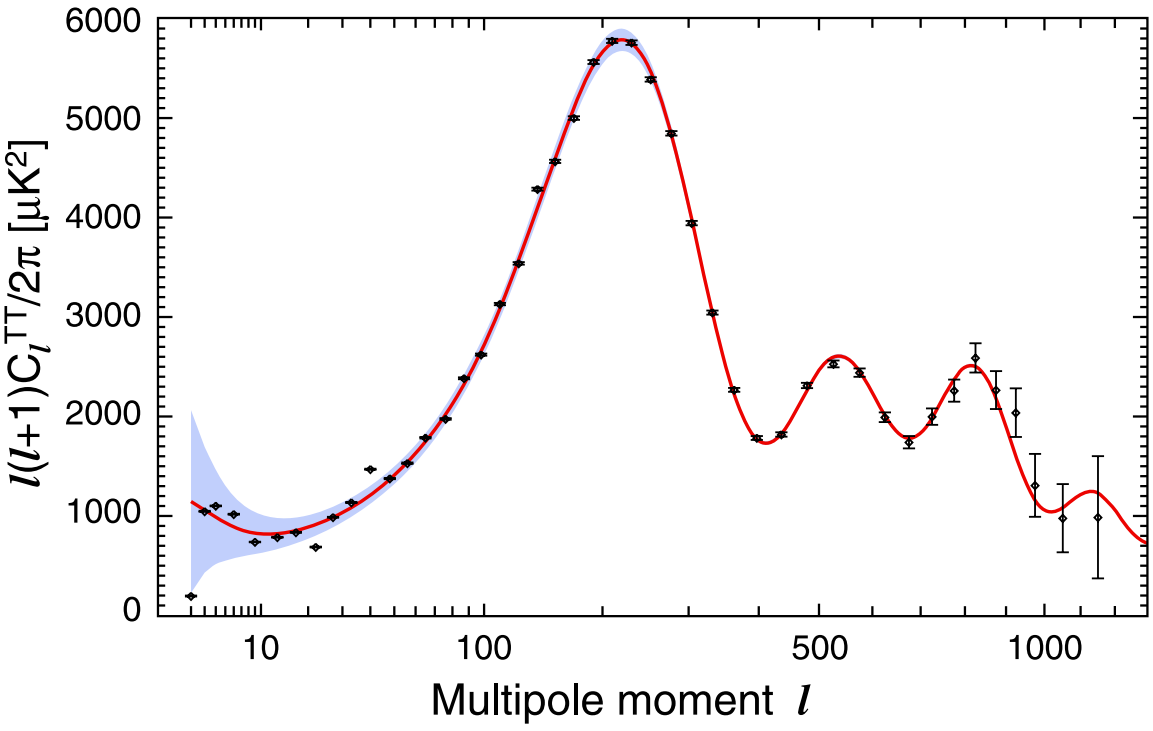

Figure 1.9 The 7-year temperature power spectrum from WMAP. The third acoustic peak and the onset of the Silk damping tail are now well measured by WMAP. The curve is the ΛCDM model best fit to the 7-year WMAP data: $\Omega_b h^2 = 0.02270$, $\Omega_b h^2 = 0.1107$, $\Omega_\Lambda = 0.738$, $\tau = 0.086$, $n_s = 0.969$, $\Delta_R^2 = 2.38\times\ 10^{-9}$, and $A_{SZ} = 0.52$ (see Larson et al. 2011 for details on these parameters). The plotted errors include instrument noise, but not the small, correlated contribution due to beam and point source subtraction uncertainty. The gray band represents cosmic variance. A complete error treatment is incorporated in the WMAP likelihood code. The points are binned in progressively larger multipole bins with increasing l; the bin ranges are included in the 7-year data release. Figure taken from Larson et al. (2011).

The study of the CMB leads directly to fundamental information such as the shape of the universe (Komatsu et al. 2011), and indirectly to information such as the Hubble constant (Larson et al. 2011, see Sec. 1.1) that gives the rate of expansion of the universe and the redshift of galaxies (interpreted as the recessional velocity) as a proportion of their distance.

1.4.4 Cosmic radio background

The cosmic radio background (CRB) is poorly known due to our location within our galaxy, which emits and absorbs at these wavelengths. The CRB was measured over twenty-five years ago Clark, Brown & Alexander 1970, but the truly extragalactic contribution (not contamination from our own galaxy) to this radio background is still debatable. What seems clear from recent results reported by the Absolute Radiometer for Cosmology, Astrophysics, and Diffuse Emission (ARCADE) 2 collaboration (Singal et al. 2010b) is that the surface brightness of the background is several times higher than that which would result from currently observed radio sources such as sub-mm galaxies and radio loud quasars. From independent reasons, this discrepancy could not be explained by truly diffuse background neither extragalactic nor from our galaxy. Other possible low-radio-flux contributions are discussed in Singal et al. (2010a) such as radio supernovae, radio quiet quasars, and star-forming galaxies. In that work, the authors claim that such as discrepancy between observed and resolved background would have been produced by ordinary star-forming galaxies at $z > 1$ characterized by an evolving radio/far-IR correlation, which changes toward the radio loud with redshift.

1.4.5 Diffuse extragalactic background light

The formation and evolution of galaxies in the universe is accompanied unavoidably by emission of radiation. All this radiated energy is still streaming through the universe, although much is now at longer wavelengths due to redshifting by the expansion of the universe and absorption/re-emission by dust. The photons mostly lie in the range $\sim$ 0.1-1000 μm, i.e., ultraviolet (UV), optical, and IR, and produce the second most energetic diffuse background after the CMB, thus being essential for the full energetic balance of the universe. We will model and discuss thoroughly in this Thesis the radiation accumulated by star formation processes through most of the life of the universe, plus a contribution from AGNs to this wavelength range, known as the diffuse EBL.

Historical review

This section has been adapted from Hauser & Dwek (2001). The question about why the sky at night is dark for the human eye was already stated by Johannes Kepler in 1610, but was not clearly expressed until 1823 by Heinrich Wilhelm Matthäus Olbers

and later published by Johann Elert Bode in 1826 (see Harrison 1990 for a historical review). Currently, the answer seems clear: the main reason concerns primarily the finite age of the galaxies, in conjunction with other factors such as the finite speed of light, and secondarily (contrary to the general belief) the expansion of the universe (Wesson, Valle & Stabell 1987; Wesson 1991). First calculations of the optical background coming from integrated starlight from galaxies within general relativity were made by Shakeshaft (1954), McVittie & Wyatt (1959), Sandage & Tammann (1964), and Whitrow & Yallop (1964, 1965). The last model took into account absorption by the IGM and other galaxies (Whitrow & Yallop 1965). Absorption/re-emission by the ISM was not considered yet.

Peebles in 1965 (see Peebles 1993, unpublished lecture, pp. 146-147) called the attention to the community about the lack of direct knowledge of the EBL. There were only observational upper limits on the EBL from the detection of cosmic-ray protons with energies $\sim 10^{10}$ GeV. These protons would have been attenuated by photon-pion production by a large EBL (Peebles 1969). It was clear from these measurements that the existing EBL was not energetically enough to close the universe. Other work by Partridge & Peebles (1967a) showed that in order to produce the observed local abundances, young galaxies must have been more luminous than older systems. They correctly concluded in a companion work (Partridge & Peebles 1967b) that the EBL is much fainter than the foreground radiation from our Solar System and galactic sources by means of calculating the integrated IR background that would be produced by young galaxies using different cosmological scenarios assuming no dust in galaxies. These works stimulated observational programs to eventually measure the EBL. In 1970 only high upper limits were known for the EBL. Harwit (1970) realized about how EBL measurements would constrain the understanding of different galaxy types, given the fact that every population would contribute mainly to a given EBL wavelength range. For example, measurement of the far-IR background would set limits on the number and duration of luminous far-IR episodes in quasars (Kleinmann & Low 1970; Low 1970). The high far-IR luminosity of galaxies in the local universe had led Low & Tucker (1968) to predict an IR background peaking at a wavelength longer than 50 μm, with a total energy 1%-10% of that in the recently discovered CMB. This prediction was substantially correct as we will see in Chap. 2. Harwit (1970) reviewed as well how the EBL would attenuate cosmic and γ-rays by different mechanisms such as photo-pion production with protons, inverse Compton with electrons, and electron-positron pair production with γ-ray photons. Another review by Longair & Sunyaev (1972) also described the status of the overall DEBRA at that time, highlighting the high uncertainties in the EBL knowledge. Since the mid-1970s, many different modelings have been proposed with different degrees of sophistication and complexity such as Kaufman (1976), Stecker, Puget & Fazio (1977), Negroponte (1986), Bond, Carr & Hogan (1986, 1991), Hacking & Soifer (1991), Beichman & Helou (1991), Franceschini et al. (1991, 1994).

Direct detection, lower limits from galaxy counts, and upper limits from VHE γ-ray observations

The first direct measurement of the EBL came from the COBE satellite (Hauser et al. 1998; Lagache et al. 2000; Cambrésy et al. 2001), and later from the Infrared Telescope in Space (IRTS) (Matsumoto et al. 2005). These data are highly contaminated by foregrounds mainly from zodiacal light. Zodiacal light comes from the scatter of light emitted from the Sun by a cloud of finely dispersed dust that orbits and encloses the Sun in a disk-shaped volume symmetrically distributed about the ecliptic plane. The spectrum of zodiacal light is not well known, however there is work on that direction (Chary & Pope 2010). Fig. 1.10 shows a recent estimation of the zodiacal spectrum, which is orders of magnitude brighter at some wavelengths that the faint EBL. From Fig. 1.10 is clear that direct measurement in the near-IR (~ 1 μm) are hard, in the mid-IR even harder, and in the far-IR (~ 100 μm) easier than at shorter wavelengths. Moreover, there are other contaminating foregrounds such as the integrated galaxy light (from stellar light and light re-processed by the ISM) and cometary dust in our Solar System.

On the other hand, it is possible to account for all the light coming from galaxies making very deep galaxy counts (e.g., Madau & Pozzetti 2000; Fazio et al. 2004; Béthermin et al. 2010). This will set a strict lower limit to the EBL, and even an excellent measurement of it when the observations are deep enough. This is the case of the data in some optical bands presented in Madau & Pozzetti (2000) that are coming from the HST in the Hubble Deep Field. In the far-IR, this approach is less reliable than at shorter wavelengths due to the fact that light here is diffracted, sensitivity of detectors sharply drops and source confusion increases.

Other limits are possible from very high energy (VHE) (30 GeV-30 TeV) γ-ray observations. VHE γ-ray coming from extragalactic sources are attenuated by electron-positron pair production (Nikishov 1962; Gould & Schréder 1966). This attenuation modifies the observed VHE spectra in an exponential way, thus assuming properties of the intrinsic spectra (or EBL-corrected, these are the spectra that we would observe if there were no effect from the EBL) it is possible to set constraints on the EBL. When the redshift of the source is known and assuming a maximum hardness slope to the EBL-corrected spectra, we can derive upper limits to the background (e.g., Aharonian et al. 2006; Mazin & Raue 2007; Albert et al. 2008). These limits are dependent of the assumptions and will be discussed thoroughly in Chap. 5. Other applications are derived from the knowledge of the EBL:

(i) From the EBL and redshift of the source known, it is possible to study intrinsic properties of the source (e.g., Abdo et al. 2011; Aleksić et al. 2011b,c).

(ii) From the EBL and intrinsic properties of the source known, it is possible to estimate the redshift (Prandini et al. 2010; Yang & Wang 2010)

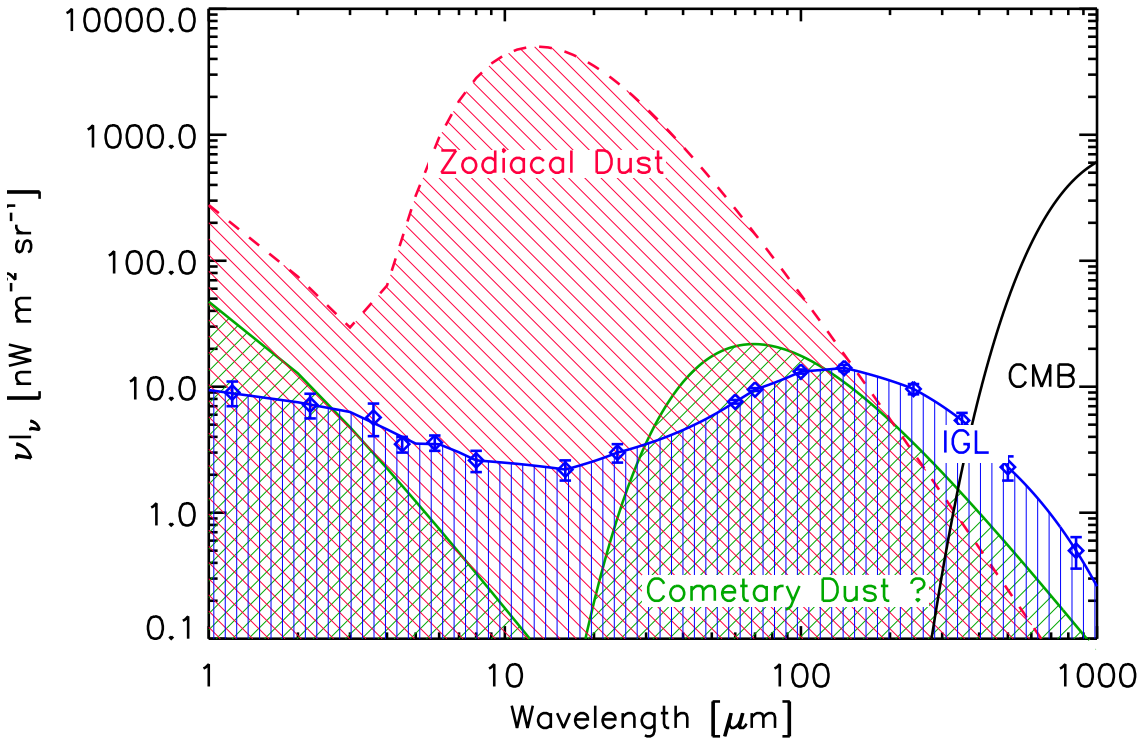

Figure 1.10 Estimates of the relative contributions of the zodiacal dust and integrated galaxy light (IGL) in a typical extragalactic field. The latter would be isotropic and independent of choice of field. A tentative estimate of the contribution from isotropically distributed dust in the outer Solar System is also labeled as cometary dust. Also shown is the intensity of the cosmic microwave background (CMB). Figure taken from Chary & Pope (2010)

(iii) From the redshift and intrinsic properties of the source known, it is possible to set limits on the EBL (e.g., Aharonian et al. 2006; Mazin & Raue 2007; Albert et al. 2008).

Understanding the EBL is essential, both for the entire process of galaxy evolution and for γ-ray astronomy. Despite its fundamental importance, its overall spectrum and evolution has never been determined directly neither from observed LFs, over a wide redshift range, nor from any multiwavelength observation of galaxy SEDs. This is the goal of the next chapter.

Part I

Modeling the extragalactic background light

2

Extragalactic background light from galaxy SED-type fractions

2.1 Introduction

As we saw in Sec. 1.4.5, the direct measurement of the EBL is a very difficult task subject to high uncertainties. This is mainly due to the contribution of zodiacal light, some orders of magnitude larger than the EBL (e.g., Hauser & Dwek 2001; Chary & Pope 2010). There are some measurements in the optical (Bernstein 2007) and in the near-IR (e.g., Cambrésy et al. 2001; Matsumoto et al. 2005), but there is not general agreement about the reliability of these data sets (Mattila 2006). In addition, these near-IR data appear to give intensity levels for the EBL in contradiction with the observation of VHE (30 GeV-30 TeV) photons from extragalactic sources (Aharonian et al. 2006; Mazin & Raue 2007; Albert et al. 2008). Little is known about the mid-IR from direct detection due to the higher contamination from zodiacal light at those wavelengths (see Fig. 1.10). Measurements with the Far-Infrared Absolute Spectrometer (FIRAS) instrument on board COBE, in the far-IR (Hauser et al. 1998; Lagache et al. 2000), are thought to be more reliable. Other observational approaches set reliable lower limits on the EBL, such as measuring the integrated light from discrete extragalactic sources (e.g., Madau & Pozzetti 2000; Fazio et al. 2004).

There are also other authors that focus on studying galaxy properties based on EBL results (Fardal et al. 2007), or on modeling a region of the EBL spectrum (**?**). On the other hand, there are phenomenological approaches in the literature that predict an overall EBL model (i.e., between 0.1-1000 μm and for any redshift). These are basically of four kinds:

(i) Forward evolution, which begins with cosmological initial conditions and follows a forward evolution with time by means of SAMs of galaxy formation (see Sec. 1.3 for an introduction), e.g., Primack et al. (1999), Somerville et al. (2011)

(hereafter, SGPD11) and Gilmore et al. (2011) (hereafter, GSPD11).

(ii) Backward evolution, which begins with existing galaxy populations and extrapolates them backwards in time, e.g., Malkan & Stecker (1998), Stecker, Malkan & Scully (2006), Franceschini, Rodighiero & Vaccari (2008) (hereafter, FRV08).

(iii) Evolution of the galaxy populations that is inferred over a range of redshifts. The galaxy evolution is inferred here using some quantity derived from observations such as the star formation rate (SFR) density of the universe, e.g., Kneiske et al. (2002), Finke, Razzaque & Dermer (2010), Kneiske & Dole (2010).

(iv) Evolution of the galaxy populations that is directly observed over the range of redshifts that contribute significantly to the EBL. The model described in Domínguez et al. (2011) and in this Thesis, which we term empirical, belongs to this category.

The type (i) SGPD11 and GSPD11 models discuss the same galaxy formation SAM but in different contexts: SGPD11 contains details of the model used in calculating the bolometric luminosity history of the universe and comparison with data, and GSPD11 focuses on the derived EBL and γ-ray attenuation. The SGPD11-GSPD11 model is based on an updated version of the semi-analytic theoretical approach described in Somerville et al. (2008) from the growth of super-massive black holes and their host galaxies within the context of the hierarchical ΛCDM cosmological framework. This is based in part on Somerville & Primack (1999), Somerville, Primack & Faber (2001), and in the simulations summarized by Hopkins et al. (2008a), and Hopkins et al. (2008b). We consider that these types of models are complementary to the observational approach taken here.

We consider the type (ii) FRV08 model the most complete observationally-based work of those mentioned above. They base their EBL modeling on galaxy LFs, quantities which are directly observed and well understood. FRV08 exploit a variety of data to build evolutionary schemes according to galaxy morphology. They account for the contribution from early, late-type galaxies and a starburst population to the EBL. They use observed near-IR LFs from the local universe to $z = 1.4$ for describing the early and late-type galaxies. For the starburst population they use an optical and only local LF. Different prescriptions are used to extrapolate the evolution of the different morphological types to higher redshifts, and corrections to fit their results to other observational data are applied.

Type (iii) models are not directly based on galaxy data. Instead, they are built from some parametrization of the history of the SFR density. This is a quantity derived using several different methods, each of which have different and significant uncertainties and biases. The SFR density is combined with uncertain assumptions about the emitted galaxy spectral energy distribution (SED) evolution as well.

Our type (iv) EBL estimates (the first approach in this category) will be compared in detail with the type (i) forward evolution semi-analytical galaxy formation model

by SGPD11 and GSPD11, and the type (ii) observationally motivated model by FRV08. The other works mentioned are briefly compared with our EBL calculations in Sec. 7.

Our aim in this paper is to develop an EBL model that is as observationally-based and realistic as possible, yet fully reproducible, including a quantitative study of the main uncertainties in the modeling that are directly due to the data. This constrains the range of the background intensity and its implications to γ-ray astronomy. One important application of the EBL for γ-ray astronomy is to recover the unattenuated spectra of extragalactic sources. Our goal is to measure the EBL with enough precision that the uncertainties due to the EBL modeling, in these recovered unattenuated spectra, are small compared with other effects such as systematic uncertainties in the γ-ray observations. Examples of this are discussed in Sec. 5.

Our model is based on the rest-frame K-band galaxy LF by Cirasuolo et al. (2010) (hereafter, C10) and on multiwavelength galaxy data from the All-wavelength Extended Groth Strip International Survey (AEGIS)[1] (Davis et al. 2007; Newman et al. 2011) of about 6000 galaxies in the redshift range 0.2-1. These data sets are put together in a very transparent and consistent framework. The C10 LF is used to count galaxies (and therefore to normalize the total EBL intensity) at each redshift. The LF as well as our galaxy sample are divided in three magnitude bins according to the absolute rest-frame K-band magnitude i.e., faint, middle, and bright (defined quantitatively later). Within every magnitude bin a SED-type is statistically attached to each galaxy in the LF assuming SED-type fractions that are function of redshift within those magnitude bins. This is estimated from fitting our AEGIS galaxy sample to the 25 galaxy SED templates from the Spitzer Wide-Area Infrared Extragalactic Survey (SWIRE) library. Then, luminosity densities are calculated from these magnitude bins from every galaxy population at all wavelengths, and finally all the light at all redshifts is added up to get the overall EBL spectrum. The results are linked with γ-ray astronomy and with the current understanding on galaxy evolution.

Throughout this Thesis, a standard ΛCDM cosmology is assumed, with matter density $\Omega_m = 0.3$, vacuum energy density $\Omega_\Lambda = 0.7$, and Hubble constant $H_0 = 70$ km s^{-1}Mpc^{-1}.

2.2 Data description

2.2.1 K-band galaxy luminosity function

The evolving galaxy LF in rest-frame K-band provided by C10 from $z = 0$ to 4 is used. This evolving LF is the most accurate measurement to date of cosmological galaxy evolution in the near-IR, where dust absorption is less severe than in optical bands. The k-corrections in this band are less severe than in the optical as well.

[1] http://aegis.ucolick.org/

Band	λ_{eff} [μm]	Observatory	Req.	UL [μJy]
FUV	0.1539	GALEX	ext	-
NUV	0.2316	GALEX	ext	-
B	0.4389	CFHT12K	det	-
R	0.6601	CFHT12K	det	-
I	0.8133	CFHT12K	det	-
K_S	2.14	WIRC	det	-
IRAC 1	3.6	IRAC	det	-
IRAC 2	4.5	IRAC	obs	1.2
IRAC 3	5.8	IRAC	obs	6.3
IRAC 4	8.0	IRAC	obs	6.9
MIPS 24	23.7	MIPS	obs	30

Table 2.1 The photometric bands in our galaxy sample. For each we show the effective wavelength, the data source, the requirement for that band to be included for a given galaxy in our sample (det: a detection in this band is required; obs: observation in this band is required, but not necessarily a detection; ext: this band is considered extra information when available), and the 5σ upper limit in that band in cases where there is no detection.

The choice of the C10 LF to normalize the model is also based on the smooth and well-studied shape of the galaxy SEDs in the near-IR, unlike others in UV or mid-IR wavelengths.

The resulting evolving LF is based on the UKIDSS Ultra Deep Survey (Lawrence et al. 2007), which has a large area and depth, and hence reduces the uncertainties due to cosmic variance and survey incompleteness. We refer the reader interested in details to that work. It is important to note that they give a parametrization of the evolution of the LF corrected from incompleteness and fitted by a Schechter function (Schechter 1976) over redshift, $\Phi(M_K^z, z)$, where M_K^z is rest-frame K-band absolute magnitude at redshift z. The strongest assumption that they make is to keep constant the faint-end slope α in their parametrization.

2.2.2 Galaxy sample description

A multiwavelength galaxy catalogue built from AEGIS (Davis et al. 2007; Newman et al. 2011) for this work is used. This catalogue contains 5986 galaxies, all in the Extended Groth Strip (EGS). It is required that every galaxy in the sample have 5σ detections in the B, R, I, K_S and Infrared Array Camera (IRAC) 1 bands, and observations (but not necessarily detections) in the IRAC 2, 3, 4 and Multiband Imaging Photometer for Spitzer (MIPS) 24 bands (see Table 2.1). These 5σ upper limits are given by the following fluxes: 1.2, 6.3, 6.9 and 30 μJy, for IRAC 2, 3, 4 and MIPS 24 respectively, according to Barmby et al. (2008) for the IRAC bands and Dickinson

et al. (2007) for MIPS 24. They are also summarized in Table 2.1. In addition, 1129 of these galaxies have Galaxy Evolution Explorer (GALEX) detections in the far-UV and 2345 galaxies in the near-UV. In our sample, 4376 galaxies have the highest quality spectroscopic redshifts measured by the Deep Evolutionary Exploratory Probe 2 team (DEEP2 DR3, Newman et al. 2011), with the DEIMOS spectrograph (Faber et al. 2003) on the Keck II telescope in an area of about 0.7 deg^2 in the sky. All the other galaxies in the sample (1610 galaxies) have secure photometric redshifts, more than 80% with uncertainty in redshift less than 0.1. The redshift covered is between 0.2-1 (almost 60% of the age of the universe) for a total sample of 5986 galaxies. For our purpose we will not distinguish between spectroscopic or photometric redshifts. This assumption will be discussed in Sec. 2.5.1.

The optical photometry (B, R and I bands) was taken from imaging with the CFH12K camera (Cuillandre et al. 2001) on the Canada-France-Hawaii Telescope (CFHT) 3.6 m. The integration time for these observations was 1 hr in B and R, and 2 hr in I, per pointing. More details may be found in Coil et al. (2004).

The near-IR photometry in the K_S band is from the Wide-field Infrared Camera (WIRC) (Wilson et al. 2003) camera on the Hale 5 m telescope at the Palomar observatory. This data set is the most restrictive constraint on the area of our sample, therefore our galaxy catalogue is K_S limited. The EGS field was surveyed to different depth for different sub-regions up to $K_S = 22.5$ in the AB magnitude system. The details may be found in Conselice et al. (2008).

The mid-IR data are from the IRAC and MIPS cameras on board the Spitzer Space Telescope. The details may be found in Barmby et al. (2008) and in Dickinson et al. (2007) describing the FIDEL survey, the source of our 24 μm data.

In addition, some data in the UV in two different bands 0.1530, 0.2310 μm from the GALEX (Morrissey et al. 2007) are included in our catalogue. This data set is part of the GALEX Deep Imaging Survey and the details may be found in Salim et al. (2009).

Source catalogue from each of these imaging data sets where cross-matched using a Bayesian method, which took into account prior information from the surface densities of sources in each band (Huang et al. 2010). The IRAC 1 data were used as the primary reference catalogue.

It is important to note that all our data are public, except the MIPS 24 photometry, the cross-match catalogue, and the photometric-redshift catalogue (Huang et al. 2010). These will be released to the public soon.

The histogram of the redshift distribution of the AEGIS sample is shown in Fig. 2.1 in the four redshift bins considered in our calculations. Note the larger number around $z \sim 0.7$, mainly due to the weighting scheme of the DEEP2 survey, which tends to select galaxies at $z > 0.7$ based on color-color criteria, plus the effect in the opposite direction of losing faint galaxies at higher redshifts.

In order to calculate the absolute magnitudes in U, B and K-band, we have computed the best-fitting template taken from the Bruzual & Charlot (2003) stellar

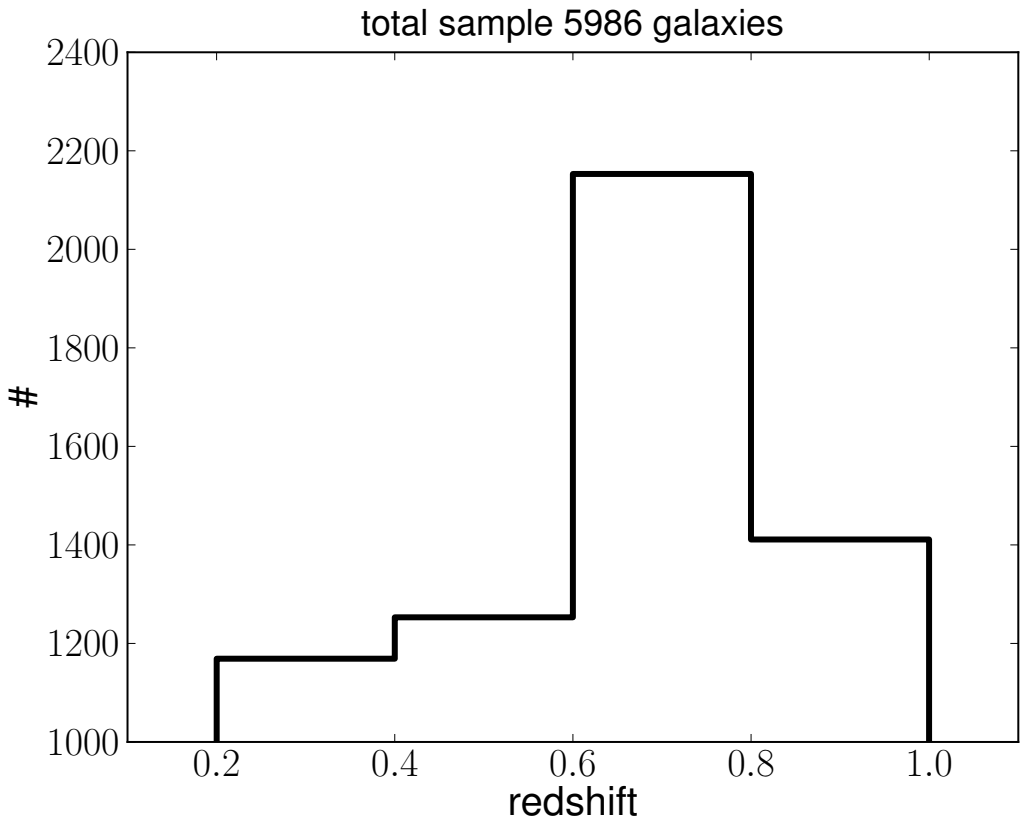

Figure 2.1 Histogram of the number of galaxies versus redshift of our sample in the four redshift bins considered in this work.

population models to the data in the photometric bands B, R, I, K_S, IRAC 1 and FUV, NUV and IRAC 2 when available, using the code `FAST` (Fitting and Assessment of Synthetic Templates, see the Appendix in Kriek et al. 2009 for details). `FAST` makes a χ^2 minimization from a grid of Bruzual & Charlot (2003) models. We chose a stellar IMF given by Chabrier (2003), an exponentially declining SFR $\sim \exp(-t/\tau)$ with τ ranging from 10^7-10^{10} Gyr, (the same range for the ages), metallicities by mass fraction in the range 0.004-0.050 (solar metallicity is 0.02 in these units), and optical extinction A_v from 0-10 following the Calzetti et al. (2000) extinction law. We calculate the absolute magnitudes from the best-fitting model using the U Bessel filter, the B filter from CFHT12K, and the same K-band filter from the UKIDSS survey, the same filter where the LF from C10 was estimated. All the transmission curves for these filters can be found in the default distribution of `Le PHARE`.

The sample was not corrected for incompleteness. However it is estimated here how this affects our results. The color-dependent incompleteness of the DEEP2 survey was studied in Willmer et al. (2006). They estimated a relation between the

rest-frame $U-B$ color versus the absolute magnitude in the B-band M_B for which galaxies fainter than this relation have color-dependent incompleteness. We show in Fig. 2.2 color-magnitude diagrams of our AEGIS galaxy sample for four different redshift bins. The black line is taken from Fig. 4 in Willmer et al. (2006). Galaxies located to the right of this line are likely missing. This figure is color coded according to the calculated best-fitted SWIRE template (see Sec. 2.2.3 and Sec. 2.4.1). The number of galaxies lying to the right of the relation, thus suffering color-dependent incompleteness, are only of 1.8%, 2.3%, 7.3% and 9.3% for the different redshift bins presented in Fig. 2.2.

Fig. 2.3 shows rest-frame $U-B$ versus absolute magnitude in the K-band in the three magnitude bins considered in this work to show an estimation on the galaxy number in each bin and their SED-types. We will describe this figure in the context of cosmological evolution in Sec. 2.5.4.

Thus to recap, the normalizations of the EBL in our model is given by the K-band LF of C10, and our galaxy SED-type fractions give the relative contribution of every galaxy type to the total luminosity density. The assignment of SED-types to the galaxy population at a given redshift is done individually for three ranges in K-band absolute magnitude, as it will be discussed in Sec. 2.3. Moreover, most of the contribution to the EBL (between 70-90%) comes from around the knee of the LF ($L_\star$ according to the Schechter parametrization) as shown in Fig. 2.4 for the rest-frame K-band luminosity density (calculated directly from the integration of the C10 LF) and not from the faintest galaxy population where we suffer some small color-dependent incompleteness. Fig 2.4 also shows that the contribution from the bright-end increases with redshift decreasing the impact of any color-dependent effect. As the remaining color-independent incompleteness does not have any effect on the galaxy SED-type fractions in our model or the overall normalization (which is set by the K-band LF), we conclude that our results are quite robust and the effect from incompleteness in our sample is minimal.

2.2.3 Galaxy spectral energy distribution library

The galaxy SEDs found in the SWIRE template library[2] (Polletta et al. 2007) are used. This library contains 25 templates, representative of the local galaxy population, defined as 3 elliptical galaxies, 7 spirals galaxies, 6 starbursts, 7 AGN galaxies (3 type I AGN, 4 type II AGN), and 2 composite (starburst+AGN) templates all covering the $\sim$ 0.1-1000 μm wavelength range. See Table 2.2 for a summary. The elliptical (quiescent), spiral (star-forming) and starburst (very star-forming) IR templates were generated with the `GRASIL` code (Silva et al. 1998) based on observations. The 7 spirals range from early to late types (i.e., S0 - Sdm). The starburst templates correspond to the SEDs of NGC 6090, NGC 6240, M 82, Arp 220, IRAS 22491-1808, and IRAS 20551-4250. In all of the spiral and starburst templates, the spectral region

[2]http://www.iasf-milano.inaf.it/∼polletta/templates/swire_templates.html

Template	Galaxy type
Ell2	Elliptical (2 Gyr old)
Ell5	Elliptical (5 Gyr old)
Ell13	Elliptical (13 Gyr old)
S0	Spiral 0
Sa	Spiral a
Sb	Spiral b
Sc	Spiral c
Sd	Spiral d
Sdm	Spiral dm
Spi4	Spiral c
NGC 6090	Starburst
M 82	Starburst
Arp 220	Starburst/ULIRG
IRAS 20551-4250	Starburst/ULIRG
IRAS 22491-1808	Starburst/ULIRG
NGC 6240	Starburst/Sey2
Sey2	Seyfert 2
Sey1.8	Seyfert 1.8
IRAS 19254-7245	South Seyfert 2+Starburst/ULIRG
QSO2	Type 2 QSO
Torus	Type 2 QSO
Mrk 231	Seyfert 1, BAL QSO, Starburst/ULIRG
QSO1	Type-1 QSO
BQSO1	Type-1 QSO
TQSO1	Type-1 QSO

Table 2.2 Summary of the templates and their galaxy type according to the SWIRE template library.

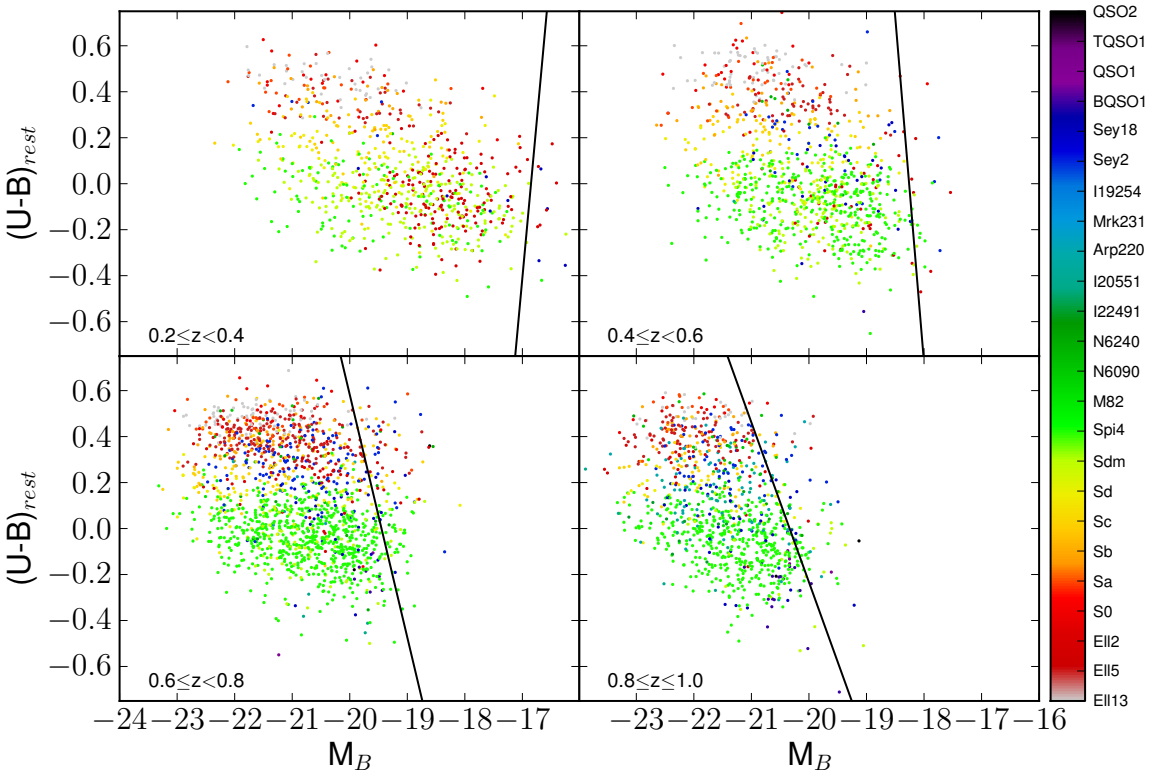

Figure 2.2 Rest $U - B$ color versus B-band absolute magnitude diagram for four different redshift bins to illustrate the incompleteness of our galaxy sample after the cuts explained in Sec. 2.4.1. The black line is taken from Fig. 4 in Willmer et al. (2006). Galaxies to the right of this line may suffer for a color selection effect. The fractions of these galaxies are 1.8%, 2.3%, 7.3% and 9.3% for each of the redshift bins respectively. The color code corresponds to the best-fitting galaxy SED-type from the SWIRE library (e.g., Ell13, elliptical 13 Gyr old; Sa, early-type spiral; Spi4, very late-type spiral; I20551, starburst; Sey18, Seyfert galaxy 1.8, QSO2, quasi-stellar object with some ratio between optical and infrared fluxes). Magnitudes are in Vega system converted from AB system using the relations $U_{Vega} = U_{AB} - 0.73$ and $B_{Vega} = B_{AB} + 0.11$ from Willmer et al. (2006).

between 5-12 μm, where many broad emission and absorption features are observed, was replaced by observed IR spectra from the PHT-S spectrometer on board the Infrared Space Observatory and from IRS on Spitzer. Some examples of these templates are shown in Fig. 2.5.

We are aware that these templates do not include high-redshift galaxies ($z >$ 0.3). This effect will be taken into account in a future version of our EBL model

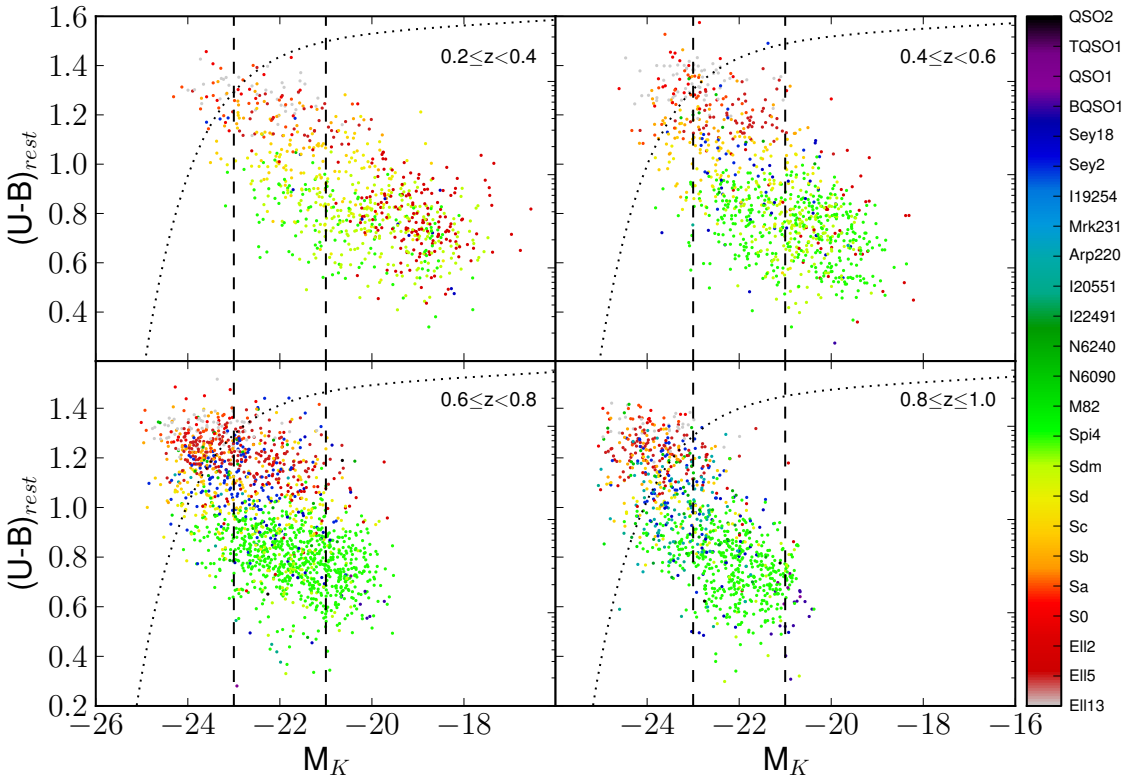

Figure 2.3 Color-magnitude diagram in the same four different redshift bins showing the galaxies of our sample after the cuts explained in Sec. 2.4.1, for the magnitude bins defined in the text for the integrals in Eq. 2.3. It is over plotted the luminosity function by Cirasuolo et al. (2010) in the mean of every redshift bin with arbitrary units in the logarithmic y-axis. The color code is the same that in Fig. 2.2. Magnitudes are in AB magnitude system.

when higher-redshift galaxy SEDs are released, including very vigorous starbursts and AGNs not present in the local universe. The limitation of using local templates for high-redshift galaxies has been addressed in some works such as Murphy et al. (2009), where they conclude that for ULIRGs in the redshift range between $1.4 < z < 2.6$, IR luminosities are overpredicted when they are derived only using MIPS 24 photometry, thus showing a different behaviour than local ULIRGs. It has been also shown by Menéndez-Delmestre et al. (2009) that sub-millimeter galaxies in the redshift range between $0.65 < z < 3.2$ show a larger polycyclic-aromatic-hydrocarbon (PAH) emission than local analogs, suggesting a more extended dusty star-forming region than seen in local ULIRGS.

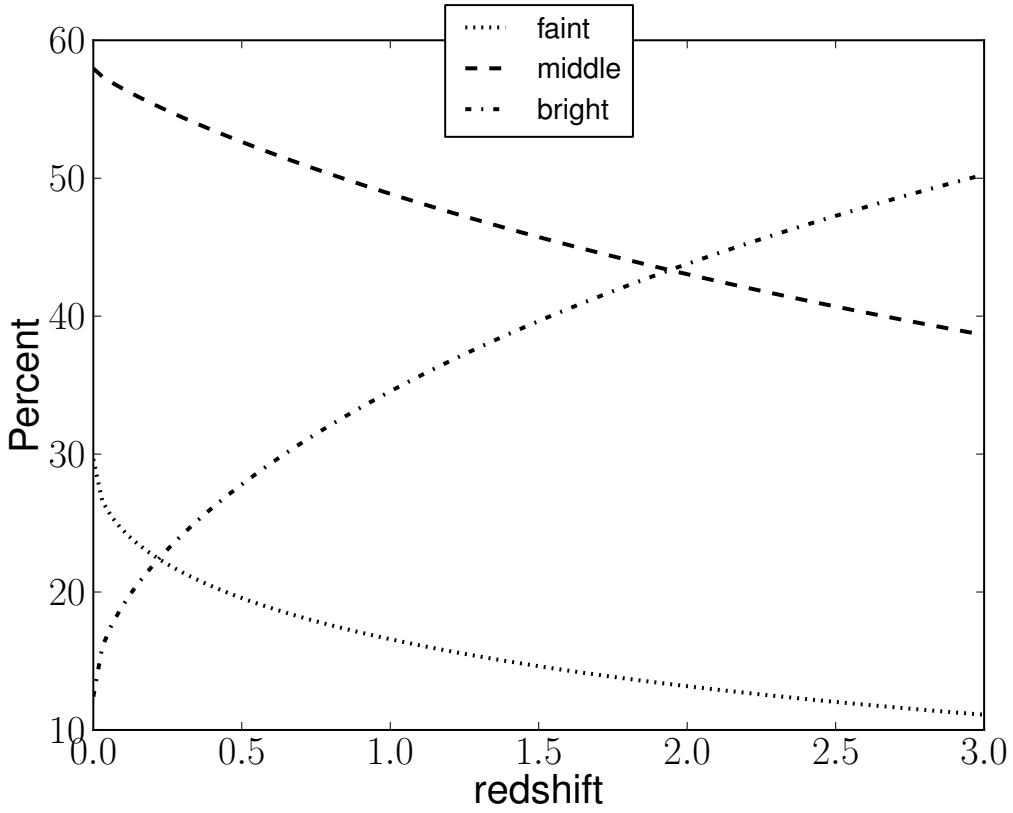

Figure 2.4 Contribution from the three different magnitude bins defined in Sec. 2.3 to the total of the co-moving rest-frame K-band luminosity density calculated directly from the luminosity function (LF) by Cirasuolo et al. (2010). The bulk of the light comes from the middle and bright-end of the LF, where the Schechter parameter $L_\star$ is. Note the increment with redshift of the bright-end contribution which decreases the impact of a possible color-selection effect or mis-typing (see Sec. 2.5.1) at the highest redshift in our galaxy sample.

2.3 Methodology

The empirical approach of the EBL evolution directly observed over the range of redshifts that contribute significantly to the EBL is followed. This is type (iv) according to the classification given in Sec. 2.1. As briefly explained in Sec. 2.1, our aim is to calculate the EBL integrating over redshift luminosity densities. These quantities are estimated attaching statistically SEDs to the galaxies given by the LF by C10 in three different magnitude bins. This is achieved using galaxy SED-type fractions between $z = 0.2 - 1$ by finding the best-fitting template of the 25 SED templates in the SWIRE library describing every galaxy in the AEGIS galaxy sample. Two different

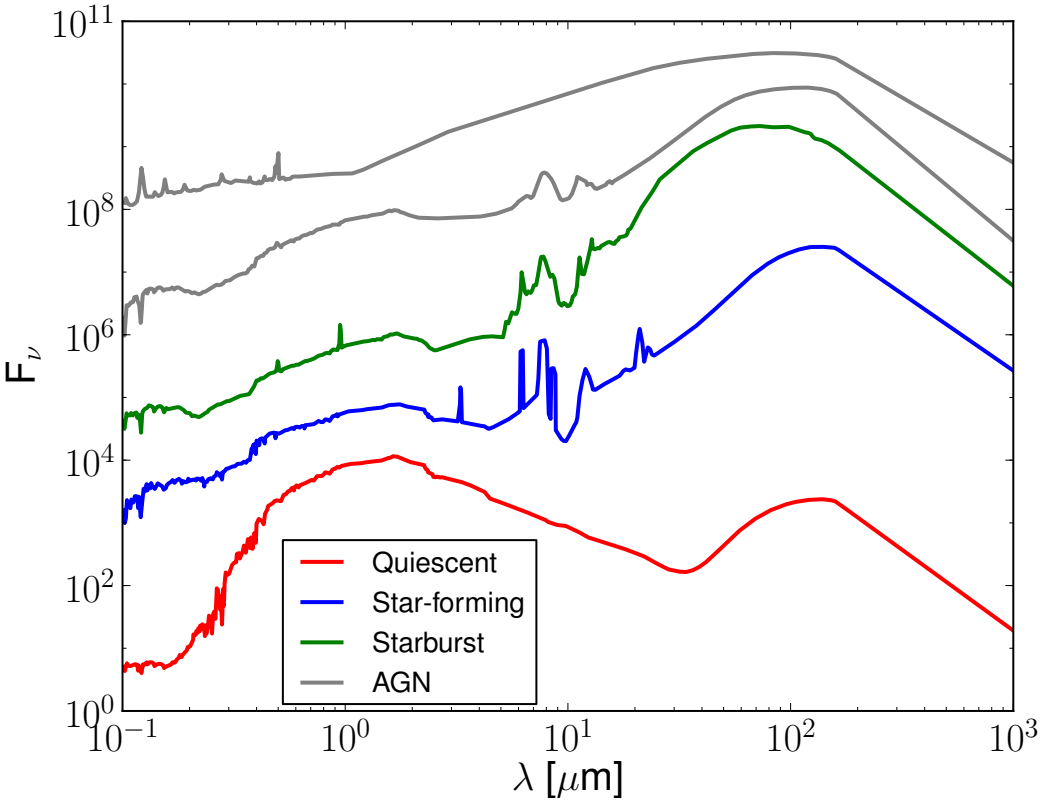

Figure 2.5 Spectral energy distributions for some galaxy templates from the SWIRE library. We show here (from the bottom to the top) an early type quiescent galaxy (Ell13), a very late star-forming galaxy (Spi4), a starburst galaxy (I22491) and two different AGN galaxies: a Seyfert II, and a quasi-stellar object type I (QSO1). The y-axis is in arbitrary units.

extrapolations for the galaxy SED-type fractions for $z > 1$ are assumed leading to the same evolving EBL intensity from the UV to the mid-IR but different far-IR.

The `Le PHARE` v2.2 (Photometric Analysis for Redshift Estimations) code is used to find the best-fitting SWIRE SED template for every galaxy in the sample. `Le PHARE` is a publicly available code[3] (Arnouts et al. 2002; Ilbert et al. 2006) mainly aimed to calculate photometric redshifts, but with the possibility to find the best-fitting template (among any library introduced as input) for galaxies with known redshift. `Le PHARE` makes use of a χ^2 fitting procedure weighted from normalizations in every detected bands, and with the possibility to set upper limits for fluxes in some bands based on non-detections. From the fact that we have required observations in several bands to build our catalogue, we set for every galaxy in the fitting procedure

[3]http://www.cfht.hawaii.edu/~arnouts/LEPHARE/cfht_lephare/

upper limits on the bands where there is no a 5σ detection. The information at all bands is used in the fitting.

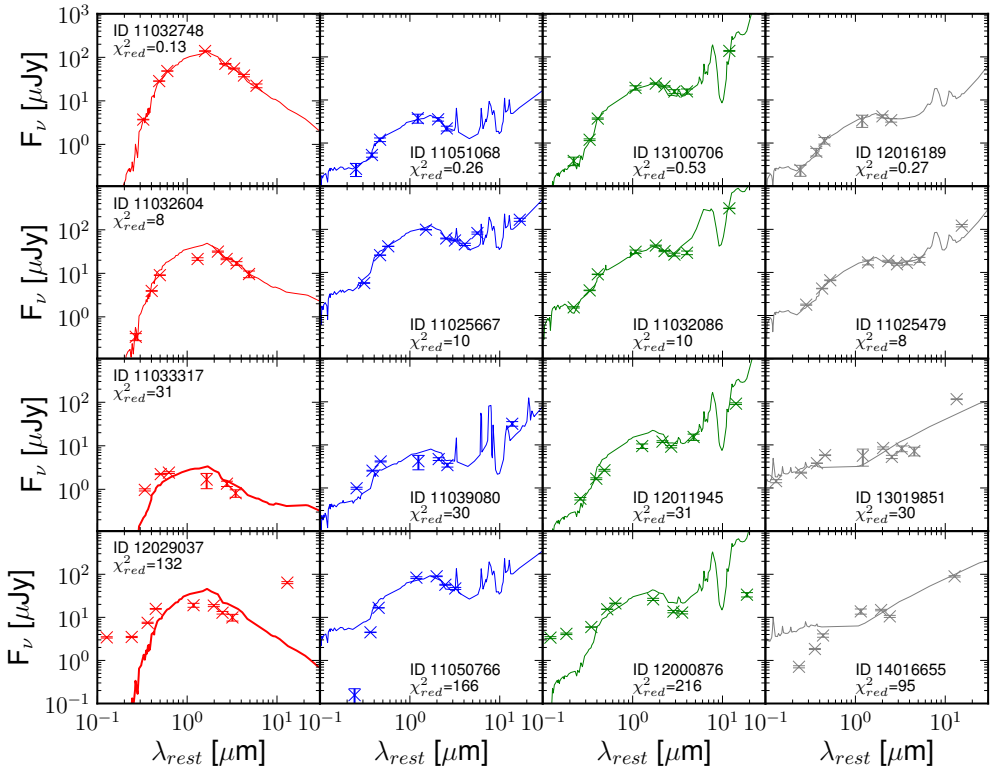

Figure 2.6 Examples of the best fits (upper panel), fits around χ^2_{red}=10 (second upper panel), fits around χ^2_{red}=30 (second lower panel) and the worst fits (lower panel). The columns are from left to right: quiescent, star-forming galaxies, starbursts, and AGN galaxies. The AEGIS identification number is shown for the galaxy along with χ^2_{red} given by the fitting code `Le PHARE` described in Sec. 2.3. The information at all bands is used in the fitting.

For every galaxy, templates are rejected if they predict a flux in a given band that is higher than the upper limit for that band. The equations used for the fitting procedure are shown in Eq. 2.1, with the parameter s given by Eq. 2.2:

$$\chi^2 = \sum_i \left(\frac{F_{obs,i} - sF_{temp,i}}{\sigma^2} \right)^2 \tag{2.1}$$

$$s = \sum_j \left(\frac{F_{obs,j} F_{temp,j}}{\sigma_j^2} \right) / \sum_j \left(\frac{F_{temp,j}^2}{\sigma_j^2} \right) \tag{2.2}$$

The notation is the following: i refers to a given band, j to the band used for the scaling, F_{obs} is the observed flux, F_{temp} is the flux from the templates, σ is the 1σ statistical uncertainty of the photometric measurement, and s is the scaling factor that is chosen to minimize the χ^2 values ($d\chi^2/ds = 0$). For each galaxy in the sample, we use a redshift given by either spectroscopic or photometric data (see Sec. 2.2.2 for details on our sample).

We define the co-moving luminosity density at the rest-frame wavelength λ as follows:

$$
\begin{aligned}
j_i(\lambda, z) &= j_i^{faint} + j_i^{mid} + j_i^{bright} = \\
&= \int_{M_2=-21.0}^{M_1=-16.6} \Phi(M_K^z, z) f_i T_i(M_K^z, \lambda)(1+z) dM_K^z + \\
&\quad \int_{M_3=-23.0}^{M_2=-21.0} \Phi(M_K^z, z) m_i T_i(M_K^z, \lambda)(1+z) dM_K^z + \\
&\quad \int_{M_4=-25.0}^{M_3=-23.0} \Phi(M_K^z, z) b_i T_i(M_K^z, \lambda)(1+z) dM_K^z \\
&\qquad\qquad [\text{erg s}^{-1}\text{Mpc}^{-3}\text{Hz}^{-1}]
\end{aligned}
\tag{2.3}
$$

where M_K^z in Eq. 2.3 is the rest-frame absolute magnitude in K-band at redshift z. The SEDs are given by a function $T_i(M_K^z, \lambda) = L_\nu$ (with units of erg s^{-1}Hz^{-1}) with i representing the different SWIRE SED types. We note that this function is dependent on M_K^z, since $T_i(M_K^z, 2.2)$ is the luminosity per Hz at the effective wavelength 2.2 μm for a galaxy with M_K. The fraction of faint, medium, and bright galaxies (f_i, m_i, b_i, the three different magnitude ranges) of each of the 25 classes is taken into account, according to their M_K^z, over redshift.

The magnitude ranges are defined in rest-frame K-band absolute magnitude using the AB magnitude system according to the different M_i in the integration limits in Eq. 2.3. The faintest magnitude limit corresponds to the faintest galaxy in our sample, the medium range is chosen to lead to roughly equal numbers of galaxies in each bin in the three magnitude bins, and the brightest magnitude corresponds to the brightest galaxy in our sample. This separation is done to take into account the fact that for the same fraction of a given SED type, the contribution to the luminosity density will be different depending on luminosity. At any rate, fainter galaxies than M_1 are too faint to contribute significantly to the EBL even if their number density is fairly large. The same is true for galaxies brighter than M_4: in spite of their high luminosity their density is not high enough to contribute.

The function $\Phi(M_K^z, z)$ in Eq. 2.3 is the Schechter parametrization of the evolving LF as given by C10 in co-moving frame. The factor $(1+z)$ comes from the k-correction to account for the change in the definition of the local absolute magnitude M_K^0 with the redshift, i.e.,

$$k(z) = (1+z)\frac{T(M_K^z, \lambda)}{T(M_K^0, \lambda)} \tag{2.4}$$

The co-moving total luminosity density is calculated adding the luminosity density from the 25 SWIRE SED types, i.e.,

$$j_{total}(\lambda, z) = \sum_i j_i(\lambda, z) \tag{2.5}$$

We note that the total luminosity density at 2.2 μm $j_{total}(2.2, z)$ is just the integral of the C10 LF.

The quantity defined by Eq. 2.5 gives us an estimate of the total amount of light emitted by galaxies per unit volume at a given wavelength and redshift.

The history of the SFR density ρ in the universe is then computed using the following approximation,

$$\rho = 1.74 \times 10^{-10}(j_{IR} + 3.3 j_{2800})/L_\odot \quad [\mathrm{M_\odot\ yr^{-1} Mpc^{-3}}] \tag{2.6}$$

where j_{IR} is the total bolometric infrared luminosity density integrated from 8-1000 μm, j_{2800} is the luminosity density at 0.28 μm, and $L_\odot = 3.839 \times 10^{33}$ erg s^{-1} the solar bolometric luminosity. This equation is taken from Wuyts et al. (2009), who add the UV and IR contributions (unobscured plus obscured), using calibrations for the local universe by Kennicutt (1998) and a Salpeter IMF (Salpeter 1955).

If Eq. 2.5 is integrated from some redshift z to $z_{max} = 4$ (up to where the LF is given), the EBL flux seen by an observer at redshift z, due to the radiation emitted from z_{max} down to z is obtained,

$$\lambda I_\lambda(\lambda, z) = \frac{c^2}{4\pi\lambda}\int_z^{z_{max}} j_{total}[\lambda(1+z)/(1+z'), z']\left|\frac{dt}{dz'}\right| dz'$$

$$[\mathrm{nW\ m^{-2} sr^{-1}}] \tag{2.7}$$

This is what we call co-moving EBL spectrum, which is given in intensity units. The factor dt/dz' takes into account the assumed cosmology (e.g., Peebles 1993), and is given explicitly by

$$\left|\frac{dt}{dz'}\right| = \frac{1}{H_0(1+z')\sqrt{\Omega_m(1+z')^3 + \Omega_\Lambda}} \tag{2.8}$$

with H_0, Ω_m and Ω_Λ given by the parameters of the ΛCDM cosmology, exactly the same used by C10 for the LF.

z_{mean}	Quiescent	Star-forming	Starburst	AGN	Total non-rejected/rejected
0.3	235 (29%)/77 (24%)	554 (69%)/169 (52%)	1 (0%)/23 (7%)	14 (2%)/55 (17%)	804/324
0.5	157 (16%)/38 (16%)	756 (77%)/133 (47%)	13 (1%)/13 (5%)	58 (6%)/67 (32%)	984/241
0.7	328 (20%)/59 (13%)	1079 (66%)/149 (32%)	55 (3%)/38 (8%)	175 (11%)/221 (47%)	1637/467
0.9	144 (14%)/22 (7%)	607 (58%)/104 (32%)	164 (16%)/21 (6%)	127 (12%)/182 (55%)	1042/329

Table 2.3 Galaxy SED-type fractions for our galaxy sample after applying the χ^2_{red} cuts (see Sec. 2.4.1). Numbers are shown for galaxies non-rejected and rejected by the cuts, respectively. The total of non-rejected plus rejected galaxies is 5828. This is less than 5986, our total number of galaxies, because `Le PHARE` could not get any fit for 158 galaxies.

In our approach, it is possible to directly calculate the contribution to the EBL from all redshift bins, as well as the evolution of the EBL spectrum with redshift and the processes related to this evolution, by sources of all the 25 SED types considered.

2.4 Results

2.4.1 Galaxy SED-type fractions

As explained in Sec. 2.3, the `Le PHARE` code is used to fit every galaxy in our sample to the 25 SWIRE templates. For clarity, we will compress in our discussion (but not in our calculations, where they will remain independent) the 25 SED-types in the SWIRE library to four groups: quiescent, star-forming galaxies, starbursts, and AGN galaxies. We choose this nomenclature to clarify that our classification is multiwavelength-SED based, and not morphological.

We note that the fitting procedure is relatively sensitive to the errors on the photometric measurements leading to uncertainties in the galaxy SED-type fractions of ± 0.1. For our model we set a lower limit of 6% to all the photometric errors. The effect of different treatments of errors in the photometry is discussed thoroughly in Sec. 2.5.1 and it is shown in this section the uncertainties due to this effect on our galaxy SED-type fractions and on the EBL estimation.

To avoid accounting for bad fits, which do not correctly describe the galaxy photometric data, a cut in $\chi^2_{red} = \chi^2/n$ is applied, with χ^2 given by `Le PHARE` (Eq. 2.1) and n degrees of freedom (bands with detections). We have checked carefully that $\chi^2_{red} \leq 30$ is a good value for quiescent, star-forming and starburst galaxies, but AGN galaxies are systematically worse fits, probably due to the fact that there is a large range in AGN SED shapes due to multiple emission components which cannot be easily encapsulated in a few templates.

Fig. 2.6 shows some examples of good and bad fits in for the four different main galaxy types with low χ^2_{red} in the top row, some fits around $\chi^2_{red} \sim 10$ in the second row, other fits around $\chi^2_{red} \sim 30$ the third row and some very bad fits (with very high χ^2_{red}) in the bottom row. Due to the fact that AGN galaxies are systematically worse fits, two different cuts depending on the galaxy-SED type fitted are used for our model. These values are $\chi^2_{red} \leq 30$ for quiescent, star-forming and starburst galaxies, and $\chi^2_{red} \leq 10$ for AGNs. As for the uncertainties on the photometric errors, we show the uncertainties due to these cuts for the galaxy SED-type fractions and the EBL and discuss them in Sec. 2.5.1.

After applying these cuts there are still 4467 galaxies remaining, i.e., ∼75% of the original sample. Fig. 2.7 shows a histogram of the galaxy SED-types in the total sample after the cuts, and the classification (shown with different colors) of the four main galaxy groups considered in this discussion. We find 19% quiescent, 67% star-forming galaxies, 5% starbursts, and 8% AGN galaxies.

A bimodality between quiescent and star-forming galaxies is clearly found. Most

	$z = 0.3$	0.5	0.7	0.9	Total
faint	507	411	251	49	1218
middle	255	452	899	530	2136
bright	43	121	487	462	1113

Table 2.4 Number of galaxies (after applying the χ^2_{red} cuts, see Sec. 2.4.1) in every magnitude and redshift bin used to calculate the galaxy SED-type fractions in Fig. 2.9.

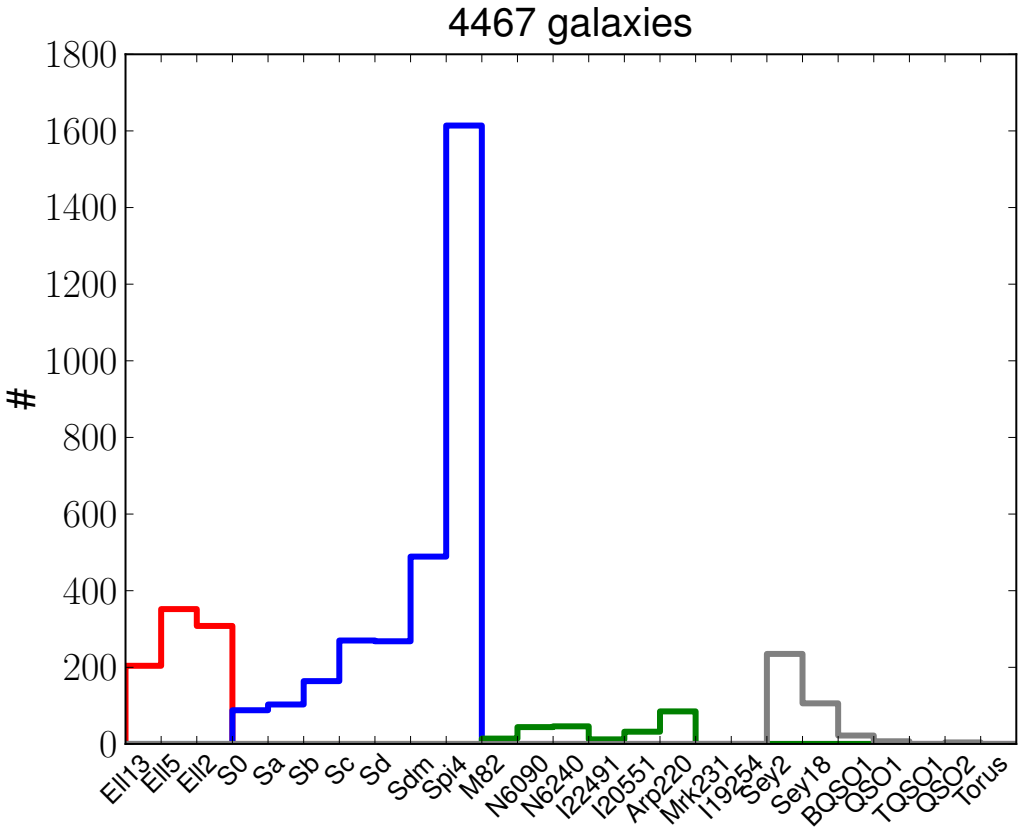

Figure 2.7 Galaxy SED-types for the sample after removing the worst fits ($\sim$ 25% of the total sample, see Sec. 2.4.1). We have 864 quiescent (in red, 19%), 2996 star-forming galaxies (in blue, 67%), 233 starbursts (in green, 5%), and 374 AGN galaxies (in gray, 8%) from a total of 4467 galaxies. The x-axis describes the names of the 25 SED templates from the SWIRE library as described in Table 2.2.

of the quiescent galaxies are $\leq$ 5 Gyr old, late-type elliptical (Ell5 and Ell2, according to the SWIRE classification). The bulk of the star-forming population is late-type spirals with the PAH region measured using Spitzer data (Spi4, according to the SWIRE classification). In the starburst-like galaxies case, the Arp 220-like galax-

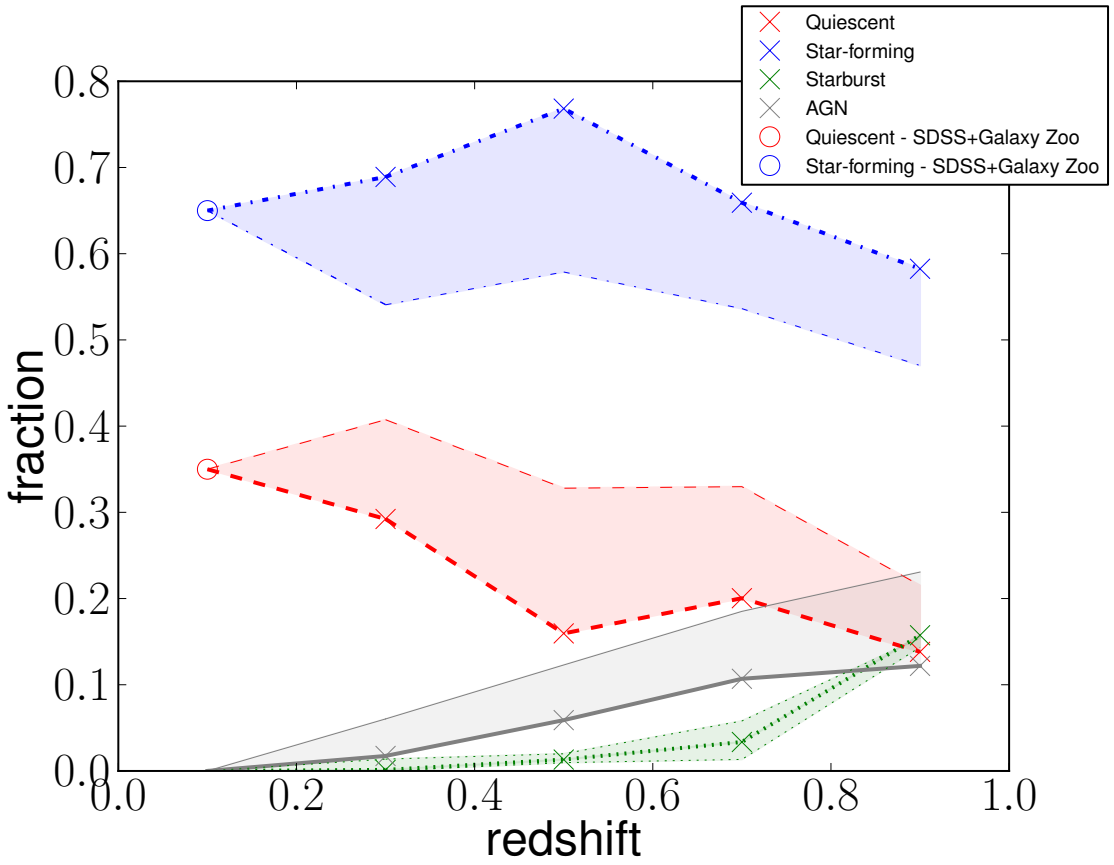

Figure 2.8 Galaxy SED-type fractions from our catalogue (after the χ^2_{red} cuts, see Sec. 2.4.1) of the different populations versus redshift according to our multiwavelength fits. We mark with crosses our fractions from $z = 0.9 - 0.3$. The lines represent the linear interpolation that we use to calculate galaxy SED-type fractions for all redshift: dashed-red line represents quiescent galaxies, dotted-dashed-blue line represents star-forming galaxies, dotted-green line represents starburst galaxies, and solid-gray line represents AGN galaxies. The circles at $z = 0.1$ are fractions computed from the SDSS-based sample (see text). We show with a shadow area the uncertainties from our lower limit for the errors as well as for our χ^2_{red} cut for fits. The uncertainties are around ± 0.1.

ies are dominant. The AGN-like population is clearly dominated by Seyfert-type galaxies, especially type II.

Table 2.3 and Fig. 2.8 show the galaxy SED-type fractions for four different redshift bins up to $z = 1$, where we have chosen bins of Δz=0.2 for statistical reasons. The shadow regions are the uncertainties due to the lower limits on the photometric errors for the catalogue and for the χ^2_{red} cuts. This region is calculated changing the lower limits from 1-10% in steps of 1% and applying extreme cases for the cuts

for every lower limit. The boundaries from these calculations lead to the shadow regions. The fractions adopted for the model are marked with crosses and wider lines. We observe that the fraction of quiescent galaxies increases by a factor ~ 2 from $z \sim 0.9 - 0.3$, while the star-forming fraction keeps roughly constant for the full redshift range peaking at $z = 0.5$. Starburst-type galaxies decrease very quickly from $z \sim 0.9$ and reach almost 0 at $z \sim 0.5$. On the other hand, the AGN-type fraction is roughly constant from $z \sim 0.9 - 0.7$, and then decreases to 0.02 at $z \sim 0.3$. This result should not be considered a complete picture of the evolution of the galaxy populations in the universe since these fractions depend on the color-magnitude limits of the survey as Fig. 2.2 shows. But what it is certainly described is the population of galaxies that contribute the most to the EBL around the knee of the LF (the middle and bright region of the LF, see Fig. 2.4).

Fig. 2.9 shows the galaxy SED-type fractions for the three different magnitude bins defined in Eq. 2.3 and explained in the previous section, Sec. 2.3. These are the galaxy SED-type fractions used directly in Eq. 2.3 to calculate the luminosity densities. Table 2.4 lists the number of galaxies in every magnitude and redshift bin used to estimate the galaxy SED-type fractions showed in Fig. 2.9.

The galaxy SED-type fractions are extrapolated to lower redshift ($z \sim 0$) by using results from Goto et al. (2003), that use data from the Sloan Digital Sky Survey (SDSS). They give galaxy fractions according to a morphological classification. They are converted to SED classification by using two different observational works, using the Galaxy Zoo catalogue from SDSS data, on the abundances of blue-elliptical galaxies ($f_{be} = 5.7 \pm 0.4\%$, Skibba et al. 2009) and red spirals ($f_{rs} \sim 25\%$ Schawinski et al. 2009). Utilizing these works we calculate galaxy SED-type fractions for the local $0 < z < 0.2$ universe as follows: in Fig. 12 and 15 of Goto et al. (2003) we see morphology-density and morphology-radius relations respectively. From the bin with the largest number density in any of those figures, we have the fractions of galaxies with early ($\sim 14\%$), intermediate-type ($\sim 26\%$), early-disc ($\sim 35\%$), and late-disc ($\sim 25\%$) morphology. The fractions of elliptical galaxies are the fractions of early galaxies, $f_{ell} \sim 14\%$ and the fraction of spirals are the intermediate-type, plus the early-disc, plus late-disc galaxies, $f_{spi} \sim 86\%$. From the Galaxy Zoo papers (Skibba et al. 2009; Schawinski et al. 2009) these fractions are estimated for the local universe according to Eq. 2.9 and Eq. 2.10: $f_{quies} \sim 35\%$ of quiescent and $f_{sf} \sim 65\%$ of star-forming galaxies.

$$\begin{aligned} f_{quies} &= f_{ell} - (f_{ell} \times f_{be}) + (f_{spi} \times f_{rs}) = \\ &= 0.14 - (0.14 \times 0.057) + (0.86 \times 0.25) = 0.35 \end{aligned} \tag{2.9}$$

$$\begin{aligned} f_{sf} &= f_{spi} - (f_{spi} \times f_{rs}) + (f_{ell} \times f_{be}) \\ &= 0.86 - (0.86 \times 0.25) + (0.14 \times 0.057) = 0.65 \end{aligned} \tag{2.10}$$

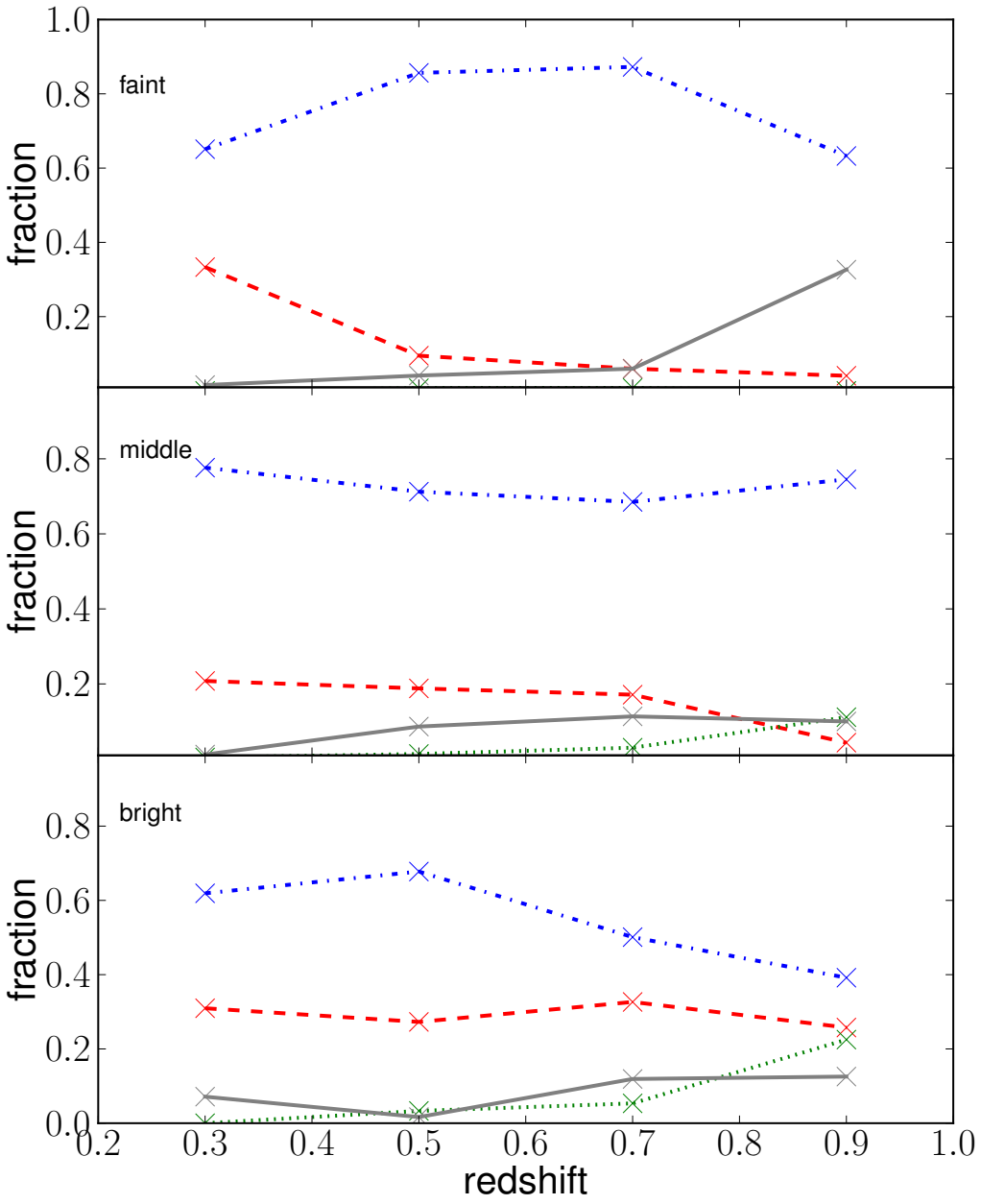

Figure 2.9 Galaxy SED-type fractions (after applying the χ^2_{red} cuts, see Sec. 2.4.1) of the different populations (the lines are the same as in Fig. 2.8) versus redshift in the three different magnitude bins defined in the text for Eq. 2.3. See Table 2.4 for number of galaxies in every magnitude and redshift bin.

We have to keep in mind that these numbers are calculated from a different sample and a direct comparison with our sample may be not accurate. Note as well that our definition for quiescent and star-forming is not exactly the same as that the red and blue classification from Galaxy Zoo, but very similar. Some of our very early-type star-forming galaxies are red according to that classification, but the results do not change much because of the fewer number of these galaxies. In the opposite direction to this effect we note as well that `Le PHARE` prefers to fit some early-type star-forming galaxies as late-type red galaxies due to their bluer optical colors but very little dust re-emission, if any, according to the SWIRE templates.

To be able to compute the local EBL with accuracy, as well as its evolution out to the redshifts of the most distant objects detected by ground-based VHE γ-ray telescopes, i.e., $z \leq 0.6$ (Albert et al. 2008), we would need to extrapolate the galaxy SED-type fractions to $z > 1$. It is expected that the local EBL has contributions from these larger redshifts, although the behavior is different for the optical/near-IR and the far-IR due to the spectral region where the different populations contribute.

For the high-redshift universe ($z > 1$, where there are no galaxies in our sample) two different cases are considered for the evolution of the galaxy SED-type fraction. It is shown that our results are not changed significantly except in the far-IR by these two choices. For the redshifts less than those of the most distant known γ-ray sources, and redshifts where future sources are likely to be found in the near future by imaging atmospheric Čerenkov telescopes (IACTs), it is found almost no change in the EBL even with a fairly large adjustment in the evolution of galaxy-SED type fractions. This is discussed in Sec. 2.5.1 and here we show the uncertainties of the EBL and others quantities calculated due to these assumptions. The *fiducial* choice is to keep constant the fractions computed for our highest redshift bin. This choice is made for simplicity, due to the difficulty in the multiwavelength classification of distant galaxies with current instruments. But we do note that there is strong evidence from several observational results by Reddy et al. (2005), Pérez-González et al. (2008), Taylor et al. (2009) and Wuyts et al. (2009) which suggest no further evolution at higher redshifts of the quiescent population. All these independent works claim that the fraction of distant non star-forming red objects in the high-redshift universe keep constant around 24-33% of the total number of galaxies up to $z > 2.5$. We find at $z \sim 0.9$ around 14% of quiescent galaxies, which it is kept constant for higher redshifts. We note here the red-galaxy incompleteness for DEEP2, implying that our fractions might underestimate the actual number of mainly quiescent galaxies in the faint-end of the LF (as seen in the very low number of quiescent fractions in Fig. 2.9), due to the difficulty for the DEEP2 survey to characterize faint-red galaxies for $z > 0.8$. The impact of this effect is decreased by taking into our catalogue galaxies with photometric redshift. In any case, there are no consequences for the EBL results as previously discussed in Sec. 2.2.2, because the bulk of the light comes from the region of the LF around $L_\star$ where we are basically complete.

As alternative approach, we choose to increase linearly with redshift the starburst-

like fraction from our calculated 16% at $z = 0.9$ up to 60% at $z = 2$, while decreasing at the same rate the quiescent and star-forming galaxies. The weight of every one of the 25 SWIRE templates is changed in the same proportion. The fractions are kept constant at $z = 2$ for $z > 2$. This approach is called *high-starburst* and it is used to determine a likely upper limit on the EBL at long wavelengths (see Sec. 2.4.3).

2.4.2 Luminosity densities

The local galaxy luminosity density is shown in Fig. 2.10 calculated using Eq. 2.5. The solid-black line is computed from the sum of the contributions from all the 25 SED-types. An excellent agreement is found with the observational data from independent surveys over all wavelengths. We note that our different assumptions for the high-redshift fractions lead necessarily to the same result because this is the light emitted at $z = 0$.

Fig. 2.11 shows the evolution over redshift of the luminosity densities at different wavelengths for both of our extrapolations for the high-redshift fractions. We show with dot-dashed-orange line the galaxy formation SAM prediction by SGPD11 and postpone the discussion to Sec. 2.5.3. The upper-left panel shows the rest-frame 0.28 μm, which is in good agreement with the observational results by Gabasch et al. (2006) and Dahlen et al. (2007) for $z < 1.5$, and somewhat lower between $z = 2 - 1.5$ than the Dahlen et al. (2007) data. This quantity is also directly related with the SFR density through Eq. 2.6. The upper-right panel shows the rest-frame B-band, which is in good agreement with some observational results, such as Norberg et al. (2002), Gabasch et al. (2004), Ilbert et al. (2005); but around a 15-20% higher than Faber et al. (2007). At $z > 1$ we are a factor ~ 2 higher than the data by Dahlen et al. (2005). The lower-left panel shows the rest-frame K-band, among some observational results by Arnouts et al. (2007) and Barro et al. (2009). The lower-right panel shows the evolution of our calculated total IR luminosity over redshift, that given by the FRV08 model and from observations by Rodighiero et al. (2010). We note a general good agreement with these data (we are a a factor 1.5 higher around $z \sim 1$) for our *fiducial* extrapolation of SED-types beyond $z = 1$, but we are predicting a higher luminosity density for the *high-starburst* assumption. The agreement with FRV08 is pretty good, except for the lowest redshifts. The total IR luminosity is also directly related with the SFR density through Eq. 2.6.

2.4.3 Star formation rate density history

Fig. 2.12 shows the history of the SFR density of the universe computed from our modeling using Eq. 2.6. It is also plotted the prediction using the same equation, from the luminosity densities provided by SGPD11, and a compilation of observational works from Pérez-González et al. (2008) using different estimators, assuming a Salpeter stellar IMF. We are aware that this IMF is not as good description of the observations as other IMFs such as Chabrier (2003), but we are concerned here on

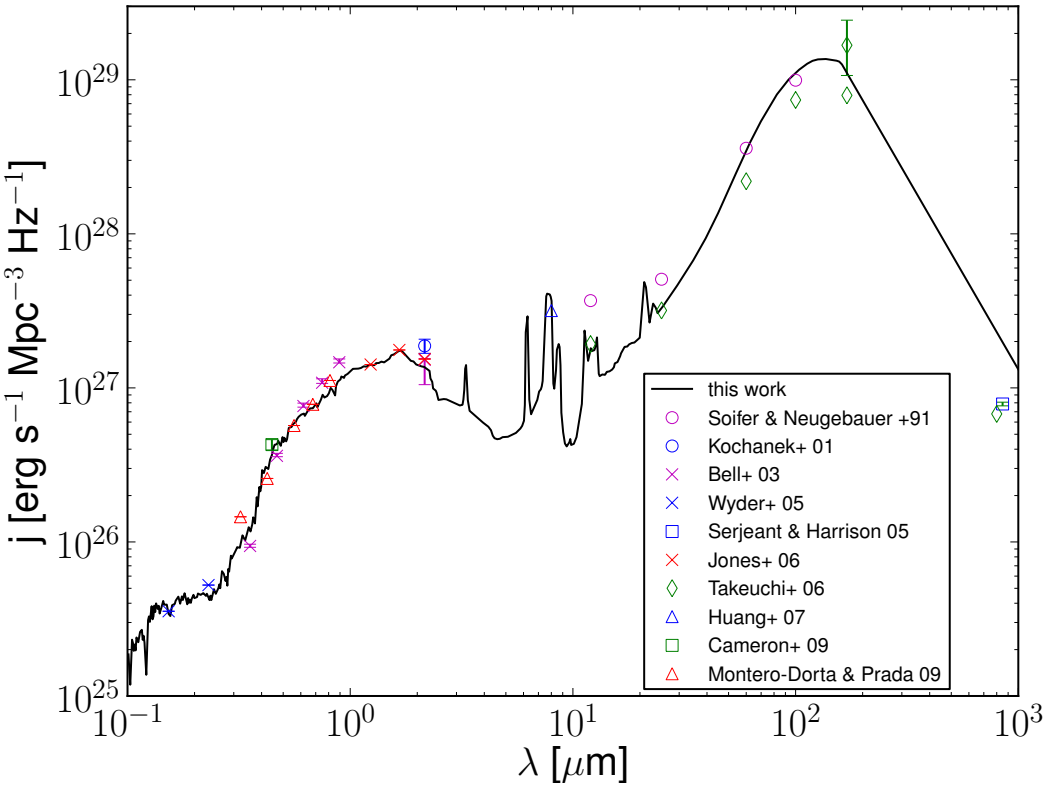

Figure 2.10 Comparison between our estimation of the local luminosity density (black line) and observational data from different surveys: 12, 25, 60, 100 μm from Soifer & Neugebauer (1991); K-band from Kochanek et al. (2001); u, g, r, i, z, K-band from Bell et al. (2003); FUV, NUV from Wyder et al. (2005); 850 μm from Serjeant & Harrison (2005); bj, rf, J, H, K-band from Jones et al. (2006); 12, 25, 60, 100, two different analysis for 170, 800 μm from Takeuchi et al. (2006) (two different analysis); 8 μm from Huang et al. (2007); B-band from Driver et al. (2008) and Cameron et al. (2009); and u, g, r, i, z from Montero-Dorta & Prada (2009).

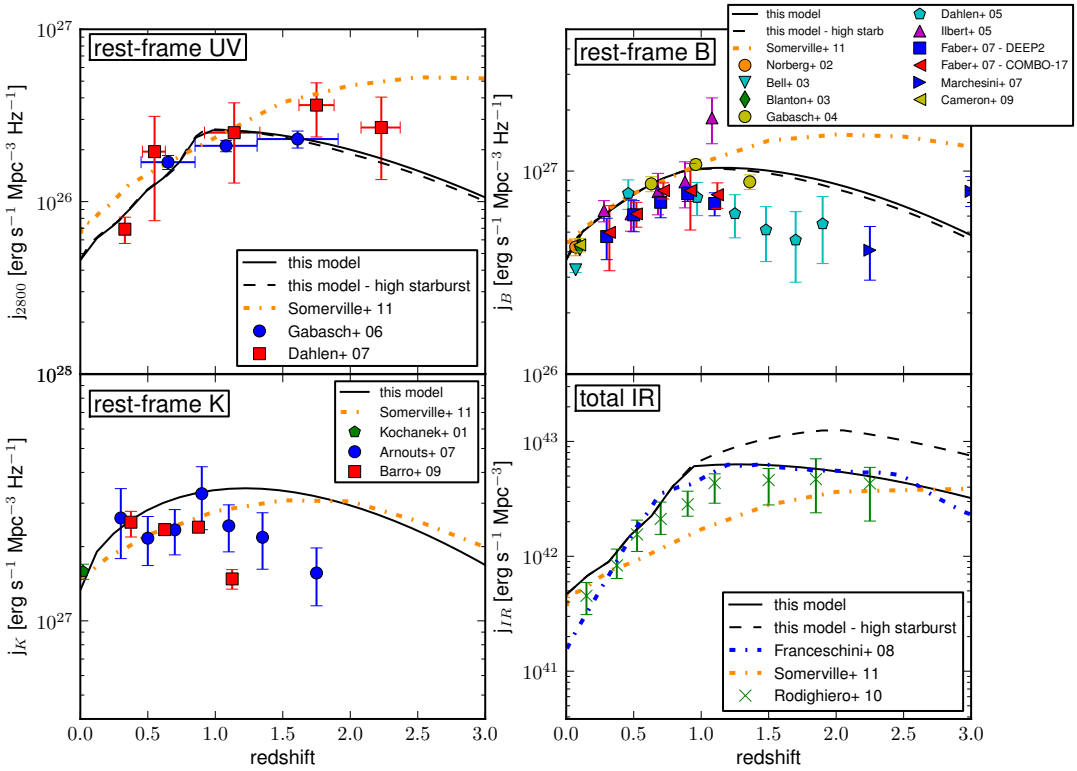

Figure 2.11 Comparison between the calculated luminosity densities versus redshift for different spectral bands with observational data (solid-black line, for our *fiducial* extrapolation; dashed-black line for our *high-starburst* extrapolation for the galaxy SED-type fractions for $z > 1$; see Sec. 2.4.1). We also show as dot-dashed-orange line the model from Somerville et al. 2011. *Upper-left panel*: rest-frame UV at 0.28 μm and data from Gabasch et al. (2006) and Dahlen et al. (2007). *Lower-left panel*: rest-frame K-band and observational data from Arnouts et al. (2007) and Barro et al. (2009). It is important to note that this is just the integral of the LF by C10 between M_1 and M_4 in Eq. 2.3. *Upper-right panel*: rest-frame B-band and observational data from a compilation from Faber et al. (2007) from these works: Norberg et al. (2002), Bell et al. (2003), Blanton et al. (2003a), Gabasch et al. (2004), Dahlen et al. (2005), and Ilbert et al. (2005). Data from Marchesini et al. (2007) and Cameron et al. (2009) are plotted as well. *Lower-right panel*: integrated IR from 8-1000 μm data from Rodighiero et al. (2010) and the phenomenological estimations by Franceschini et al. (2008).

showing a comparison with the compilation of SFR data, which is given by a Salpeter IMF. The data from $z = 3-1.5$ are roughly reproduced. Our results are in agreement

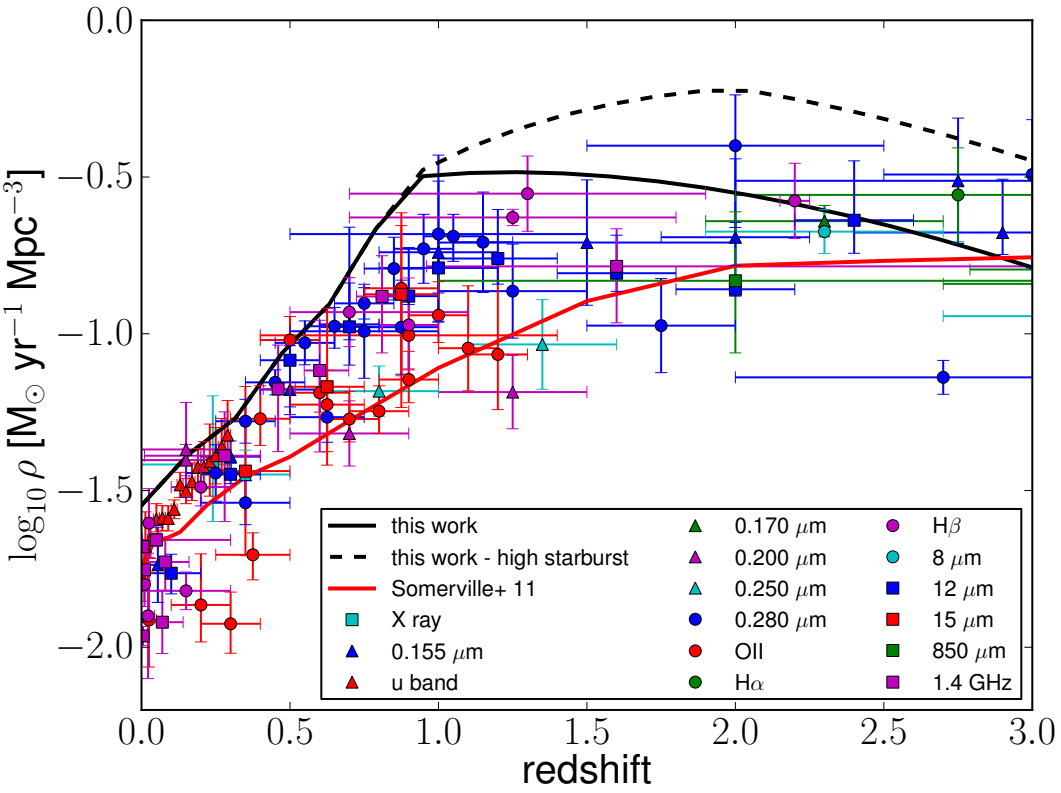

Figure 2.12 Comparison between the calculated star formation rate density computed using Eq. 2.6 for a Salpeter initial mass function, the prediction using the same equation from the luminosity densities provided by Somerville et al. (2011) (red-solid line), and some observational data from different estimators shown in the legend. The compilation of data points is taken from Pérez-González et al. (2008). The solid and dashed-black lines are from the different extrapolations for the galaxy SED-type fractions for $z > 1$ (see Sec. 2.4.1).

within errors with the upper data envelope from $z = 1.5 - 0.7$. We systematically predict a factor ~ 1.3 higher SFR than the observational data between $z = 0.7 - 0$. For the *high-starburst* assumption a considerably higher SFR density is estimated. This *high-starburst* case is motivated by the increasing star formation rate density to $z \sim 2$ in Fig. 2.12, and the increasing specific star formation rate to $z \sim 2$ (Reddy et al. 2006; Daddi et al. 2007). But Fig. 2.12 also indicates that our *high-starburst* is an extreme assumption.

We want to call attention to the large uncertainties on the observational data estimates for the SFR for all redshifts. These uncertainties are especially important for the higher redshifts, mainly because local calibrations are used in the estimations,

and also the uncertainties of the corrections due to dust absorption. The same is true for Eq. 2.6 which is calibrated using observed local galaxy properties and these might indeed evolve in redshift.

2.4.4 Extragalactic background light

The local EBL ($z = 0$) estimated using our method is shown in Fig. 2.13. The solid-black line is the EBL calculated by our *fiducial* model[4] using Eq. 2.7. Observational data are plotted. Empty symbols are direct measurements: 0.3, 0.555, 0.814 μm by Bernstein (2007); 1.43, 1.53, 1.63, 1.73, 1.83, 1.93, 2.03, 2.14, 2.24, 2.34, 2.44, 2.54, 2.88, 2.98, 3.07, 3.17, 3.28, 3.38, 3.48, 3.58, 3.68, 3.78, 3.88, 3.98 μm by Matsumoto et al. (2005) using IRTS; 1.25, 2.2 μm (slightly shifted for clarity) by Cambrésy et al. (2001); 2.2, 2.5 μm by Gorjian, Wright & Chary (2000); 60, 100 μm by Finkbeiner, Davis & Schlegel (2000) all these using DIRBE; 65, 90, 140 (slightly shifted for clarity), 160 μm by Matsuura et al. (2010) using AKARI; 100, 140, 240 μm by Lagache et al. (2000); 140 (slightly shifted for clarity), 240 μm by Schlegel, Finkbeiner & Davis (1998); 140, 240 μm by Hauser et al. (1998) all these using FIRAS. Filled symbols are galaxy-count data, usually considered lower limits: 0.1530, 0.2310 μm by Xu et al. (2005) using GALEX; 0.1595, 0.2365 μm by Gardner, Brown & Ferguson (2000) using HST and STIS; 0.36, 0.45, 0.67, 0.81, 1.1, 1.6 (slightly shifted for clarity), 2.2 μm (slightly shifted for clarity) by Madau & Pozzetti (2000) using HST and ground-based telescopes; 1.25, 1.60, 2.12 μm by Keenan et al. (2010) using Subaru; 3.6 μm by Levenson & Wright (2008); 3.6, 4.5, 5.8, 8.0 μm by Fazio et al. (2004) with a reanalysis of the last point by Franceschini et al. 2008 all these using IRAC; 15 μm by Metcalfe et al. (2003) using ISO; 15 μm by Hopwood et al. (2010) using AKARI; 24 μm by Papovich et al. (2004) and Chary et al. (2004); 24 (slightly shifted for clarity), 70, 160 μm by Béthermin et al. (2010) using MIPS; 71.4 μm by Frayer et al. (2006) using MIPS; 100, 160 μm by Berta et al. (2010) using Herschel. The colored-solid lines (Aharonian et al. 2006; Mazin & Raue 2007; Albert et al. 2008) are upper limits from γ-ray astronomy using different blazars (see Chap. 5 for details). The dot-dashed-blue line, and the dashed-red line are the predictions from the models by Franceschini et al. (2008) and Gilmore et al. (2011), respectively. It is usual to consider data from galaxy counts as lower limits. We find a very low background from UV to mid-IR, along the lower limits from galaxy counts. In the UV our model is lower than the Gardner, Brown & Ferguson (2000) data, but we consider these data suspect, due to very poor statistics on their number counts at the faintest magnitudes and the fact that they are systematically higher than the UV data from GALEX (Xu et al. 2005), an experiment with higher sensitivity and better statistics.

In the mid-IR region between 7-15 μm our results are a factor ~ 1.2 higher than other models. A lower background than FRV08 is estimated from 15-50 μm by a factor as large as ~ 1.5. Our results are still compatible with the limits from galaxy

[4]Intensity files at different redshifts are publicly available at http://side.iaa.es/EBL/

z	Quiescent	Star-forming	Starburst	AGN	I_{bol} [nW m^{-2}sr^{-1}]
0.0	4.71 (7%)	39.70 (57%)	20.45 (30%)	4.41 (6%)	69.26
0.2	3.86 (5%)	38.96 (54%)	24.54 (34%)	5.25 (7%)	72.60
0.6	2.35 (3%)	31.98 (44%)	31.94 (44%)	5.77 (8%)	72.05
1.0	1.46 (3%)	21.66 (38%)	28.97 (51%)	4.36 (8%)	56.46
2.0	0.51 (3%)	6.46 (36%)	9.87 (54%)	1.34 (7%)	18.18

Table 2.5 Contribution from the different galaxy populations to the bolometric intensity of the extragalactic background light at different redshifts in co-moving frame as defined by Eq. 2.11 to the *fiducial* extrapolations (see Sec. 2.4.1).

counts. On the contrary, we predict about the same far-IR light than FRV08 and a factor $\sim 2-3$ larger than GSPD11, higher than the galaxy counts and in very good agreement with most of the direct measurements. The high flux we predicted in the far-IR (in comparison GSPD11) is a characteristic of the SWIRE galaxy SEDs we use, given by the `GRASIL` code which is used to calculate the far-IR emission, and the relation between the near-IR and the far-IR in the templates.

In the same figure, we also plot upper limits using solid-color lines from γ-ray attenuation studies. The cyan and yellow solid lines by Mazin & Raue (2007) were computed for the so-called *realistic* and *extreme* cases, where the authors considered different upper limits for the spectral slopes of VHE emission from blazars of $E^{-1.5}$ (Aharonian et al. 2006; Albert et al. 2008) and $E^{-2/3}$, respectively. Our calculation is compatible with the upper limits from the extreme case, but marginally disagrees with the realistic case for the largest wavelengths. We will discuss these issues further in Chap. 5.

Fig. 2.13 also shows the uncertainties in our modeling due to the uncertainties on the Schechter parameters of the LF given by C10, the errors in the photometric catalogue, as explained at the beginning of this section, the uncertainties on the χ^2_{red} cut applied, and uncertainties due to the extrapolations for the galaxy-SED types for $z > 1$. All the possibilities are calculated and the extreme cases are plotted. The uncertainties from the UV up to the mid-IR are dominated by the errors in the photometry and the cuts. The directions from both effects are different: the uncertainties from the photometry are below the *fiducial* model, the uncertainties from the cuts are above it. In the far-IR the uncertainties in the extrapolations to $z > 1$ dominate with a factor ~ 1.5. These effects will be thoroughly discussed in Sec. 2.5.1.

The evolution of the EBL is important to account for the history of the galaxy emission and the processes involved, as well as to properly calculate the attenuation for VHE γ-rays for the high-redshift universe. We show, in Fig. 2.14, the co-moving intensity level of the EBL for different redshifts, the contribution to the EBL at those redshifts from the four main SED groups to our *fiducial* extrapolation, and the predictions for the EBL by other models. In Table 2.5 we quantify this evolution,

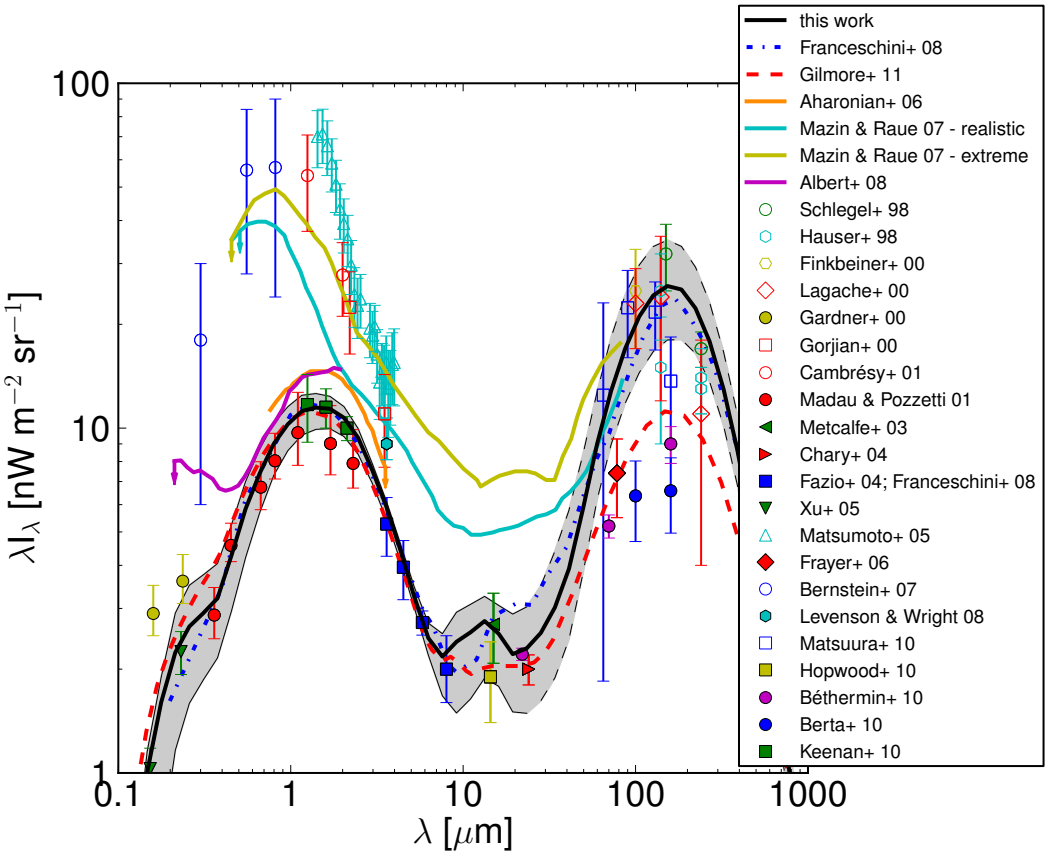

Figure 2.13 The solid-black line is the extragalactic background light calculated by the *fiducial* extrapolation of the galaxy SED-type fractions for $z > 1$. Uncertainties in the our EBL estimation are shown with a shadow area. These EBL uncertainties include the uncertainties in Schechter parameters of the LF by Cirasuolo et al. (2010), photometric errors in the galaxy catalogue, χ^2_{red} cuts applied and extrapolations of the galaxy SED-type fractions for $z > 1$ (see Sec. 2.4.1). The envelope of the shadow region within the dashed line at wavelengths above 24 μm shows the region where there is no photometry in our galaxy catalogue. The EBL uncertainties are thoroughly discussed in Sec. 2.5.1.

where the bolometric intensity is defined according to Eq. 2.11, i.e.,

$$I_{bol} = \int \nu I_\nu d\ln\nu \tag{2.11}$$

We should note that the starburst population contributes 54% to the co-moving bolometric EBL at $z = 2$, but only 30% for the local universe. We note as well that the far-IR peak in the SED is higher relative to the near-IR peak at these redshifts; this is due to the fact that a large fraction of the energy radiated from starburst systems is at far-IR wavelengths. We also note that the total bolometric intensity

peaks at $z \sim 0.6-0.2$, because the far-IR peaks at higher energetic wavelengths there as seen in Fig. 2.14.

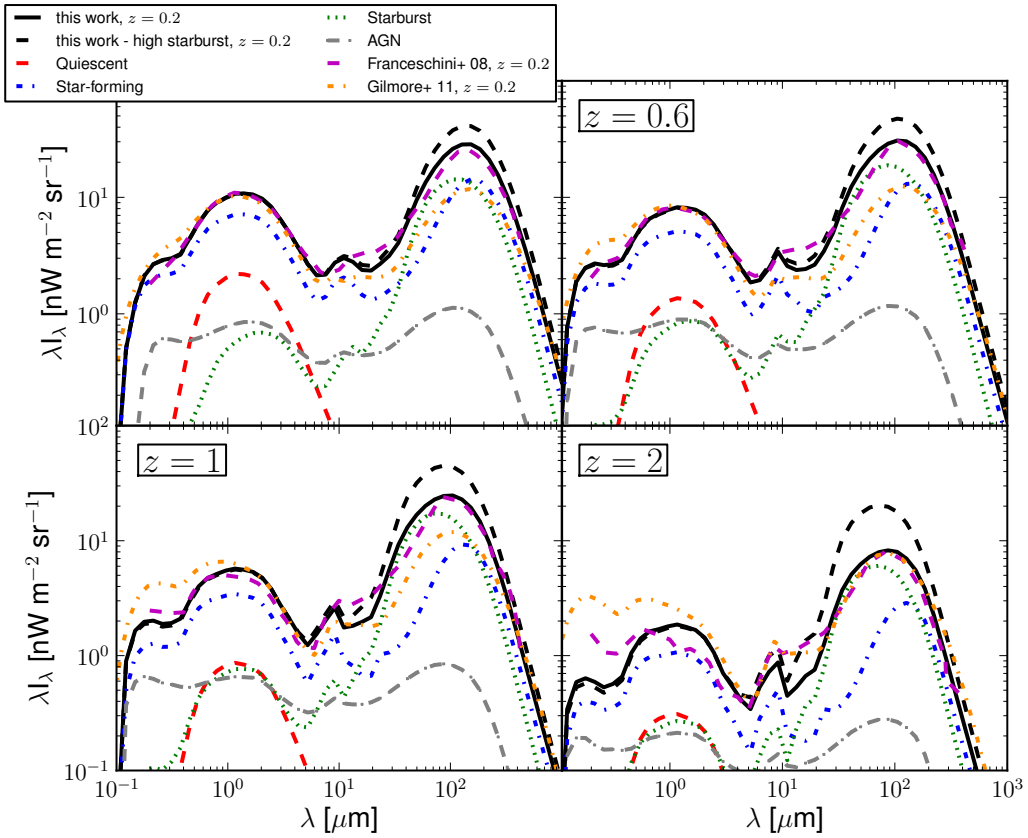

Figure 2.14 Extragalactic background light (EBL) in co-moving frame predicted by our model at different redshifts for the two assumptions for the extrapolation of the fractions for $z > 1$ (see Sec. 2.4.1). The contribution to the EBL from quiescent (red-dashed line), star-forming galaxies (blue-dotted-dashed line), starbursts (green-dotted line), and AGN galaxies (gray-dotted-long-dashed line) to the *fiducial* model are shown. For comparison, the predictions from other models are shown using magenta-dashed line for Franceschini et al. (2008) and orange-dot-dashed line for Gilmore et al. (2011).

Another important observable is the buildup of the local intensities for different wavelengths. This is the fraction of the local EBL at a given wavelength that was already in place at a given redshift. This is shown in Fig. 2.15 for several wavelengths. As an example, we see that ∼70% of the local EBL at $\lambda = 0.445$ μm and 2.2 μm comes from $z < 1$, 50% of the EBL below ∼180 μm was already in place at $z = 1$, but it is only $\sim$ 40% at 240 μm. It is significant that the EBL at shorter wavelengths mostly come from sources at much lower redshifts than the larger ones (see Lagache,

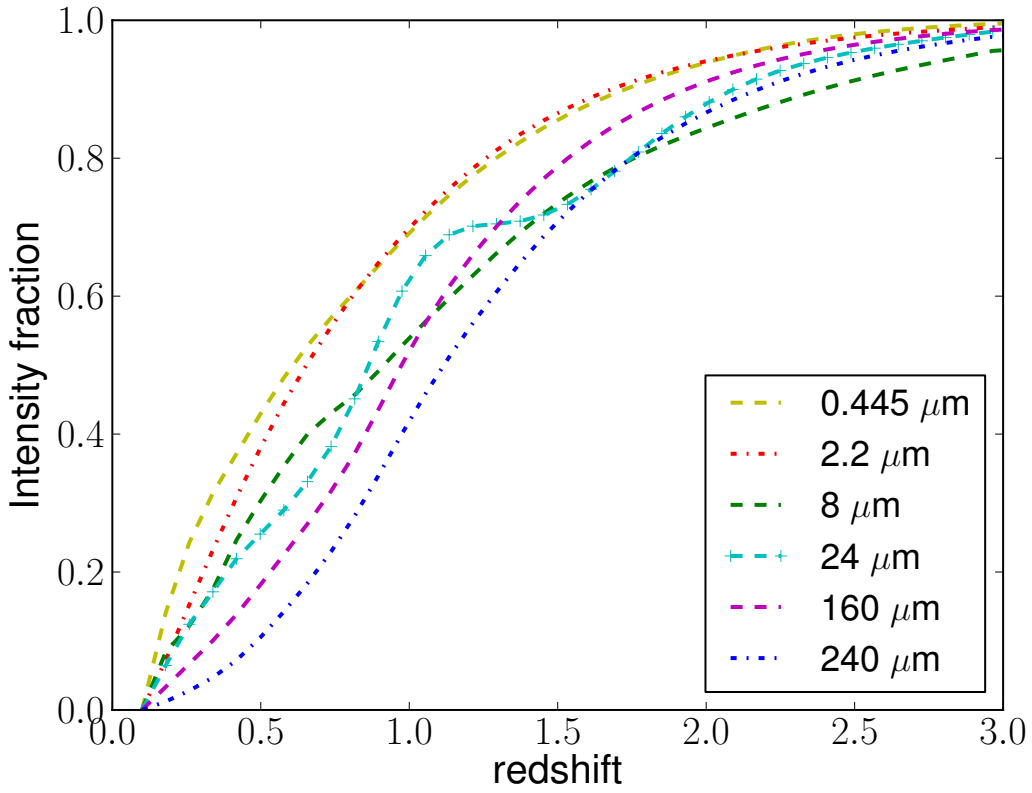

Figure 2.15 Buildup of the extragalactic background light (EBL) at different wavelength normalized to $z = 0.1$. For example, according to the *fiducial* model $\sim 70\%$ of the local EBL at 2.2 μm comes from $z < 1$, but only $\sim 40\%$ of the local EBL at 240 μm.

Puget & Dole 2005).

Fig. 2.16 shows a comparison between the EBL buildup for our model, FRV08, GSPD11, and the observational work by LeFloc'h et al. (2009) based on data from MIPS at 24 μm up to $z \sim 1.5$ in the COSMOS field. The main contribution to the EBL at 24 μm comes from star-forming and starburst-type galaxies. This region of the SEDs is highly dependent on the non-smooth PAH features. We observe a general agreement, but reaching a factor 40% difference at $z \sim 1.2$ for the *fiducial* extrapolation. The uncertainties here are large (see Sec. 2.5.1).

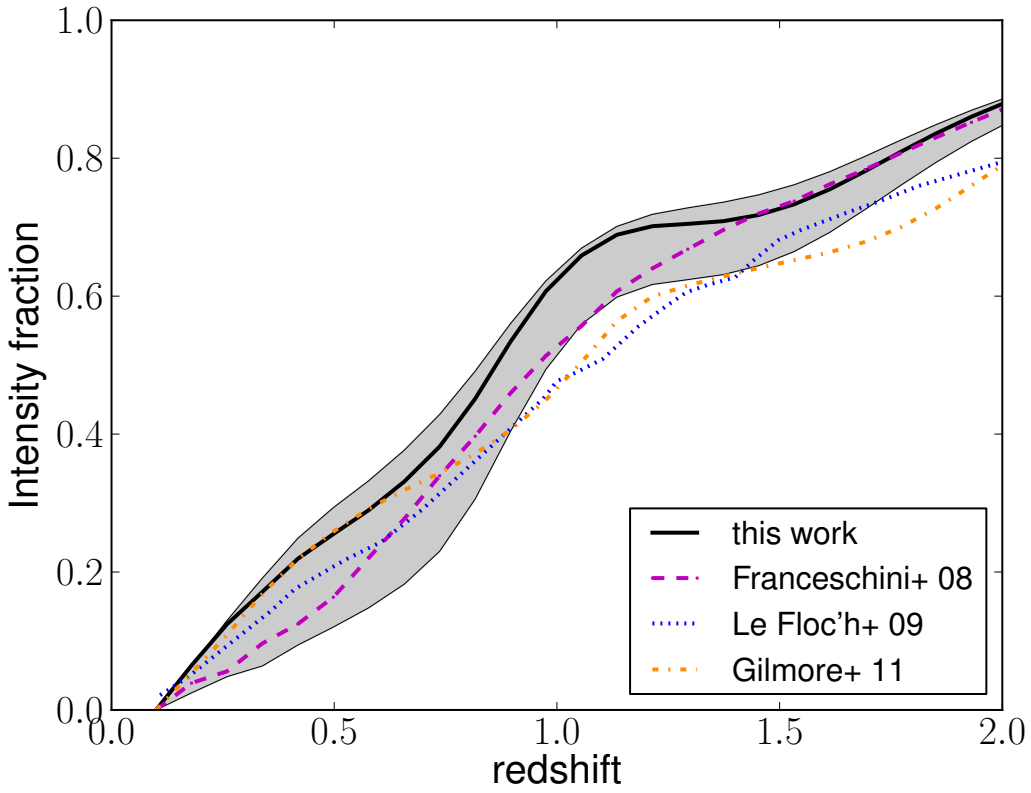

Figure 2.16 Buildup of the extragalactic background light (EBL) at 24 μm obtained from different phenomenological models, normalized to $z = 0.1$, compared with the Spitzer/MIPS data by LeFloc'h et al. (2009). For example, according to our *fiducial* extrapolation (see Sec. 2.4.1), about 75% of the local EBL at 24 μm was already in place at $z \sim$1.5. Uncertainties in the modeling are shown with a shadow region (see Fig. 2.13). The curve from Franceschini et al. (2008) has been calculated by us from their published EBL densities.

2.5 Discussions and comparison with semi-analytic models

2.5.1 Discussion on EBL uncertainties

As explained in Sec. 2.3, we adopt a lower limit to the photometric errors higher than those in the AEGIS catalogue. Different lower limits are set from 1-10% of the photometric measurements. That is, if the error in any band is lower than our limit then we set it to the limit. The results are sensitive to the limit choice in R and I (where the errors in the catalogue are the lowest), but not for the other bands. The galaxy SED-type fractions change for lower limits 1-6%, but there is little change if the level is set higher than 6%. The change is mostly for the quiescent and star-

forming galaxy fractions. If we use the errors in the catalogue without any change, we find 10% more quiescent galaxies at $z = 0.3$ than for a lower limit of 6%, which decreases to $\sim 3\%$ more quiescent galaxies at $z = 0.9$ than for a lower limit of 6%, as shown in Fig. 2.8. The change is mostly in Ell2-type galaxies, according to the SWIRE classification. We have investigated those quiescent galaxies that change their best fit to star-forming galaxies upon raising the lower limit on the errors, and find that they are often fitted much better by a star-forming SED. In many cases they even have detection in MIPS 24, clearly indicating ongoing star formation. On the other hand, based on the comparison of our photometric measurements to those of other catalogues we estimate that any error in the photometry lower than $\sim 5\%$ should not be considered very reliable. For those reasons we set the lower limit at 6% for model. The uncertainties due to this are below the *fiducial* model in Fig. 2.13, and for the reasons stated an EBL in this region should not be considered very likely (and therefore, neither is their derived attenuation in Fig. 5.4).

Another source of uncertainty accounted for in Fig. 2.8 and Fig. 2.13 is the χ^2_{red} cut that separates good and bad SED fits. The main change occurs for AGNs, where for a relaxation in the cut (from $\chi^2_{red} = 10$ to 20), the fraction can increase by as much as 10% at $z = 0.9$, and by a smaller fraction at $z = 0.3$. These changes affect the EBL in the following way: higher AGN fractions increase the UV as well as the mid-IR, while higher quiescent fractions decrease the flux at those wavelengths. This effect affects the uncertainties above the *fiducial* model and an EBL intensity in this shadow region is considered more reliable than the region below the *fiducial* model (the same for their derived attenuation in Fig. 5.4). While χ^2_{red} cuts do not have an appreciable effect on the far-IR flux, there is a substantial change arising from the choice of extrapolation in SED-types above $z \sim 1$, as we find in the *high-starburst* assumption. Fig. 2.13 also accounts for the uncertainties in the Schechter parameters of the LF given by C10 but these are small.

Two major potential problems for our modeling might be a color-dependent selection effect and the extrapolation of the galaxy SED-type fractions for $z > 1$. It was already shown in Sec. 2.2.2 that the color-selection effect is rather small. From the fact that most of the light in the EBL comes from the knee of the LF around $L_\star$, where our sample does not suffer any color-dependent selection effect, we do not consider this to be a significant problem for our EBL calculation. Our estimated galaxy SED-type fractions appear to be consistent with works by others as well. For example, our results agree with Blanton (2006) and Faber et al. (2007), who find roughly no evolution for late-type (blue) galaxies from $z \sim 1 - 0$ within a 10% range, and an increment of the early-type (red) population in the same redshift range by at least a factor 2. We also highlight that the galaxy SED-type fractions that we calculated for the local universe smoothly link with our independently-derived results at $z \sim 0.3$.

Regarding the galaxy SED-type fraction extrapolations, we have considered two rather different approaches which basically lead to the same evolving luminosity den-

sities and EBL for the optical/near-IR range where γ-ray attenuation occurs, as shown in Fig. 2.11 and Fig. 2.14, respectively. This fact is due to the shape of the stellar emission, because the contribution to the optical/near-IR peak is very similar for quiescent, star-forming and starburst galaxies for a given M_K. We recall here that the normalization to our model is fixed by the rest-frame K-band LF by C10. The only difference between our extrapolations is at the far-IR peak, where our results are considered to be less robust for this reason, as well as for the reasons stated below regarding the SWIRE templates and the lack of photometric data. Deeper observations by future galaxy surveys will help in characterizing the galaxy SED-fractions up to higher redshifts.

It was also checked how the fractions change if the detection limit is relaxed from 5σ to 3σ for the bands where there are observations, but no detections. Many more quiescent galaxies than in the 5σ case were found, even a factor larger than 2, due to the low detection limit on the MIPS 24 instrument, but generally they are not good fits.

In our work we have not differentiated between the spectroscopic and secure photometric redshifts. This is an approximation, and it is necessary to check that this is consistent with our results. We find that the galaxy SED-type fractions derived from both sub-catalogues are clearly compatible and the trends are the same.

Galaxies fitted to a starburst SED may instead be very late-type star-forming galaxies (or viceversa), because both SED templates are rather similar in the regions where we have data. This may be called mis-typing and its effect is expected to be larger for faint galaxies, because the major fraction of faint galaxies are star-forming or starburst and not massive quiescent or AGN galaxies. Such small galaxies are probably rather metal poor and thus lacking dust. Hence, their SEDs are probably more like star-forming galaxies rather than starbursts (in agreement with our results in Fig. 2.9). It is a source of uncertainty in the mid and far-IR (underestimating or overestimating light) and might explain the excess found in Fig. 2.11 and 2.12 compared with the data. Far-IR data would help in resolving this issue, but the number of galaxies with detection in MIPS 70 is rather low to make statistical estimations. Herschel data will be very useful thanks to its good spatial resolution and deep photometry in the far-IR.

Another source of uncertainties in our model that quantitatively we have not accounted for arises from the use of local SED templates to fit galaxies at $z > 0.3$. This comes from the fact that the SWIRE templates are based on observations of local galaxies, and we expect that they become worse fits when the redshift is increasing. This problem will be addressed by new data from Wide-field Camera 3 (WFC3) on HST and the next generation of ground and space optical/near-IR telescopes such as the James Webb Space Telescope.

The lowest EBL flux in Fig. 2.13 is given by the case with the highest number of quiescent galaxies and lowest number of AGN galaxies, which corresponds to the case of using the low errors in the catalogue and our χ^2_{red} cuts. The highest EBL flux

occurs with fewer quiescent galaxies and the highest fraction of AGN galaxies. This is the case with the 6% lower limit for the errors in the photometry and without a χ^2_{red} cut. Using the lower limits from galaxy counts in the UV and in the optical we may rule out at $> 2\sigma$ the mixing of galaxy SED-type fractions predicting the highest fractions of quiescent galaxies and fewest AGNs in Fig. 2.8. We do not consider the VHE observations to exclude the models with higher far-IR, because the discrepancy is for wavelengths longer than 60 μm where those limits may not be reliable for the reasons stated in Chap. 5. Further VHE observations might indeed constrain our galaxy SED-type fractions.

Thus to recap, the EBL uncertainties from the UV up to the mid-IR are low enough to recover the spectra of γ-ray sources with energies lower than ~ 10 TeV, but the EBL uncertainties have to be reduced in the far-IR (for neglecting uncertainties due to the EBL modeling) to correct higher energy sources. Additional photometry is needed there to clearly distinguish between star-forming and starburst galaxies, therefore to reduce the mis-typing, as well as a better understanding on the far-IR region of the galaxy SEDs at $z > 0.3$. Characterizing the galaxy SED-type fractions at $z > 1$ will reduce these uncertainties in the far-IR as well.

2.5.2 Discussion of the results

The local luminosity density from galaxies is observationally well constrained over all wavelengths from 0.1-1000 μm. As shown in Fig. 2.10, the prediction of the local luminosity densities is in very good agreement with observational results.

Fig. 2.11 showed the evolving rest-frame UV luminosity density as well. These results agree well with the observational data by Gabasch et al. (2006) and Dahlen et al. (2007) within uncertainties, but they are a factor ~ 1.6 below the data for $z = 1.7$ and 2.2. It was also compared in Fig. 2.11 the evolution of the rest-frame luminosity in the K-band from our calculations to independent observational works. Some disagreement was found that in the case of Barro et al. (2009) might be explained by the fact that they do not correct their sample for incompleteness and only consider the brightest sources, unlike the LF by C10. Therefore their results should be considered as lower limits. The direct comparison in Fig. 2.11 with the rest-frame luminosity density in B-band showed that our luminosity in that band is not in contradiction with other independent works. We are doing really well reproducing the data from Norberg et al. (2002), Gabasch et al. (2004) and Ilbert et al. (2005). We might be indeed overestimating the light in this band 15-20% for $z < 1$ according to the data by Faber et al. (2007) and a factor ~ 2 for $z > 1$ according to the data by Dahlen et al. (2005), but this latter does not significantly affect our results for the local EBL because as we already showed in Fig. 2.15, most of the optical/near-IR light comes from $z < 1$. The comparison with the bolometric IR luminosity density with the observational works by FRV08 and Rodighiero et al. (2010) is very good, even though we are a factor ~ 2 higher around $z \sim 1$.

A good agreement was found with the upper envelope of the data cloud on the calculations for the SFR history from $z \sim 1.5$ down to the local universe using Eq. 2.6 (see Fig. 2.12), using our *fiducial* extrapolation. According to Magnelli et al. (2009) at around $z \sim 1$ the main contributor to the star formation is the obscured IR contribution, instead of the UV. We may be overpredicting some of this obscured IR light around $z \sim 1$ due to the lack of far-IR photometric data in our galaxy catalogue that allow a clear classification between late star-forming and starburst galaxies as discussed in Sec. 2.5.1. With the *high-starburst* extrapolation of the galaxy-SED-type fractions was checked that increasing the starburst-like population a factor ~ 3 from $z \sim 1-2$, we may get a flatter SFR density history up to $z \sim 2$, but even higher than the observational data. This *high-starburst* assumption does not change our general picture of the local EBL, but increases the far-IR peak a factor ~ 1.5 (as it was considered in Fig. 2.13 and was shown explicitly in Fig. 2.14 for some other redshifts).

The EBL calculated in this work is matching the data from galaxy counts from the UV up to the mid-IR (see Fig. 2.13), except the data found in Levenson & Wright (2008). Higher intensities than the data from galaxy counts were calculated in the far-IR but in agreement with direct detections. The EBL evolution shown in Fig. 2.14 is in good agreement with FRV08 up to $z = 1$. At higher redshift our results are different in the UV and optical/near-IR. This may be due to the fact that FRV08 extrapolate the galaxy evolution, while in our model this evolution is entirely based on the observed LF by C10 up to $z = 4$. See Sec. 2.5.3 for a comparison with the results by GSPD11.

There are some works in the literature where the contribution from AGN galaxies to the EBL is studied. According to recent works that focus in the mid-IR (e.g., Silva, Maiolino & Granato 2004; Matute et al. 2006) this contribution should not be larger than 10-20%. This is in agreement with our results: we find that the AGN-galaxy contribution to the bolometric EBL is 6% for the *fiducial* extrapolation (Table 2.5) and 13% for the case with the largest AGN fraction in Fig. 2.8. For the wavelength range between 1-20 μm the AGN contribution from our model is also between 8-16%. We estimate that this contribution to the co-moving bolometric EBL slightly increases with redshift.

The EBL buildup was studied in Fig. 2.15 and 2.16. It was found that most of the local UV/optical/near-IR EBL was built up at $z < 1$, while the far-IR EBL was mostly built up at $z > 1$. This result for the far-IR light agrees well with the observational work by Devlin et al. (2009), but disagrees with Chary & Pope (2010). In any case, our uncertainties in the far-IR are very large. Differences up to 40% were found in the buildup of the local EBL at 24 μm. These differences are due to the fact that a very small change in the mid-IR region leads to a very strong difference in this buildup plot, and to the mid-IR peak that we get at larger redshifts (see Fig. 2.14) due to the shape of the galaxy SEDs. We point out here that the EBL buildup is on how the light is being built up, and not about the absolute intensity value.

2.5.3 Comparison with SAMs

In this section we compare our EBL estimation against the EBL model described in SGPD11 and GSPD11, which is based on SAMs of galaxy formation (see Sec. 1.3 for an introduction). The comparison for γ-ray attenuation will be thoroughly discussed in Chap. 5. We notice that slightly different cosmological parameters were used for our model and that by SGPD11. The latter uses the latest values from WMAP5, which slightly affect all the results in the local universe as well as their evolution.

We already saw in Fig. 2.11 the comparison between our observational luminosity densities and the theoretical prediction by SGPD11 for the co-moving luminosity density versus redshift in the UV, in the near-IR (K-band), in the optical (B-band) and for the bolometric IR luminosity. We note that our K-band luminosity density evolution is given exclusively by the C10 LF, because at that band our choice of galaxy SED fractions does not affect our results. This quantity is above the prediction by SAMs by a factor around 20% from $z \sim 2$ down to the present universe. The UV from this SAM is above our results for all redshift, except at $z \sim 1$. At $z \sim 2$ is a factor 4 higher. For the B-band luminosity density the agreement is excellent from $z \sim 1$ down to the local universe. For $z > 1$ SAMs predict a factor of several more light than our observationally-based approach. We may see the consequences of this for the EBL evolution in Fig. 2.14 for high redshifts where the excess of light has not been diluted by the expansion of the universe. For the bolometric IR luminosity SAMs seem to systematically predict at least a factor ~ 2 less light than our calculations and the one by FRV08. This difference is maximized around $z \sim 1$ up to a factor ~ 4.

Fig. 2.12 showed a comparison between our SFR density estimation and that predicted by SGPD11 as calculated by using the Eq. 2.6. From $z \sim 3 - 1$ our SFR densities have different a behaviour: for our observational model increases up to $z = 1$ and for SGPD11 keeps constant down to $z \sim 1.7$. For lower redshifts both models decline down to the local universe.

In general a very good agreement between the local EBL from the UV up to the mid-IR predicted by our method and the SAM of SGPD11-GSPD11 was seen in Fig. 2.13. A factor ~ 1.5 higher intensity is found in the local UV from SAMs, and around the same factor lower intensity around 15 μm. For the far-IR peak, the difference comes from the different templates used for the dust component in the far-IR, which is given by the `GRASIL` code in the case of the SWIRE templates (which we use), and by a interpolation between the observed 70 and 160 μm by MIPS in the case of the templates used by these SAMs (Rieke et al. 2009).

The agreement on the evolution is very good as well as seen in Fig. 2.14, even though at high redshift ($z > 2$), GSPD11 predicts a factor of several more light in the UV. This is due to galaxies within the faint end of the theoretical LF at $z > 2$. We recall that our observational model seems to already be overproducing light in the B-band for $z > 1.5$ according to data in Dahlen et al. (2005) (see Fig. 2.11).

2.5.4 Overview on the cosmological picture

The evolutionary path that we have in mind to interpret the evolution of the galaxy SED-type fractions is the following (see Sec. 1.2 an introduction): AGNs are mostly formed by mergers between galaxies during hierarchical growth of dark matter halos (e.g., Hopkins et al. 2009). When the merging galaxies are gas rich (also known as wet mergers), inflows of gas are produced leading to starburst galaxies and to the mass growth of the central black hole. The central black hole activity begins to expel the gas. Eventually, the gas is exhausted, switching off the AGN. The galaxy continues forming stars as a star-forming galaxy until the gas is fully depleted, then becomes a quiescent galaxy (Hopkins et al. 2008a; Hopkins et al. 2008b).

It is now a well known observational fact that galaxies are bimodal in some properties such as colors (Strateva et al. 2001; Blanton et al. 2003b). They group in two different regions in color-magnitude diagrams defining the red sequence and the blue cloud. Galaxies forming stars are in the blue cloud. Some galaxies have their star formation quenched when they become satellite galaxies in a larger halo, they cease to accrete gas, and they join the red sequence. Central galaxies form in the blue cloud, but they join the red sequence when they form a super-massive black hole and/or their halo mass exceeds approximately $10^{12}\mathrm{M}_{\odot}$ and/or they become satellite galaxies in a cluster. The most massive red galaxies cannot have simply be quenched central blue galaxies, since the latter are not massive enough; thus they must have been created by mergers without much star formation (also known as dry mergers). This effect is shown in Fig. 2.4, taking into account that the K-band absolute magnitude M_K is a good tracer of the galaxy stellar mass, as shown in Brinchmann & Ellis (2000).

Massive galaxies today (very bright M_K) form their stars first, which is known as *downsizing* (Cowie et al. 1996; Pérez-González et al. 2008). This initially seemed at odds with the hierarchical nature of the ΛCDM paradigm, in which small halos form first and agglomerate into larger ones. But the idea that star formation is efficient only in dark matter halos with a narrow range of masses naturally explains how the phenomenon of downsizing arises: halos that are massive today passed through the star-forming mass band between 10^{8}-$10^{12}\mathrm{M}_{\odot}$ earlier and thus formed their stars earlier than halos that are less massive today (Croton 2009; Conroy & Wechsler 2009).

A careful examination of Fig. 2.4 reveals some interesting trends. We find that all the oldest galaxies ($\sim$ 13 Gyr old, Ell13) are in the red sequence. However, the younger quiescent galaxies ($\sim$ 5 Gyr old, Ell5) can be found in the red sequence as well as in the green valley (the region between the red sequence and the blue cloud). For the youngest quiescent galaxies ($\sim$ 2 Gyr old, Ell2) we find that for $z > 0.6$ they populate the green valley, while for $z < 0.6$ they belong to the blue cloud. All the early-type star-forming galaxies (S0, Sa) are in the red sequence. Later-type star-forming galaxies such as Sb and Sc start to populate the green valley as well as the red sequence. Most of the very late-type star-forming galaxies (Sd, Sdm, Spi4)

populate the blue cloud. Starburst galaxies are mainly in the green valley, but some of them are in the bluer region of the red sequence and in the redder region of the blue cloud. The same happens to AGNs, but they tend to be in the blue cloud more than in the red sequence.

We note that the increasing rate of quiescent galaxies as z declines is roughly the same as the decreasing rate of starburst-type galaxies from $z \sim 0.9-0.7$. One possible explanation would be the direct transformation of starbursts (either merger or huge-cold-gas reservoir triggered) directly to quiescent galaxies, without an intervening stage of significant star formation. Another explanation is that the characteristic time in which starburst-like galaxies consume their cold gas is the same that in which star-forming galaxies consume their lower cold-gas reservoir. Thus the specific SFRs of these populations are different, but the rate at which starbursts enter the star-forming sequence is the same as the rate at which star-forming galaxies become quiescent. From $z \sim 0.7 - 0.3$ the fraction of starbursts is very low, so the constant increase of the red sequence is modeled as due to AGNs preventing gas from cooling and forming stars.

Part II

Observation of extragalactic γ-ray sources with Čerenkov telescopes

3

The imaging atmospheric Čerenkov technique

3.1 Introduction: Čerenkov radiation and its detection

The γ-rays from astrophysical sources cannot penetrate through the atmosphere (see Fig. 3.1), therefore the direct observation of astrophysical γ-ray sources from the ground is not possible. However these γ-rays and other particles entering into the atmosphere hit nuclei initiating Čerenkov cascades (Čerenkov 1934). This effect consists in the emission of radiation by a charged particle going through a medium with a speed larger than the speed of light in that medium. When this phenomena happens in the atmosphere, the emitted spectrum has a peak in the blue-violet due to absorption and scattering. Other particles such as other nuclei, muons, electrons and photons with different energies are produced as well. The Čerenkov effect is related with the polarization that makes the charged particle going through the medium. Radiation is emitted with an angle θ given by the next equation

$$\cos\theta = \frac{1}{n\beta} \tag{3.1}$$

where n is the refraction index of the medium and $\beta = v/c$ is the speed of the charged particle divided by the speed of the light in the vacuum. Note that this equation imply the limit $n\beta > 1$ from which the Čerenkov effect is possible. We are interested on studying the UV/blue photons that come to the telescopes' mirrors ending up in the telescopes' cameras.

Fig. 3.2 shows two different cascades. At the left, a shower originated by a γ-ray is shown. This interacts with a nucleus producing an electron-position pair. The electron produces Čerenkov light and the positron annihilates leading to new pairs. At the right it is shown how a hadronic cosmic ray interacts with a nucleus producing pions both charged leading to neutrino production and neutral leading to other two

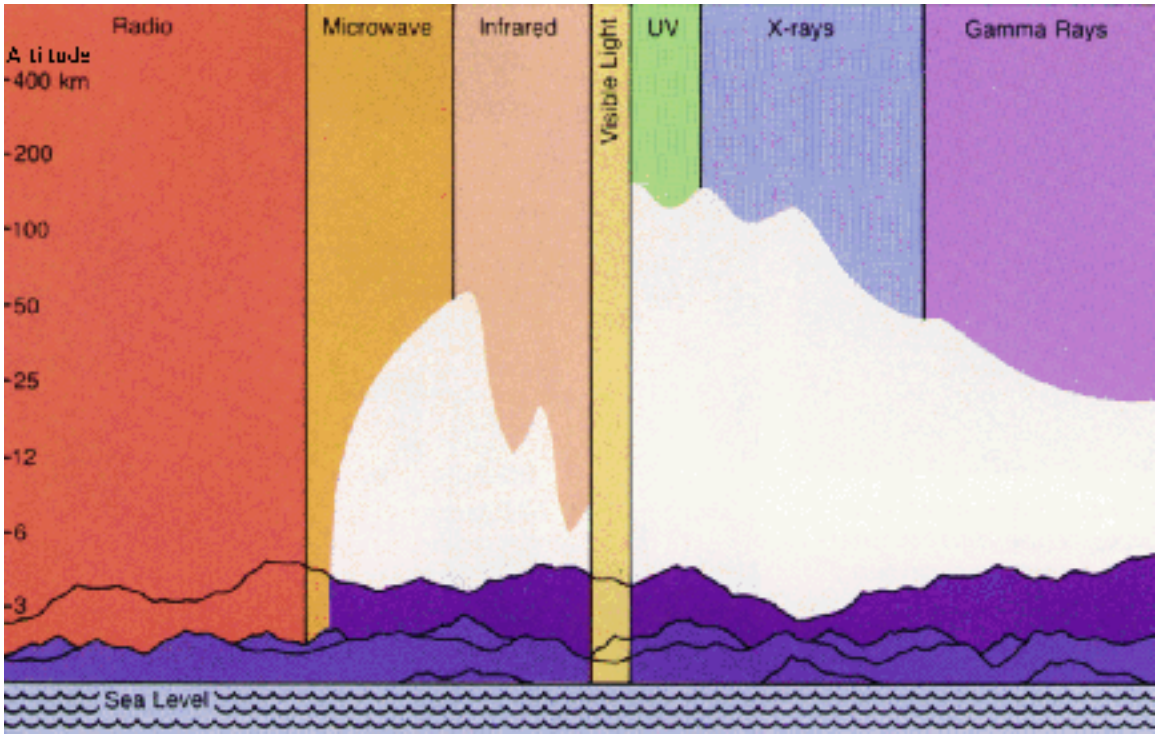

Figure 3.1 Image from http://imagine.gsfc.nasa.gov/docs/introduction/emsurface.html. Transparency of the Earth's atmosphere to the electromagnetic spectrum. It is shown with a white color the height at which the atmosphere is opaque to different wavelengths.

γ-rays energetic enough to produce electron-positron pairs, which continue the shower development.

The emitted Čerenkov spectrum in the atmosphere is shown in Fig. 3.3. These photons are emitted very fast $\sim$10 ns and very faint $\sim$200 ph/m^2 (for a 1 TeV photon when the cascade reaches 2 km above sea level, see Fig. 3.4 for other examples). The area that cover the maximum distance from the center of the cascade is called Čerenkov pool. Lenses sensitive to the UV and with large collection areas, and very fast electronic are needed in order to detect these pulses. A former generation of Čerenkov telescopes such as CACTUS, PACT, STACEE, TIBET, ARGO or HAWC just made photon count due to their lack of a charged-coupled device (CCD) camara. Other Čerenkov telescopes such as MILAGRO used a water pool as medium to generate the showers, instead of the atmosphere.

More recent generation telescopes use CCD cameras, which permit to obtain cascade images. These are known as IACTs. These images allow a much better characterization of the showers and consequently, a much better background rejection. The main properties of the images are:

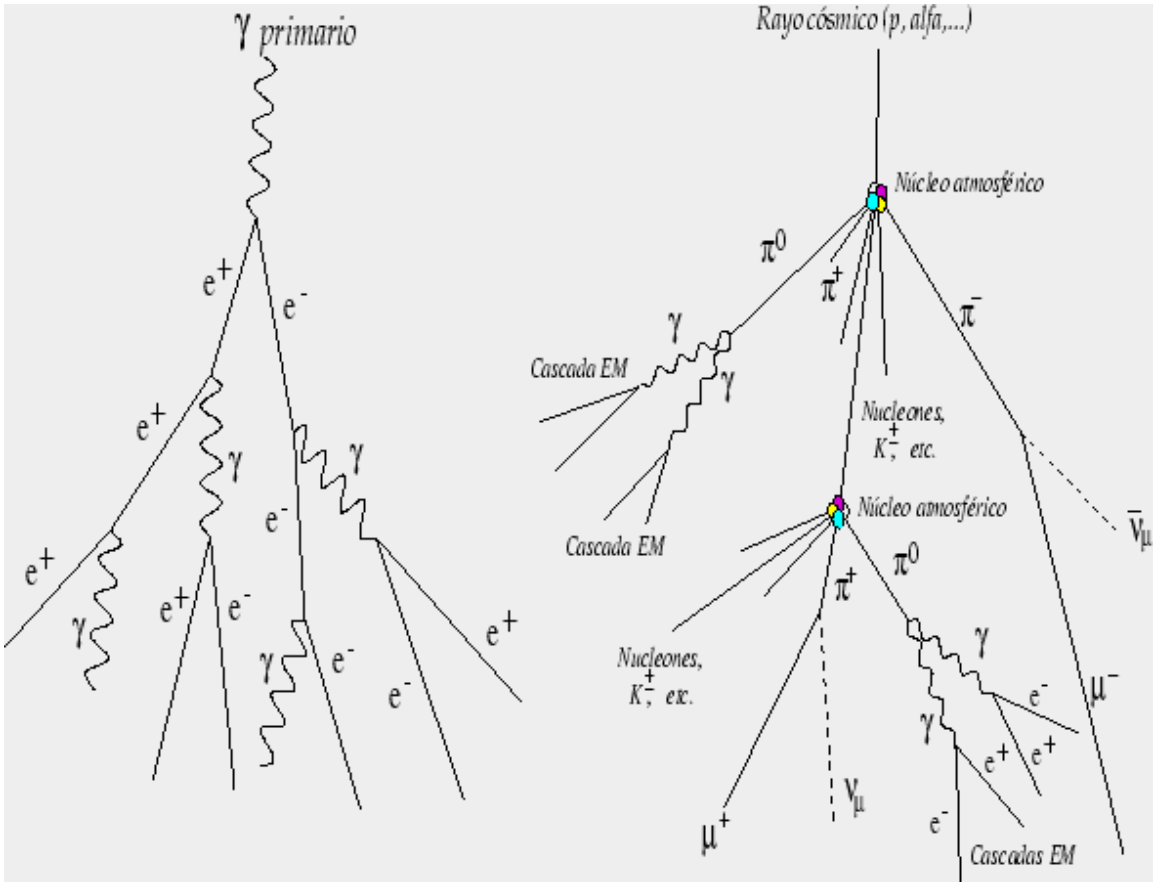

Figure 3.2 Development of a Čerenkov cascade originated by (*left*) a γ-ray photon and (*right*) an hadron.

- Intensity: related with the energy of the primary particle.
- Orientation: related with the original direction of the primary particle.
- Shape: related with the nature of the primary particle.

IACTs are characterized by sensitivity to γ-rays between 50 GeV-30 TeV, a collection area of the order of the Čerenkov pool, background rejection of $\sim$95%, an angular resolution $\sim 0.1^\circ$ and quite small field of view (FoV).

With one telescope the direction of the primary particle is found from the cut of the cascade with the telescope. A much better reconstruction of the shower parameters is possible when more than one telescope observe the same shower. This is called stereoscopy. Stereoscopy works the best when the telescopes are situated at distances of the order of the Čerenkov pool away from each other. Notice that with two telescopes, it is not possible to use the stereoscopic technique for showers coming from the plane perpendicular to both telescopes.

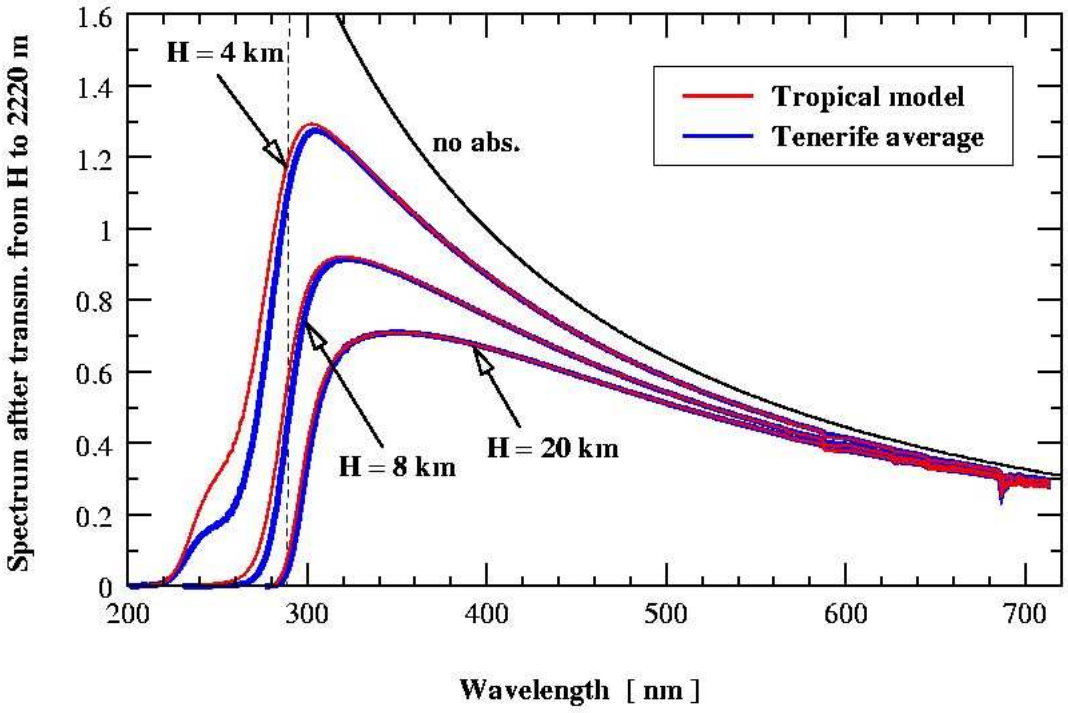

Figure 3.3 Typical spectrum of the Čerenkov radiation through the atmosphere.

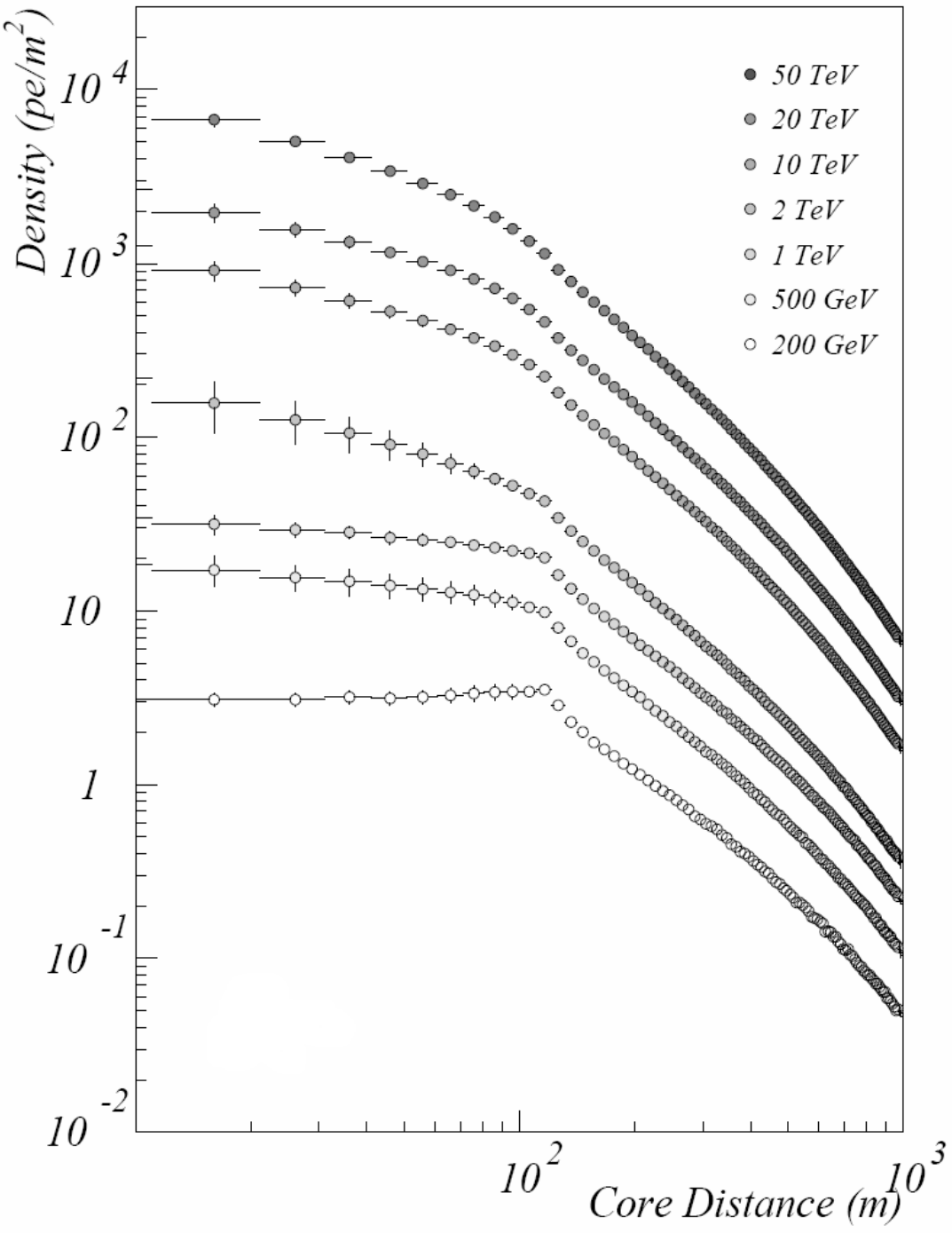

Figure 3.4 Photon density at sea level of some Čerenkov cascades originated by γ-ray photons with different energies.

	MAGIC, VERITAS, HESS high sensitivity	**EGRET, Fermi** low energy threshold	**MILAGRO, TIBET, ARGO, HAWC** FoV / high duty cycle
energy range	50 GeV-50 TeV	0.1 GeV-100 GeV	100 GeV-100 TeV
area	$\geq 10^4$ m^2	1 m^2	$\geq 10^4$ m^2
background rejection	$\geq 99\%$	libre	$\geq 95\%$
angular resolution	0.05°	0.1°-0.3°	0.3°-0.7°
FoV	0.003 sr	2.4 sr	≥ 2 sr
duty cycle	10%	$\geq 90\%$	$\geq 90\%$
main usages	energy spectrum with high resolution study known source at other wavelengths limited sky exploration	sky exploration extended sources transient sources simultaneous neutrino observations	sky exploration extended sources transient sources simultaneous neutrino observations

Table 3.1 General characteristics of past and current γ-ray detectors.

The main advantages of the stereoscopic system over a single-telescope system (thanks to the better reconstruction of the shower parameters) are better energy resolution and better background rejection that allows them to be sensitive to lower energies.

Table 3.1 briefly review the main characteristics of past and current IACTs and other γ-ray detectors on the ground as well as in orbit.

3.2 MAGIC: the lowest energy threshold of current IACT

The Major Atmospheric Gamma Imaging Čerenkov (MAGIC) telescope has been built with the clear goal to lower the energy threshold for γ rays. For many unanswered physics questions, a low energy threshold holds the key. The general argument is the absolute necessity to explore the electromagnetic spectrum at all wavelengths, and the absence, at the present time, of any instrument exploring the energy region between some tens of GeV and several hundred GeV with adequate sensitivity. At lower energies, satellite experiments, in particular EGRET, have contributed substantial knowledge. Their energy range and sensitivity is being very much improved by the EGRET successor, Fermi, (successfully launched in June, 2008), but even Fermi has the limit of detector size, and will have to be supplemented by complementary terrestrial observations. Pre-MAGIC γ-ray telescopes, on the other hand, had typically an energy threshold of several hundred GeV.

The interest to this relatively narrow energy band, from 10 to 100 GeV, is motivated not only by the natural desire to enter a new domain which remains a *terra incognita*, but also because it provides a bridge between high energy (HE) (30 MeV-30 GeV) and VHE astronomy, and thus may allow key inspections of the current concepts concerning both the GeV and TeV regimes. Moreover, there are good scientific reasons to lower the energy threshold, such as the careful study of the EBL and γ-ray horizon (see Chap. 2 and Sec. 6.2.2), AGNs, GRBs, cold dark matter, quantum gravity, galactic sources such as supernova remnants, plerions, and pulsars, etc. In each of the mentioned fields, a low energy threshold would mean the access to an invaluable and critical information on several physical processes.

3.3 An overview of the MAGIC telescopes

The MAGIC telescopes are two IACT telescopes located in the island of La Palma (Spain) at the Roque de Los Muchachos Observatory (28.76 N, 17.89 W, 2200 m a.s.l.) and operated by a large European collaboration. The MAGIC experiment was designed in the late 1990s and built in 2001-2003. The first telescope, the MAGIC-I telescope (a single-dish mirror of 17 m diameter), was inaugurated in 2004 and is presently the largest single IACT in the world. It has a sensitivity as impressive as 1.6% of the Crab Nebula emission in 50 hours of observation time, an energy resolution

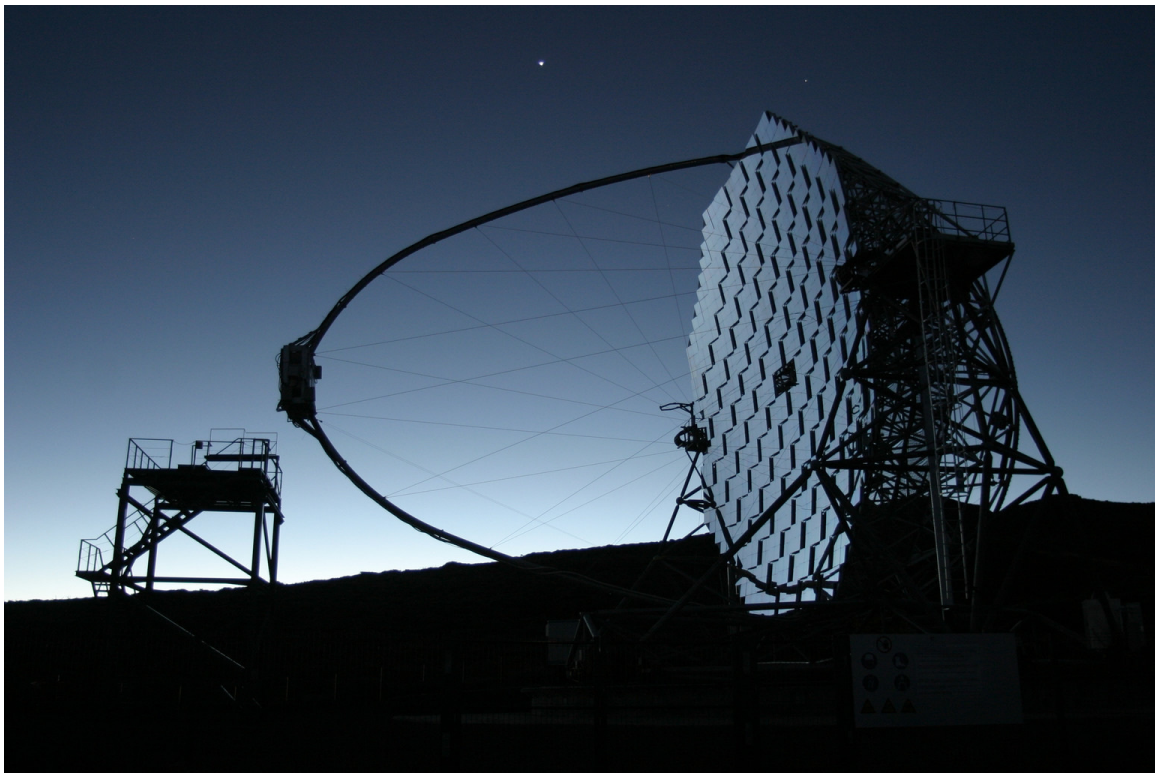

Figure 3.5 The MAGIC-I telescope in the sunset. The camera box is clearly seen 17 m in front of the 239 m^2 reflecting surface, which consists of 956 square mirrors of 50 cm side. The whole structure wights around 60 tons.

around 25% at 100 GeV and an angular resolution slightly better than 0.1 deg at this same energy. A second MAGIC telescope (located 85 meters away from MAGIC-I and with same dimensions than the telescope currently in operation) was inaugurated last April 2009 and started data taking that same year 2009. MAGIC-II has made possible to improve the excellent marks reached up with MAGIC-I thanks to a factor 2 better sensitivity, a better energy resolution and an even lower energy threshold. The project is funded primarily by the funding agencies BMFB (Germany), MPG (Germany), INFN (Italy), MICINN (Spain), and the ETH Zurich (Switzerland). The next sections have been adapted from Sánchez-Conde (2009).

Some key points and goals of the MAGIC telescopes are:

- High Čerenkov photon-to-photoelectron conversion efficiency.
- The largest collecting mirror (17 m diameter) in the world to date.
- Lowest energy threshold ever obtained with an IACT. This fact, together with a high sensitivity, makes possible to explore the energy gap between ∼25 GeV and 150 GeV.

Figure 3.6 The MAGIC telescopes at the Roque de los Muchachos Observatory in La Palma island, as seen in the sunset from the East. Each MAGIC telescope is a single dish mirror of 17 m diameter, the largest collecting mirror in the world to date. They are 85 m far from each other following sensitivity Montecarlo studies.

- Fast movement of the telescopes to anywhere in the sky (in less than ∼40 seconds), with the clear intention of observing prompt emission from GRBs following satellite alerts.

- Capability to operate the telescopes even with moonlight (Albert et al. 2007). This makes possible to increase the observation time by roughly a factor 2.

- Stereoscopic system. This observation mode has decreased even more the energy threshold of the experiment, as well as increased the sensitivity by a factor 2.

In the following we will briefly review the main characteristics of the MAGIC experiment. This review is only strictly valid for the MAGIC-I telescope. MAGIC-II (recently inaugurated) is essentially a clone of MAGIC-I with some technical improvements, and will be presented separately in section 3.5. A more detailed description of the whole experiment can be found in Baixeras et al. (2003) and Borla et al. (2009).

3.4 Main technical characteristics

The most critical technical parameters of MAGIC-I could be summarized as follows (see Fig. 3.5):

- Active mirror surface 239 m^2, made of square elements 49.5 cm x 49.5 cm; $f/D = 1.03$.
- Support frame of carbon fiber made for minimum weight and maximum stiffness.
- Hexagonal camera of 1.05 m diameter, with an inner area of 396 photomultipliers (PMTs) of 1" diameter each, surrounded by 180 PMTs of 1.5" diameter, arranged in four concentric rings. All tubes have an effective quantum efficiency of 25 to 30%.
- The camera is kept as light as possible, held by an aluminum support stiffened by a web of thin cables.
- Analogue signals are transmitted from the camera to the control house via optical fibers; only the amplifiers and laser diode modulators for transmission are inside the camera housing. Digitization is achieved by new fast analog-to-digital converters (FADCs) with a sampling frequency of 2 GHz.
- The threshold for gamma detection is at present as low as ∼50 GeV for low zenith angles. In addition, by means of a recently developed technical configuration, it was possible to reach an energy threshold around 25 GeV for some specific observations (Aliu et al. 2008).
- The average time to reposition the MAGIC telescopes anywhere on the observable sky is less than 40 seconds (despite a moving weight of ∼60 tons).

Frame

The frame of each telescope roughly follows the concept of a large (17 m diameter) solar concentrator with alt/az mount, which was already built and tested a few years ago as part of the German solar power research program. The main mirror support dish consists of a three layer space frame made from carbon fiber-epoxy tubes, which are lighter and more rigid than aluminum. Knots to join the tubes are made from aluminum.
The weight of the frame, including the lower drive ring for azimuthal movement, is about 9 tons (the whole telescope and the undercarriage weights 64 tons). This frame structure keeps the inertia of the telescope low enough for it to be repositioned within 40 s at any position in the sky; this allows, for the first time, the capability of fast repositioning to follow-up GRBs, which is a extremely valuable and unique

feature among current IACTs. The frame structure guarantees wind resistance up to < 170 km/h and stability for complete ice coverage up to 3 cm thickness.

Drive

The MAGIC telescope is driven by high precision servo-motors. The azimuth axis of the telescope is equipped with two 11 kW motors, while the elevation axis has a single 11 kW motor. In azimuth the movement is limited to a range of 450°, while in zenith to -10°.
The position of the telescope is measured in the mechanical telescope frame by three absolute 14-bit shaft-encoders. With this configuration is possible to monitor the telescope position with an accuracy of 0.02°. By using a high sensitivity CCD camera mounted on the reflector frame, the precision of the tracking system can be verified by monitoring both LEDs installed in the camera frame and stars from the celestial background (Starguider System). With this star-field tracking monitor system it has been measured that the telescope tracks to better than a 1/10 of a pixel size.

Mirrors

The Čerenkov light produced by air showers is collected and focused to the camera by an octagonal shape tessellated mirror reflector of 239 m^2 area. The overall curvature of the reflector is parabolic to minimize the spread in the arrival time of the Čerenkov photons to the camera plane. To assure high optical quality images at the camera, the focal length to diameter ratio (f/D) is set to 1 (to lower astigmatism over 3.6 deg diameter in the focal plane). The 239 m^2 reflecting surface consists of 956 square mirrors of 50 cm side and 34 to 36 m radius of spherical curvature, depending on the position of the mirror in the parabolic dish. Each one is made of an aluminum honeycomb structure; a heating/drying system in case of ice or dew formation; a reflecting 5 mm-thick plate of diamond-milled aluminum and a quartz coating layer. Mirrors are grouped into panels of four; each panel is provided with two motors and a laser pointing to the camera lids, allowing a fine focusing during data-taking through the Active Mirror Control. This is necessary in order to correct the residual deformation of the reflector when the telescope is repositioned. The surface global reflectivity is about 85% in the wavelength range 300-650 nm.

Camera

The camera is the most critical element in the performance of a Čerenkov telescope. In the camera, the conversion from Čerenkov photons to photo-electrons takes place and this affects the energy threshold, as it depends directly on this conversion efficiency. In addition, the quality of the shower images which are recorded in the camera is relevant for the posterior γ/hadron separation. The MAGIC-I camera is

composed by an hexagonal board of 1.5 m diameter, placed in the mirror focal plane, which hosts 577 high quantum efficiency (QE) PMTs, of which 397 1" inner pixels and 180 1.5" outer pixels. Light from the reflector is transmitted to each PMT through a Winston cone with an hexagonal end, so that there are no blind regions in the camera; the total FoV results equal to $3.5° \times 3.8°$. A special wavelength-shifter coating enhances QE up to an average 20% between 250 and 700 nm wavelength. Since typical duration of Čerenkov flashes is on the order of a few nanoseconds, PMTs are designed to give a fast response with 1 ns full width at half maximum (FWHM). High voltage supply is independent for each PMT and remotely controlled by the camera control software. Finally, the camera is equipped with heating and cooling systems to prevent the reaching of the dew point and to dissipate the heat from phototubes. In summary, the MAGIC camera has the following features:

- **Fine granularity**: it allows to better deals with low energy shower images and also allows for a more efficient γ/hadron discrimination. Moreover, the integrated noise per pixel is reduced and trigger threshold at the discriminator level can be lowered. This facilitates the reduction of the energy threshold.
- **Large field of view**: the $3.5° \times 3.8°$ camera FoV makes possible to record most of shower images (showers up to 10 TeV for low zenith angles).
- **Low noise**: the detection of Čerenkov pulses suffers from a strong background of night sky background photons. Therefore, the response of the whole system has to be fast in order to reduce the width of the pulses at trigger level to only a few nanoseconds.
- **Low gain operation**: it reduces the noise level recorded by the camera. In order to be able to operate the telescope under moonlight, we are forced to operate with a relatively low gain around $\sim 10^4$, in contrast to typical gains around 10^6.

Readout and Trigger

Analogue signals from PMTs are pre-amplified and then transmitted via optical fibers to the electronics room located in the control house, where they will be processed. Only the amplifiers and laser diode modulators for transmission are inside the camera housing. Digitization is achieved by new FADCs with a sampling frequency of 2 GHz. As for the trigger system, it has the purpose of a first discrimination between signal and background. At this very early stage, however, it is not possible to perform a rejection of hadron-like images with respect to the γ-like ones: this should be done later in an offline analysis chain. The trigger is segmented in three levels:

Level 0: it acts as a flag for lighted PMTs. A phototube is considered lighted if its current exceeds a fixed threshold; if this happens, a digital signal is generated by L0 and processed by the next trigger stages.

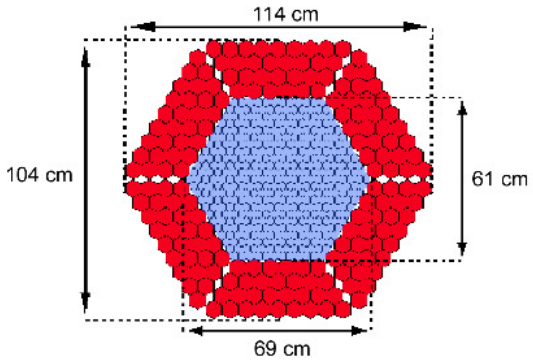

Figure 3.7 *Left*: The MAGIC camera with the lids opened. The hexagonal shape, composed by 577 PMTs, is clearly seen in the picture. *Right*: Pixel scheme of the camera, with 397 1" inner pixels (blue) and 180 1.5" outer pixels (red). The total FoV is 3.5°×3.8°.

Level 1: this level involves only 325 inner pixels, grouped into 19 overlapping macrocells of 37 pixels each. A temporal coincidence (few ns) among a certain number of neighboring pixels within a macrocell is required: this constraint is motivated with the intention of selecting compact configurations like the elliptic shapes typical from Čerenkov flashes.

Level 2: the last trigger stage performs a fast evaluation of size, shape and orientation of the image, in order to make an effective background rejection and to reduce the trigger rate.

The digitized data which successfully approves all the trigger levels are stored in disks and backed-up into tapes. In addition, every day, data from the last night are copied to the Barcelona and Würzburg Datacenters, where they are kept and made available to the analyzers.

3.5 The MAGIC stereoscopic system

As already commented, a second MAGIC telescope was inaugurated last April 2009 at La Palma. Therefore, now MAGIC is a stereoscopic system of IACTs with the two largest dishes in the world. The second 17 m diameter telescope is located 85 m far from MAGIC-I. The MAGIC experiment, with its large reflector area, high quantum efficiency PMT, optical signal transmission and fast digitization, has been benefited from an improved shower reconstruction and increased background rejection thanks to the simultaneous observation by using two telescopes. The stereo observation (as previously discussed) results in a better angular resolution (with an improvement of 20%), better energy estimation (with an energy resolution improving from 25% to

15%), and higher cosmic-ray background rejection. The flux sensitivity of the two-telescope system is about 3 times better than that of a single telescope (MAGIC-I) at energies below 200 GeV (see Fig. 3.8).

The structure of the second telescope is almost identical with that of the MAGIC-I telescope. The lightweight reinforced carbon-fiber reflector frame, the drive system, and the active mirror control (AMC) are only marginally improved with respect to the first telescope. New developed components are introduced for improving the performance of the new telescope. Larger 1 m^2 mirrors elements have been developed as well as ultra fast sampling rates, low power consumption readout system, and increased QE PMTs. As for the camera, it is placed in the focus of the reflector at a distance of 17.5 m from the elevation axis of the telescope structure. MAGIC-II has an improved camera equipped uniformly with 1039 pixels of 0.1° diameter each, covering a trigger radius of 1.25° and a FoV of 3.5°. Every seven pixels are grouped in a hexagonal configuration to form one cluster.

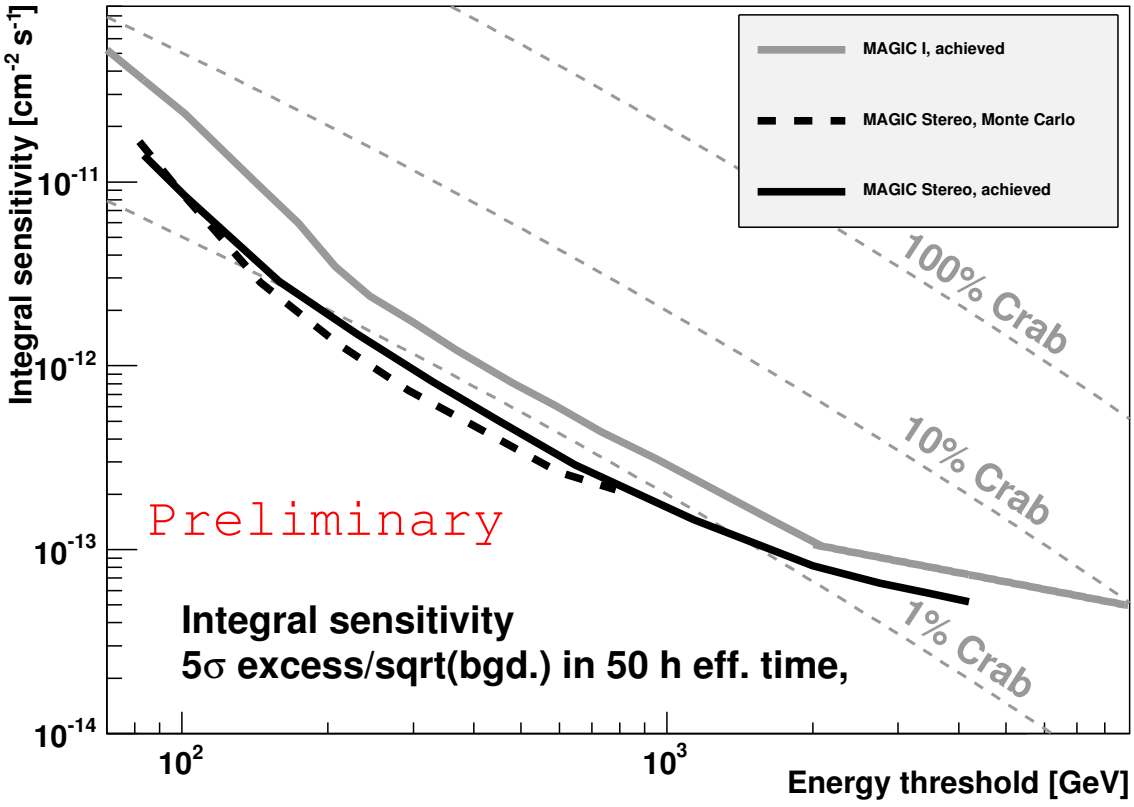

Figure 3.8 Integral sensitivity of MAGIC-II is compared with MAGIC-I. The sensitivity is defined as integral flux of gamma events, exceeding the background fluctuation by factor 5, in 50 hours of observation. Figure from private communication.

The two telescopes can be operated both in a single mode, by observing two

different regions in the sky, and in a stereoscopic mode, with a simultaneous observation of the same region. The stereoscopic observation mode leads to a more precise reconstruction of the shower parameters as well as a stronger suppression of the background. This was already described in Sec. 3.1.

4

Data analysis with the MAGIC standard analysis tools: the case of GRB 100316A and PKS 1222+216

4.1 Introduction

The main goal of the MAGIC data-analysis chain is to distinguish between a shower originated by a γ-ray photon from the source that we are interested in, or from any other source considered as background. This chapter is not intended to be a detailed description of the MAGIC analysis tools but briefly describe the main aspects of a standard analysis and apply them to a couple of real cases: one is the observation of the GRB 100316A with redshift unknown where no signal is found. The another one is the observation of the blazar PKS 1222+216 in a flaring state where a very clear signal is found. This source is in principle interesting for EBL studies due to its high redshift.

4.2 MAGIC standard analysis software

The MAGIC standard analysis software (`MARS`) allows to reconstruct the properties of γ-rays coming from astrophysical sources. `MARS` is a collection of programs written in `C++` in the framework of the `ROOT` data analysis object-oriented software maintained at CERN[1]. Another independent MAGIC analysis software exists used mainly by the MAGIC Würzburg group, which is named `MARS Cheobs Edition` (Bretz & Dorner 2009).

The main executable programs contained in `MARS` with their functionality are:

[1] http://root.cern.ch

- `callisto` (CALibrate LIght Signals and Time Offsets): signal extraction and calibration steps.
- `star` (STandard Analysis and image Reconstruction): image cleaning and calculation of quality parameters.
- `superstar` (SUPER STandard Analysis and image Reconstruction): stereo and energy reconstruction.
- `osteria` (Optimize STandard Energy Reconstruction and Image Analysis): application of random forest training.
- `melibea` (MErge and Link Image parameters Before Energy Analysis): calculation of the likelihood that an event was triggered by a γ-ray or hadron (this is called hadroness) and second quality cuts.
- `celestina` (CELestial INstantaneous Appearance): calculation of the skymap only in a single-telescope (mono) mode.
- `caspar`: calculation of the skymap in mono and stereo mode.
- `zinc` (Zinc Is Not Celestina): calculation of the skymap in mono and stereo mode.
- `fluxlc`: flux, spectrum, and light-curve estimation.

4.3 Analysis chain

The data analysis strategy has to be chosen accordingly to the particular characteristics of the astrophysical source and observation conditions such as background light, zenith angle range, angular size or the expected spectrum. Here the main steps during a standard data reduction chain with `MARS` are summarized.

(i) **First data quality selection**: this is done according to information given every night by the observers in the so-called runbook and data quality check plots.

(ii) **Signal extraction**: determination of the charge content and arrival time of the Čerenkov pulses in fast analog-digital converter counts and slices, respectively, for each photomultiplier of the camara.

(iii) **Calibration**: this is done after subtraction of the pedestal signal. It consists in the conversion of each pixel's charge from counts to photo-electrons and correction of the arrival times of individual pixels from individual cable length differences.

(iv) **Image cleaning**: the calibrated images are cleaned according to light content of pixels and arrival time distributions.

(v) **Image parametrization**: the images are described according to Hillas parameters (see Sec. 4.4).

(vi) **Second data quality selection**: according to quantities such as event rate before and after image cleaning, cloudiness and humidity.

(vii) **Event classification** as a γ-ray coming from the source or background origin.

(viii) **Energy estimation** of individual events.

(ix) **Determination of the direction** of the original particle.

(x) **Determination of the excess events** coming from the source, and the statistical significance of this excess. The creation of a sky map of the position of the excess event is possible here.

(xi) **Differential, integral flux, and light curve determination** (or upper limits to the flux if no significant signal is found).

4.4 Image parameters

Many different parameters are calculated to describe the images in the camera after these have been cleaned from noise. This is useful to recognize the nature and physical properties of the primary particle. The IACT technique is based on the Hillas parameters (see Fig. 4.1 and Hillas 1985), which are calculated from the spatial charge distribution in the camara. Furthermore, other parameters are used for a better characterization of the primary particle. The main image parameters may be classified as dependent or independent of the source position in the camara. Some source independent parameters are:

(i) **Size**: Sum of the pixel charges. It is roughly proportional to the energy of the primary particle that originated the shower and therefore it is used as the main indicator to estimate its energy.

(ii) **Length**: root mean square (RMS) spread of the light along the major axis of the shower. It is related with its longitudinal development.

(iii) **Width**: RMS spread of the light along the minor axis of the shower. It is related with its transverse development.

(iv) **M3Long**: Third moment of the image along its major axis that indicates the shower direction.

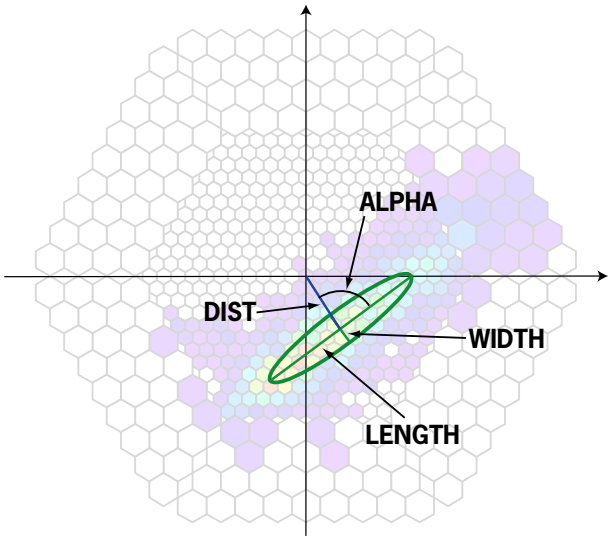

Figure 4.1 Representation of the main Hillas parameters described in the text.

(v) **Leakage**: Ratio between pixel charges in the outermost ring of the camara to the parameter **size**.

(vi) **Conc**[n]: Ratio between the light content in the n brightest pixel and the total light in the image.

(vii) **Asym**: Distance from the brightest pixel to the center of the image.

(viii) **Time RMS**: Arrival time spread of the Čerenkov photons in the pixels belonging to the cleaned image.

Some source dependent parameters are:

(i) **Dist**: Angular distance between the center of gravity of the image and the expected source position in the camera.

(ii) **Alpha or** α: Angle between the major axis of the shower image and a straight line from the center of gravity of the image and the expected source position in the camera. Images from astrophysical γ-ray showers will point to the source position in the camara, and therefore they will have small α values. On the other hand, showers from hadronic origin will be isotropically distributed and their α distribution tends to be flat. This is the most powerful parameter to distinguish between a γ-ray or hadronic-originated shower.

(iii) **Time gradient**: Magnitude of the time profile of the event. It comes from a linear fit of the arrival time versus the space coordinate along the major axis.

The description of these parameters has been adapted from Oya (2010).

4.5 Data run classification and observational modes

During the data acquisition, the digitized events are collected in files called runs. There are three main kinds of runs.

- **Data Run**. Data runs are triggered by the level-1 trigger. Each run typically contains about 50000 events and requires more than 900 MByte of disk space. Data runs can be divided in three typologies according to the chosen observation mode. If the chosen observation mode is the On-Off mode one have:
  - On data runs that are collected while the telescope is pointing to the source.
  - Off data runs are collected with a pointing telescope position of about 3° off the supposed source. If the Off data runs are taken in the same experimental conditions with respect to the On data ones, they permit to evaluate the background around the pointed source.

  While, if the chosen observation mode is the Wobble mode one has only:

  - Wobble data runs that are collected with the telescope pointing slightly off-source, at an angular distance of about 0.4° from the camera center, in a point conventionally called W1. Every 20 minutes the telescope moves to the opposite point W2 with respect to the camera center. This observation mode permit the acquisition of On and Off data at the same time, with the same experimental conditions and in the same FoV. On the other hand, this mode induces a loss of telescope sensitivity of about 20% because sensitivity is best at the camera center (Bretz 2005). Additionally, the wobble mode is not suitable for extended sources for the necessity of having non-overlapping regions of camera between On and Off is not satisfied. Nevertheless the MAGIC collaboration has studied some point-like sources by using this technique obtaining good results (Albert et al. 2006).

- **Pedestal Run**. These runs collect information about the background not coming from showers, i.e. mainly of the light of the night sky background. The trigger is activated with fixed frequency. Pedestal runs take also into account the electronic chain noise. A pedestal run is recorded every hour along the data taking.

- **Calibration Run**. Since the conversion factor of the recorder signal from FADC counts to photo-electrons can vary by up to 10% over a night, it is necessary to compute it very often. In order to obtain this result, a light pulser with a series of very bright LEDs was installed at the center of the telescope reflector. The LEDs emit short light pulses of known wavelength that uniformly

illuminate the camera. The response from each pixel, to a series of light pulses, determines, then, the conversion from extracted signals to incident number of photo-electrons. Calibration runs are usually recorded after the pedestal ones and, additionally, the automatic calibration trigger sends interleaved calibration pulses with a fixed frequency of 50 Hz during all the data taking. The collected raw data are then transferred to the Barcelona PIC Data-center and to the Würzburg one every night. In the data-centers, the runs are grouped into *sequences*: each sequence contains at least one pedestal and calibration run and the successive data runs for an average duration of 1 hour.

4.6 Monte Carlo simulations

It is essential for the reconstruction and interpretation of shower parameters to develop Monte Carlo (MC) simulation of Čerenkov cascades originated by γ-ray photons. MAGIC uses the software `Corsika 6.019` (Heck et al. 1998) for this goal. Outputs of this code with information on the photons that reach the ground, from a γ-ray originated shower, are introduced in another MAGIC program called `reflector`. This program simulates the absorption and scattering of the Čerenkov photons in the atmosphere, and the optical properties of the telescopes' mirrors. The output are data files with information about the positions and directions of photons in the camara plane. With this information, the response of the PMT and both trigger and data acquisition (DAQ) systems are simulated with the program `camera`. The point spread function is introduced at this point as well. Finally, this output is ready to be introduced in the MAGIC analysis chain as observed raw data. Further information may be found in Majumdar et al. (2005).

4.7 Mono analysis of the γ-ray burst GRB 100316A

Introduction

This GRB with unknown redshift was observed by MAGIC the night of March 16th, 2010 at 02:23:00 UC triggered by the Burst Alert Telescope (BAT) instrument on board the Swift satellite. The alert was received by MAGIC 28 s after the GRB happened. Then the automatic GRB procedure started. Due to technical issues the observation did not begin until 02:31:37 UT. The observation finalized at 06:06:42 UT under twilight. Here we describe the results of the automatic procedure set for quick analysis GRB alerts. At the time of the observation the automatic procedure was not set up for stereo observations, therefore here is presented the analysis of the observation performed with a single telescope. I analyzed this source as a flare advocate of the MAGIC GRB working group.

	Time [UT]		Zenith angle [deg]	
Time slot 1	02:31:37	02:51:23	53	51
Time slot 2	02:54:03	04:32:43	51	45
Time slot 3	04:32:43	06:06:42	45	43

Table 4.1 Summary of the observation of the GRB 100316A on March, 16h 2010.

Analysis and results

The observation was performed under dark time and very variable humidity. The data was taken in On mode. The zenith angle of the observation was wide and the automatic analysis split the full data set into the three samples described in Table 4.1. The random forest method was used to separate showers originated by γ-rays and hadron events, and the time image cleaning algorithm and time parameters were applied.

The following cuts were applied in `osteria` (see Sec. 4.4 for a description of every quantity):

- Hillas parameters: leakage < 0.2, core pixels > 2, islands < 4, size > 60.
- Spark: $1.5 - 4 \cdot \log \text{conc} > \log \text{size}$; $1.5 - 4 \cdot \log \text{conc} > \log \text{size}$
- Car flashes: $\log\left(\frac{width \cdot length}{297 \cdot dist}\right) > -0.3$

Finally, after the random forest training, the following filter cuts were chosen:

- Dist parameter: $0.25^\circ < \text{dist} < 1.0^\circ$
- Further cuts: islands < 2

`osteria` applied a re-sizing of the hadron distribution, in bins of zenith angle, but no explicit re-zenithing. The zenith angle was not used as a training parameter for random forest. However, the MC was chosen such that the zenith angle ranges match well.

The so-called α plots are shown in Fig. 4.2 for different energy bins. This plot shows the distribution of the Hillas parameter α (already described in Sec. 4.4) as red crosses. The Off data are taken from three positions that are symmetrical with respect to the telescope pointing directions and they are shown in blue. The tentative significances in every energy bin indicate that no signal is found.

Light curves were calculated for the entire data set. No significant excess over background could be found for this time period. Fig. 4.3 shows the light curves per energy bin and Fig. 4.4 the corresponding evolution of the background.

Upper limits were calculated using the Rolke method (Rolke, López & Conrad 2005) with 95% confidence level and 30% systematic uncertainty. This 30% is obtained by the quadratic sum of the following contributes, principally due to the differences between the real observational conditions and the simulated ones:

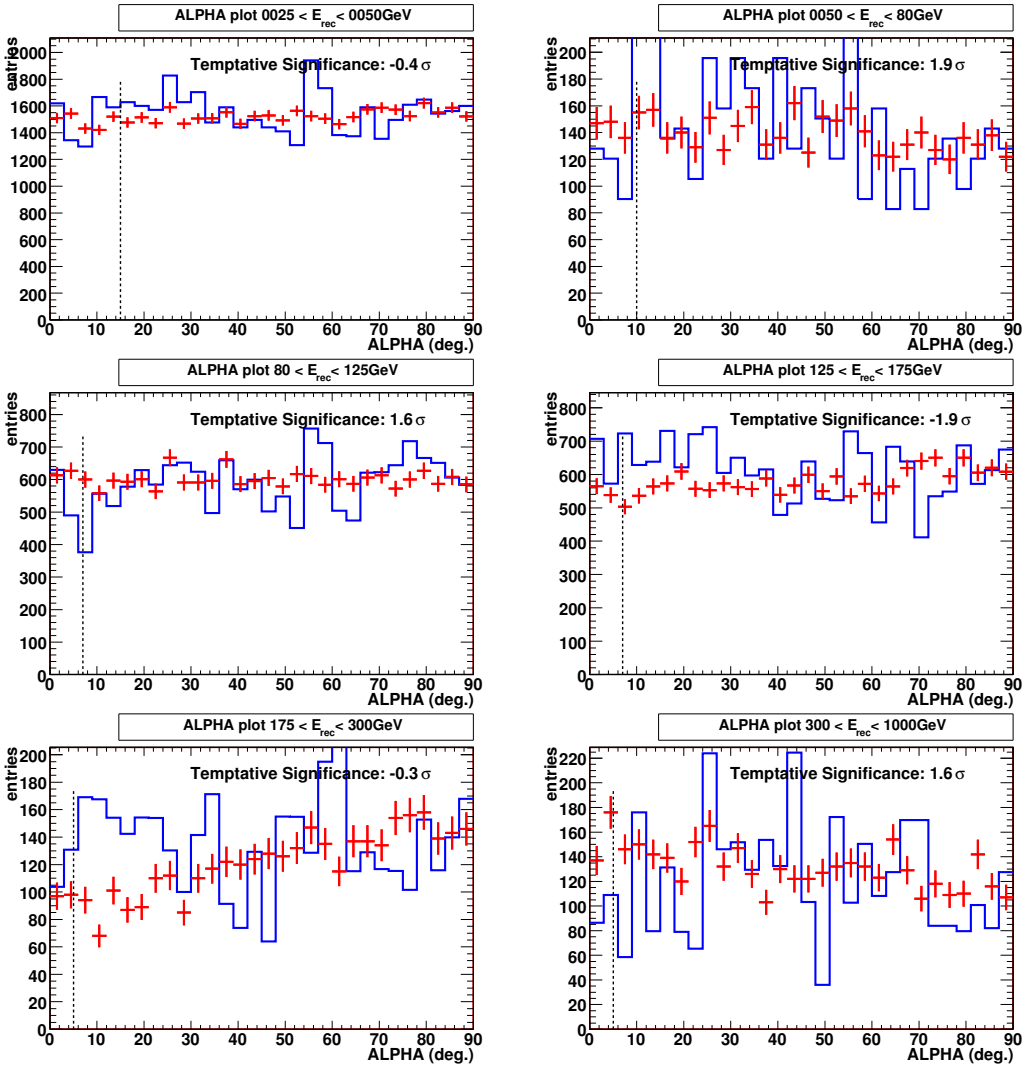

Figure 4.2 Distribution of the angle between the major axis of the shower image and a straight line from the center of gravity of the image and the expected source position in the camera (α) marked as red crosses. The Off data are taken from three positions that are symmetrical with respect to the telescope pointing directions and it is shown in blue

(i) atmospheric model (the standard one do not perfectly match La Palma atmosphere) 15%.

(ii) atmospheric summer-winter variations 15%.

(iii) Mie scattering and other types of atmospheric extinction 10%.

(iv) trigger inefficiency 10%.

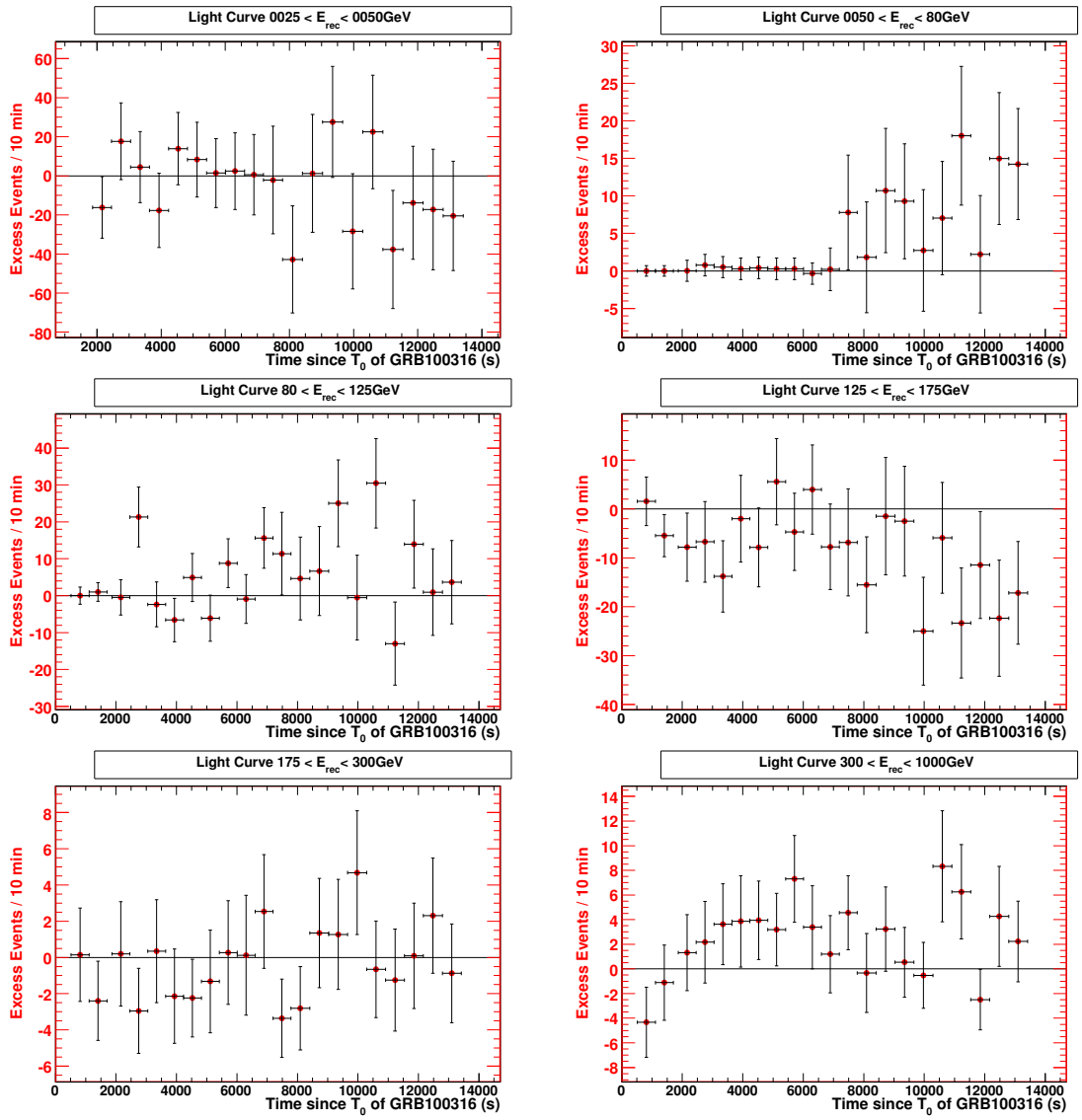

Figure 4.3 Light curves (or excess events in 10 min bins versus time) for different energy bins.

(v) non perfectly agreement between the real data and the simulated ones 5 - 10%.

Another type of uncertainty that must be considered when interpreting the resulting upper limits is the systematic error on the absolute energy scale, since it is not yet automatically implemented. The systematic uncertainty on the absolute energy scale is of about 20% resulting by the quadratic sum of the two following contributes:

(i) another 15 - 20% of uncertainty due to atmospheric conditions.

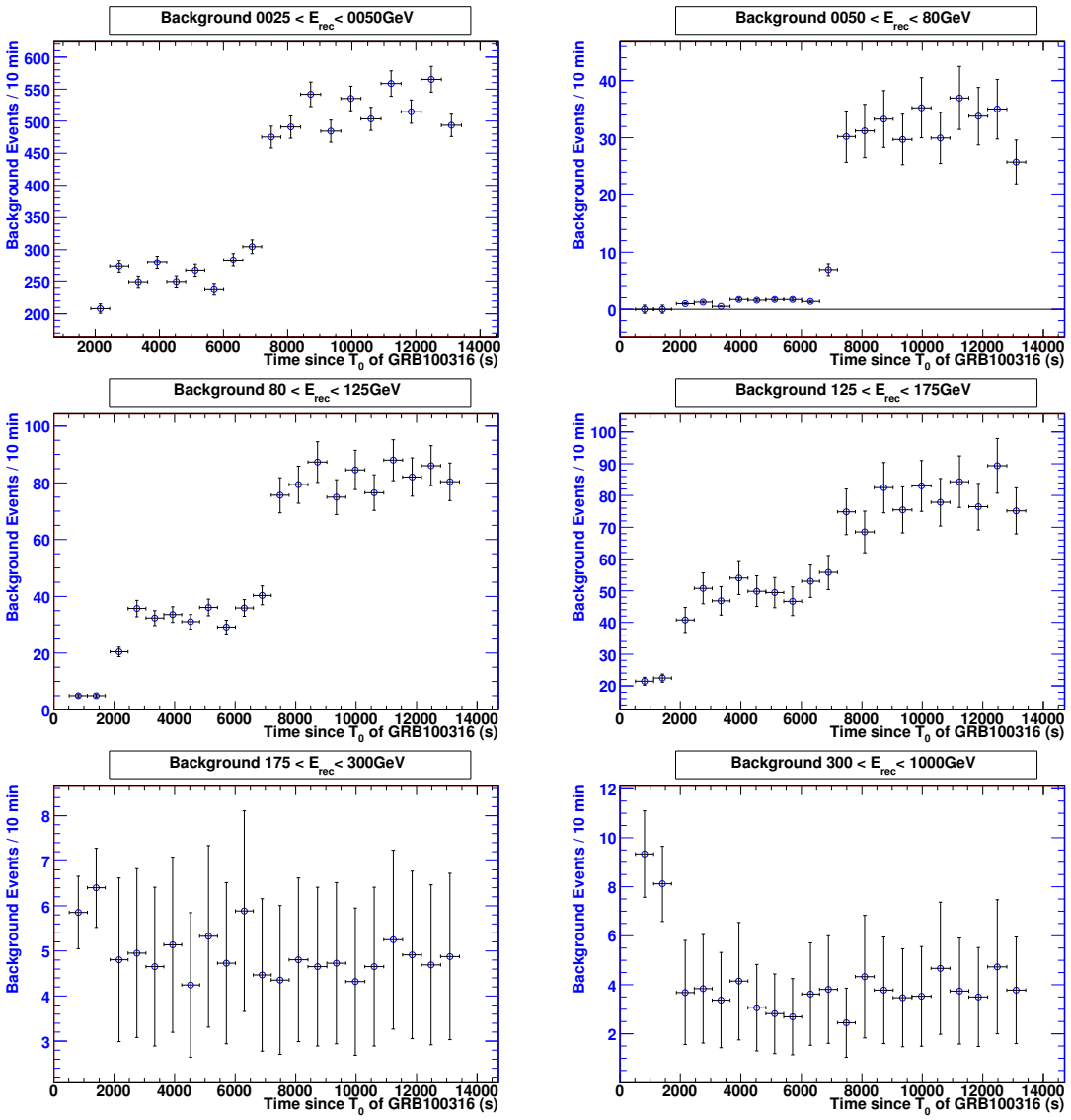

Figure 4.4 Evolution of the background events from the light curves for different energy bins.

(ii) an uncertainty on the absolute calibration of about 10% due to a not yet implemented correction on the PMTs aging.

We point out here that 1 Crab or Crab unit (C. U.) is the unit of differential flux that is emitted by the Crab Nebula, which is equal to:

$$1 \text{ C.U.} \equiv 1.5 \times 10^3 \Big(\frac{E}{\text{GeV}}\Big)^{-2.58} \text{ ph cm}^{-2} \text{ s}^{-1} \text{ TeV}^{-1}$$

The skymap of the entire observation for energies larger than 200 GeV is shown

E [GeV]	$\langle E \rangle$ [GeV]	HADRONNESS cut	α cut	Upper Limits $\left[\frac{\text{ph}}{\text{cm}^2\,\text{keV}\,\text{s}}\right]$	Upper Limits $\left[\frac{\text{erg}}{\text{cm}^2}\right]$	Upper Limits C.U.	rough expectation C.U.
175- 300	204.6	0.15	5	$4.5{\cdot}10^{-19}$	$3.6{\cdot}10^{-8}$	0.28	(0.71)
300-1000	510.4	0.10	5	$1.9{\cdot}10^{-20}$	$9.3{\cdot}10^{-9}$	0.12	(0.10)
These upper limits correspond to 1186 s from 02:31:37 UT to 02:51:23 UT							
175- 300	210.9	0.15	5	$3{\cdot}10^{-19}$	$1.2{\cdot}10^{-7}$	0.20	(0.32)
300-1000	493.6	0.10	5	$4.5{\cdot}10^{-20}$	$1{\cdot}10^{-7}$	0.27	(0.04)
These upper limits correspond to 5920 s from 02:54:03 UT to 04:32:43 UT							
125- 175	135.3	0.40	7	$8.5{\cdot}10^{-19}$	$1.4{\cdot}10^{-7}$	0.18	(0.58)
175- 300	218.4	0.15	5	$3.1{\cdot}10^{-19}$	$1.3{\cdot}10^{-7}$	0.22	(0.16)
300-1000	480.8	0.10	5	$3.4{\cdot}10^{-20}$	$7.1{\cdot}10^{-8}$	0.19	(0.04)
These upper limits correspond to 5638 s from 04:32:43 UT to 06:06:42 UT							

Table 4.2 Upper limits on the VHE γ-ray emission from GRB 100316A.

in the upper panels of Fig. 4.5. There is no hint of signal from the coordinates consistent with the GRB. However, there is what seems an excess of photons (with a significance $\sim 4\sigma$) from an unknown source some tenth of degree off. In the lower panels of Fig. 4.5 the skymap is re-plotted in order to center the position of the excess. There is currently a detailed analysis ongoing of this excess, in order to clarify its nature. In both cases (upper and lower panels) shown in Fig. 4.5, the background has been calculated from Off data taken in similar conditions than the On observations.

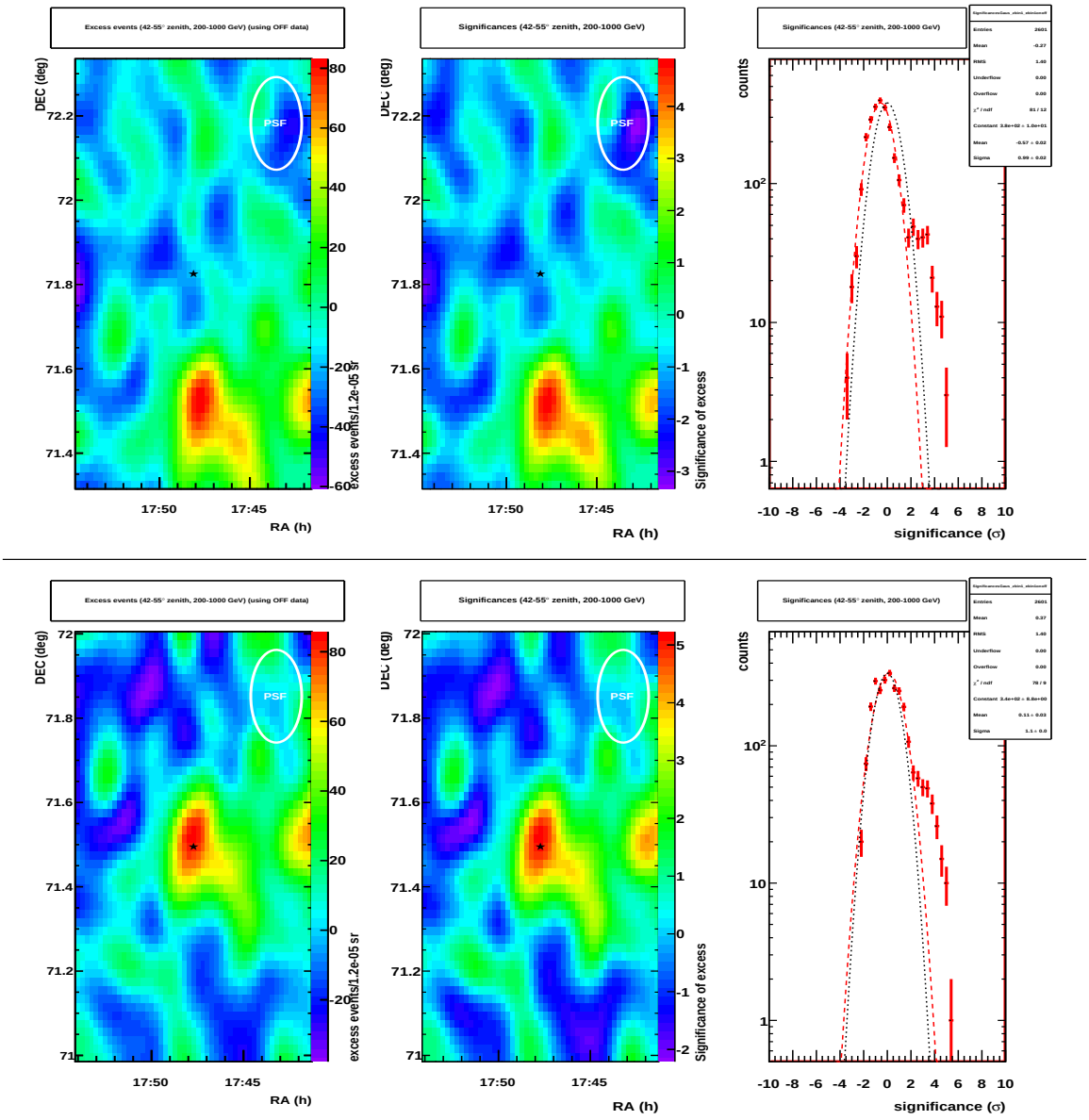

Figure 4.5 Skymaps of the entire observation for energies larger than 200 GeV. *Upper panels*: Skymaps centered at the position of the GRB. On the left side, the number of excess events is shown, while in the middle and right side the corresponding significances are shown. There is an excess of VHE photons around the coordinates 16:48 h, 71.5°. *Lower panels*: Skymaps centered at the position of the excess of VHE photons shown in the upper panels. The PSF is shown for comparisons.

4.8 Stereo analysis of the blazar PKS 1222+216

Introduction

This blazar at $z = 0.435$ discovered by the MAGIC collaboration (Aleksić et al. 2011b) is the second most distant flat spectrum radio quasar (FSRQ) (see Chap. 5) known in the VHE regime after 3C 279 ($z = 0.536$, which was discovered by the MAGIC collaboration as well, Albert et al. 2008). The stereo observation and analysis were essential for this detection. This source was followed by MAGIC from May 3rd until June 19th, 2010 under a target of opportunity proposal with Fermi. The light-curve by Fermi had a very high variability as shown in Fig. 4.6. On the night of June 17th under soft moon-light conditions the source was detected in a flaring state. The on-site analysis showed a hint of signal that triggered further quick analysis that confirmed the signal. These are the data that we will analyze in this section and that will be described as a demonstration of the stereo MAGIC standard analysis chain. This analysis should be considered as a cross-check analysis of the official analysis that will be published by the collaboration in Aleksić et al. (2011b). The source was observed the following days showing no signal.

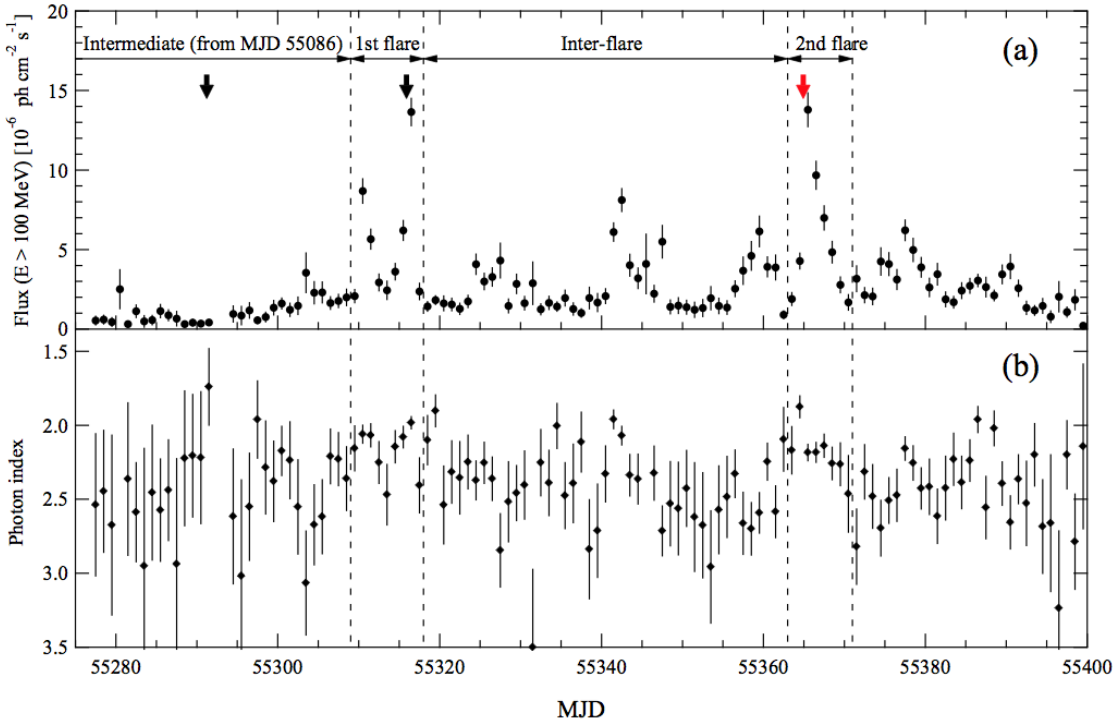

Figure 4.6 Fermi light-curve over part of the period of time where PKS 1222+216 was followed by MAGIC. The date of the MAGIC discovery (MJD 55364.9) is marked with a red arrow. Figure taken from Tanaka et al. (2011).

Run Number	Event rate [Hz]	Zenith angle [deg]	Event number
05008001.001	80.2832	27.0977	17121
05008001.002	83.7677	27.8469	16623
05008001.003	81.1509	28.5865	17206
05008001.004	80.2039	29.3664	17192
05008001.005	79.17	30.146	17165
05008001.006	81.2242	30.7738	10317
05008002.001	80.6623	32.3493	17557
05008002.002	85.1976	33.1222	17337
05008002.003	84.2923	33.876	17562
05008002.004	83.603	34.3967	6046
total: 10 runs/0.523257 h	81.8198	30.5179	

Table 4.3 Summary of the main parameters of the observation of the blazar PKS 1222+216 on Jun 17th, 2010 with the MAGIC-I telescope.

Analysis and results

The total time observed on the night of Jun 17th, 2010 was 30 minutes. There was a soft moon light that allow us to use the standard analysis chain (thought for dark-night observations), instead of a more complicated analysis accounting for a strong background from the moon. Wobble observations were performed (see 4.5). For simplicity, there are MC files that already went through the main steps of the analysis chain such as `superstar`, `osteria`, and `melibea` available to the MAGIC collaboration thanks to Karsten Berger. These MC files are convenient when standard conditions are present such as this case. These MC files are used in this analysis.

Our analysis is started using the outputs of the `star` program, which are obtained directly from an automatic procedure that run the first steps of the analysis in a MAGIC server. A quick check of the data quality is presented in Table. 4.3 and Table. 4.4 for data taken with MAGIC-I and MAGIC-II telescopes, respectively. It is shown in those tables that the event rate is stable and therefore, initially, the quality of the data is good.

The data are then processed through the `superstar`, `osteria`, and `melibea` programs as described in Sec. 4.3. The data θ^2 plot (obtained with `odie`) is shown in Fig. 4.7, where standard cuts for low energy analysis (June 2010) are used. θ represents the angular distance between the nominal and the reconstructed source position, i.e., the distance between the camera center and the source position found with the Disp method. These cuts are MHadronness.fHadronness < 0.28 && MHillas_1.fSize > 55 && MHillas_2.fSize > 55 and ensure a sensitivity of ~ 1.8 C. U. obtained, which implies a very clear detection (normally a source is considered detected when its significance is above 5σ).

When the source is detected the next step is to run `fluxlc`. With this program

Run Number	Event rate [Hz]	Zenith angle [deg]	Event number
05008001.001	71.8857	26.8451	5252
05008001.002	72.5549	27.1188	5436
05008001.003	74.2796	27.3934	5398
05008001.004	75.0805	27.6654	5291
05008001.005	78.088	27.9203	5139
05008001.006	79.9718	28.1735	5253
05008001.007	74.1872	28.4378	5415
05008001.008	73.6982	28.7135	5463
05008001.009	73.5181	28.9903	5385
05008001.010	74.4747	29.2653	5483
05008001.011	74.9374	29.5407	5448
05008001.012	74.1631	29.8186	5410
05008001.013	73.9624	30.0967	5464
05008001.014	72.5257	30.3753	5459
05008001.015	73.2161	30.6569	5458
05008001.016	75.7928	30.902	4109
05008002.001	72.6778	32.0949	5499
05008002.002	72.1328	32.3795	5665
05008002.003	74.8689	32.6625	5402
05008002.004	78.6987	32.9305	5536
05008002.005	78.4972	33.1986	5439
05008002.006	79.5232	33.4656	5548
05008002.007	78.1951	33.7316	5570
05008002.008	76.7908	34.0057	5583
05008002.009	75.2714	34.2797	5501
05008002.010	78.4459	34.4736	2325
total: 26 runs/0.506269 h	75.1308	30.5245	

Table 4.4 Summary of the main parameters of the observation of the blazar PKS 1222+216 on Jun 17th, 2010 with the MAGIC-II telescope.

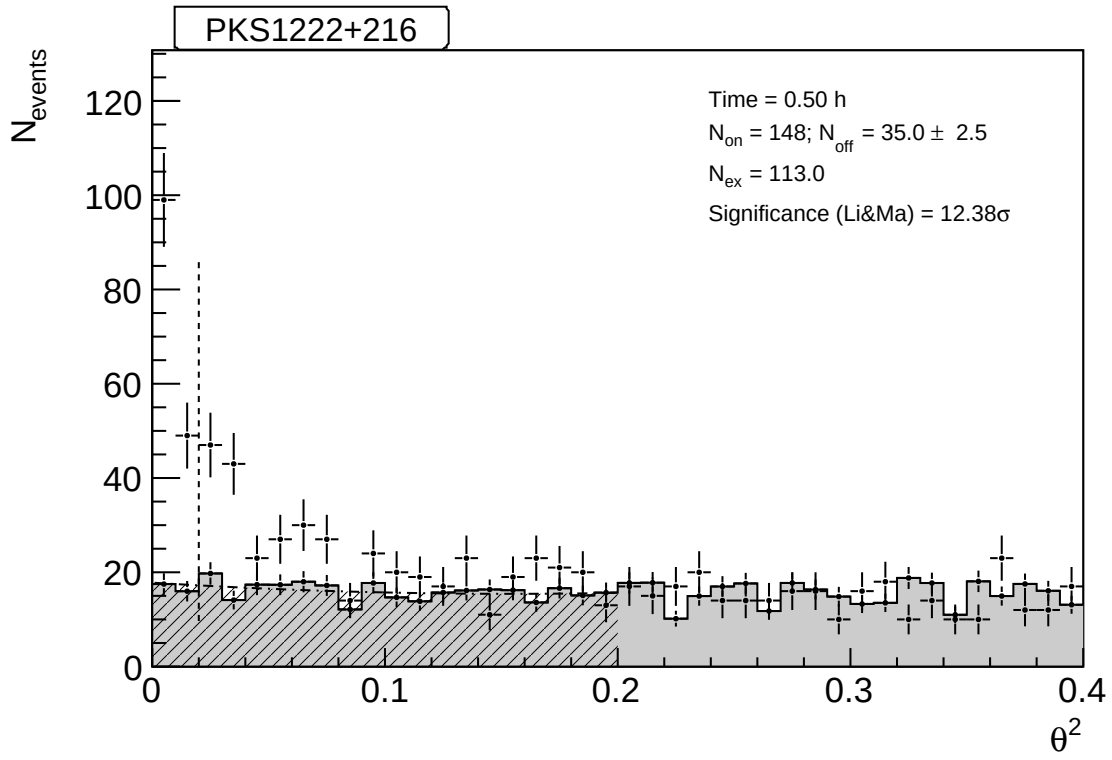

Figure 4.7 Distribution of squared angular distances (θ^2) between photon directions and the position of PKS 1222+216. The Off data are taken from three positions that are symmetrical with respect to the telescope pointing directions. A detection with a statistical significance of 12.38 σ is obtained.

the spectrum and light curve are plotted. It is considered these efficiency cuts in the `fluxlc` configuration: 0.7 for α and 0.6 for hadrons.

The spectrum (Fig. 4.8) shows the differential flux versus energy in different energy bins with their uncertainties. The data are fitted by a χ^2 minimization procedure to a power law,

$$\left.\frac{dF}{dE}\right|_{obs} = F_0 E^{-\Gamma_{obs}} \tag{4.1}$$

with $F_0 = (1.20 \pm 1.57) \times 10^{12}$ TeV^{-1}cm^{-2}s^{-1}, $\Gamma_{obs} = 4.02 \pm 0.74$, and $\chi_{red} = 0.85/2$. It is worth to say that it is not strictly correct to fit the VHE observed spectrum of non-local extragalactic sources to a power law due to the expected exponential attenuation by the EBL. Despite this fact, this is a common practice to compare different observations.

The light-curve (Fig. 4.9) shows the evolution with time of the integral flux. It is very noticeable the very fast flux variability of the order of minutes. This fact has consequences for the emission mechanisms in this type of astrophysical sources that

are discussed in Aleksić et al. (2011b).

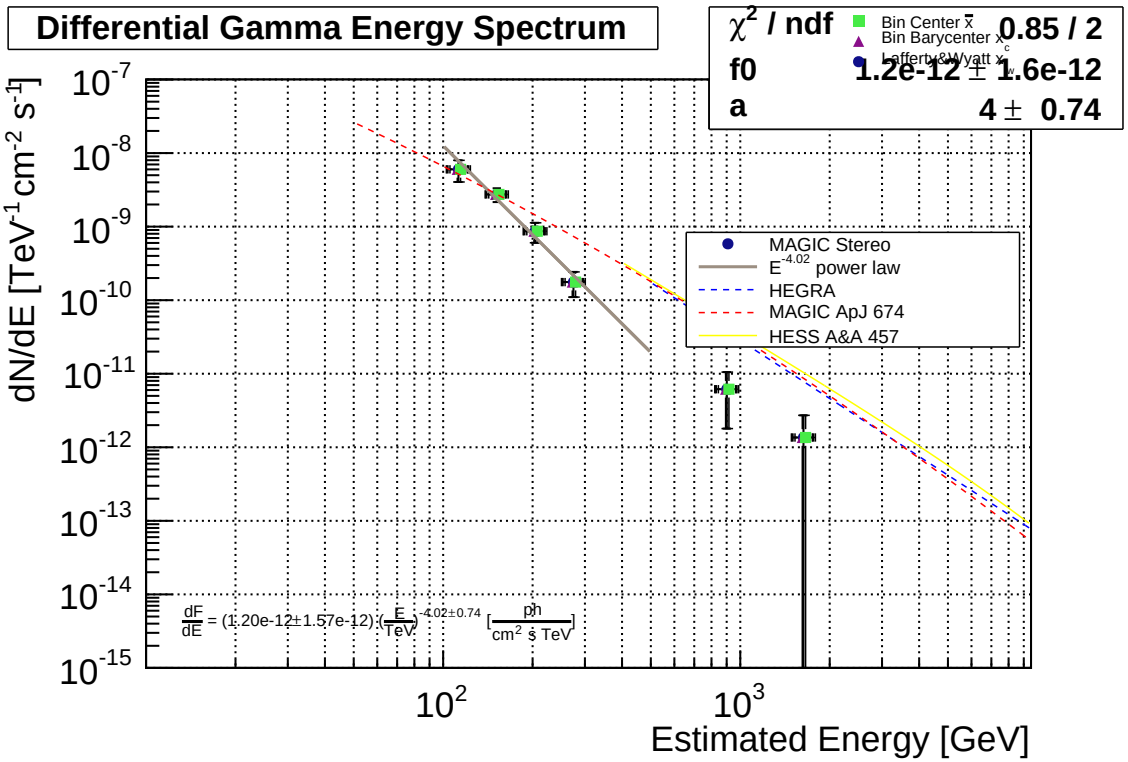

Figure 4.8 Differential energy spectrum of PKS 1222+216 before unfolding from the flare detected on Jun 17th, 2010 described in the text.

The significance skymap of the observed region is shown in Fig. 4.10. The skymap is obtained with the `zinc` program. The source *hot spot* is clearly visible and by comparison with the telescopes' point spread function (PSF), this figure shows that the source can be considered point-like.

The last step in the MAGIC analysis chain is called unfolding. This is implemented in a `ROOT` macro named `CombUnfold.C`. The unfolding is necessary in order to calculate the true energy from the energy estimated from the Čerenkov showers. This is done to take into account the finite energy resolution of the instrument and the biases in the energy reconstruction through the MAGIC analysis chain. Basically, it is necessary to calculate a correlation matrix that relates those two quantities. There are different unfolding techniques, but usually for a MAGIC publication the Tikhonov method is used. For that reason this method will be used here as well. All the details about the application of the unfolding to MAGIC data may be found in Albert et al. (2007). The final results for the unfolded energy spectrum of PKS 1222+216 corresponding to the flare observed by MAGIC on Jun 17th is shown in Fig. 4.11. As we see the spectrum calculated by our analysis is compatible within uncertainties with the official spectrum published in Aleksić et al. (2011b). In that paper, implications

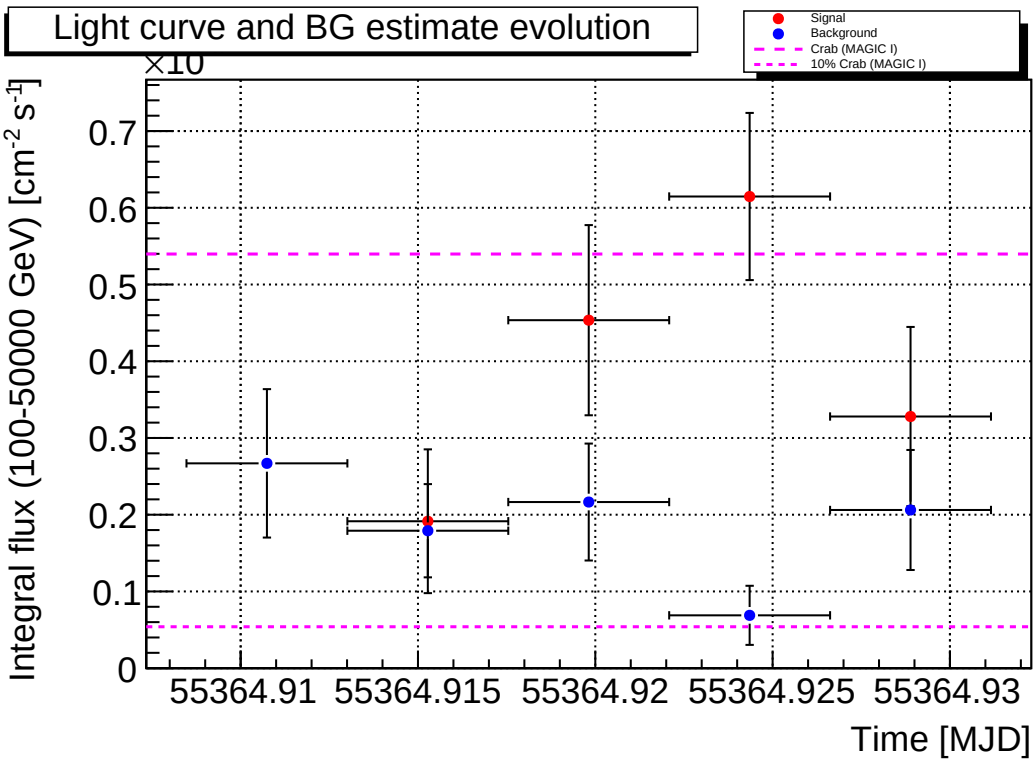

Figure 4.9 Variability of the integral flux versus time during the observation of the flare carried on Jun 17th, 2010.

for EBL and emission mechanisms in FSRQ are discussed. At the end of Chap. 5, limits for the EBL are derived here as well from these observations.

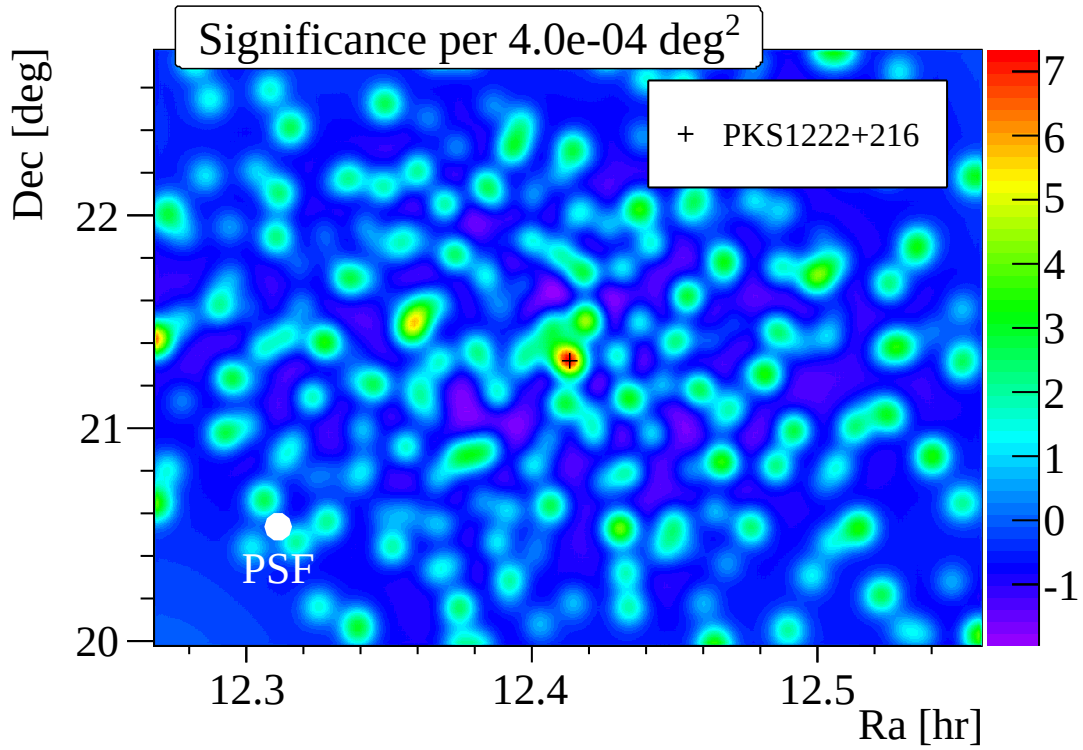

Figure 4.10 Significance skyplot of the region around PKS 1222+216.

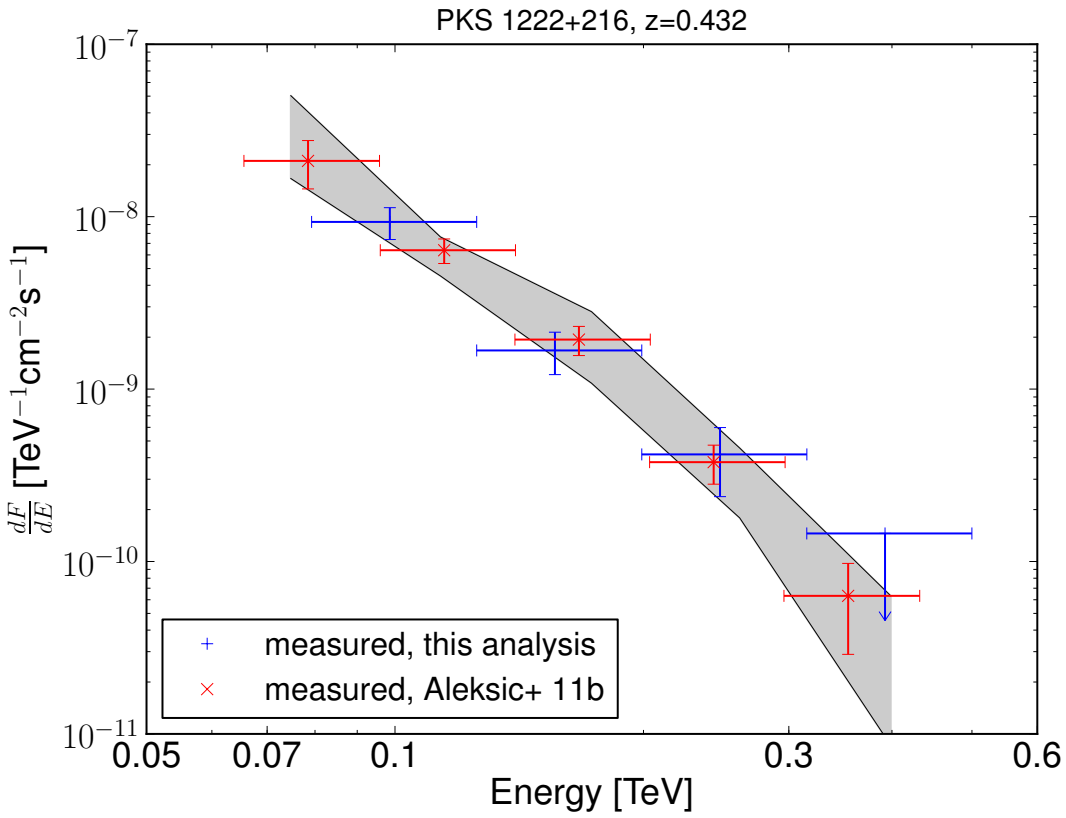

Figure 4.11 Unfolded differential energy spectrum of PKS 1222+216 calculated from the analysis presented here, and the spectrum published in Aleksić et al. (2011b). The gray shaded area represents the systematic uncertainties given for the analysis in Aleksić et al. (2011b). Both spectra are unfolded using the Tikhonov method (see text for details).

Part III

Interpretation of extragalactic VHE spectra

5

γ-ray attenuation

5.1 Theoretical background

The EBL has important implications for the interpretation of data taken using recent VHE experiments (the Fermi satellite, Gehrels & Michelson 1999; and IACTs, such as MAGIC, VERITAS, and HESS; Lorenz 2004; Weekes et al. 2002; Hinton 2004, respectively), due to the photon-photon pair production between γ-ray photons traveling across cosmological distances and EBL photons (see Nikishov 1962; Gould & Schréder 1966).

Blazars are an important source of extragalactic γ-ray emission and have become a relevant tool for indirectly measuring the EBL. These objects are believed to be an extreme category of AGNs. There is no general agreement on how AGNs might be classified. Despite this fact, Fig. 5.1 shows a tentative classification based on morphology and SED features. Their emission, which occurs at all wavelengths of the electromagnetic spectrum, comes from super-massive black holes (with masses $\geq 10^7$ $M_\odot$) swallowing matter accreted from their surroundings. In general, AGNs are characterized by a beamed emission perpendicular to the accretion disc known as jets, which are pointing toward us in the case of blazars. Other AGNs whose jets are not directly pointing to us may also be detected if they are close enough (M 87 Aharonian et al. 2004; Centaurus A Aharonian et al. 2009). Fig. 5.2 shows the extragalactic γ-ray sky known to date.

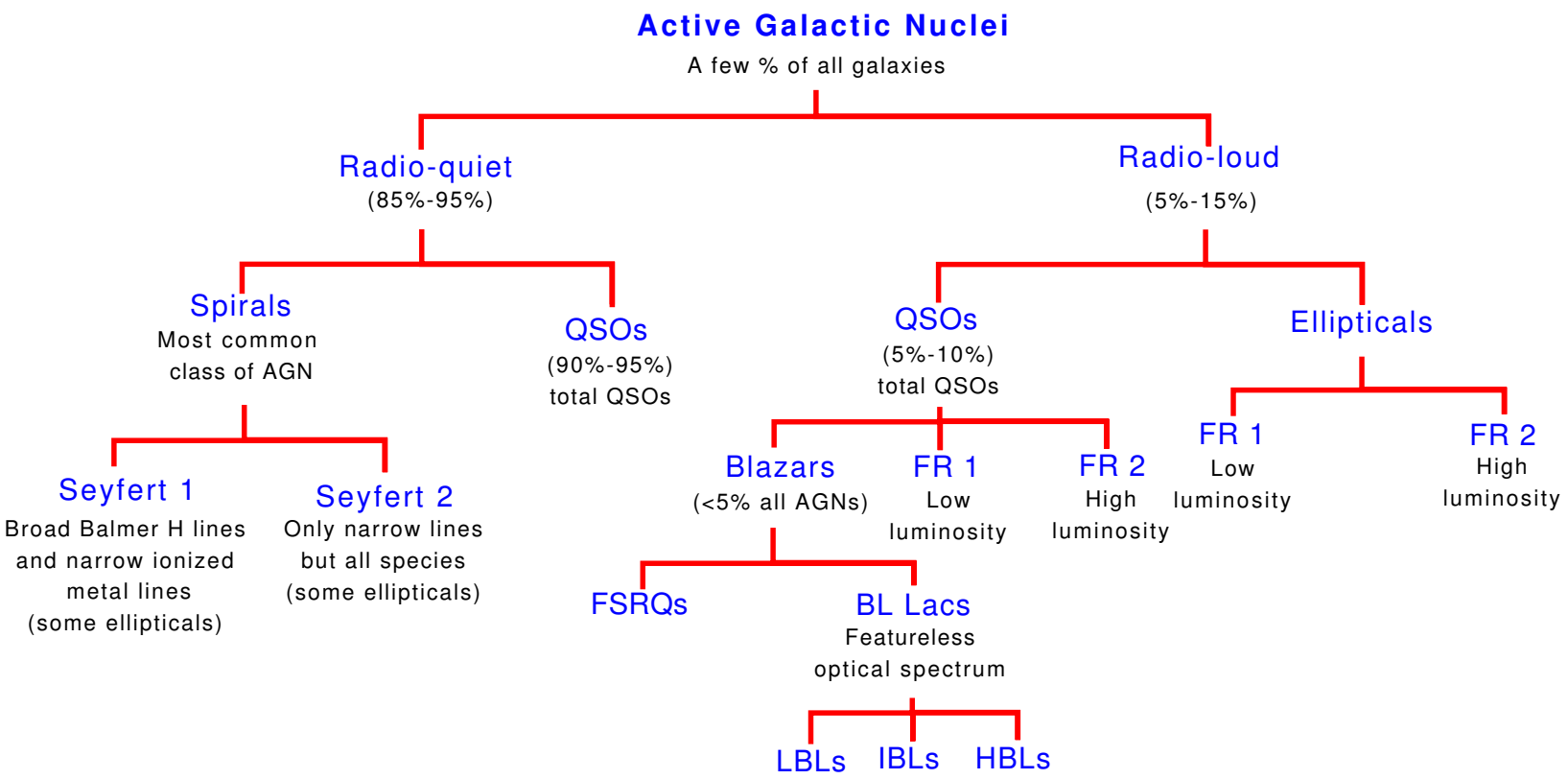

Figure 5.1 AGN classification based on their morphology and SED.

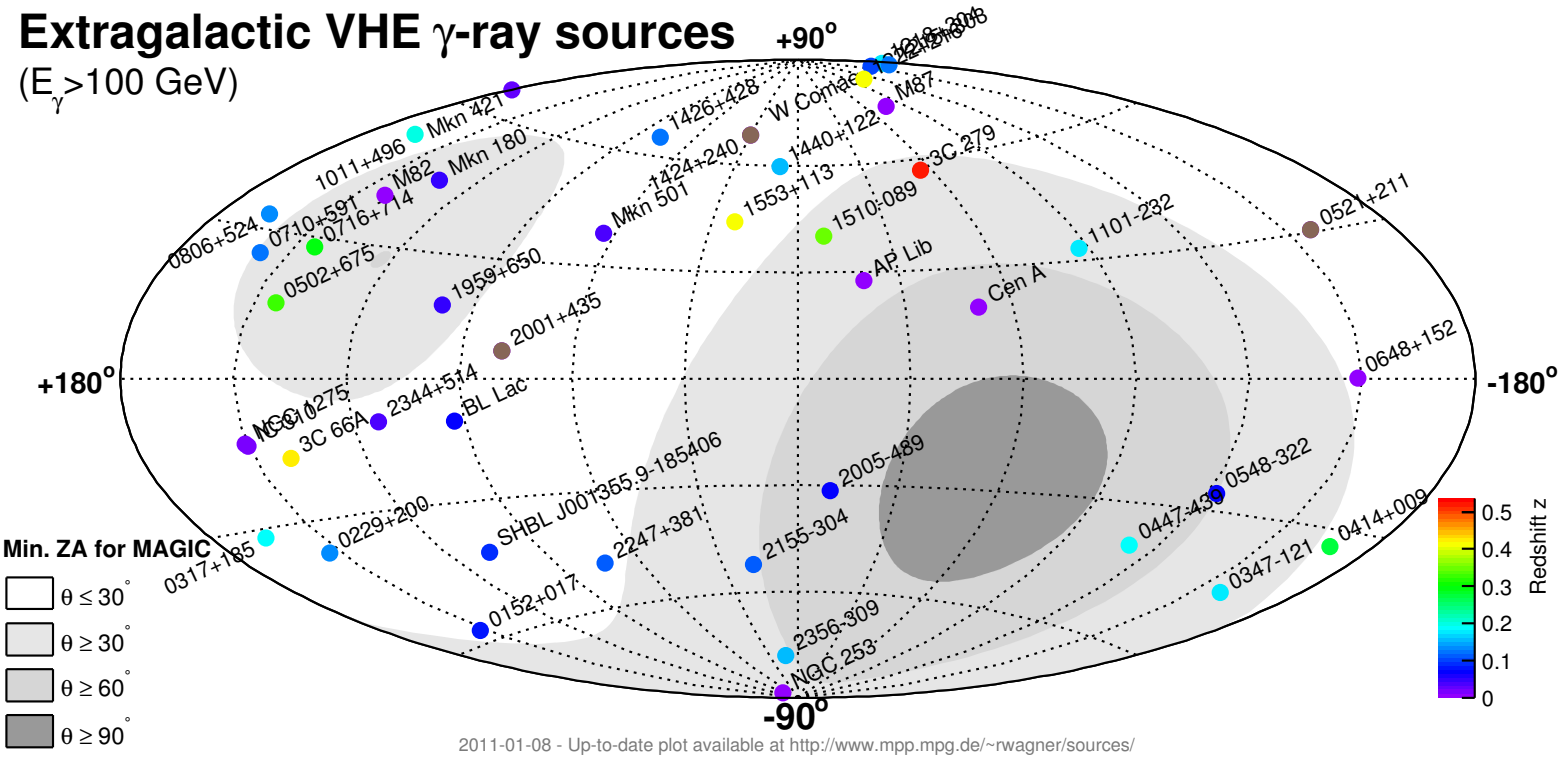

Figure 5.2 Extragalactic skymap in the VHE range up-to-date by January 8, 2011. The sources are color coded by their redshift. It is shown with different gray-shadow regions the sky that is accessible by the MAGIC telescopes. Figure from http://www.mppmu.mpg.de/∼rwagner/sources/

The current theoretical models for the emission by this class of objects are of two kinds: leptonic or hadronic. Both models predict a spectrum with two peaks, the first one localized from radio to X-rays due to synchrotron radiation from relativistic electrons (leptonic model), or protons (hadronic model). However, the second peak has a different nature. While in the leptonic model it is due to inverse Compton (IC) scattering of the same population of electrons that produce the synchrotron peak (Böttcher 2007), in the hadronic model, nuclear photo-disintegration is advocated to explain the second peak (Sikora et al. 2009). (Fig. 5.3 shows typical SEDs for the different types of blazars according to leptonic models, also known as leptonic synchrotron self Compton (SSC) models.) Both models face serious difficulties in explaining intrinsic (i.e., EBL-corrected) VHE power law indexes harder than 1.5, and fail to explain slopes harder than 2/3. The intrinsic spectrum is the spectrum that we would observe if there were no effect from the EBL.

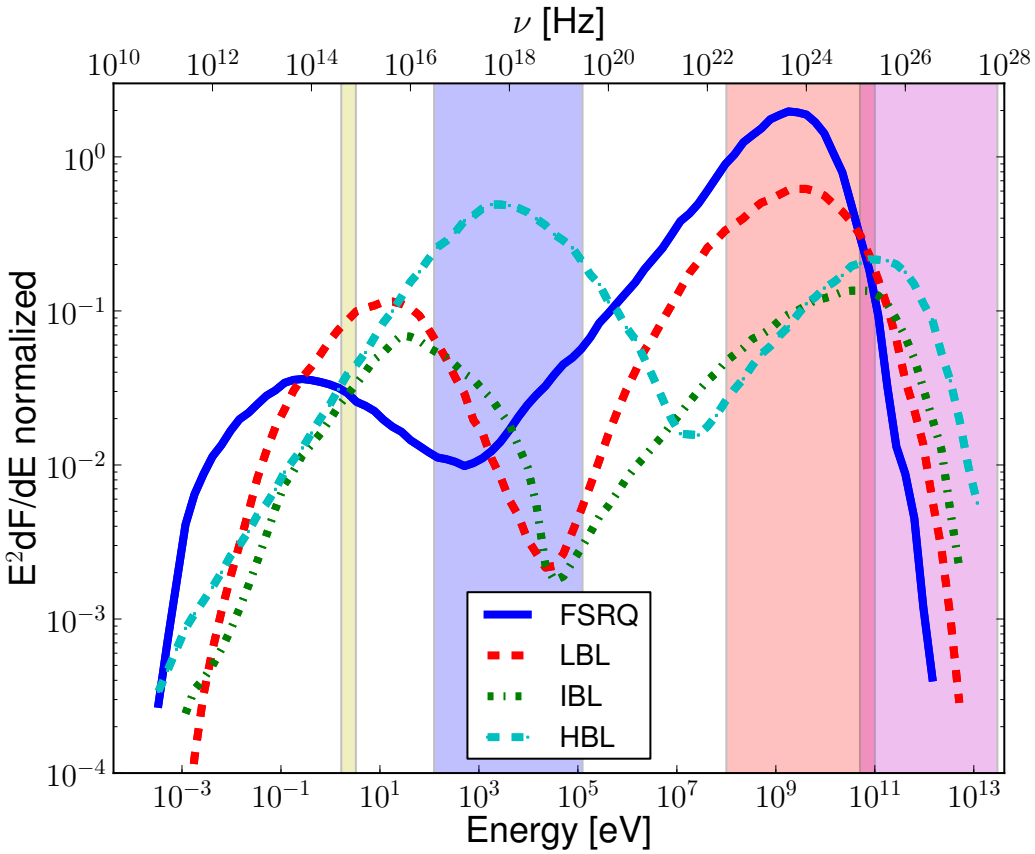

Figure 5.3 Emitted SED from different types of blazars. Different interesting regions are shown as shadow regions, from left to right: optical, X-rays, energy range at which Fermi is sensitive, and energy range at which IACTs are sensitive to. Note the overlap between the Fermi and IACTs observational range.

The EGRET satellite observed AGNs in the local universe (hence not very attenuated), claiming that all of them have spectral indexes $E^{-\Gamma_{int}}$ with $\Gamma_{int} \geq 1.5$ in the high energy regime (Hartman et al. 1999). This result has been confirmed by the Fermi collaboration (within uncertainties), which has published a catalogue of AGNs detected by the Fermi LAT all-sky survey during its first year in operation (Abdo et al. 2010a). From this observational fact, and the theoretical issues above, it is usually conservatively consider that no AGN could have an intrinsic VHE spectrum fitted by a power law with an index harder than 1.5. Some authors such as Katarzyński et al. (2006), Stecker, Baring & Summerlin (2007), Böttcher, Dermer & Finke (2008) and Aharonian et al. (2008) provide some mechanisms within standard physics to reach slopes harder than 1.5, but never harder than $\Gamma_{int} = 2/3$.

The EBL may be constrained using VHE observations of extragalactic sources if their intrinsic emitted spectra are known. As mentioned above, γ-ray photons coming from cosmological distances are attenuated by photon-photon pair production by EBL photons. The cross section of this reaction depends of the product shown in the left side of Eq. 5.1,

$$\sqrt{2\varepsilon E(1-\cos\theta)} \geq 2m_e c^2 \tag{5.1}$$

$$\varepsilon_{th} \equiv \frac{2m_e c^2}{E(1-\cos\theta)} \tag{5.2}$$

where, in the rest-frame at redshift z, E is the energy of the γ photon, ε is the energy of the EBL photon, and θ is the angle of the interaction, which defines an energy threshold ε_{th} for the EBL-photon energy given in Eq. 5.2 with m_e the electron mass.

The cross section peaks at about twice ε_{th}, which produces a peak in the interaction at $\lambda\ [\mu\text{m}] = 1.24E$ [TeV]. From this property, a γ-ray with energy 1 TeV interacts mainly with a photon of the EBL with wavelength $\sim 1\ \mu$m. The details may be found for example in Madau & Phinney (1996).

For a given observed spectrum of a source at redshift z we can find the intrinsic spectrum by assuming a particular EBL model and multiplying by the attenuation factor to *de-absorb* the spectrum using Eq. 5.3, i.e.,

$$\left.\frac{dF}{dE}\right|_{int} = \left.\frac{dF}{dE}\right|_{obs} \exp\left[\tau(E,z)\right] \tag{5.3}$$

where the subscript *obs* means observed, *int* is intrinsic, and $\tau(E,z)$ is the optical depth dependent on the observed energy E of the γ photon for a given EBL photon density and redshift,

$$\tau(E,z) = \int_0^z \left(\frac{dl'}{dz'}\right) dz' \int_0^2 d\mu \frac{\mu}{2} \int_{\varepsilon_{th}}^{\infty} d\varepsilon'\ \sigma_{\gamma\gamma}(\beta') n(\varepsilon', z') \tag{5.4}$$

$$\beta' = \frac{2m_e^2 c^4}{E\varepsilon\mu(1+z)^2} \tag{5.5}$$

with $dl'/dz' = c|dt'/dz'|$ given by Eq. 2.8, $\mu = 1 - \cos\theta$, $\sigma_{\gamma\gamma}$ the photon-photon pair production cross section, β' is given by Eq. 5.5 and n is the proper number density per unit energy of EBL photons[1]. We show in Fig. 5.4 the optical depth and attenuation for sources at $z = 0.1$, 0.3, 0.6 and 1.

Since the EBL produces an attenuation of the VHE spectra, a mere detection of VHE photons (using some constraint on the intrinsic blazar power spectrum) places an upper limit on the EBL density. Some upper limits have been derived by different authors, fitting EBL models to the density level where the condition $\Gamma_{int} = 1.5$ is satisfied, building *ad-hoc* EBL models. We plotted those limits in Fig. 2.13 (Aharonian et al. 2006; Mazin & Raue 2007; Albert et al. 2008). Each of those upper limits comes from the study of different blazars with a different measured energy spectrum. Due to the peak of the interaction previously mentioned, each of the studies constrains different ranges on the EBL. Aharonian et al. (2006) used the VHE spectrum of the blazar 1ES 1101-232 at $z = 0.186$ observed from 0.2-3 TeV, scaling the model by Primack et al. (2001) multiplying the total EBL intensity by a constant to satisfy the $\Gamma_{int} = 1.5$ condition. Albert et al. (2008) used the spectrum of 3C 279 at $z = 0.536$ observed from 0.08-0.5 TeV, scaling a slightly modified model by Kneiske et al. (2002). Mazin & Raue (2007) used a compilation of blazars at different redshifts and observed at different energies, and splines from a grid as EBL densities. They make two different assumptions about the maximum Γ_{int} leading to two different upper limits (called by the authors *realistic* and *extreme*).

We saw in Fig. 2.13 that the *fiducial* EBL model described in Chap. 2 (hereafter all the results in this section are discussed for this, unless otherwise stated) is below the upper limits at all wavelengths, except at the largest wavelengths, where slightly exceeds the limits from the *realistic* case by Mazin & Raue (2007). This fact is discussed in Sec. 5.2 and it is explained why we do not consider this a major problem. Another limit not plotted comes from the blazar 1ES 0229+200 at $z = 0.140$ (Aharonian et al. 2007). Its study set a lower limit in the slope of the local EBL spectrum between 2-10 μm, $\alpha \geq 1.10 \pm 0.25$, to satisfy the limit on AGN's spectra $\Gamma_{int} \geq 1.5$. We remark that they set the limit only on the slope, not on the intensity level. We have fitted our model in that wavelength range, to a power law $\propto \lambda^{-\alpha}$ getting $\alpha = 1.19 \pm 0.07$. Our model is thus compatible with this constraint.

It is also possible to set upper limits on the unknown redshift of blazars assuming an EBL model and finding the redshift by which the EBL-corrected spectrum satisfies $\Gamma_{int} = 1.5$ (Prandini et al. 2010; Yang & Wang 2010). We apply that method to the PG 1553+133 spectrum observed by MAGIC (Albert et al. 2007), assume an EBL-corrected spectrum given by a power law and find an upper limit at $z \leq 0.85 \pm 0.07$ in agreement with the lower limit ($z \geq 0.4$) found by Danforth et al. (2010) using absorption features in the Ly-α forest of the blazar.

As shown in Fig. 5.4, our EBL model implies about the same attenuation as

[1] Attenuation files are publicly available at http://side.iaa.es/EBL/

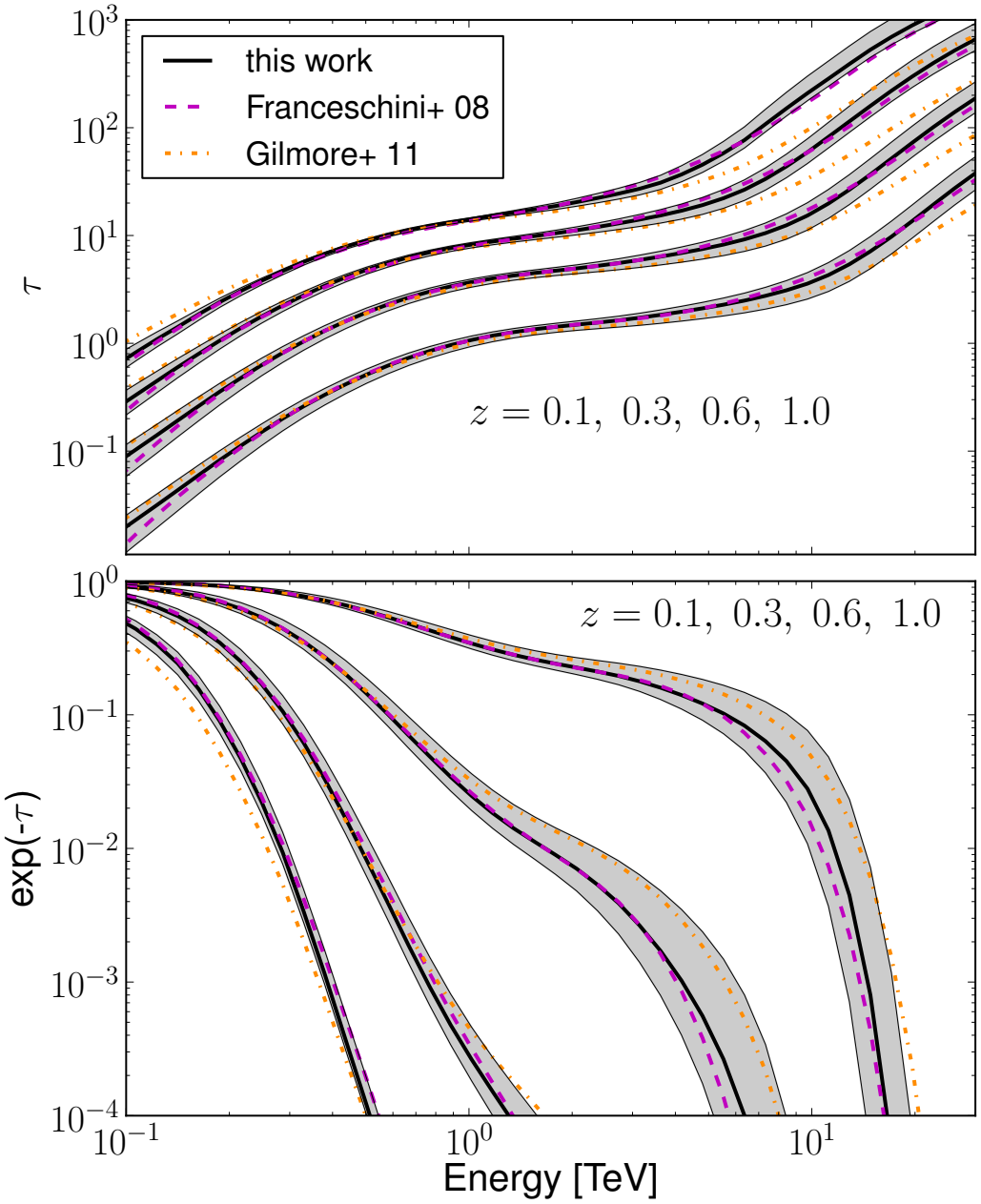

Figure 5.4 *Upper panel*: Optical depth versus observed energy of γ-ray photons for sources at different redshifts (from bottom to top z = 0.1, 0.3, 0.6 and 1), due to the extragalactic background light computed for our model in solid-black line, for Franceschini et al. (2008) in dashed-magenta line, and for Gilmore et al. (2011) in orange-dot-dashed line. *Lower panel*: Flux attenuation versus observed energy of γ-ray photons for fictitious sources at different redshifts (from right to left z = 0.1, 0.3, 0.6 and 1). We have calculated attenuation for the Franceschini et al. (2008) and Gilmore et al. (2011) models using the EBL data provided by the authors. The EBL uncertainties in Fig. 2.13 are propagated to the optical depth and flux attenuation. They are shown here with a shadow region.

other recent models we compare to over all the energy range observed by the current generation of IACTs. Larger transparency than the observationally-based model by FRV08 is found (roughly a factor ~ 2 in flux, but still within the uncertainties) for γ-ray photons with energies between $\sim 6 - 15$ TeV for $z \sim 0.1$, but a factor ~ 2 in flux less transparent than the GSPD11 theoretical approach around ~ 10 TeV. For the large-redshift case, our model predicts about the same attenuation as FRV08, but a factor ~ 1.5 more transparency than GSPD11 for sub-TeV energies. Note that a small difference in the optical depth has large effects on the spectra due to the exponential in Eq. 5.3, e.g., a factor 1.5 in optical depth leads to a factor ~ 5 in attenuation.

5.2 Application of this EBL model to extreme known blazars

We now proceed to test whether the observed spectra of the three most constraining AGNs known in the VHE range due to their hard spectrum, or to their large redshift, satisfy the condition that the intrinsic spectrum corrected by the attenuation derived with our model has $\Gamma_{int} \geq 1.5$. We consider the blazars: Mrk 501 at $z = 0.034$ detected by the HEGRA system of Čerenkov telescopes in 1997 (Aharonian et al. 1999, with a reanalysis by Aharonian et al. 2001), FSRQ 3C 279 at $z = 0.536$ discovered at VHE by MAGIC (Albert et al. 2008), the blazar 3C 66A discovered by VERITAS at $z = 0.444$ (Acciari et al. 2009) and later confirmed by MAGIC (Aleksić et al. 2011a), and the detection of the FSRQ PKS 1222+216 at $z = 0.432$ by MAGIC (Aleksić et al. 2011b). For PKS 1222+216 the official analysis is used here instead of the analysis performed in Chap. 4. All of them were detected in a flaring state. All these blazars are plotted in Fig. 5.5 showing in the legends that the condition $\Gamma_{int} \geq 1.5$ is satisfied. Fig. 5.5 also shows uncertainties from the EBL modeling as well as statistical and systematic errors with a shadow region. The straight red line is the best-fitting power law for every blazar with index Γ_{int}. The first uncertainties in the index are due to the EBL modeling as shown in Fig. 5.4, and the second uncertainties are statistical plus systematic errors in all blazars, except 3C 66A where only statistical errors are shown.

Mrk 501

The highest energy bins in this measurement, where it is observed a significant deviation from a power law (see Fig. 5.5 upper-left panel), are affected by the far-IR EBL at $\lambda > 60$ μm. This is the region of the EBL spectrum where it was found a disagreement with the *realistic* (but not *extreme*) upper limits of Mazin & Raue (2007). The problem comes from the very low statistics and high systematic uncertainties at such high energies (Aharonian et al. 1999). A later reanalysis of the same observation

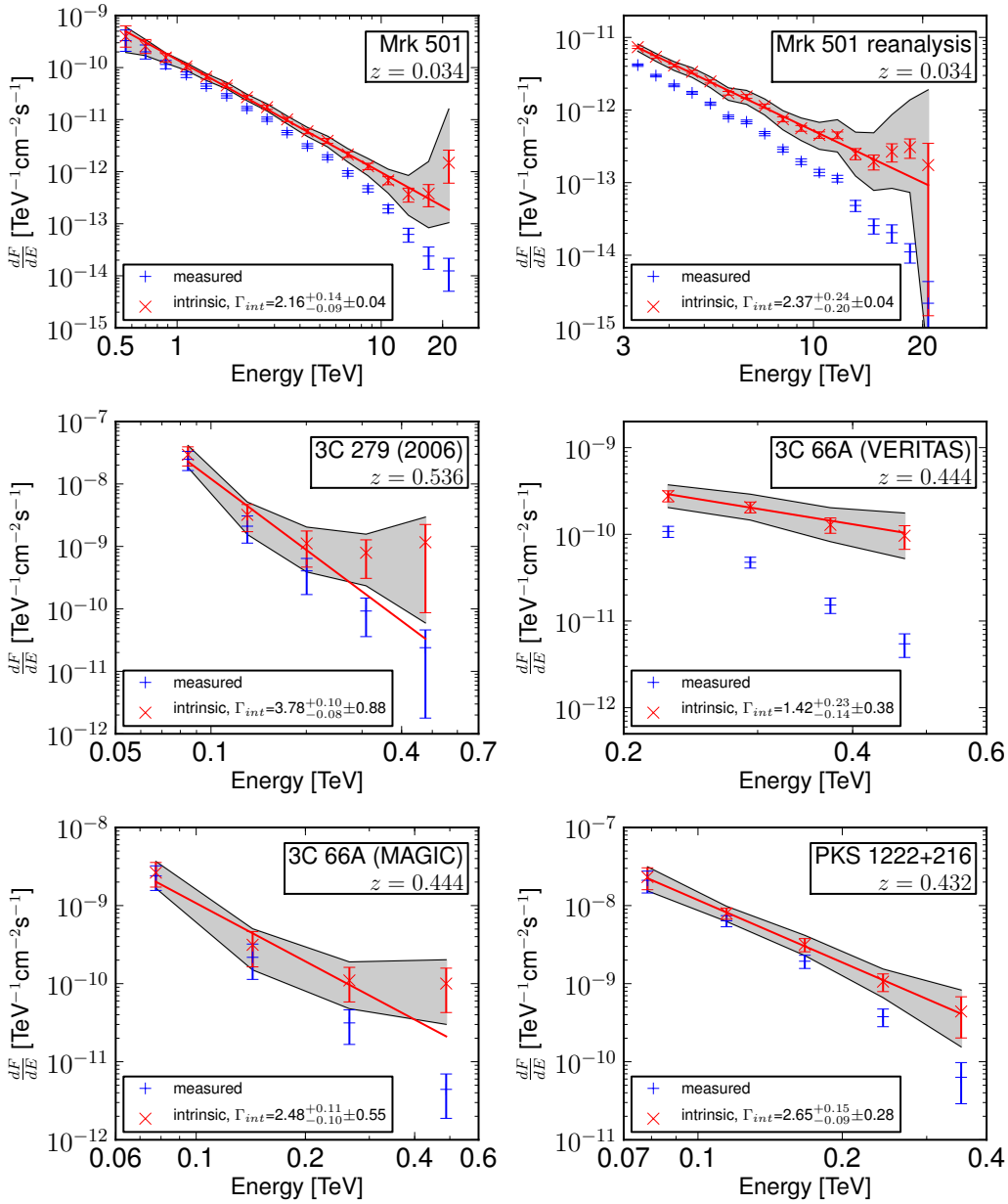

Figure 5.5 Very high energy spectra measured (blue) and EBL-corrected from the attenuation calculated with our EBL model (using the *fiducial* extrapolation for the galaxy SED-type fractions at $z > 1$, in red) of three extreme blazars: Mrk 501 observed in very high state up to energies larger than 20 TeV (upper-left panel, Aharonian et al. 1999) and a reanalysis of the same data (upper-right panel, Aharonian et al. 2001), 3C 279 a FSRQ with the highest redshift ($z = 0.536$) ever detected for a VHE γ-ray source (middle-left panel, Albert et al. 2008), 3C 66A a BL Lac with probably (because its redshift, $z = 0.444$ is not very secure) the highest redshift ever detected for an object of this class (middle-right panel, Acciari et al. 2009 and lower-left panel, Aleksić et al. 2011a), and PKS 1222+216 ($z = 0.432$) another high redshift FSRQ recently discovered by the MAGIC collaboration (Aleksić et al. 2011b).

done in Aharonian et al. (2001) accounts for larger systematic uncertainties as shown in Fig. 5.5 upper right panel.

This exponential behaviour for the highest energy bin was already observed from the first EBL models (e.g., Malkan & Stecker 1998; Primack et al. 1999; Kneiske et al. 2002), whose EBL levels were higher than the more recent ones. This fact was discussed thoroughly in Dwek & Krennrich (2005), and even some exotic explanations such as Lorentz invariance violation (Stecker & Glashow 2001) were proposed. More recent EBL models with a more transparent universe (such as our model, FRV08 and GSPD11) relax such predictions. The solutions to exponential spectra and photon pileup could involve widespread problems with the photon statistics and systematic uncertainties in the observations (as suggests the results from the later reanalysis), or new mechanisms extending the normal SSC model, using external regions close to the γ-ray source with target photons. The EBL uncertainties in the far-IR leading to the attenuation uncertainties at these high energies as shown in Fig. 5.5, might contribute to the solution as well.

Another observed flare with better statistics with the current generation of IACTs up to such high energies as $\sim$ 20 TeV would be very helpful in constraining these possibilities.

3C 279

Fig. 5.5 shows in the middle-left panel the EBL-corrected VHE spectrum for this source for the 2006 campaign. An external photon field providing target photons for IC (such as that provided by a broad-line emission region) might be necessary to explain the flat behavior at the largest energy bins, as discussed in Albert et al. (2008). Instrumental systematic uncertainties might explain this behavior as well. We note here that our model is already matching the lower limits from galaxy counts at the wavelengths where γ-ray attenuation with the observed energies occurs, and a much lower EBL density than the one calculated in this work does not seem realistic. The attenuation uncertainties from the EBL modeling are too low at this redshift and these energies to explain that spectral behaviour.

3C 66A

Fig. 5.5 shows in the middle-right panel and in the lower-left panel the EBL-corrected VHE spectrum for this source from two different observations. The former by VERITAS (Acciari et al. 2009) and the latter by MAGIC (Aleksić et al. 2011a). The EBL-corrected slope is well within the 1σ limit of the $\Gamma_{int} \geq 1.5$ according to the calculated intrinsic index for both cases. It is important to note that the redshift considered for this object is calculated using just one emission line and is thus not very secure (see discussion in Bramel et al. 2005). Its attenuation might be indeed

overestimated if the redshift is lower than assumed.

PKS 1222+216

The interaction of VHE γ-rays with low energy photons of the isotropic EBL is a process with an energy dependent threshold, thus leading to an imprint of the EBL density on the measured VHE γ-ray spectra of extragalactic sources. For PKS 1222+216 ($z = 0.432$), the measured spectrum spans from 70 GeV to 400 GeV probing mostly EBL photons in the range 0.1 - 1 μm (i.e., UV to near-IR) as discussed at the beginning of this chapter. I contributed to the EBL discussion from the detection of this source published in Aleksić et al. (2011b) and briefly presented here.

The EBL constraints using VHE γ-rays are usually derived assuming an intrinsic spectrum of the source (e.g., Aharonian et al. 2006). In FSRQs, the presence of dense radiation fields of soft photons can lead to the internal absorption of VHE γ-rays within the source causing features in the observed data mimicking harder than intrinsic spectra (e.g., Sitarek & Bednarek 2008). However, for realistic spectral distributions of the internal photon fields it should not change the EBL limits significantly (Tavecchio & Mazin 2009). When simultaneous data from Fermi/LAT and IACTs exist, the LAT photon index above few GeV, which is free from internal or external absorptions, can be used to constrain the intrinsic photon index in VHE (e.g., Finke & Dermer 2010; Georganopoulos, Finke & Reyes 2010; Finke & Razzaque 2009) reducing the uncertainties on the assumptions used.

Here, we utilize the simultaneous Fermi/LAT data for PKS 1222+216 to constrain the intrinsic photon index in the VHE, in addition to the test done in Fig. 5.5 where we showed that $\Gamma_{int} > 1.5$. Assuming the EBL absorption by Domínguez et al. (2011) the simultaneous Fermi/LAT and MAGIC spectrum can be described by a broken power law, with parameters $\Gamma_1 = 1.85$ for $E < E_{break}$ and $\Gamma_2 = 2.64$ for $E > E_{break}$ with $E_{break} = 3.6$ GeV. In order to derive upper limits on the VHE γ-ray opacity, we used a method similar to the one utilized by Georganopoulos, Finke & Reyes (2010): the intrinsic spectrum in the VHE regime is assumed to follow the extrapolation of the Fermi/LAT. This is a conservative assumption since in reality the spectrum could be softened with increasing energy due to the intrinsic properties of the source (e.g., reaching the energies corresponding to the maximum energy of the electrons). We use then $\Gamma_{int} = 2.4$ (the hardest spectral index at VHE, which would still be consistent with the Fermi/LAT and MAGIC data) to derive an upper limit (95% confidence level) on the optical depth (τ_{max}) for VHE γ-rays:

$$\tau_{max}(E) = \log\left[\frac{F_{int}(E)}{F_{obs}(E) - 1.64 \times \Delta F(E)}\right] \tag{5.6}$$

where $F_{int}(E)$ is the maximum intrinsic flux at energy E, $F_{obs}(E)$, and $\Delta F(E)$ are the MAGIC measured flux and its error, respectively.

The derived limits on the optical depth are shown in Fig. 5.6 by the black arrows together with a compilation of the predicted optical depths for a source at $z = 0.432$ computed according to recent EBL models. We note that the limits confirm previous constraints on the EBL models in the UV to near infrared regimes derived using VHE (Aharonian et al. 2006; Mazin & Raue 2007; Albert et al. 2008) and HE spectra (Abdo et al. 2010b). Moreover, the constraints on the optical depth become tighter with increasing energy underlying that an intrinsic softening of the PKS 1222+216 spectrum at an energy significantly below 400 GeV is incompatible with these EBL models.

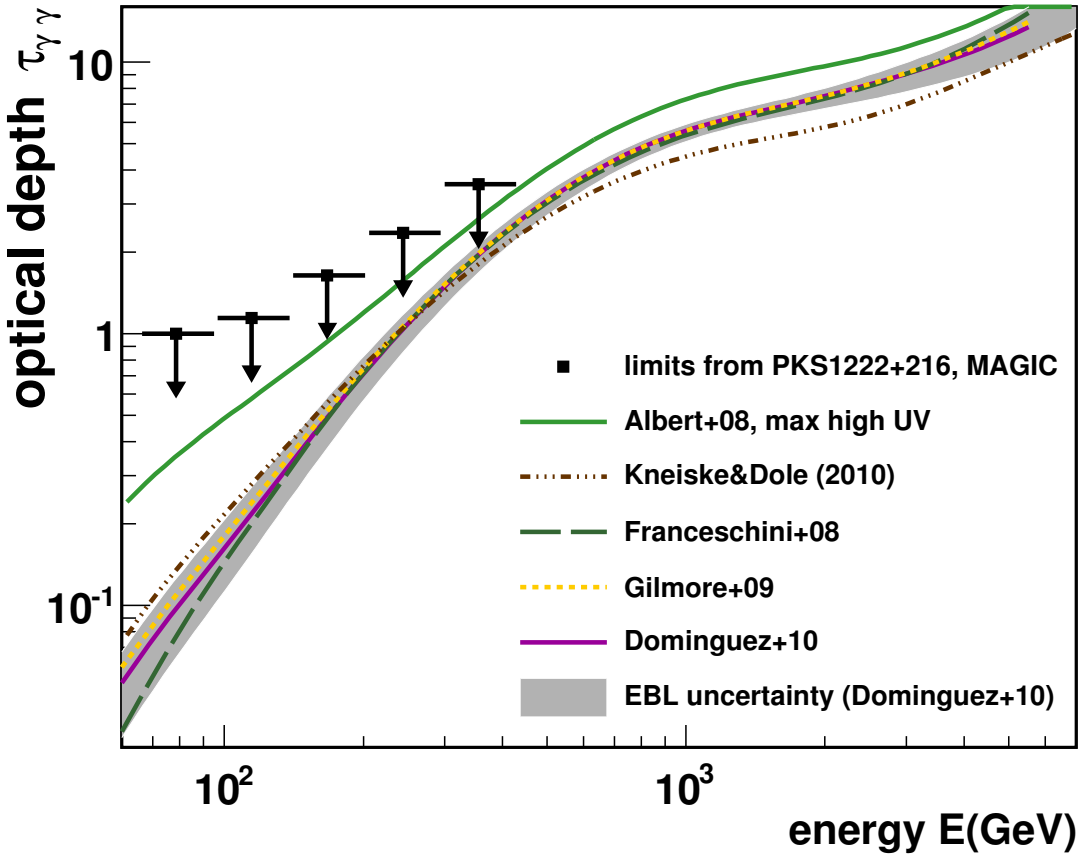

Figure 5.6 Optical depth along the line of sight to PKS 1222+216 ($z = 0.432$) for a range of EBL models and the limits from the MAGIC measurement, assuming the limiting intrinsic photon index $\Gamma_{int} = 2.4$. The gray-shaded area shows the uncertainties in the EBL determination as derived in Domínguez et al. (2011) (see Chap. 2 and Sec. 2.5.1 for a discussion on the uncertainties from the modeling). The computed upper limits on the optical depth (see Sec. 5.2 for details) correspond to 95% confidence limit.

5.3 Conclusions on the limits from blazars

It is concluded from the study of these extreme blazars that our EBL is generally compatible with the hardness of the EBL-corrected slopes expected from theoretical arguments. However, it is clear that a simple SSC model cannot explain any flatness at the highest energies of the EBL-corrected spectra of either Mrk 501 or 3C 279, which suggests that some extension to the model may be necessary such as an external photon region, a better understanding of the IACT systematic uncertainties, or even a revision of the propagation mechanisms mainly through the intergalactic medium (see Sánchez-Conde et al. 2009 and Chap. 6). It is a very interesting result from Fig. 5.4, Fig. 5.5, and Fig. 5.6 that all the realistic EBL models (Franceschini, Rodighiero & Vaccari 2008; Domínguez et al. 2011; Gilmore et al. 2011) show a little spread among each other. Though the EBL models are derived following different approaches, they all seem to agree that most of the sources in the universe which contributed to the EBL are already resolved. In addition, the uncertainties in the recovered unattenuated EBL spectra are dominated by statistical and systematical uncertainties in the observations rather than on EBL modeling (see next section).

5.4 Propagation of the EBL uncertainties to the γ-ray attenuation

As shown in Fig. 5.4 the uncertainties in the attenuation are dependent on the observed γ-ray energy as well as the redshift: the higher the energy or the redshift, the higher the uncertainties in the attenuation. The attenuation uncertainties shown were calculated from the uncertainties in our EBL modeling, which were shown in Fig. 2.13, explained in Sec. 2.4 and will be thoroughly discussed in Sec. 2.5.1. For sub-TeV energies up to around 1 TeV the uncertainties in the flux attenuation are never higher than a factor ~ 2 and generally lower. The uncertainties in the EBL-corrected spectra in this case are dominated by other effects (see indexes in Fig. 5.5). For energies larger than 10 TeV the uncertainties are around a factor of several. The uncertainties in the EBL-corrected spectra up to such high energies due to the EBL modeling are considerable. These high uncertainties are derived from the EBL in the far-IR region due to the very fast increment of the EBL photon density (n, see Eq. 5.4) with longer wavelengths. Observations of sources at low redshift but energies larger than ~ 10 TeV will set constraints on these uncertainties.

6

Axion-like particle imprint in cosmological VHE spectra

6.1 Theoretical background

The existence of axions is predicted by the Peccei-Quinn mechanism, which is currently the most compelling explanation to solve the CP problem in quantum chromo dynamics (QCD) (Peccei & Quinn 1977). Moreover, amongst all the valid candidates proposed to constitute a portion or the totality of the non-baryonic cold dark matter content predicted to exist in the universe, hypothetical non-thermal axions, or in a more generic way, axion-like particles (ALPs), where the mass and the coupling constant are not related to each other, may represent a good option: they might exist in sufficient quantities to account for the estimated dark matter density and they might interact very weakly with the rest of the particles (Raffelt 2005). There is an additional property of ALPs that makes them even more attractive and that could have important implications for its detectability, i.e., they can oscillate into photons and vice-versa in the presence of an electric or magnetic field (Dicus 1978, Sikivie 1983). This is analogous to that predicted to occur between neutrinos of different flavors, and a similar behavior is expected in the case of the recently proposed chameleons as well (Burrage, Davis & Shaw 2009). This characteristic is the main vehicle used at present to carry out an exhaustive search of ALPs by experiments like PVLAS, ADMX, and CAST (Zavattini et al. 2006; Duffy et al. 2006; Andriamonje et al. 2007).

The oscillation of photons to ALPs (and vice-versa) could have important implications for astronomical observations. This argument was first investigated in the optical band by Csáki, Kaloper & Terning (2002), where authors proposed the existence of axions to be the cause of the observed supernova Ia dimming. In this context, the observed dimming might be explained as a result of an efficient photon to axion conversion instead of a cosmic acceleration (albeit this proposal was rejected some time later due to some chromatic problems e.g., Mirizzi, Raffelt & Ser-

pico 2008). Photon/axion oscillations were also studied by the same authors in Csáki et al. (2003) as an alternative explanation for those photons arriving Earth from very distant sources at energies above the GZK cutoff.

Recently, it has been proposed that, if ALPs exist, they could distort the spectra of γ-ray sources, such as AGNs (Sánchez-Conde et al. 2009) and that their effect may be detected by current γ-ray experiments (the Fermi satellite, Gehrels & Michelson 1999; and IACTs, such as VERITAS, HESS, and MAGIC (Weekes et al. 2002; Hinton 2004, Lorenz 2004). In that work the photon/axion mixing was revisited, for the first time handling under the same consistent framework the mixing that takes place inside or near the γ-ray sources together with that one expected to occur in the intergalactic magnetic field (IGMF). In the literature, both effects have been considered separately. Depending on the source dimension, magnetic field, ALP mass and coupling constant, both effects might produce significant spectral distortions, or one effect could be more important than the other. However, the mixing that may happen inside the Milky Way due to galactic magnetic fields was neglected. At present, a concise modeling of this effect is still very dependent on the largely unknown morphology of the magnetic field in the galaxy. Furthermore, in the most idealistic/optimistic case, this effect would produce an enhancement of the photon flux arriving at Earth of about 3% of the initial photon flux emitted by the source (Simet, Hooper & Serpico 2008). This is in contrast with what they found for the IGMFs: although there is also little information on the strength and morphology of the IGMFs, the derived photon/axion mixing in this case they showed to be crucial for a correct interpretation of the observed flux. They came to this conclusion using a conservative value of $B = 0.1$ nG for the IGMF strength, well below the current upper limits of $\sim$ 1 nG. They also carried out a detailed analysis of the mixing when varying IGMF strength and source distance. Results that differed from previously published ones and predictions of effects that were not noted in the literature yet were found.

At energies larger than 10 GeV, and especially above 100 GeV, it will be necessary to properly account for the EBL in the IGMF mixing calculations. As already discussed in Chap. 5, the EBL introduces an attenuation in the photon flux due to e^-e^+ pair production that comes from the interaction of the γ-ray source photons with infrared and optical-UV background photons (Domínguez et al. 2011 and Chap. 5). In Sánchez-Conde et al. (2009) detection prospects and observational strategies for current γ-ray instruments (Fermi and IACTs) were given. Now, in this chapter some of these prospects and strategies will be applied to real VHE observations. This work will be presented and extended in Domínguez, Sánchez-Conde & Prada (2011). Here, the postulated existence of ALPs will be applied to the VHE spectra of the extreme blazars already presented in Chap. 5 and will be discussed as a possible solution to the *too-hard* spectra problem commented at the end of that chapter.

My participation in Sánchez-Conde et al. (2009) includes all the EBL analysis and interpretation, which is further detailed in the next sections.

6.2 The formalism

At present, the Peccei-Quinn mechanism remains as the most convincing solution to solve the CP violation of QCD. As early as in 1978, Weinberg (1978) and Wilczek (1978) realized independently that a consequence of this mechanism is the existence of a pseudo-scalar boson, the axion. One generic property of axions is a two-photon interaction of the form:

$$\mathcal{L}_{a\gamma} = -\frac{1}{4\ M}\ F_{\mu\nu}\overline{F}^{\mu\nu} a = \frac{1}{M}\ \mathbf{E}\cdot\mathbf{B}\ a \tag{6.1}$$

where a is the axion field, M is the inverse of the photon/axion coupling strength, F is the electromagnetic field-strength tensor, $\overline{F}$ its dual, $\mathbf{E}$ the electric field, and $\mathbf{B}$ the magnetic field. The axion has the important feature that its mass m_a and coupling constant are inversely related to each other. There are, however, other predicted states where this relation does not hold; such states are known as ALPs. An important and intriguing consequence of Eq. 6.1 is that ALPs oscillate into photons and vice-versa in the presence of an electric or magnetic field. In fact this effect represents the keystone in ongoing ALP searches carried out by current experiments.

In this work, we will make use of the photon/axion mixing as well, but this time by means of astrophysical magnetic fields. As already mentioned, we will account for the mixing that takes place inside or near the γ-ray sources together with that one expected to occur in the IGMFs. We will do it under the same consistent framework. Furthermore, it is important to remark that it will be necessary to include the EBL in our formalism, in particular in the equations that describe the intergalactic mixing. Its main effect we should remember is an attenuation of the photon flux, especially at energies above 100 GeV. We show in Fig. 6.1 a diagram that outlines our formalism. Very schematically, the diagram shows the travel of a photon from the source to the Earth in a scenario with axions. In the same figure, we show the main physical cases that one could identify inside our formalism: mixing in both the source and the IGMF, mixing in only one of these environments, the effect of the EBL, axion to photon reconversion in the IGMF, etc. A quantitative description of the photon/axion mixing phenomenon in both the source and the IGMFs can be found in the next two subsections.

6.2.1 Mixing inside and near the source

It has been recently proposed that an efficient conversion from photons to ALPs (and vice-versa) could take place in or near some astrophysical objects that should host a strong magnetic field (Hooper & Serpico 2007).

Given a domain of length s, where there is a roughly constant magnetic field and plasma frequency, the probability of a photon of energy E_γ to be converted into an ALP after traveling through it can be written as (Mirizzi, Raffelt & Serpico 2007; Hochmuth & Sigl 2007):

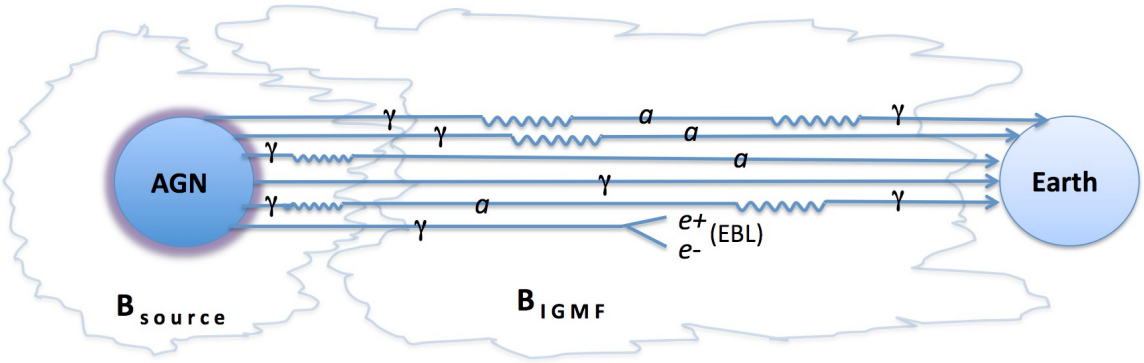

Figure 6.1 Sketch of the formalism used in this work, where both mixing inside the source and mixing in the IGMF are considered under the same consistent framework. Photon to axion oscillations (or vice-versa) are represented by a crooked line, while the symbols γ and a mean γ-ray photons and axions respectively. This diagram collects the main physical scenarios that we might identify inside our formalism. Each of them are schematically represented by a line that goes from the source to the Earth.

$$P_0 = (\Delta_B\ s)^2\ \frac{\sin^2(\Delta_{osc}\ s/2)}{(\Delta_{osc}\ s/2)^2} \tag{6.2}$$

Here Δ_{osc} is the oscillation wave number:

$$\Delta^2_{osc} \simeq (\Delta_{CM} + \Delta_{pl} - \Delta_a)^2 + 4\Delta^2_B, \tag{6.3}$$

Δ_B that gives us an idea of how effective is the mixing, i.e.,

$$\Delta_B = \frac{B_t}{2\ M} \simeq 1.7 \times 10^{-21}\ M_{11}\ B_{mG}\mathrm{cm}^{-1} \tag{6.4}$$

where B_t the magnetic field component along the polarization vector of the photon and M_{11} the inverse of the coupling constant.

Δ_{CM} is the vacuum Cotton-Mouton term, i.e.,

$$\begin{aligned} \Delta_{CM} &= -\frac{\alpha}{45\pi}\left(\frac{B_t}{B_{cr}}\right)^2 E_\gamma \\ &\simeq -1.3 \times 10^{-21}\ B^2_{mG}\left(\frac{E_\gamma}{\mathrm{TeV}}\right)\mathrm{cm}^{-1} \end{aligned} \tag{6.5}$$

where $B_{cr} = m_e^2/e \simeq 4.41 \times 10^{13}$ G the critical magnetic field strength (e is the electron charge).

Δ_{pl} is the plasma term:

$$\Delta_{pl} = \frac{w^2_{pl}}{2E} \simeq 3.5 \times 10^{-20}\left(\frac{n_e}{10^3\mathrm{cm}^{-3}}\right)\left(\frac{\mathrm{TeV}}{E_\gamma}\right)\mathrm{cm}^{-1} \tag{6.6}$$

where $w_{pl} = \sqrt{4\pi\alpha n_e/m_e} = 0.37 \times 10^{-4} \mu\text{eV}\sqrt{n_e/\text{cm}^{-3}}$ the plasma frequency, m_e the electron mass and n_e the electron density.

Finally, Δ_a is the ALP mass term:

$$\Delta_a = \frac{m_a^2}{2E_\gamma} \simeq 2.5 \times 10^{-20} m_{a,\mu eV}^2 \left(\frac{TeV}{E_\gamma}\right) \text{cm}^{-1} \tag{6.7}$$

Note that in Eqs. 6.4-6.7 we have introduced the dimensionless quantities $B_{mG} = B/10^{-3}$ G, $M_{11} = M/10^{11}$ GeV and $m_{\mu eV} = m/10^{-6}$ eV.

Since we expect to have not only one coherence domain but several domains with magnetic fields different from zero and subsequently with a potential photon/axion mixing in each of them, we can derive a total conversion probability (Mirizzi, Raffelt & Serpico 2007) as follows:

$$P_{\gamma\to a} \simeq \frac{1}{3}[1 - \exp(-3NP_0/2)] \tag{6.8}$$

where P_0 is given by Eq.(6.2) and N represents the number of domains. Note that in the limit where $N\ P_0 \to \infty$, the total probability saturates to 1/3, i.e. one third of the photons will convert into ALPs.

It is useful here to rewrite Eq. 6.2 following Hooper & Serpico (2007), i.e.,

$$P_0 = \frac{1}{1 + (E_{crit}/E_\gamma)^2}\ \sin^2\left[\frac{B\ s}{2\ M}\sqrt{1 + \left(\frac{E_{crit}}{E_\gamma}\right)^2}\right] \tag{6.9}$$

so that we can define a characteristic energy, E_{crit}, given by:

$$E_{crit} \equiv \frac{m^2\ M}{2\ B} \tag{6.10}$$

or in more convenient units:

$$E_{crit} \equiv \frac{m_{\mu eV}^2\ M_{11}}{0.4\ B_G} \qquad [\text{GeV}] \tag{6.11}$$

where the subindices refer again to dimensionless quantities: $m_{\mu eV} \equiv m/\mu eV$, $M_{11} \equiv M/10^{11}$ GeV and $B_G \equiv$ B/Gauss; m is the effective ALP mass $m^2 \equiv |m_a^2 - \omega_{pl}^2|$. Recent results from the CAST experiment (Andriamonje et al. 2007) give a value of $M_{11} \geq 0.114$ for axion mass $m_a \leq 0.02$ eV. Although there are other limits derived with other methods or experiments, the CAST bound is the most general and stringent limit in the range 10^{-11} eV $\ll m_a \ll 10^{-2}$ eV.

At energies below E_{crit} the conversion probability is small, which means that the mixing will be small. Therefore we must focus our detection efforts at energies above this E_{crit}, where the mixing is expected to be large (also known as *strong mixing regime*). As pointed out in Hooper & Serpico (2007), in the case of using typical parameters for an AGN in Eq. 6.11, E_{crit} will lie in the GeV range given an ALP mass of the order of $\sim \mu$eV.

	Parameter	3C 279 (2006)	3C 279 (2007)	3C 66A (MAGIC/VERITAS)	PKS 1222+216
Source parameters	R [pc]	0.2	0.3	0.4	0.2
	B [G]	0.15	0.10	0.01	0.15
	n_e [cm^{-3}]	19992	2.22	0.42	19992
	L [pc]	0.02	0.03	0.04	0.02
Intergalactic parameters	z	0.536	0.536	0.444	0.432
	B_{IGM} [nG]	0.1 & 1	0.1 & 1	0.1 & 1	0.1 & 1
	n_{IGM} [cm^{-3}]	10^{-7}	10^{-7}	10^{-7}	10^{-7}
	L_{IGM} [Mpc]	1	1	1	1
ALP parameters	M [GeV]	1.14×10^{10}	1.14×10^{10}	1.14×10^{10}	1.14×10^{10}
	m_a [neV]	$0.42 \leq m_a \leq 1.68$	$0.42 \leq m_a \leq 1.68$	$0.42 \leq m_a \leq 1.68$	$0.42 \leq m_a \leq 1.68$

Table 6.1 Parameters used to calculate the total photon/axion conversion in both the source (for the three AGNs considered, 3C 279, 3C 66A, and PKS 1222+216) and in the IGM. R is one order of magnitude larger than the length of the domains, which is taken as the radius of B region as discussed in Sánchez-Conde et al. (2009), n_e is the electron density in the source, M the photon/ALP coupling constant, and m_a the ALP mass (which is changed in order to obtain E_{crit} within our range of interest). The values related to 3C 279 were obtained from Aleksić et al. (2011c). The 3C 66A parameters are from Abdo et al. (2011). There is no modeling in the bibliography for PKS 1222+216, therefore we use the same parameters that for the 2006 3C 279 one-zone broad line region case from Aleksić et al. (2011c). This choice is made for simplicity, but supported by the fact that PKS 1222+216 is a FSRQ as 3C 279. As for the IGM, n_{IGM} (density of the IGM) was obtained from Peebles (1993), and B_{IGM} (magnetic field in the IGM) was chosen to be well below the upper limit typically given in the literature. See text for details.

To illustrate how the photon/axion mixing inside the source works, we show in Fig. 6.2 an example for an AGN (3C 279 observed by the MAGIC collaboration in 2006, Albert et al. 2008) modeled by the parameters listed in Table 6.1. We use an ALP mass of 1 μeV to obtain a critical energy that lie in the GeV energy range; we get $E_{crit} = 1.9$ GeV according to Eq. 6.11. Note that the main effect just above this critical energy is an attenuation in the total expected intensity of the source. However, note also that the attenuation starts to decrease at higher energies (>1 TeV) gradually. The reason for this behavior is the crucial role of the Cotton-Mouton term at those high energies, which makes the efficiency of the source mixing to decrease as the energy increases (see Eq. 6.5 and how it affects to Eq. 6.3). Indeed, the photon attenuation induced by the mixing in the source completely disappears at energies above around 10 TeV in this particular example. On the other hand, one can see in Fig. 6.2 a sinusoidal behavior just below the critical energy as well as just below the energy at which the source mixing disappears due to the Cotton-Mouton term. However, it must be noted that a) the oscillation effects are small; b) these oscillations only occur when using photons polarized in one direction while, in reality, the photon fluxes are expected to be rather non-polarized; and c) the above given expressions are approximations and actually only their asymptotic behavior should be taken as exact and well described by the formula. Therefore, the chances of observing sinusoidally-varying energy spectra in astrophysical source, due to photon/axion oscillations, are essentially zero.

6.2.2 Mixing in the IGMF

The strength of the IGMFs is expected to be many orders of magnitude weaker (∼nG) than that of the source and its surroundings (∼G). Consequently, as described by Eq. 6.11, the energy at which photon/axion oscillation occurs in the IGM is many orders of magnitude larger than that at which oscillation can occur in the source and its vicinity. Despite the low magnetic field $\mathbf{B}$, the photon/axion oscillation can take place due to the large distances, since the important quantity defining the probability for this conversion is the product $\mathbf{B} \times \mathbf{s}$, as described by Eq. 6.9. Assuming $B \sim$0.1 nG or 1 nG, and $M_{11} = 0.114$ (coincident with the upper limit reported by CAST in Andriamonje et al. 2007), then the effect can be observationally detectable ($E_{crit} <$ 1 TeV) only if the ALP mass is $m_a < 6 \times 10^{-10}$ eV. If m_a was larger than this value, then the consequences of this oscillation could not be probed with the current generation of IACTs, that observe up to few tens of TeV [1].

It is important to stress that at energies larger than 10 GeV, and especially larger than 100 GeV, besides the oscillation to ALPs, the photons should also be affected by the diffuse radiation from the EBL. The EBL introduces an attenuation in the

[1] The next generation of IACTs (namely CTA Doro 2009) aim for an order of magnitude of improvement at the highest energies, reaching few hundreds of TeV; but that instrument will not be in operation till 2015 or later.

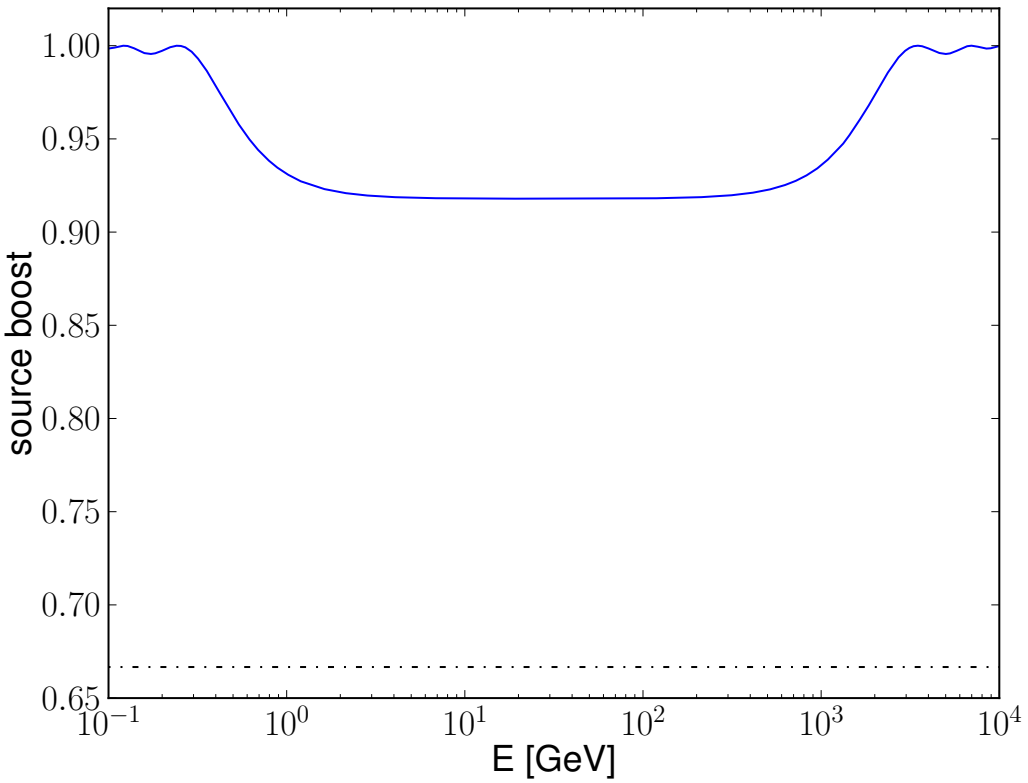

Figure 6.2 Example of photon/axion oscillations inside the source or vicinity, and its effect on the source intensity (solid-blue line), which was normalized to 1 in the figure. We used the parameters given in Table 6.1 to model the AGN (3C 279 observed in 2006 by the MAGIC collaboration, Albert et al. 2008) source, but we adopted an ALP mass of 1 μeV. This gives $E_{crit} = 1.9$ GeV. The dot-dashed line represents the maximum (theoretical) attenuation given by Eq. 6.8, and equal to 1/3.

photon flux due to $e^{-}e^{+}$ pair production that comes from the interaction of the γ-ray source photons with infrared and optical-UV background photons for the energies under consideration (see Chap. 5). Therefore, it will be necessary to modify the above equations to properly account for the EBL in our calculations. These equations can be found in Csáki et al. (2003), where the photon/axion mixing in the IGMF was also studied, although for other purposes and a different energy range. We note that the same equations were also used in de Angelis, Roncadelli & Mansutti (2007) to study for the first time the photon/axion mixing in the presence of IGMFs for the same energy range that we are considering in this work.

There is little information on the strength and morphology of the IGMFs. As for the morphology, several authors reported that space should be divided into several

domains, each of them with a size for which the magnetic field is coherent. Different domains will have randomly changing directions of **B** field of about the same strength (Kronberg 1994; Furlanetto & Loeb 2001). The IGMF strength is constrained to be smaller than 1 nG (Grasso & Rubinstein 2001), which is somewhat supported by the estimates of ∼0.3-0.9 nG that can be inferred (de Angelis, Persic & Roncadelli 2008) from recent observations of the Pierre Auger Observatory (Abraham et al. 2008). On the other hand, there is controversy on the possibility of generating such a strong magnetic field. Detailed simulations yield IGMFs of the order of 0.01 nG so that they can later reproduce the measured **B** fields in nearby galaxy clusters (Sigl, Miniati & Enßlin 2004; Dolag et al. 2005). Given this controversy, we decided to use 0.1 nG as well as 1 nG in our calculations.

In our calculations, we assume that the photon beam propagates over N domains of a given length, the modulus of the magnetic field **B** roughly constant in each of them. We will take, however, randomly chosen orientations, which in practice will be also equivalent to a variation in the strength of the component of the magnetic field involved in the photon/axion mixing. If the photon beam is propagating along the y axis, the oscillation will occur with magnetic fields in the x and z directions since the polarization of the photon can only be along those axis. Therefore, we can describe the beam state by the vector (γ_x, γ_z, a). The transfer equation will be, according to Csáki et al. (2003):

$$\begin{pmatrix} \gamma_x \\ \gamma_z \\ a \end{pmatrix} = \mathrm{e}^{iEy} \left[T_0 \, \mathrm{e}^{\lambda_0 y} + T_1 \, \mathrm{e}^{\lambda_1 y} + T_2 \, \mathrm{e}^{\lambda_2 y} \right] \begin{pmatrix} \gamma_x \\ \gamma_z \\ a \end{pmatrix}_0 \tag{6.12}$$

where:

$$\begin{aligned} \lambda_0 &\equiv -\frac{1}{2\,\lambda_\gamma}, \\ \lambda_1 &\equiv -\frac{1}{4\lambda_\gamma} \left[1 + \sqrt{1 - 4\,\delta^2} \right] \\ \lambda_2 &\equiv -\frac{1}{4\,\lambda_\gamma} \left[1 - \sqrt{1 - 4\,\delta^2} \right] \end{aligned} \tag{6.13}$$

$$T_0 \equiv \begin{pmatrix} \sin^2\theta & -\cos\theta\sin\theta & 0 \\ -\cos\theta\sin\theta & \cos^2\theta & 0 \\ 0 & 0 & 0 \end{pmatrix} \tag{6.14}$$

$$T_1 \equiv \begin{pmatrix} \frac{1+\sqrt{1-4\,\delta^2}}{2\sqrt{1-4\,\delta^2}}\cos^2\theta & \frac{1+\sqrt{1-4\,\delta^2}}{2\sqrt{1-4\,\delta^2}}\cos\theta\sin\theta & -\frac{\delta}{\sqrt{1-4\,\delta^2}}\cos\theta \\ \frac{1+\sqrt{1-4\,\delta^2}}{2\sqrt{1-4\,\delta^2}}\cos\theta\sin\theta & \frac{1+\sqrt{1-4\,\delta^2}}{2\sqrt{1-4\,\delta^2}}\sin^2\theta & -\frac{\delta}{\sqrt{1-4\,\delta^2}}\sin\theta \\ \frac{\delta}{\sqrt{1-4\,\delta^2}}\cos\theta & \frac{\delta}{\sqrt{1-4\,\delta^2}}\sin\theta & -\frac{1-\sqrt{1-4\,\delta^2}}{2\sqrt{1-4\,\delta^2}} \end{pmatrix}$$

$$T_2 \equiv \begin{pmatrix} -\frac{1-\sqrt{1-4\,\delta^2}}{2\sqrt{1-4\,\delta^2}}\cos^2\theta & -\frac{1-\sqrt{1-4\,\delta^2}}{2\sqrt{1-4\,\delta^2}}\cos\theta\sin\theta & \frac{\delta}{\sqrt{1-4\,\delta^2}}\cos\theta \\ -\frac{1-\sqrt{1-4\,\delta^2}}{2\sqrt{1-4\,\delta^2}}\cos\theta\sin\theta & -\frac{1-\sqrt{1-4\,\delta^2}}{2\sqrt{1-4\,\delta^2}}\sin^2\theta & \frac{\delta}{\sqrt{1-4\,\delta^2}}\sin\theta \\ -\frac{\delta}{\sqrt{1-4\,\delta^2}}\cos\theta & -\frac{\delta}{\sqrt{1-4\,\delta^2}}\sin\theta & \frac{1+\sqrt{1-4\,\delta^2}}{2\sqrt{1-4\,\delta^2}} \end{pmatrix} \tag{6.15}$$

θ being the angle between the x-axis and $\mathbf{B}$ in each single domain. δ a dimensionless parameter equal to:

$$\delta \equiv \frac{B\,\lambda_\gamma}{M} \simeq 0.11 \left(\frac{B}{10^{-9}\,\mathrm{G}}\right)\left(\frac{10^{11}\,\mathrm{GeV}}{M}\right)\left(\frac{\lambda_\gamma}{\mathrm{Mpc}}\right) \tag{6.16}$$

that represents the number of photon/axion oscillations within the mean free path of the photon λ_γ. Notice that if there was no EBL, the quanta beam would be equipartitioned between the ALP component and the two photon polarizations after crossing a large number of domains. However, the EBL introduces an energy dependent mean free path λ_γ for the photon.

We fix the λ_γ parameter using the model already described in Chap. 2. From here, we obtain λ_γ as the distance given by the so-called γ-ray horizon (see Fig. 6.3) for the energy considered. Additionally, we have to take into account that the energy of each photon will change continuously for a photon traveling towards us from cosmological distances, due to the cosmological redshift. This effect may have a very important role in the calculations of the photon/axion mixing, since e.g., for a source at a distance of 1000 Mpc (i.e., $z \sim 0.3$) every photon arrives at Earth with 30% less energy. We account here for this effect for the first time in the literature by computing at each step (distance) the new energy of the photon due to cosmological redshift, and then using this new energy as the input energy needed for the calculation of λ_γ. We did not include in the formalism, however, those secondary photons that may arise from the interaction of the primary source photons with the EBL (Essey et al. 2010).

Fig. 6.4 and Fig. 6.5 shows two examples on how the ALP mixing works only in the IGM and taking into account both the effect within the source and through the IGM, respectively. Further details on the whole formalism may be found in Sánchez-Conde et al. (2009).

Thus to recap the photon/ALP mixing is dependent on the following parameters:

- ALP: the ALP mass m_a, the photon/ALP coupling constant M.

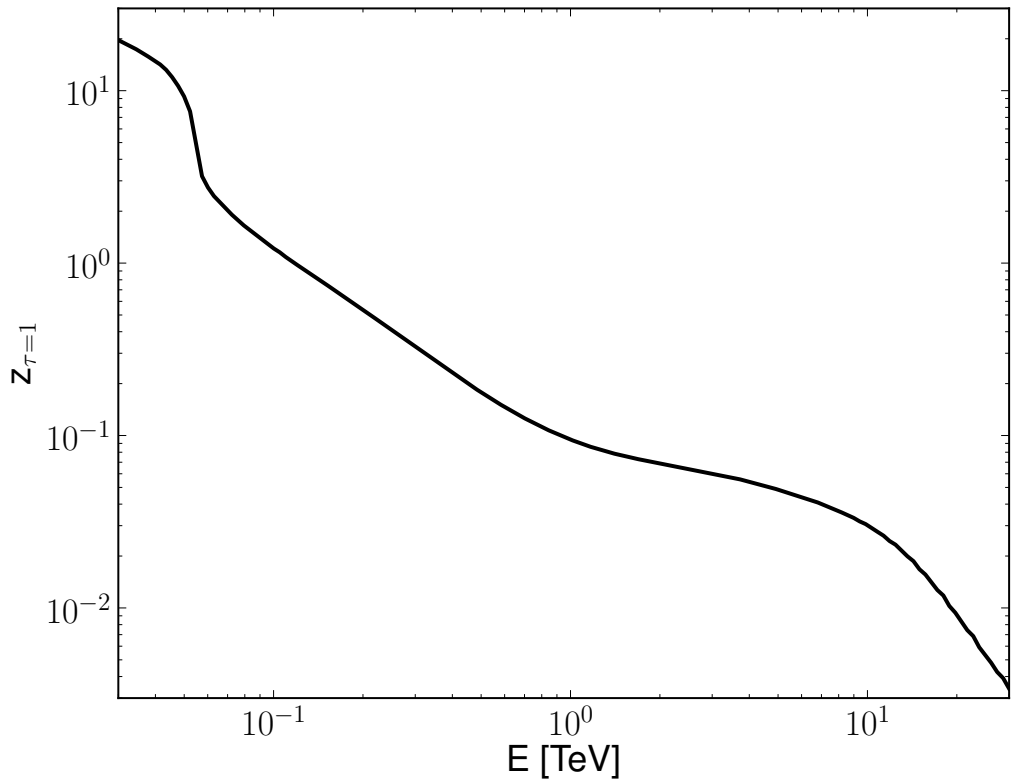

Figure 6.3 γ-ray horizon for the EBL model described in Chap. 2. It is defined as the redshift at which, for a given energy E, the optical depth τ is the unity.

- Source: magnetic field intensity B (equal for all the possible domains), jet radius R, electron density n_e.
- IGM: magnetic field intensity B_{IGM}, distance to the source z, electron density n_{IGM}, EBL spectral intensity.

6.3 Application to extreme known blazars

In this section, we aim the detection of intensity boosts, due to the existence of ALPs, expected to be present in extragalactic spectra observed by IACTs (shown e.g., in Fig. 6.5 at the highest energies). Note that other approaches might be taken as well, such as detecting the drop in intensity at E_{crit} shown also in Fig. 6.5. The latter strategy will be followed elsewhere.

Our methodology for studying any possible hint of signature introduced by ALPs in observed VHE spectra is based on a few assumptions:

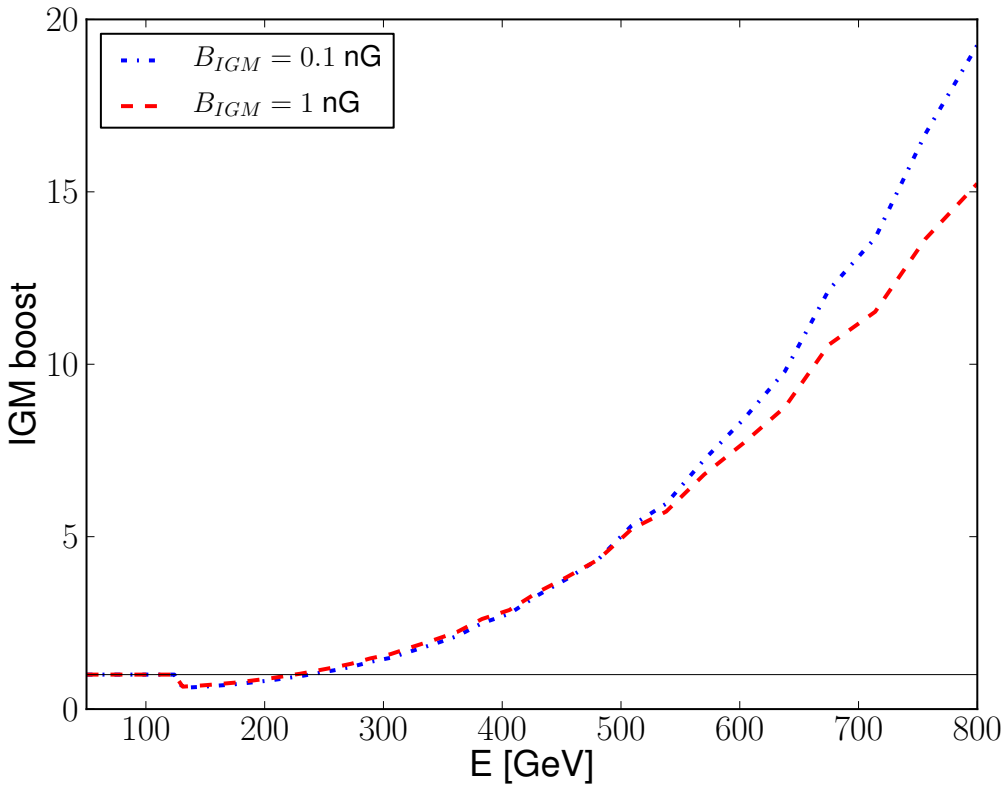

Figure 6.4 Boost factor in the IGM introduced by the existence of ALP versus energy of the γ-ray photon. We here show the case corresponding to $E_{crit} = 125$ GeV and two values of the IGMF, namely $B_{IGM} = 0.1$ nG (blue) and $B = 1$ nG (red). We used 3C 279 at $z = 0.536$ (Albert et al. 2008) as the source of the γ-ray photons. The results for this AGN will be described in detail in Sec. 6.3. The thin solid black line is the unity, i.e., no effect in the spectrum induced by ALPs.

(i) The intrinsic spectra emitted from the sources are well described by simple power laws, which is a good approximation for the relatively small energy ranges considered in the blazars studied here.

(ii) M_{11} has an optimistic value, so that we can get the maximum photon/ALP oscillation, but still within present experimental limits.

(iii) The value E_{crit} lies in the energy range measurable by IACTs.

(iv) The EBL is well known and given by the model described in Chap. 2, which is already supported by the convergence of our results and other observational works such as Franceschini, Rodighiero & Vaccari 2008). This is summarized in Chap. 7.

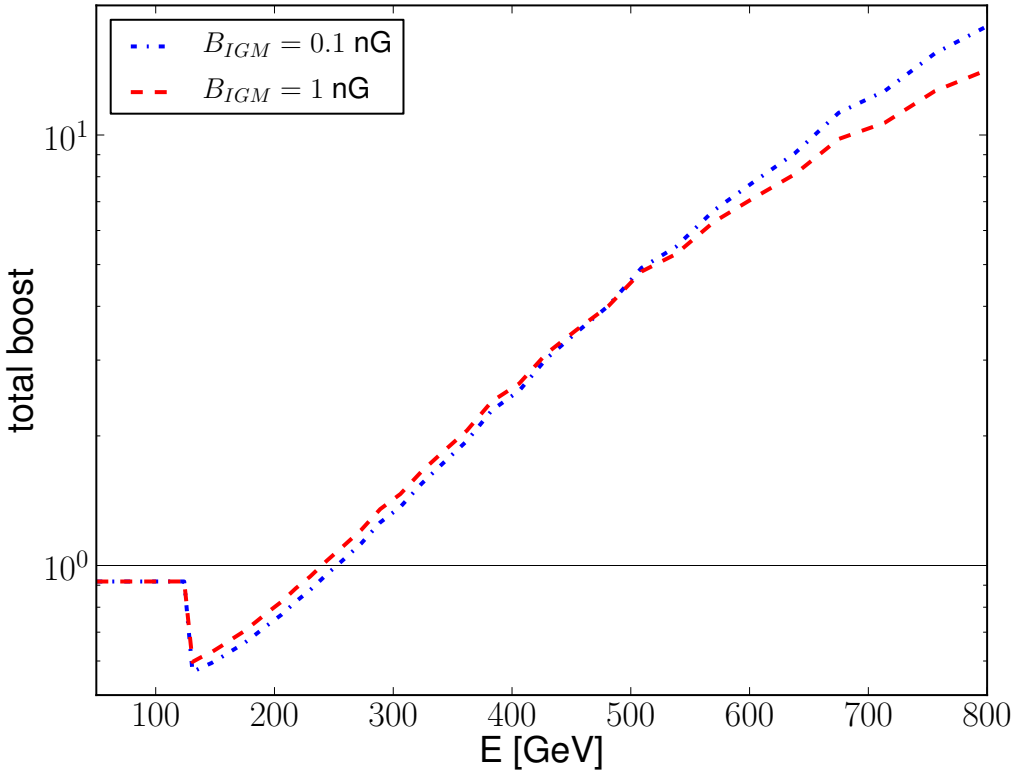

Figure 6.5 Total boost factor introduced by the existence of ALP versus energy of the γ-ray photon. We here show the case corresponding to $E_{crit} = 125$ GeV and two values of the IGMF, namely $B_{IGM} = 0.1$ nG (blue) and $B = 1$ nG (red). We used 3C 279 at $z = 0.536$ (Albert et al. 2008) as the source of the γ-ray photons. The results for this AGN will be described in detail in Sec. 6.3. The thin solid black line is the unity, i.e., no effect in the spectrum induced by ALPs. This time the y axis is plotted in logarithmic scale to highlight the effect of photon/ALP mixing in the source, which introduces a flux attenuation at those energies below E_{crit}.

The effect of ALPs, on γ-rays being emitted by the sources, are computed:

(i) Within the source: modeling every source using the best fit to a SSC model (see Chap. 5) from the bibliography. These are calculated using multiwavelength observations.

(ii) Through the IGM: two different values of $B_{IGM} = 0.1$ nG and $B_{IGM} = 1$ nG are used due to its large uncertainties at present.

(iii) The value of the ALP mass m_a is chosen in combination with B_{IGM} in order to end up with a value of E_{crit} within the energy range of every measured spectrum.

These critical energies range from 50 to 800 GeV and were computed in steps of 75 GeV.

The relevant parameters are described in Table 6.1. We now carefully describe our methodology when applied to 3C 279, which was later repeated for other potentially interesting blazars according to their high redshift.

3C 279

We show in Fig. 6.6 and Fig. 6.7 the effect of ALPs on the VHE data from 3C 279 ($z = 0.536$). These spectra were measured by the MAGIC collaboration in two different epochs (Albert et al. 2008; Aleksić et al. 2011c) when this FSRQ was in different flaring states. To model the mixing within the source, we use the SSC parameters given for both cases in Aleksić et al. 2011c. For the 2006 observations the one-zone broad line region is used, while we choose the two-zone VHE model for the 2007 data. Different steps are followed in order to obtain the final results. These steps are explicitly shown in Fig. 6.6 and are the following (note that only the last step is plotted from Fig. 6.7 on):

Step 1) The measured VHE spectrum (blue crosses) is corrected by both the effect from EBL (green circles), and EBL plus ALPs (red squares). The case with $E_{crit} = 200$ GeV and $B_{IGM} = 0.1$ GeV is plotted in Fig. 6.6 as an example.

Step 2) Both corrected (or de-absorbed) spectra are fitted to simple power laws. The spectral indexes and the $\chi^2_r = \chi^2/n$ of the fits are shown (with n degrees of freedom).

Step 3) The best-fit power laws obtained from Step 2 are then absorbed again by EBL (solid green line), and EBL plus ALPs (solid red line). It is noticeable the drop in flux at E_{crit} (in this particular case 200 GeV) related with that drop at E_{crit} previously shown in Fig. 6.5. This step is done in order to check how well the measured spectrum is recovered in the cases accounting for only the EBL effect and including the ALP effect as well. The reduced χ^2 labeled in the figure corresponds to the corrected best-fit power law given in Step 2.

Step 4) Steps 1 to 3 are then repeated by varying E_{crit} in 75 GeV steps within the energy range in consideration for two different values of B_{IGM}. The best fit among all the cases is plotted here as a solid red line. The two most extreme cases bracket the shadow region. For this particular source, the best fit is obtained for $E_{crit} = 125$ GeV. Note that this is indeed a better fit than the spectrum only considering the EBL attenuation.

The only source parameter that we need and that is not directly given in Aleksić et al. 2011c is n_e (electron density). To calculate this, Eq. 6.17 is used (F. Tavecchio,

MAGIC collab., private communication):

$$n_e = \int_{\gamma_{min}}^{\gamma_b} K\gamma^{-n_1} d\gamma + \int_{\gamma_b}^{\gamma_{max}} K\gamma^{-n_2} d\gamma \tag{6.17}$$

K is a normalization factor in the electron distribution, n_1 and n_2 are the spectral indexes of the broken power law describing the electron distribution between γ_{min} and γ_{max} with a break at γ_b.

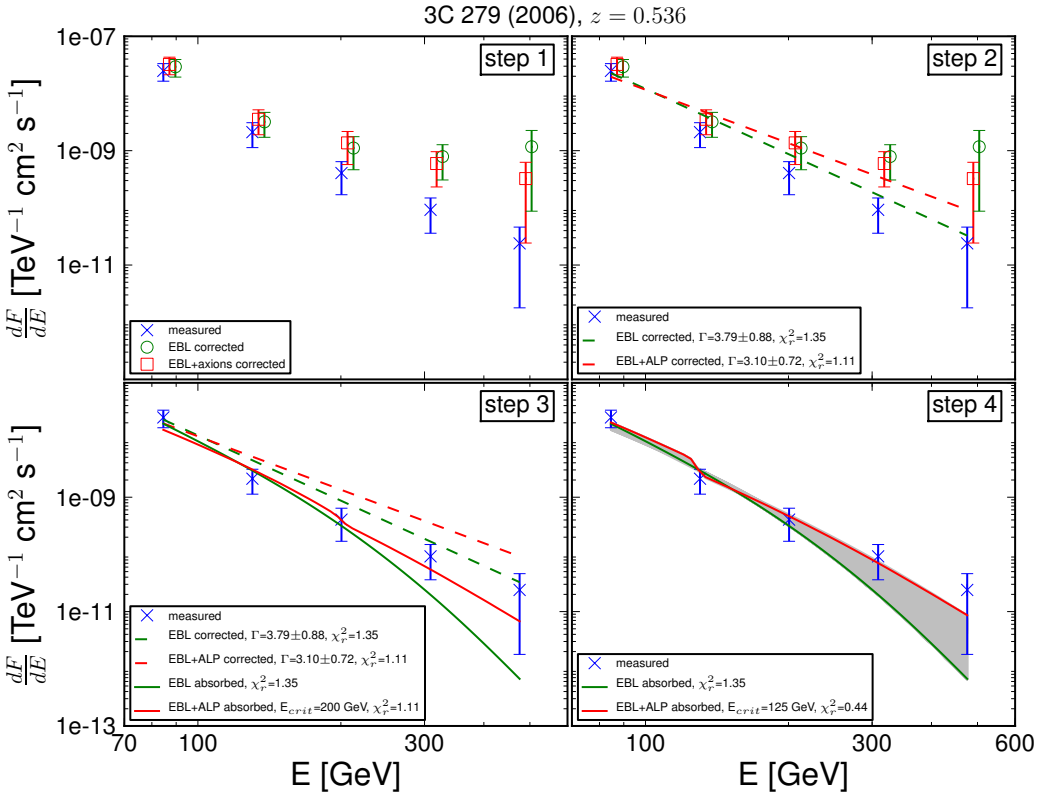

Figure 6.6 Effect of ALPs in the 3C 279 spectrum obtained from 2006 MAGIC data (Albert et al. 2008). See the text for a detailed explanation on every given step.

3C 66A

The same procedure described above for the previous blazar is followed here. 3C 66A ($z = 0.444$) was observed in a flaring state by the Very Energetic Radiation Imaging Telescope Array System (VERITAS) collaboration (Acciari et al. 2009) and more recently by the MAGIC collaboration (Aleksić et al. 2011a). As mentioned in Chap. 5, the redshift considered for this object is calculated using just one emission line and is

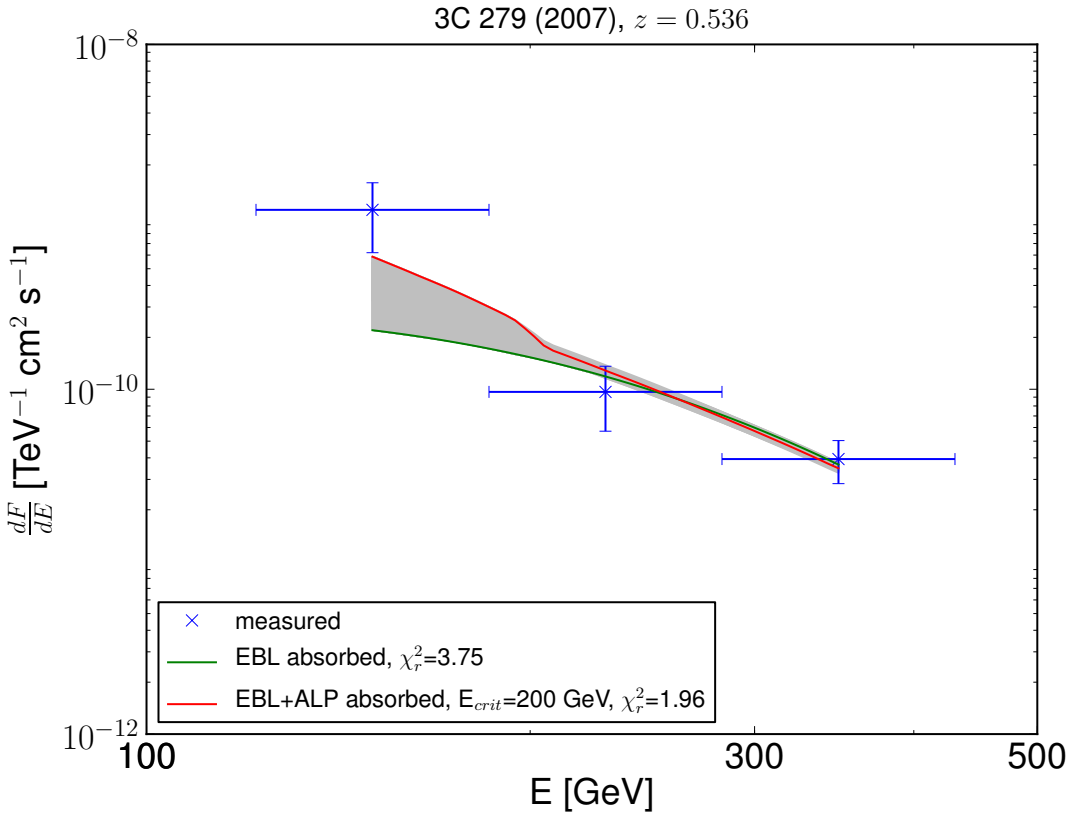

Figure 6.7 Effect of ALPs in the 3C 279 spectrum obtained from 2007 MAGIC data. In blue, the spectral data as measured by the MAGIC Collaboration (Aleksić et al. 2011c). These data are corrected by EBL absorption and a power law is fitted to the corrected points. Then, this power law is absorbed by EBL again leading to the green line. The measured data are also corrected by EBL absorption taking into account the effect of ALPs. The points corrected in this way are later affected by the EBL plus photon/ALP mixing leading to the red line (see text and Fig. 6.6 for further details). Note that the case where ALPs are considered is a better fit to the measured points rather than the case where only EBL absorption is accounted for.

thus not very secure (see discussion in Bramel et al. 2005). We model the source using the parameters given in Table 6.1, which were extracted from Abdo et al. (2011) and were computed by the authors using a SSC model. As in the previous case, the only source parameter that we need and that is not directly given is n_e (electron density). This time to calculate this quantity from the parameters given in Abdo et al. (2011) Eq. 6.18 is used (L. Reyes, VERITAS collab., private communication).

$$L_e = D^2 \pi L^2 c m_e c^2 \int_0^\infty n_e(\gamma) \gamma d\gamma \sim D^2 \pi L^2 c n_e \gamma_{min} m_e c^2 \tag{6.18}$$

Where L_e is the luminosity of the electron population, c is the speed of light, m_e the electron mass, D the Doppler factor, L the radius of the B region, and γ_{min} is the low energy cutoff. The assumption that most of the electron energy is at the lower energies (close to γ_{min}) has been used, which is a good approximation given the power law shape of the electron distribution.

Fig. 6.8 and Fig. 6.9 show the spectrum as measured by VERITAS and MAGIC, respectively. In both figures, we use a color-coded and plot the curves in a way similar to that given in Fig. 6.6 for 3C 279. In the case of the spectrum measured by VERITAS both fits (with and with no ALP effect) represent good fits. This is important, as it represents a good check of our ALP formalism: in those cases where the data are well understood and reproduced by conventional physics (regarding EBL and source modeling), ALPs should not introduce any additional effect and should therefore be irrelevant if included, exactly as it happens in Fig. 6.8. However, in the case of the spectrum measured by MAGIC (Fig. 6.9), it is obvious that the one considering the existence of ALPs is a better fit.

PKS 1222+216

The same procedure described above for the previous blazar is followed here. The FSRQ PKS 1222+216 ($z = 0.432$) was observed in a flaring state by the MAGIC collaboration (Aleksić et al. 2011b). We model the source using the same parameters that were used for 3C 279 given in Table 6.1, since there is no a precise multiwavelength modeling of this blazar yet. We use a color-coded and plot the curves in a way similar to that given in Fig. 6.6 for 3C 279. As in the case of the 3C 66A spectrum measured by VERITAS (Fig. 6.8) both fits (with and with no ALP effect) represent good fits. This is important, as discussed for 3C 66A, as it represents a good check of our ALP formalism.

Discussion and future work

We have shown a plausible alternative explanation to the turn up observed at the highest energies in the VHE spectra corrected by EBL absorption of the most distant blazars (see Fig. 5.5). This feature is indeed challenging for the current understanding on the emission mechanisms in blazars and/or the propagation of VHE photons through the IGM. While the spectra corrected only by EBL absorption hardly describe observations, the spectra corrected taking into account the existence of ALPs in all the cases presented is a better fit. It is noticeable that all the blazars roughly agree on the E_{crit} that best fit the data (of the order of ~ 100 GeV).

We do not claim to have shown that ALPs indeed exist. Others possible explanations within standard physics to the turn up in the VHE spectra might exist such as large systematic and statistical uncertainties in the measurements or γ-ray photons from secondary interactions (Essey et al. 2010). A larger source statistics and a more detailed study is needed, but we aimed here to show that the ALP possibility

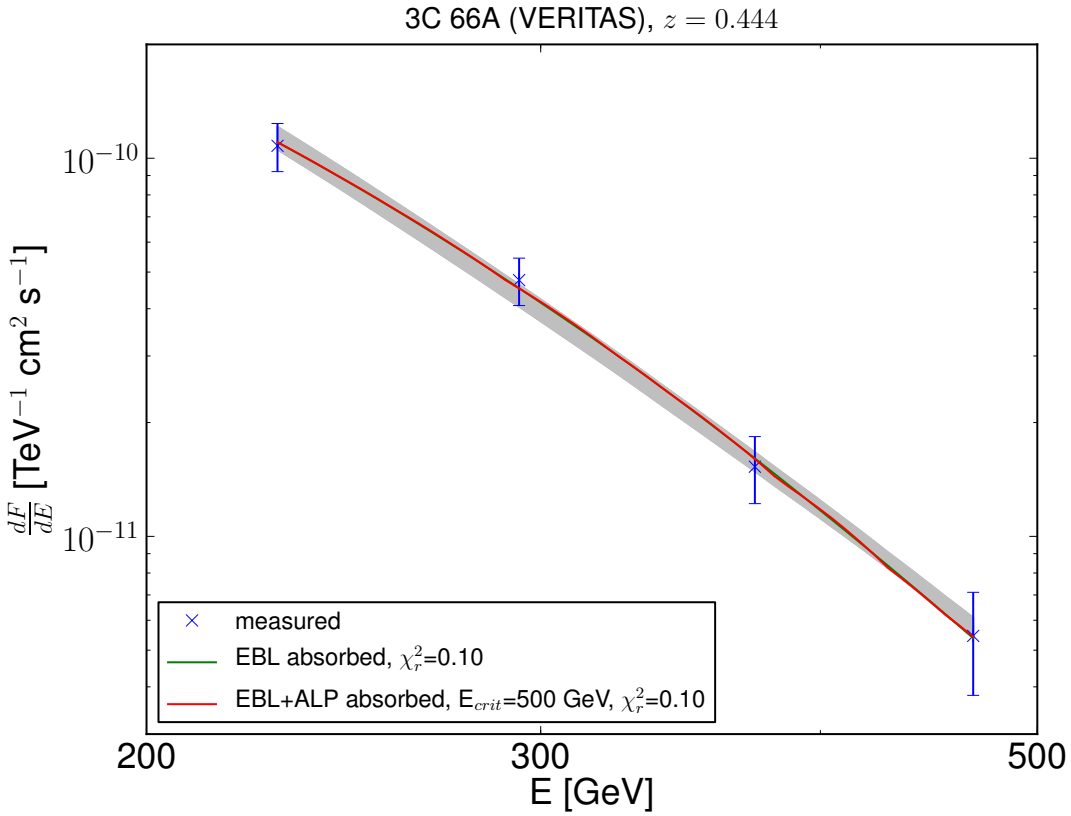

Figure 6.8 Effect of ALPs in 3C 66A spectrum. In blue, the spectral data as measured by the MAGIC Collaboration (Acciari et al. 2009). These data are corrected by EBL absorption and a power law is fitted to the corrected points. Then, this power law is absorbed by EBL again leading to the green line. The measured data are also corrected by EBL absorption taking into account the effect of ALPs. The points corrected in this way are later affected by the EBL plus photon/ALP mixing leading to the red line (see text and Fig. 6.6 for further details). In this case, the EBL corrected spectrum reproduces observations as well as a scenario where ALPs are included. The case corresponding to $E_{crit} = 500$ GeV is shown here, but we note that any other E_{crit} will lead to a good fit as well.

deserves further studies. A more detailed study on the search of any ALP hint in the VHE spectra of extragalactic sources as well as a discussion of its consequences in the EBL and dark matter context will be soon presented in Domínguez, Sánchez-Conde & Prada (2011). Only mentioning that, in case that ALPs exist with the properties discussed here, the EBL upper limits derived from observation of VHE spectra of blazars (Aharonian et al. 2006; Mazin & Raue 2007; Albert et al. 2008) should be revised.

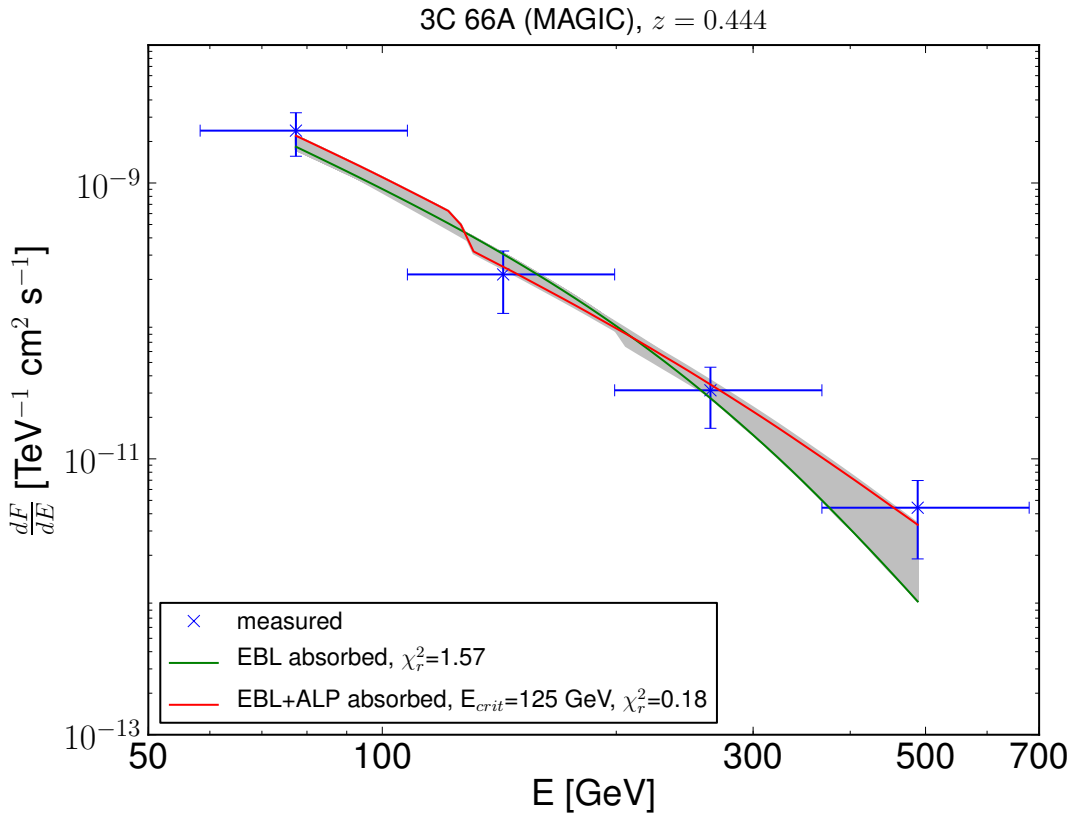

Figure 6.9 Effect of ALPs in 3C 66A spectrum. In blue, the spectral data as measured by the MAGIC Collaboration (Aleksić et al. 2011a). These data are corrected by EBL absorption and a power law is fitted to the corrected points. Then, this power law is absorbed by EBL again leading to the green line. The measured data are also corrected by EBL absorption taking into account the effect of ALPs. The points corrected in this way are later affected by the EBL plus photon/ALP mixing leading to the red line (see text and Fig. 6.6 for further details). Note that the case where ALPs are considered is a better fit to the measured points rather than the case where only EBL absorption is accounted for.

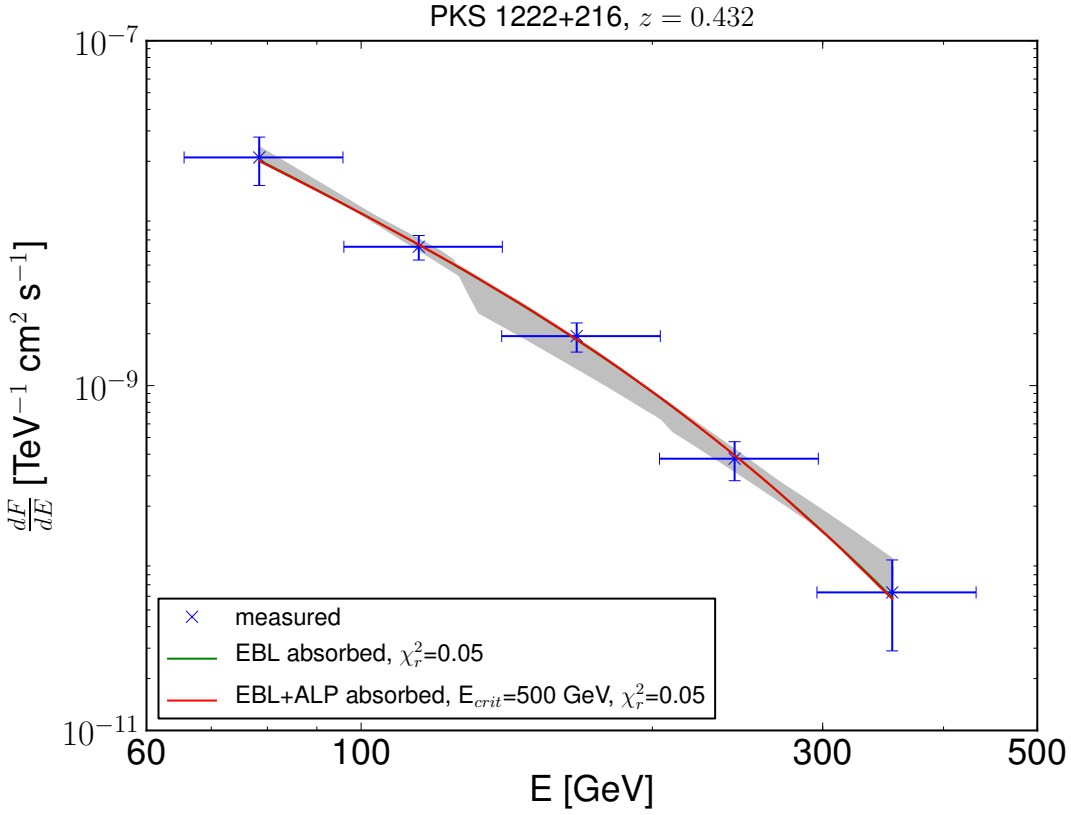

Figure 6.10 Effect of ALPs in PKS 1222+216 spectrum. In blue, the spectral data as measured by the MAGIC Collaboration (Aleksić et al. 2011b). These data are corrected by EBL absorption and a power law is fitted to the corrected points. Then, this power law is absorbed by EBL again leading to the green line. The measured data are also corrected by EBL absorption taking into account the effect of ALPs. The points corrected in this way are later affected by the EBL plus photon/ALP mixing leading to the red line (see text and Fig. 6.6 for further details). In this case, the EBL corrected spectrum reproduces observations as well as a scenario where ALPs are included. The case corresponding to $E_{crit} = 500$ GeV is shown here, but we note that any other E_{crit} will lead to a good fit as well.

Part IV

Conclusions and future work

7

Conclusion remarks

A novel, robust and powerful method based on observations to derive the evolving spectrum of the extragalactic background light (EBL) between 0.1-1000 μm was presented in Chap. 2. This model is based on the observed rest-frame K-band galaxy luminosity function (LF) over redshift by Cirasuolo et al. (2010) (C10), combined with an estimation of galaxy SED-type fractions based on a multiwavelength sample of ~ 6000 galaxies from AEGIS. This model has the following main advantages over other existing EBL models: transparent methodology, reproducibility, and utilizing direct galaxy data. The best available data sets are used (C10's LF and the AEGIS galaxy catalogue) observed over a wide redshift range. The galaxy evolution is directly observed in the rest-frame K-band up to $z = 4$. Observed galaxies up to $z = 1$ from the UV up to 24 μm with spectral energy distributions (SEDs) of 25 different types (from quiescent to rapidly star-forming galaxies, and including AGN galaxies) are taken into account in the same observational framework. A study of the uncertainties to the model directly from the data (such as uncertainties in the Schechter parameters of the C10 LF and the errors in the photometric catalogue) was done, and their propagated uncertainties to the γ-ray attenuation were studied.

A brief comparison with results from other recent EBL models is made here: Stecker, Malkan & Scully (2006) estimate a local EBL in the UV a factor of several higher than us, and in contradiction with recent γ-ray observations (Abdo et al. 2010b). A comparison with the FRV08 results was thoroughly presented through Sec. 2.4. In general, our results are in good agreement, despite the fact that our modelings are different. Finke, Razzaque & Dermer (2010) have five different models based on different parametrization of the star formation rate (SFR) density of the universe and initial mass functions (IMFs). The local EBL from the UV to the near-IR are similar to ours for their models *C* and *E*. Kneiske & Dole (2010) claim to model a strict lower limit for the EBL. However our results for the local EBL in the UV are lower than the calculation by Kneiske & Dole (2010), but are in agreement with the robust lower limits from galaxy counts in the UV by Madau & Pozzetti (2000) and Xu

et al. (2005). In the near-IR, the model by Kneiske & Dole (2010) is not compatible with the lower limits by Keenan et al. (2010). Our observationally-based approach was also thoroughly compared with the results from the semi-analytic model (SAM) of galaxy formation by SGPD11 and GSPD11 in Sec. 2.5.3. Our EBL results are in general in good agreement at least for $z < 2$, even though this SAM predicts more light (by up to a factor of several) than our observational approach in the UV, and a factor $\sim 2-3$ less light in the far-IR.

Our methodology provides a tool for calculating the EBL more accurately at the longest wavelengths when a better understanding on the far-IR galaxy SEDs, new photometry, and deeper LFs at those wavelengths are available from the Herschel Space Observatory.

Two extrapolations of the galaxy SED-type fractions to $z > 1$ were considered, showing that these assumptions only affect the far-IR. It was calculated that the population with SED features of quiescent local galaxies increases a factor ~ 2 since $z \sim 1$. The star-forming population remains roughly constant, while the starburst-like population decreases very quickly from around $\sim 20\%$ at $z \sim 1$. The AGN-like population decreases slower than the starburst-like population from almost 20% at $z \sim 1$ to just around 2% at $z \sim 0.3$. Data from the future James Webb Space Telescope will help to determine the galaxy SED-type fractions at $z > 1$.

A low intensity local EBL ($z = 0$) was found, matching the lower limits from galaxy counts up to ~ 30 μm. For longer wavelengths, our model predicts higher intensities than the data from galaxy counts, in agreement with direct measurements.

A description of the Čerenkov technique and the imaging atmospheric Čerenkov telescopes MAGIC (a stereoscopic system) is presented in Chap. 3. Chap. 4 describes the MAGIC standard analysis chain with two real application cases: GRB 100316A as part of my work as flare advocate in the MAGIC collaboration, and PKS 1222+216 because of its large redshift, which is interesting for EBL studies. A good agreement is found between my own analysis and the official analysis published in Aleksić et al. (2011b).

In Chap. 5, it is described how extragalactic very high energy (VHE) spectra are distorted by the presence of the EBL, and how VHE observations set constraints on this radiation field. Our EBL results are also compatible with all the upper limits from γ-ray astronomy according to the standard framework for the propagation of VHE photons through the universe, even though to account for the highest energies detected by Aharonian et al. (1999) for Mrk 501 we have to assume a $\Gamma_{int} < 1.5$, appeal to statistical and systematic uncertainties on this VHE spectrum, or attenuation uncertainties due to uncertainties in the EBL for such high energies as discussed in Sec.5.3. Other interesting possibility (which is studied in Chap. 6) comes from non-standard physics. The existence of axion-like particles (ALPs) would produces an oscillation axion-photon with observational consequences. Focusing in the energy range observable for current IACTs, we assume some properties for ALPs and look for any imprint of them in VHE blazars among the literature. Our main conclusion

is that the possibility of the existence of ALPs deserves further studies.

The EBL uncertainties in far-IR leading to attenuation uncertainties of a factor of several for energies larger than $\sim$ 10 TeV needs to be addressed by the current and next generation of IR telescopes providing new photometric data and a better understanding of the galaxy IR emission. The γ-ray astronomy may constrain these uncertainties from a better understanding of the emission mechanisms at those high energies (helped with simultaneous multiwavelength observations) and of the instrumental systematic uncertainties. Observations aimed to measure photons with energies higher than $\sim$ 10 TeV at $z < 0.3$ are encouraged.

It is worth mentioning that high energy γ-rays are detected by Fermi for $z \leq 2.5$ from AGNs (Abdo et al. 2010a) and for $z \leq 4.5$ (Abdo et al. 2009) from GRBs. The reasons for these high redshift detections include a larger γ-ray flux at lower energies and a lower density of EBL target photons that can interact with these γ-rays. Understanding the evolution of the EBL at UV wavelengths is essential to interpreting observations of these high-redshift sources. New observations of AGNs as well as the first GRB detection in the VHE range would help to make new and stronger constraints on the EBL; see Gilmore, Prada & Primack (2010).

The universe, according to our observationally-based model, is more transparent than the estimation from FRV08 (a factor $\sim$ 2 in flux) for VHE photons coming from low-redshift sources ($z \sim 0.1$) for energies between $\sim 6 - 15$ TeV, but still the uncertainties here from the EBL modeling are large (a factor of several). The same attenuation than FRV08 is estimated for other energies. For VHE photons coming from larger-redshift sources ($z \sim 1$), roughly the same attenuation as FRV08 is estimated. Here the attenuation uncertainties (for energies available to γ-ray telescopes) due to the uncertainties on the EBL modeling are low in comparison with other effects. At these redshifts the uncertainties on the EBL-corrected spectra are dominated by instrumental systematic uncertainties. We may conclude that it is not expected to observe any such high redshift ($z \sim 1$) multi-TeV γ-ray photons from blazars with the current or even next telescope generation such as the Cherenkov Telescope Array (CTA, Doro 2009), but we indeed expect a promising future for sub-TeV detections at these high redshifts.

8

Future work

My research interests are mainly focused on understanding different aspects of galaxy evolution, both from the observational and theoretical point of view. I am interested and have experience on studying galaxies in the ultraviolet, optical, and infrared as well as within the sub-TeV and TeV energy regime. I will describe in the following sections the main projects that I would like to work on as an extension of my ongoing research.

Galaxy properties and their evolution from z=1.2 to the local universe

Evolution of the green valley

It is now a well known fact that some galaxy properties such as colors are bimodal. Galaxies tend to be either red (red sequence) or blue (blue cloud). In a color histogram the region between these two main population is known as the green valley. Are these green valley galaxies dusty analogues to blue cloud galaxies or are they a transition between galaxies in the blue cloud and the red sequence? There are recent claims that the green valley from the local universe up to $z \sim 2.5$ is mostly populated by dusty galaxies that after a dust correction appear to be well within the blue cloud (Brammer et al. 2009). I checked these claims using a sample of more than 7000 galaxies from the AEGIS collaboration with multiwavelength information from GALEX, CFHT, WIRC, IRAC, and MIPS24 between $z = 0.2 - 1.2$. Most of the redshifts were measured by DEEP2 and independent age indicators such as $D4000$ are also available in my catalog. My preliminary findings are that after applying a dust correction to the galaxy colors the green valley is still significantly populated (as found by Maller et al. (2009) for the local universe) and that the color bimodality is lost when the dust correction is applied (see Fig. 1). This also might indicate the evolution with redshift of the characteristic time to which galaxy move from the

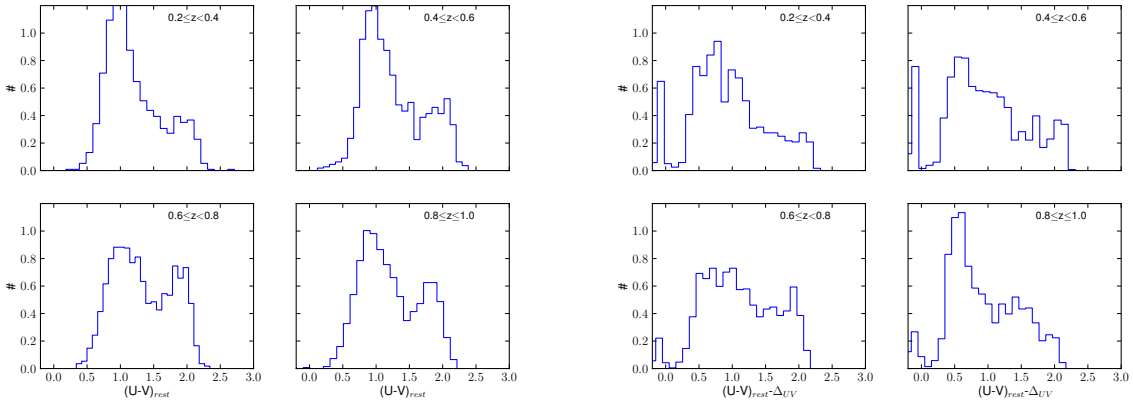

Figure 8.1 Preliminary. Histograms showing in different redshift range (U-V)$_{rest}$ (*left panel*) and (U-V)$_{rest}$ corrected by dust absorption (*right panel*).

blue cloud to the red sequence. This would have important consequences for the theoretical understanding of galaxy evolution. This is a work that I am leading in collaboration with S. Faber, D. Koo, F. Prada, J. Primack, and A. Dekel.

Relationship between galaxy morphology and SED

I am exploiting the multiwavelength galaxy catalog described above trying to relate the morphological information (Sersic indexes, axis ratios, G/M20, ...) that the AEGIS collaboration provided me with the multiwavelength SED classification derived in Chap. 2 (or in Domínguez et al. (2011)). This will set a solid picture of the galaxy evolution between $z = 0.2 - 1.2$ from observations. Preliminary results (see Fig. 2) show that quiescent-elliptical galaxies increase in number with redshift, while the number of quiescent-spiral galaxies decrease. I am leading this work (already ongoing) in collaboration with J. Primack and F. Prada.

Principal component analysis of a multiwavelength galaxy sample

Recently, Williams et al. (2009) claimed that using two rest-frame colors $(U - V)$ and $(V - J)$ red galaxies due to dust and to old stellar population are distinguishable in this color-color diagram. The same catalog described above will be useful for answering the question whether there are more degrees of freedom in the overall galaxy SEDs. For this goal, a mathematical technique called principal component analysis is very convenient. Finding all these degrees of freedom will be really interesting to improve semi-analytical models of galaxy formation. I am already familiar with this technique and have developed the code for its application to the galaxy SEDs. Fig. 3 shows AEGIS galaxies in four different redshift bins using the two first principal components. The color code shows galaxy type according to the multiwavelength

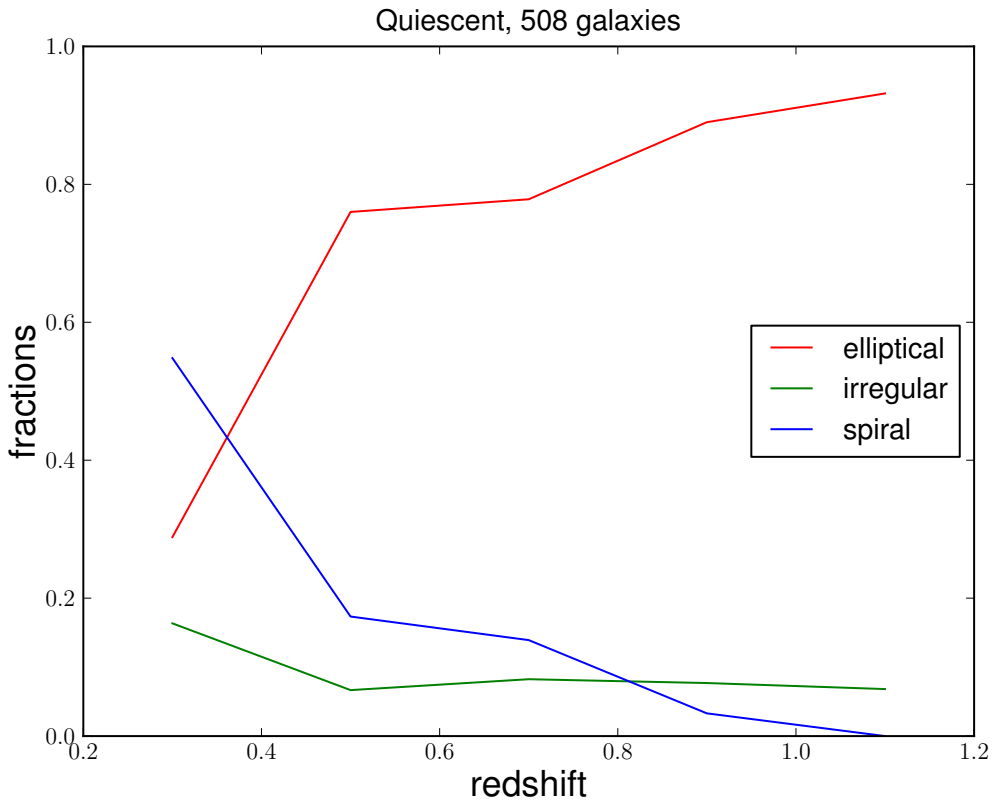

Figure 8.2 Preliminary. Galaxy morphology measured by the AEGIS collaboration for quiescent galaxies according to the multiwavelength-SED classification in Domínguez et al. (2011)

SED classification found in Domínguez et al. (2011). I am leading this work already ongoing in collaboration with S. Faber, J. Primack, R. Somerville, and F. Prada.

Galaxy SED-type fractions in the local universe

An analogous galaxy SED classification to that presented in Chap. 2 (or in Domínguez et al. 2011) will be extremely interesting in the local universe. I want to build a multiwavelength galaxy catalog using data from Sloan, 2MASS, Spitzer, among other surveys and telescopes and apply a similar procedure using overall galaxy-SED templates.

Improvement of the EBL modeling in the far-IR

With the release of Herschel data I am interested on constraining with more precision the EBL in the far-IR, which was the region with higher uncertainties in my

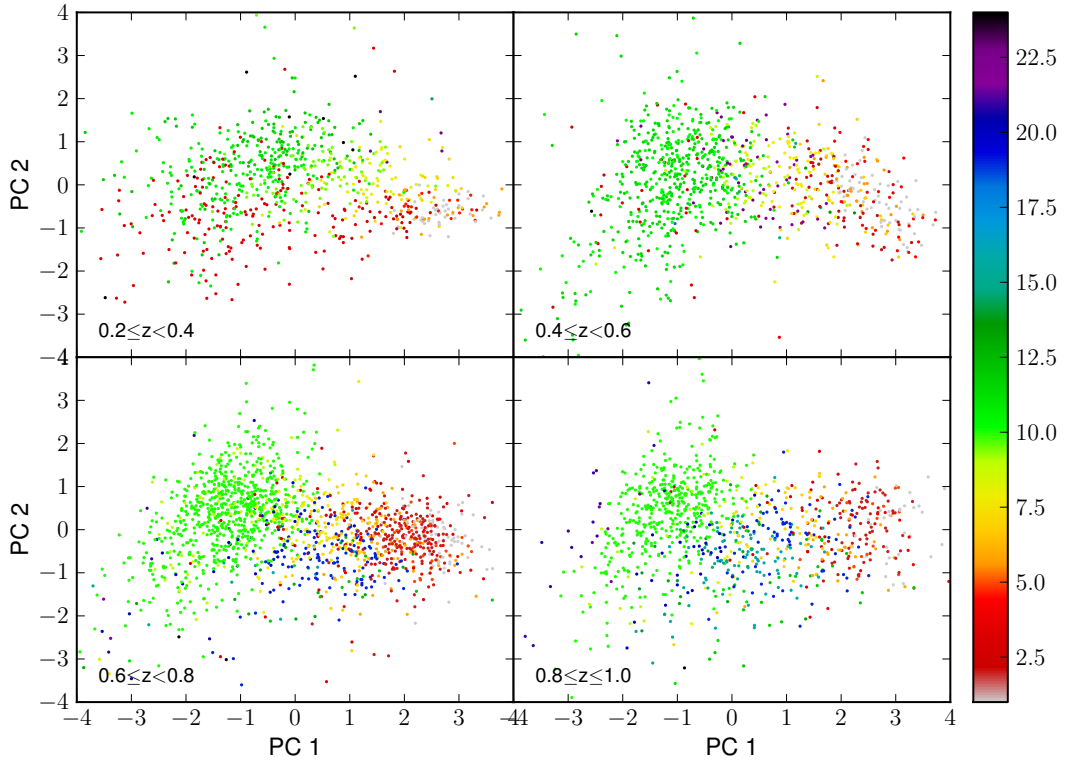

Figure 8.3 Preliminary. Principal component analysis (PCA) on a multiwavelength galaxy catalog in four different redshift bins. The color-code represents the different galaxy types already classified in Domínguez et al. (2011). It is used only the stellar component in the PCA.

modeling in presented in Chap. 2 (or in Domínguez et al. (2011)). This will set important constraints in the star formation rate history of the universe and in multi-TeV observations of local blazars.

High and very high energy astrophysics

Axion-like particle detectability in current VHE AGN spectra

I am interested on the current and future detectability of some signature in the high energy (HE - Fermi satellite) or very high energy (VHE - Cherenkov telescopes) spectra of AGNs coming from the possible existence of axion-like particles (ALPs). There are VHE observations of AGNs whose spectra are harder than previously expected from the current knowledge on the propagation of these photons through the inter-

galactic medium (considering the extragalactic background light) and their emission within the AGNs (explained by the synchrotron-self Compton model). This effect might be explained from the existence of ALPs (see details in Chap. 6). The theoretical aspects were studied in Sánchez-Conde et al. (2009). Detectability is still challenging but possible with current instruments such as the Fermi satellite and Cherenkov telescopes (MAGIC, VERITAS, HESS). If no signal from the existence of ALPs is found, at least limits on the ALP properties and the magnetic field strength in the intergalactic medium might be derived. A paper in preparation led by myself using VHE spectra is currently on-going (a preliminary draft is already written) in collaboration with M. A. Sánchez-Conde and F. Prada. I am very interested on an analogous analysis using extragalactic Fermi data.

A

Acronyms

AEGIS All-wavelength Extended Groth Strip International Survey 29

AGN active galactic nucleus 7

ALP axion-like particle 121

AMC active mirror control 82

ARCADE Absolute Radiometer for Cosmology, Astrophysics, and Diffuse Emission 21

BAT Burst Alert Telescope 90

CCD charged-coupled device 70

CFHT Canada-France-Hawaii Telescope 31

CMB cosmic microwave background 2

COBE Cosmic Background Explorer 3

CRB cosmic radio background 21

CXB cosmic X-ray background 17

C. U. Crab unit 94

DAQ data acquisition 90

DEBRA diffuse extragalactic background radiation 15

EBL extragalactic background light 15

EGB extragalactic γ-ray background 15

EGRET Energetic Gamma Ray Experiment Telescope 16

EGS Extended Groth Strip 30

FADC fast analog-to-digital converter 78

FIRAS Far-Infrared Absolute Spectrometer 27

FoV field of view 71

FSRQ flat spectrum radio quasar 97

FWHM full width at half maximum 80

GALEX Galaxy Evolution Explorer 31

GRB gamma-ray burst 17

HE high energy 75

HESS High Energy Stereoscopic System

HST Hubble Space Telescope 3

IACT imaging atmospheric Čerenkov telescope 48

IC inverse Compton 110

IGM intergalactic medium 7

IGMF intergalactic magnetic field 122

IMF initial mass function 8

IR infrared 9

IRAC Infrared Array Camera 30

IRTS Infrared Telescope in Space 23

ISM interstellar medium 7

LAT Large Area Telescope 16

LF luminosity function 14

MAGIC Major Atmospheric Gamma Imaging Čerenkov 75

MC Monte Carlo 90

MIPS Multiband Imaging Photometer for Spitzer 30

PAH polycyclic-aromatic-hydrocarbon 36

PMT photomultiplier 78

PSF point spread function 101

QCD quantum chromo dynamics 121

QE quantum efficiency 80

RMS root mean square 87

SAM semi-analytical model 12

SDSS Sloan Digital Sky Survey 46

SED spectral energy distribution 9

SFR star formation rate 28

SSC synchrotron self Compton 110

SSP simple stellar population 9

SWIRE Spitzer Wide-Area Infrared Extragalactic Survey 29

ULIRG ultra-luminous infrared galaxies 13

UV ultraviolet 21

B

Publications

Publications in refereed journals

1. *Hints of the existence of axionlike particles from the gamma-ray spectra of cosmological sources*
   M. A. Sánchez-Conde, D. Paneque, E. Bloom, F. Prada and A. Domínguez, 2009, Phys. Rev. D, 79, 123511

2. *Extragalactic background light inferred from AEGIS galaxy-SED-type fractions*
   A. Domínguez, J. R. Primack, D. J. Rosario, F. Prada, R. C. Gilmore, S. M. Faber, D. C. Koo, R. S. Somerville, M. A. Perez-Torres, P. Pérez-González, J.-S. Huang, M. Davis, P. Guhathakurta, P. Barmby, C. J. Conselice, M. Lozano, J. A. Newman and M. C. Cooper, 2011, MNRAS, 410, 2556

33 more refereed publications as a full member of the MAGIC collaboration:

1. *Very-High-Energy gamma rays from a Distant Quasar: How Transparent Is the Universe?*
   Albert et al. (including A. Domínguez), 2008, Science, 320, 1752

2. *Multiwavelength (Radio, X-Ray, and γ-Ray) Observations of the γ-Ray Binary LS I +61 303*
   Albert et al. (including A. Domínguez), 2008, ApJ, 684, 1351

3. *Very High Energy Gamma-Ray Observations of Strong Flaring Activity in M87 in 2008 February*
   Albert et al. (including A. Domínguez), 2008, ApJ, 685, L23

4. *First Bounds on the High-Energy Emission from Isolated Wolf-Rayet Binary Systems*
   Aliu et al. (including A. Domínguez), 2008, ApJ, 685, L71

5. *Probing quantum gravity using photons from a flare of the active galactic nucleus Markarian 501 observed by the MAGIC telescope*
   Albert et al. (including A. Domínguez), 2008, Physics Letters B, 668, 253

6. *Observation of Pulsed γ-Rays Above 25 GeV From the Crab Pulsar with MAGIC*
   Aliu et al. (including A. Domínguez), 2008, Science, 322, 1221

7. *Improving the performance of the single-dish Cherenkov telescope MAGIC through the use of signal timing*
   Aliu et al. (including A. Domínguez), 2009, Astroparticle Physics, 30, 293

8. *The June 2008 Flare of Markarian 421 from Optical to TeV Energies*
   Donnarumma et al. (including A. Domínguez), 2009, ApJL, 691, 13

9. *Discovery of a Very High Energy Gamma-Ray Signal from the 3C 66A/B Region*
   Aliu et al. (including A. Domínguez), 2009, ApJ, 692, L29

10. *Periodic Very High Energy γ-Ray Emission from LS I +61 303 Observed with the MAGIC Telescope*
    Anderhub et al. (including A. Domínguez), 2009, ApJ, 693, 303

11. *MAGIC upper limits to the VHE gamma-ray flux of 3C 454.3 in high emission state*
    Anderhub et al. (including A. Domínguez), 2009, A&A, 498, 83

12. *Radio Imaging of the Very-High-Energy γ-Ray Emission Region in the Central Engine of a Radio Galaxy*
    Anderhub et al. (including A. Domínguez), 2009, Science, 325, 444

13. *Search for VHE γ-ray Emission from the Globular Cluster M13 with the Magic Telescope*
    Anderhub et al. (including A. Domínguez), 2009, ApJ, 702, 266

14. *Simultaneous Multiwavelength Observations of Markarian 421 During Outburst*
    Acciari et al. (including A. Domínguez), 2009, ApJ, 703, 169

15. *Discovery of very High Energy γ-Rays from the Blazar S5 0716+714*
    Anderhub et al. (including A. Domínguez), 2009, ApJ, 704, L129

16. *Suzaku and Multi-Wavelength Observations of OJ 287 during the Periodic Optical Outburst in 2007*
    Seta H. et al. (including A. Domínguez), 2009, PASJ, 61, 1011

17. *Simultaneous Multiwavelength Observation of Mkn 501 in a Low State in 2006*
Anderhub et al. (including A. Domínguez), 2009, ApJ, 705, 1624

18. *Correlated X-Ray and Very High Energy Emission in the Gamma-Ray Binary LSI +61 303*
Anderhub et al. (including A. Domínguez), 2009, ApJ, 706, L27

19. *MAGIC upper limits on the VHE gamma-ray emission from the satellite galaxy Willman 1*
E.Aliu et al. (including A. Domínguez), 2009, ApJ, 697, 1299

20. *MAGIC Gamma-Ray Telescope Observation of the Perseus Cluster of Galaxies: implications for cosmic rays, dark matter, and NGC 1275*
J.Aleksic et al. (including A. Domínguez), 2010, ApJ, 710, 634

21. *Gamma-ray excess from a stacked sample of high-frequency peaked blazars observed with the MAGIC telescope*
MAGIC Collaboration (including A. Domínguez), 2010, arXiv, arXiv:1002.2951

22. *Search for an extended VHE gamma-ray emission from Mrk 421 and Mrk 501 with the MAGIC Telescope*
MAGIC Collaboration (including A. Domínguez), 2010, arXiv, arxiv:1004.1093

23. *Simultaneous multi-frequency observation of the unknown redshift blazar PG 1553+113 in March-April 2008*
MAGIC Collaboration (including A. Domínguez), 2010, A&A, 515, A76

24. *MAGIC observation of the GRB 080430 afterglow*
MAGIC Collaboration (including A. Domínguez), 2010, A&A, 517, A5

25. *MAGIC TeV gamma-ray observations of Markarian 421 during multiwavelength campaigns in 2006*
MAGIC Collaboration (including A. Domínguez), 2010, A&A, 519, A32

26. *Magic Constraints on γ-ray Emission from Cygnus X-3*
MAGIC Collaboration (including A. Domínguez), 2010, ApJ, 721, 843

27. *Detection of very high energy γ-ray emission from the Perseus cluster head-tail galaxy IC 310 by the MAGIC telescopes*
MAGIC Collaboration (including A. Domínguez), 2010, ApJ, 723, L207

28. *Search for an extended VHE γ-ray emission from Mrk 421 and Mrk 501 with the MAGIC Telescope*
MAGIC Collaboration (including A. Domínguez), 2010, A&A, 524, A77

29. *MAGIC Upper Limits for two Milagro-detected, Bright Fermi Sources in the Region of SNR G65.1+0.6*
MAGIC Collaboration (including A. Domínguez), 2010, ApJ, 725, 1629

30. *Observations of the Blazar 3C 66A with the MAGIC Telescopes in Stereoscopic Mode*
MAGIC Collaboration (including A. Domínguez), 2011, ApJ, 726, 58

31. *MAGIC observations and multiwavelength properties of the quasar 3C279 in 2007 and 2009* MAGIC Collaboration (including A. Domínguez), 2011, arXiv, arXiv:1101.2522

32. *PG 1553+113: five years of observations with MAGIC*
MAGIC Collaboration (including A. Domínguez), 2011, arXiv, arXiv:1101.2764

33. *MAGIC discovery of VHE Emission from the FSRQ PKS 1222+21* MAGIC Collaboration (including A. Domínguez), 2011, arXiv, arXiv:1101.4645

Papers in preparation

1. *The evolution of green valley galaxies from redshift 1.2 to the local Universe*
A. Domínguez, S. Faber, D. Koo, F. Prada, J. Primack, A. Dekel, et al., 2011

2. *New constraints for axion-like particles from very high energy spectra of cosmological sources*
A. Domínguez, M. A.Sánchez-Conde, F. Prada, 2011

3. *The bolometric luminosity history of the Universe: ΛCDM models confront observations*
R. Somerville, R. Gilmore, J. Primack and A. Domínguez, 2011

4. *Extragalactic background absorption in gamma-ray spectra*
R. Gilmore, R. Somerville, J. Primack and A. Domínguez, 2011

Bibliography

Abdo A. A., et al., 2009, Sci, 323, 1688

Abdo A. A., et al., 2010a, ApJ, 715, 429

Abdo A. A., et al., 2010b, ApJ, 723, 1082

Abdo A. A., et al., 2010, PhRvL, 104, 101101

Abdo A. A., et al., 2010, ApJ, 720, 435

Abdo A. A., et al., 2011, ApJ, 726, 43

Abraham J., et al., 2008, APh, 29, 188

Acciari V. A., et al., 2009, ApJ, 693, L104

Aharonian F., et al., 1999, A&A, 349, 11

Aharonian F. A., et al., 2001, A&A, 366, 62

Aharonian F., et al., 2004, A&A, 421, 529

Aharonian F., et al., 2006, Nature, 440, 1018

Aharonian F., et al., 2007, A&A, 475, L9

Aharonian F. A., Khangulyan D., Costamante L., 2008, MNRAS, 387, 1206

Aharonian F., et al., 2009, ApJ, 695, L40

Ajello M., et al., 2008, ApJ, 689, 666

Albert J., et al., 2006, ApJ, 638, L101

Albert J., et al., 2007, ApJ, 654, L119

Albert J., et al., 2007b, ApJL, 664, L87

Albert J., et al., 2007c, NIMPA, 583, 494

Albert J., et al., 2008, Sci, 320, 1752

Albert J., et al., 2008b, ApJ, 679, 428

Aleksić J., et al., 2011a, ApJ, 726, 58

Aleksić J., et al., 2011b, in prep.

Aleksić J., et al., 2011c, arXiv, arXiv:1101.2522

Alexander D. M., et al., 2003, AJ, 126, 539

Aliu J., et al., 2008, Science, 322, 1221

Aliu J., et al., 2009, ApJ, 695, 1

Andriamonje S., et al., 2007, JCAP, 0704, 010

Arnouts S., et al., 2002, MNRAS, 329, 355

Arnouts S., et al., 2007, A&A, 476, 137

Baixeras C., et al., 2003, Nucl.Phys.B (Proc. Suppl.), 114, 247-252

Barmby P., Huang J.-S., Ashby M. L. N., Eisenhardt P. R. M., Fazio G. G., Willner S. P., Wright E. L., 2008, ApJS, 177, 431

Barro G., et al., 2009, A&A, 494, 63

Baugh C. M., Lacey C. G., Frenk C. S., Granato G. L., Silva L., Bressan A., Benson A. J., Cole S., 2005, MNRAS, 356, 1191

Beichman C. A., Helou G., 1991, ApJ, 370, L1

Bell E. F., McIntosh D. H., Katz N., Weinberg M. D., 2003, ApJS, 149, 289

Bernstein R. A., 2007, ApJ, 666, 663

Berta S., et al., 2010, A&A, 518, L30

Bertone G., Hooper D., Silk J., 2005, PhR, 405, 279

Béthermin M., Dole H., Beelen A., Aussel H., 2010, A&A, 512, A78

Blaizot J., Guiderdoni B., Devriendt J. E. G., Bouchet F. R., Hatton S. J., Stoehr F., 2004, MNRAS, 352, 571

Blanton M. R., et al., 2003a, ApJ, 592, 819

Blanton M. R., et al., 2003b, ApJ, 594, 186

Blanton M. R., 2006, ApJ, 648, 268

Blumenthal G. R., Faber S. M., Primack J. R., Rees M. J., 1985, Nature, 313, 72

Bond J. R., Carr B. J., Hogan C. J., 1986, ApJ, 306, 428

Bond J. R., Carr B. J., Hogan C. J., 1991, ApJ, 367, 420

Borla D., et al., 2009, Procs. of the 1st International Conference on Technology and Instrumentation in Particle Physics (TIPP09), Tsukuba, Japan, 12 -17 March 2009

Böttcher M., 2007, Ap&SS, 309, 95

Böttcher M., Dermer C. D., Finke J. D., 2008, ApJ, 679, L9

Bower R. G., Benson A. J., Malbon R., Helly J. C., Frenk C. S., Baugh C. M., Cole S., Lacey C. G., 2006, MNRAS, 370, 645

Bramel D. A., et al., 2005, ApJ, 629, 108

Brammer G. B., et al., 2009, ApJ, 706, L173

Bretz T. for the MAGIC Collaboration, 2005, 29th International Cosmic Ray Conference, Pune

Bretz T., Dorner D., 2009, AIP Conf. Proc., 1085:664â€“669

Bridle A. H., 1967, MNRAS, 136, 219

Brinchmann J., Ellis R. S., 2000, ApJ, 536, L77

Broadhurst T., Umetsu K., Medezinski E., Oguri M., Rephaeli Y., 2008, ApJ, 685, L9

Bruzual G., Charlot S., 2003, MNRAS, 344, 1000

Buckley J., et al., 2008, AIPC, 1085, 902

Bullock J. S., Stewart K. R., Purcell C. W., 2009, IAUS, 254, 85

Burrage C., Davis A.-C., Shaw D. J., 2009, Phys. Rev. D, 79, 044028

Calzetti D., Armus L., Bohlin R. C., Kinney A. L., Koornneef J., Storchi-Bergmann T., 2000, ApJ, 533, 682

Cambrésy L., Reach W. T., Beichman C. A., Jarrett T. H., 2001, ApJ, 555, 563

Cameron E., Driver S. P., Graham A. W., Liske J., 2009, ApJ, 699, 105

Cattaneo A., et al., 2007, MNRAS, 377, 63

Čerenkov P.A., 1934, C.R. Acad. Sci. U.S.S.R. 2, 451

Chabrier G., 2003, PASP, 115, 763

Charlot S., Fall S. M., 2000, ApJ, 539, 718

Chary R., Elbaz D., 2001, ApJ, 556, 562

Chary R., et al., 2004, ApJS, 154, 80

Chary R.-R., Pope A., 2010, arXiv, arXiv:1003.1731

Cirasuolo M., McLure R. J., Dunlop J. S., Almaini O., Foucaud S., Simpson C., 2010, MNRAS, 401, 1166 (C10)

Clark T. A., Brown L. W., Alexander J. K., 1970, Nature, 228, 847

Coil A. L., Newman J. A., Kaiser N., Davis M., Ma C.-P., Kocevski D. D., Koo D. C., 2004, ApJ, 617, 765

Cole S., Aragon-Salamanca A., Frenk C. S., Navarro J. F., Zepf S. E., 1994, MNRAS, 271, 781

Cole S., Lacey C. G., Baugh C. M., Frenk C. S., 2000, MNRAS, 319, 168

Colless M., et al., 2001, MNRAS, 328, 1039

Conroy C., Wechsler R. H., 2009, ApJ, 696, 620

Conselice C. J., Bundy K., U V., Eisenhardt P., Lotz J., Newman J., 2008, MNRAS, 383, 1366

Copeland E. J., Sami M., Tsujikawa S., 2006, IJMPD, 15, 1753

Cowie L. L., Songaila A., Hu E. M., Cohen J. G., 1996, AJ, 112, 839

Croton D. J., et al., 2006, MNRAS, 365, 11

Croton D. J., 2009, MNRAS, 394, 1109

Csáki C., Kaloper N., Terning J., 2002, Phys. Rev. Lett., 88, 161302

Csáki C., Kaloper N., Peloso M., Terning J., 2003, JCAP, 05, 005

Cuillandre J.-C., Luppino G., Starr B., Isani S., 2001, sf2a.conf, 605

Daddi E., et al., 2007, ApJ, 670, 156

Dahlen T., Mobasher B., Somerville R. S., Moustakas L. A., Dickinson M., Ferguson H. C., Giavalisco M., 2005, ApJ, 631, 126

Dahlen T., Mobasher B., Dickinson M., Ferguson H. C., Giavalisco M., Kretchmer C., Ravindranath S., 2007, ApJ, 654, 172

Dale D. A., Helou G., 2002, ApJ, 576, 159

Danforth C. W., Keeney B. A., Stocke J. T., Shull J. M., Yao Y., 2010, ApJ, 720, 976

Davis M., et al., 2007, ApJ, 660, L1

de Angelis A., Roncadelli M., Mansutti O., 2007, PhRvD, 76, 121301

de Angelis A., Mansutti O., Roncadelli M., 2008, PhLB, 659, 847

de Angelis A., Persic M., Roncadelli M., 2008, MPLA, 23, 315

de Blok W. J. G., 2005, ApJ, 634, 227

De Lucia G., Blaizot J., 2007, MNRAS, 375, 2

Dermer C. D., 2007, AIPC, 921, 122

Devlin M. J., et al., 2009, Nature, 458, 737

Devriendt J. E. G., Guiderdoni B., Sadat R., 1999, A&A, 350, 381

Devriendt J. E. G., Guiderdoni B., 2000, A&A, 363, 851

Dickinson M., FIDEL team, 2007, AAS, 38, 822

Dicus D. A., Kolb E. W., Teplitz V. L., Wagoner R. V., 1978, Phys. Rev. D, 18, 1829

Domínguez A., et al., 2011, MNRAS, 410, 2556

Domínguez A., Sánchez-Conde M. A., Prada F., 2011, in prep.

Dolag K., Grasso D., Springel V., Tkachev I., 2005, JCAP, 1, 9

Doro M. for the CTA consortium, 2009, arXiv, arXiv:0908.1410

Driver S. P., Popescu C. C., Tuffs R. J., Graham A. W., Liske J., Baldry I., 2008, ApJ, 678, L101

Duffy L. D., et al., 2006, Phys. Rev. D, 74, 012006

Dwek E., Krennrich F., 2005, ApJ, 618, 657

Essey W., Kalashev O., Kusenko A., Beacom J. F., 2010, arXiv, arXiv:1011.6340

Faber S. M., et al., 2003, SPIE, 4841, 1657

Faber S. M., et al., 2007, ApJ, 665, 265

Fabian A. C., Barcons X., 1992, ARA&A, 30, 429

Fardal M. A., Katz N., Weinberg D. H., Davé R., 2007, MNRAS, 379, 985

Fazio G. G., et al., 2004, ApJS, 154, 39

Fields B. D., Pavlidou V., Prodanović T., 2010, ApJ, 722, L199

Finkbeiner D. P., Davis M., Schlegel D. J., 2000, ApJ, 544, 81

Finke J. D., Razzaque S., 2009, ApJ, 698, 1761

Finke J. D., Dermer C. D., 2010, ApJ, 714, L303

Finke J. D., Razzaque S., Dermer C. D., 2010, ApJ, 712, 238

Fontanot F., Monaco P., Silva L., Grazian A., 2007, MNRAS, 382, 903

Fontanot F., Somerville R. S., Silva L., Monaco P., Skibba R., 2009a, MNRAS, 392, 553

Fontanot F., De Lucia G., Monaco P., Somerville R. S., Santini P., 2009b, MNRAS, 397, 1776

Fontanot F., Somerville R. S., 2010, arXiv, arXiv:1011.0776

Franceschini A., Toffolatti L., Mazzei P., Danese L., de Zotti G., 1991, A&AS, 89, 285

Franceschini A., Mazzei P., de Zotti G., Danese L., 1994, ApJ, 427, 140

Franceschini A., Rodighiero G., Vaccari M., 2008, A&A, 487, 837 (FRV08)

Frayer D. T., et al., 2006, ApJ, 647, L9

Furlanetto S. R., Loeb A., 2001, ApJ, 556, 619

Gabasch A., et al., 2004, A&A, 421, 41

Gabasch A., et al., 2006, A&A, 448, 101

Gardner J. P., Brown T. M., Ferguson H. C., 2000, ApJ, 542, L79

Gehrels N., Michelson P., 1999, APh, 11, 277

Gentile G., Tonini C., Salucci P., 2007, A&A, 467, 925

Georganopoulos M., Finke J. D., Reyes L. C., 2010, ApJ, 714, L157

Giacconi R., Gursky H., Paolini F. R., Rossi B. B., 1962, PhRvL, 9, 439

Giacconi R., et al., 2002, ApJS, 139, 369

Gilmore R. C., Prada F., Primack J., 2010, MNRAS, 402, 565

Gilmore R. C., Somerville R. S., Primack J. R., Domínguez A., 2011, in prep. (GSPD11)

Gorjian V., Wright E. L., Chary R. R., 2000, ApJ, 536, 550

Goto T., Yamauchi C., Fujita Y., Okamura S., Sekiguchi M., Smail I., Bernardi M., Gomez P. L., 2003, MNRAS, 346, 601

Gould R. J., Schréder G., 1966, PhRvL, 16, 252

Granato G. L., Lacey C. G., Silva L., Bressan A., Baugh C. M., Cole S., Frenk C. S., 2000, ApJ, 542, 710

Grasso D., Rubinstein H. R., 2001, PhR, 348, 163

Guiderdoni B., Rocca-Volmerange B., 1987, A&A, 186, 1

Guiderdoni B., Hivon E., Bouchet F. R., Maffei B., 1998, MNRAS, 295, 877

Guo Q., et al., 2010, arXiv, arXiv:1006.0106

Hacking P. B., Soifer B. T., 1991, ApJ, 367, L49

Harrison E. R., 1990, IAUS, 139, 3

Hartman R. C., et al., 1999, ApJS, 123, 79

Harwit M., 1970, NCimR, 2, 253

Hatton S., Devriendt J. E. G., Ninin S., Bouchet F. R., Guiderdoni B., Vibert D., 2003, MNRAS, 343, 75

Hasinger G., 2004, NuPhS, 132, 86

Hauser M. G., et al., 1998, ApJ, 508, 25

Hauser M. G., Dwek E., 2001, ARA&A, 39, 249

Heck D., Knapp J., Capdevielle J. N., Schatz G., Thouw T., 1998, cmcc.book

Hillas A. M., 1985, In F.C. Jones, editor, International Cosmic Ray Conference, vol. 3 of International Cosmic Ray Conference, 445-448.

Hinton J. A., 2004, NewAR, 48, 331

Hochmuth K. A., Sigl G., 2007, PhRvD, 76, 123011

Hooper D., Serpico P. D., 2007, PhRvL, 99, 231102

Hopkins P. F., Hernquist L., Cox T. J., Kereš D., 2008a, ApJS, 175, 356

Hopkins P. F., Cox T. J., Kereš D., Hernquist L., 2008b, ApJS, 175, 390

Hopkins P. F., et al., 2009, MNRAS, 397, 802

Hopwood R., et al., 2010, ApJ, 716, L45

Huang J.-S., et al., 2007, ApJ, 664, 840

Huang J.-S., et al., 2010, in prep.

Ilbert O., et al., 2005, A&A, 439, 863

Ilbert O., et al., 2006, A&A, 457, 841

Jones D. H., Peterson B. A., Colless M., Saunders W., 2006, MNRAS, 369, 25

Kang X., Jing Y. P., Silk J., 2006, ApJ, 648, 820

Kashlinsky A., Atrio-Barandela F., Kocevski D., Ebeling H., 2008, ApJ, 686, L49

Katarzyński K., Ghisellini G., Tavecchio F., Gracia J., Maraschi L., 2006, MNRAS, 368, L52

Kaufman M., 1976, Ap&SS, 40, 369

Kauffmann G., White S. D. M., Guiderdoni B., 1993, MNRAS, 264, 201

Kauffmann G., Colberg J. M., Diaferio A., White S. D. M., 1999, MNRAS, 303, 188

Kaviani A., Haehnelt M. G., Kauffmann G., 2003, MNRAS, 340, 739

Keenan R. C., Barger A. J., Cowie L. L., Wang W.-H., 2010, ApJ, 723, 40

Kennicutt R. C., Jr., 1998, ARA&A, 36, 189

Kneiske T. M., Mannheim K., Hartmann D. H., 2002, A&A, 386, 1

Kneiske T. M., Dole H., 2010, A&A, 515, A19

Kniffen D. A., Hartman R. C., Thompson D. J., Fichtel C. E., 1973, ApJ, 186, L105

Kleinmann D. E., Low F. J., 1970, ApJ, 159, L165

Klypin A., Kravtsov A. V., Valenzuela O., Prada F., 1999, ApJ, 522, 82

Kochanek C. S., et al., 2001, ApJ, 560, 566

Komatsu E., et al., 2011, ApJS, 192, 18

Kravtsov A., 2010, AdAst, 2010

Kriek M., van Dokkum P. G., Labbé I., Franx M., Illingworth G. D., Marchesini D., Quadri R. F., 2009, ApJ, 700, 221

Kronberg P. P., 1994, RPPh, 57, 325

Lacey C., Guiderdoni B., Rocca-Volmerange B., Silk J., 1993, ApJ, 402, 15

Lagache G., Haffner L. M., Reynolds R. J., Tufte S. L., 2000, A&A, 354, 247

Lagache G., et al., 2004, ApJS, 154, 112

Lagache G., Puget J.-L., Dole H., 2005, ARA&A, 43, 727

Larson D., et.al., 2011, ApJS, 192, 16

Lawrence A., et al., 2007, MNRAS, 379, 1599

LeFloc'h E., et al., 2009, ApJ, 703, 222

Levenson L. R., Wright E. L., 2008, ApJ, 683, 585

Longair M. S., Sunyaev R. A., 1972, SvPhU, 14, 569

Lorenz E., 2004, NewAR, 48, 339

Low F. J., Tucker W. H., 1968, PhRvL, 21, 1538

Low F. J., 1970, ApJ, 159, L173

Madau P., Phinney E. S., 1996, ApJ, 456, 124

Madau P., Pozzetti L., 2000, MNRAS, 312, L9

Magnelli B., Elbaz D., Chary R. R., Dickinson M., Le Borgne D., Frayer D. T., Willmer C. N. A., 2009, A&A, 496, 57

Majumdar P., Moralejo A., Bigongiari C., Blanch O., Sobczynska D., 2005, ICRC, 5, 203

Malkan M. A., Stecker F. W., 1998, ApJ, 496, 13

Maller A. H., Berlind A. A., Blanton M. R., Hogg D. W., 2009, ApJ, 691, 394

Maraston C., 2005, MNRAS, 362, 799

Marchesini D., et al., 2007, ApJ, 656, 42

Matsumoto T., et al., 2005, ApJ, 626, 31

Matsuura S., et al., 2010, arXiv, arXiv:1002.3674

Mattila K., 2006, MNRAS, 372, 1253

Matute I., La Franca F., Pozzi F., Gruppioni C., Lari C., Zamorani G., 2006, A&A, 451, 443

Mayer-Hasselwander H. A., et al., 1982, A&A, 105, 164

Mazin D., Raue M., 2007, A&A, 471, 439

McVittie G. C., Wyatt S. P., 1959, ApJ, 130, 1

Menci N., Fontana A., Giallongo E., Grazian A., Salimbeni S., 2006, ApJ, 647, 753

Menéndez-Delmestre K., et al., 2009, ApJ, 699, 667

Metcalfe L., et al., 2003, A&A, 407, 791

Mirizzi A., Raffelt G. G., Serpico P. D., 2007, PhRvD, 76, 023001

Mirizzi A., Raffelt G. G., Serpico P. D., 2008, Lect. Notes Phys., 741, 115

Mo H., van den Bosch F., White S., *Galaxy Formation and Evolution*, Cambridge University Press

Monaco P., Fontanot F., Taffoni G., 2007, MNRAS, 375, 1189

Montero-Dorta A. D., Prada F., 2009, MNRAS, 399, 1106

Morrissey P., et al., 2007, ApJS, 173, 682

Murphy E. J., Chary R.-R., Alexander D. M., Dickinson M., Magnelli B., Morrison G., Pope A., Teplitz H. I., 2009, ApJ, 698, 1380

Negroponte J., 1986, MNRAS, 222, 19

Newman J. A., et al., 2011, in prep.

Nikishov A. I., 1962, Sov. Phys. JETP, 14, 393

Norberg P., et al., 2002, MNRAS, 336, 907

Oya I., Ph. D. Thesis, 2010

Papovich C., et al., 2004, ApJS, 154, 70

Partridge R. B., Peebles P. J. E., 1967, ApJ, 147, 868

Partridge R. B., Peebles P. J. E., 1967, ApJ, 148, 377

Peccei R. D., Quinn H. R., 1977, Phys. Rev. Lett., 38, 1440

Peebles P. J. E., 1969, RSPTA, 264, 279

Peebles P. J. E., 1993, Principles of Physical Cosmology, Princeton University Press

Pérez-González P. G., et al., 2008, ApJ, 675, 234

Perivolaropoulos L., Shafieloo A., 2009, PhRvD, 79, 123502

Perlmutter S., et al., 1999, ApJ, 517, 565

Pieri L., Bertone G., Branchini E., 2008, MNRAS, 384, 1627

Polletta M., et al., 2007, ApJ, 663, 81

Prandini E., Bonnoli G., Maraschi L., Mariotti M., Tavecchio F., 2010, MNRAS, 405, L76

Press W. H., Schechter P., 1974, ApJ, 187, 425

Primack J. R., Bullock J. S., Somerville R. S., MacMinn D., 1999, APh, 11, 93

Primack J. R., Somerville R. S., Bullock J. S., Devriendt J. E. G., 2001, AIPC, 558, 463

Punch M., et al., 1992, Nature, 358, 477

Raffelt G. G., 2005, Contribution to XI International Workshop on Neutrino Telescopes, Venice, Italy, hep-ph/0504152

Reddy N. A., Erb D. K., Steidel C. C., Shapley A. E., Adelberger K. L., Pettini M., 2005, ApJ, 633, 748

Reddy N. A., Steidel C. C., Fadda D., Yan L., Pettini M., Shapley A. E., Erb D. K., Adelberger K. L., 2006, ApJ, 644, 792

Rieke G. H., Alonso-Herrero A., Weiner B. J., Pérez-González P. G., Blaylock M., Donley J. L., Marcillac D., 2009, ApJ, 692, 556

Riess A. G., et al., 1998, ApJ, 116, 1009

Rodighiero G., et al., 2010, A&A, 515, A8

Rolke W. A., López A. M., Conrad J., 2005, NIMPA, 551, 493

Salim S., et al., 2009, ApJ, 700, 161

Salpeter E. E., 1955, ApJ, 121, 161

Sánchez-Conde M. A., Paneque D., Bloom E., Prada F., Domínguez A., 2009, PhRvD, 79, 123511

Sánchez-Conde M. A., Ph. D. Thesis, 2009

Sandage A., Tammann G. A., Mt. Wilson & Palomar Obs., Carnegie Year-book II, 64, Carnegie Inst. of Washington, pp. 35â€“37

Sanders D. B., Mirabel I. F., 1996, ARA&A, 34, 749

Schawinski K., et al., 2009, MNRAS, 396, 818

Schechter P., 1976, ApJ, 203, 297

Schlegel D. J., Finkbeiner D. P., Davis M., 1998, ApJ, 500, 525

Serjeant S., Harrison D., 2005, MNRAS, 356, 192

Shakeshaft J. R., 1954, Phil. Mag. 45, 1136

Siegal-Gaskins J. M., Reesman R., Pavlidou V., Profumo S., Walker T. P., 2010, arXiv, arXiv:1011.5501

Sigl G., Miniati F., Enßlin T. A., 2004, PhRvD, 70, 043007

Sikivie P., 1983, Phys. Rev. Lett., 51, 1415 [Erratum ibid., 1984, Phys. Rev. Lett., 52, 695]

Sikora M., Stawarz Ł., Moderski R., Nalewajko K., Madejski G. M., 2009, ApJ, 704, 38

Silva L., Maiolino R., Granato G. L., 2004, MNRAS, 355, 973

Silva L., Granato G. L., Bressan A., Danese L., 1998, ApJ, 509, 103

Simet M., Hooper D., Serpico P. D., 2008, Phys. Rev. D, 77, 063001

Singal J., Stawarz Ł., Lawrence A., Petrosian V., 2010, MNRAS, 409, 1172

Singal J., et al., 2010, ApJ, accepted, arXiv, arXiv:0901.0546

Sitarek J., Bednarek W., 2008, MNRAS, 391, 624

Skibba R. A., et al., 2009, MNRAS, 399, 966

Soifer B. T., Neugebauer G., 1991, AJ, 101, 354

Somerville R. S., Primack J. R., 1999, MNRAS, 310, 1087

Somerville R. S., Primack J. R., Faber S. M., 2001, MNRAS, 320, 504

Somerville R. S., Hopkins P. F., Cox T. J., Robertson B. E., Hernquist L., 2008, MNRAS, 391, 481

Somerville R. S., Gilmore R. C, Primack J. R, Domínguez A., 2011, in prep. (SGPD11)

Spergel D. N., et al., 2007, ApJS, 170, 377

Sreekumar P., et al., 1998, ApJ, 494, 523

Stecker F. W., Puget J. L., Fazio G. G., 1977, ApJ, 214, L51

Stecker F. W., Glashow S. L., 2001, APh, 16, 97

Stecker F. W., Malkan M. A., Scully S. T., 2006, ApJ, 648, 774

Stecker F. W., Baring M. G., Summerlin E. J., 2007, ApJ, 667, L29

Strateva I., et al., 2001, AJ, 122, 1861

Takeuchi T. T., Ishii T. T., Dole H., Dennefeld M., Lagache G., Puget J.-L., 2006, A&A, 448, 525

Tanaka Y. T., et al., 2011, arXiv, arXiv:1101.5339

Tavecchio F., Mazin D., 2009, MNRAS, 392, L40

Taylor E. N., et al., 2009, ApJ, 694, 1171

Tikhonov A. V., Klypin A., 2009, MNRAS, 395, 1915

Watkins R., Feldman H. A., Hudson M. J., 2009, MNRAS, 392, 743

Weekes T. C., et al., 2002, APh, 17, 221

Weinberg S., 1978, Phys. Rev. Lett., 40, 223

Wesson P. S., Valle K., Stabell R., 1987, ApJ, 317, 601

Wesson P. S., 1991, ApJ, 367, 399

Whitrow G. J., Yallop B. D., 1964, MNRAS, 127, 301

Whitrow G. J., Yallop B. D., 1965, MNRAS, 130, 31

Wilczek F., 1978, Phys. Rev. Lett., 40, 279

Williams R. J., Quadri R. F., Franx M., van Dokkum P., Labbé I., 2009, ApJ, 691, 1879

Willmer C. N. A., et al., 2006, ApJ, 647, 853

Wilson J. C., et al., 2003, SPIE, 4841, 451

Worsley M. A., et al., 2005, MNRAS, 357, 1281

Wyder T. K., et al., 2005, ApJ, 619, L15

Wu X., Hamilton T., Helfand D. J., Wang Q., 1991, ApJ, 379, 564

Wuyts S., et al., 2009, ApJ, 700, 799

Xu C. K., et al., 2005, ApJ, 619, L11

Yang J., Wang J., 2010, PASJ, 62, L23

Yoshida N., Stoehr F., Springel V., White S. D. M., 2002, MNRAS, 335, 762

Younger J. D., Hopkins P. F., 2011, MNRAS, 410, 2180

Zavattini E., et al., 2006, Phys. Rev. Lett., 96, 110406